The University Of Sheffield.

Modelling, Fault Detection and Control of Fault Tolerant Permanent Magnet Machine Drives

By

Bhaskar Sen

A thesis submitted in partial fulfilment of the requirements for the degree of Doctor of Philosophy

The University of Sheffield

Faculty of Engineering

Department of Electronic & Electrical Engineering

September 2015

"I know one thing: that I know nothing."

"True wisdom comes to each of us when we realize how little we understand about life, ourselves, and the world around us."

"Wonder is the beginning of wisdom."

- Socrates [470 – 399 BC]

Abstract

In order to address the issues of climate change, global warming and energy security, the adoption of plug-in electric vehicles (EV) in the transportation industry is considered as a potential solution. However reliability, availability and fail-safe operation of electrical systems is a growing concern among vehicle manufacturers and their customers.

This thesis is concerned with modelling, fault detection and control of permanent magnet machine with stator winding failures. It has been reported in various surveys that stator winding failure constitutes about 21-37% of the total failures in an electrical machine. Most winding failure start as incipient faults like inter-turn fault and develop into a complete winding failure.

In the first part of the thesis inter-turn fault in surface permanent magnet machine is modelled using analytical techniques and validated against finite element simulations. Two new techniques to model turn fault in interior permanent magnet machine is described, one based on finite element model extraction and the other using a semi-analytical technique requiring only the healthy machine data. Both these techniques are experimentally verified and the pros and cons of the two methods are discussed.

The second part of the thesis describes two new turn fault detection techniques for surface permanent magnet machines. One technique utilises the ripple current present in all pulse width modulated inverter fed motors to determine turn fault. The other is based on using the drive controller data and performing signal processing to extract the small fault signature. Both these methods are experimentally verified.

Finally a novel fault tolerant controller able to handle phase-open and phase-short condition is described. The controller is based on a stationary frame resonant control which simplifies operation under fault condition compared to a traditional synchronous frame controller commonly utilised in drives. Extensive testing is performed on a 5-phase fault tolerant machine to validate the controller.

This thesis is dedicated to my Parents,

Ruma & Siddheswar Sen

Acknowledgements

First of all, I would like to thank my supervisor, Prof. Jiabin Wang, for his continuous guidance, support and patience during the course of my PhD study. I am grateful to my 2nd supervisor, Dr. Martin Foster, for his continuous motivation and interesting discussions. I would like to express deep gratitude to the European Commission and to the MotorBrain project for providing funding for my research and for the support during the project.

I would like to express my thanks to Mr. Andy Race, Mr. John Wilkinson, Mr. Richard Garraway and Mr. Lawrence Obodo for their help in setting up the experimental rig.

I would like to thank my fellow graduate students, Mr. Akshat Mathur, Mr. Asiel Mendoza, Ms. Bing Liu, Mr. Chaohui Liu, Ms. Diana Mathew, Mr. Kalhana Colombage, Mr. Mirza Rasheduzzaman, Dr. Premlal Pillai, Mr. Panagiotis Lazari, Dr. Vipul Patel and Mr. Xiao Chen for the interesting discussions and for all the fun we had together in the past four years.

I would like to thank my mentors, Dr. Ramasamy Anbarasu and Dr. Viswanathan Kanakasabai for motivating me to pursue PhD.

Last but not the least, I would like to thank my parents, my sister and her family without whose support, help and motivation, I would never have been able to pursue my dreams.

Table of Contents

Abstract ..... **V**

Acknowledgements ..... **IX**

Table of Contents ..... **XI**

1 Introduction **1**

1.1 Trends in Transportation Sector 1

1.2 Increasing Availability 2

1.3 Propulsion Motors in Electric Vehicles 4

1.4 Electrical Machine Failures 4

1.5 Gaps in Existing Body of Knowledge 7

1.6 Thesis Outline 9

1.7 List of Publications 10

2 Analytical Modelling of Stator Turn Fault in Surface Permanent Magnet Machines **13**

2.1 Motivation 13

2.2 Literature Review 14

2.3 Reference FE model of SPM machine 15

2.4 Transient and Steady State Model 17

2.5 Analytical Modelling 19

2.5.1 Coil Definitions 19

2.5.2 Open Circuit Back-EMF 22

2.5.3 Armature Reaction Field and Airgap Inductance 26

2.5.4 Slot Leakage Inductance 30

2.6 Model Validation 36

2.6.1 BEMF Comparison 36

2.6.2 Airgap Inductance of Healthy Machine 37

2.6.3 Leakage Inductance of Healthy Machine 37

2.6.4 Overall Healthy Machine Inductance 38

2.6.5 Faulted Machine Inductance 38

2.6.6 Leakage Flux Estimation Error Analysis 41
2.6.7 Comparison with Classical Models 41
2.6.8 Fault Current Prediction 42
2.7 Conclusions 43

3 Transient Modelling of IPM with Stator Turn Fault 45

3.1 Motivation 45
3.2 Literature Review 46
3.3 Transient Machine Modelling under Stator Turn Fault 48
3.3.1 Machine Equations in *abc* Frame 49
3.3.2 Machine Equations in *dq* Frame 50
3.3.3 FE Model 52
3.3.4 Skew Computation 56
3.3.5 Inverse (Flux-Current) Lookup Algorithm for ODE solvers 61
3.4 Simulation Validation 64
3.5 Experimental Validation 68
3.6 Conclusions 75

4 Semi-Analytical Model of Interior Permanent Magnet Machine with Stator Turn Fault 77

4.1 Motivation 77
4.2 Literature Review 78
4.3 Reference FE Model for IPM Machine 79
4.4 Classical Turn Fault Model for IPM 82
4.4.1 Machine Equations in *abc* Frame 83
4.4.2 Machine Equations in *dq* Frame 85
4.5 Proposed Fault Model 87
4.5.1 MMF Distribution of the Fault Winding with Reference to Complete Phase Winding 88
4.5.2 MMF Flux Mapping 89
4.5.3 Fault Winding Interaction with Pole-Pair Winding Groups 92

4.5.4 Combined Flux-Linkages of All Pole-Pairs 97
4.5.5 Leakage Flux Calculation and Flux Linkage of Faulted Turns 98
4.5.6 Complete Turn Fault Model 101
4.6 Model Comparison with FE 102
4.7 Experimental Validation 105
4.8 Comparison of Simulation Setup Time with Direct FE Model 110
4.9 Conclusions 111

5 Online Stator Fault Detection Using Residual Currents 113

5.1 Motivation 113
5.2 Literature Review 114
5.2.1 Offline Fault Detection 114
5.2.2 Online Detection 115
5.3 Transient Machine Modelling under Stator Turn Fault 117
5.4 Steady State Voltage Analysis under Turn Fault 121
5.4.1 Phasor Analysis 122
5.4.2 Sequence Component Analysis 123
5.5 Steady State Residual Current Analysis under Turn Fault 126
5.5.1 Phasor Analysis 127
5.5.2 Sequence Component Analysis 129
5.6 Transient Machine Modelling under HRC 130
5.7 Steady State Voltage Analysis under HRC 131
5.7.1 Phasor Analysis 131
5.7.2 Sequence Component Analysis 132
5.8 Steady State Residual Current Analysis under HRC 134
5.8.1 Phasor Analysis 135
5.8.2 Sequence Component Analysis 136
5.9 Fault Detection 137
5.9.1 Extraction of Sequence Components 138

5.9.2 Residual Current extraction 150
5.9.3 Faulted Phase Detection 156
5.9.4 Fault Classification 156
5.10 Simulation Results 156
5.11 Experimental Validations 159
5.11.1 Machine Back-EMF 160
5.11.2 Plant Fitting 163
5.11.3 Healthy Machine Transient Response 164
5.11.4 Turn Fault Detection 165
5.11.5 HRC Fault Detection 171
5.11.6 Fault Classification 174
5.11.7 Comparison of Detector Output in Steady State 175
5.12 Extension to 3-phase IPM machines 180
5.13 Conclusions 188

6 Online Stator Turn Fault Detection Using PWM Ripple Current Measurement 191

6.1 Motivation 191
6.2 Literature Review 192
6.3 Transient Machine Modelling under Stator Turn Fault 193
6.4 PWM Ripple Current Based Detector Design 202
6.5 Circuit Implementation of the Detector 206
6.6 Simulation Results 207
6.7 Experimental Testing 209
6.8 Fault Detection 214
6.9 PWM Ripple Current under High resistance Connection 220
6.10 Conclusions 221

7 Stationary (abcde) Frame Fault Tolerant Current Control of Poly-phase PM Machines under Open-Circuit and Short-Circuit Faults 223

7.1 Motivation 224
7.2 Literature Review 224

7.3 Optimal Current Reference Generation 227
7.4 Discrete-Time Plant Model 231
7.5 Current Control 232
7.6 Zero Sequence Voltage Injection 240
7.7 Torque Speed Characteristics 241
7.8 Field Weakening 243
7.9 Experimental Validations 244
7.10 Conclusions 254

8 Conclusions and Future Work 257

8.1 Conclusions 257
8.2 Future Work 260

Bibliography 263
List of Figures 279
List of Tables 289
Appendix: 5-phase inverter 291

Chapter 1

Introduction

1.1 Trends in Transportation Sector

Mobility underpins our way of life. From time immemorial, humankind has tried to increase its mobility. From horses to steam engines from cars to aircraft, our pursuit has been to achieve faster means of travel. Up until the invention of the steam engine the only means of ground transportation other than on foot or horse has been animal drawn wagon or sled. In the late 19th century, the internal combustion engine (ICE) was invented which brought about the automotive revolution. Road transport now is an integral part of our lives. It has dramatically improved personal mobility and economic prosperity.

However, the use of fossil fuel as energy source for automobiles and industry has led to ever increasing carbon and greenhouse emissions which induce climate change and deterioration of air quality. In 2007 G8 summit an ambitious target of 50% reduction in global emission (relative to 1990 levels) by 2050 was adopted[1].

One way of achieving this in road transportation sector is adoption of cleaner fuels. Bio-fuel is one such option. Since bio-fuel is not based on fossilised carbon, its use is not expected to increase the overall CO_2 balance. In Brazil for example, ethanol based bio-fuel has been promoted by the government as a means of reducing the country's fossil fuel dependence. However, production of bio-fuels can put the already strained environmental resources under pressure. Hydrogen and fuel cells have been proposed but are not yet popular due to risk of handling hydrogen. Another way of achieving fuel efficiency has been hybrid and plugin hybrid vehicles, which enable the ICE engine to operate at optimal speed and efficiency, and the balance of power is

[1] http://www.g-8.de/Webs/G8/EN/News/news.html

provided by an electric motor. Finally battery electric vehicles are gaining more acceptances in the market due to better battery technologies, efficient and power dense electrical motors and increasing number of charging stations. However, unlike ICE cars, where a minor fault may not result in a complete breakdown, even a small electrical fault like a loose connector can bring an electric vehicle to a complete standstill. As electric cars become more widespread ensuring high availability is expected to become more and more important. From a consumer point of view it means that the system lasts longer and will not suffer from a catastrophic failure.

In the aerospace industry there has been a push towards more electric aircraft (MEA). Traditional hydraulic actuators have been steadily replaced by electro-hydraulic actuators which lead to reduced weight due to reduction of the hydraulic piping. Recently, the EADS demonstrated an all-electric aircraft E-Fan[2], designed to showcase the technology of electric motors for primary propulsion of the aircraft.

Therefore, ensuring fast incipient fault detection, fault tolerance and fail-safe operation is one of the key techniques that are required to ensure that a single failure of any subsystem will not cause a complete failure of the system.

1.2 Increasing Availability

Availability is the ratio of the total time of a drive capable of being used during a given interval to the length of the interval. In conventional motor drives an unexpected failure of any component leads to a motor-drive shutdown thereby reducing the availability of the system and leads to economic loss. In applications such as electric vehicles [1]–[3] and aircraft fuel pump systems [4]–[6], unexpected shutdown can lead to high repair costs or more critically lead to unsafe mode of operation of the entire system. To overcome this, in industrial and aerospace applications redundancy and/or conservative designs are commonly employed. Redundancy consists of designing two or more identical and independent systems which are either sharing the load or are designed as spare units. In case of fault, the spare units are able to take over the operation of the faulted unit. Conservative designs consist of oversizing the motor-drive system so as to minimise the likelihood of fault due to lower stress on the system.

[2] http://www.airbusgroup.com/int/en/innovation-citizenship/airbus-e-fan-the-future-of-electric-aircraft.html

However, this can significantly increase the cost of the system. In aerospace application, non-recurrent cost is not of much concern, but oversizing leads to increase in weight and in the cost competitive automotive sector, this is not an acceptable solution.

Preventive maintenance is one approach to decreasing the likelihood of unexpected downtime due to failure of a component. A given part of the drive can be replaced after a predetermined period of time, which is calculated on the basis of statistics of historic data on failure of the particular part. This approach is typically employed in the aerospace industry. However, replacement of a good working part just because it has crossed its expected lifetime is not very economically attractive.

One way to improve availability without cost penalty is to develop prognostic and condition monitoring methods to monitor the aging process of critical components. This enables the monitoring system to flag an impending failure to the operator enabling the operator to schedule preventative maintenance. Prognostic methods depend on monitoring fault indices which require long period trending and a calibrated dataset to determine when to flag a faulty component to the operator. However a sudden or a rapidly progressing fault such as a stator inter-turn fault cannot be handled by this technique.

A way to handle rapidly progressing faults is to develop diagnostic and fault detection methods to detect small incipient faults which enable application of mitigation techniques to prevent the development of the incipient fault into a system failure. This implies that the fault has to be detected at an early stage of development and therefore the detector needs to be fast. However it presents challenges in detection due to small incipient nature of the fault in a high noise environment. One such challenge is the need to robustly reject the changes in the fault indices due to load or speed changes in order to avoid false alarm.

The last line of defence in preventing a complete shutdown of a motor-drive system due to a fault that cannot be predicted or detected within a required period is the application of advanced fault tolerant controls. Fault tolerant controls as the name suggests is an advanced control system capable of maintaining continued operation of a system albeit at a reduced torque-speed envelope under fault condition.

Therefore due to an increased application of electrical machines in safety critical applications, a real-time integrated health monitoring that can detect, classify, and

predict developing faults and a fault tolerant control system is critical to reducing operating and maintenance costs while optimising the life and availability of the system.

1.3 Propulsion Motors in Electric Vehicles

Table 1-1 shows the propulsion motor technology for the most popular electric vehicles in the market today, including battery EV and hybrid EV. It can be seen, that with the exception of the Tesla S, most motors in electric vehicles are based on permanent magnet technology. Permanent magnet machines are increasing being favoured as the motor of choice for traction applications due to their high power density and overall high efficiency [1].

Table 1-1: Popular Electric Vehicles Motor Specifications[3]

Vehicle	**Motor Technology**	**Power Rating**
Tesla S	Induction motor	310 kW
Toyota Prius	Permanent magnet	60 kW
Peugeot 3008 Hybrid4	Permanent magnet	28kW
Honda Insight	Permanent magnet	10kW
Lexus CT200h	Permanent magnet	60kW
Nissan Leaf	Permanent magnet	80kW
Chevrolet Volt	Permanent magnet	111 kW

1.4 Electrical Machine Failures

Several surveys on reliability of industrial motors conducted by Electric Power Research Institute EPRI [7] and IEEE [8]–[11] concluded that stator winding failures accounts for about 21-37% of faults in electrical machines. Fig. 1-1 shows the distribution of failure of various motor components reported in [11] and indicates the winding faults account for 21% of the total. Other surveys [7], [8] showed a slightly high winding failure percentages. In any case, it can be seen that stator winding failure is the 2nd most common failure mode of industrial motors.

[3] http://www.cars-data.com

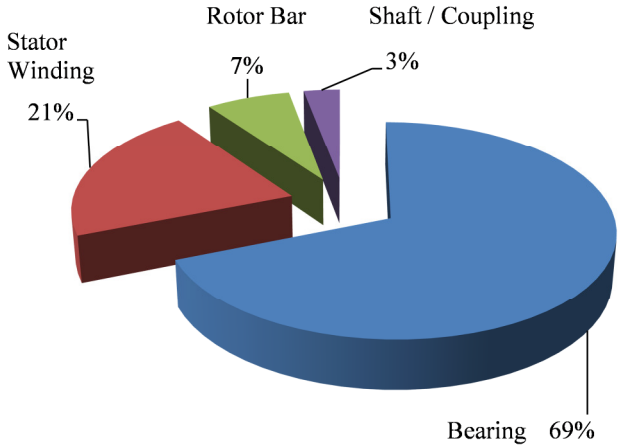

Fig. 1-1: Distribution of faults

There are many causes for accelerated aging of winding insulation.

1. **Electrical Stress**

Electrical stress caused by transients like switching is one of the major causes of insulation failures. Transients due to circuit breaker/re-closer operation have long been the cause of insulation failure in large industrial motors [12]. Transient voltages when impressed on stator windings distribute non-uniformly, with most of the voltage getting distributed in the first few turns of the phase winding closest to the motor terminal. Repeated transients have been observed to cause rapid deterioration of insulation. This is particularly true in case of variable frequency drives due to switching operation of the drive inverter [13]. Also, voids created during winding insulation or potting are sites of partial discharge that cause local heating and rapid degradation of surrounding insulation eventually leading to failure of the insulation. Sudden short circuit currents due to terminal short circuits, poses severe thermal and mechanical stress on the coils, especially the end-windings causing eventual failure.

2. **Thermal Cycling**

Temperature is a known factor in accelerating aging process in insulators [12]. Thermal cycling is among the biggest causes of failure in insulation, since it subjects the insulation and the winding through expansion and contraction, causing failure of insulation bonding, cracking of the insulation, and void

formation which due to presence of electric field of the winding starts to undergo partial discharge and eventual failure. Another mechanism is thermal aging of the winding. An increase in operating temperature of the coils can reduce the insulation lifetime significantly. For example, a 10º C rise in temperature above rating can decrease insulation life by 50% [12]. One way to reduce this effect is to reduce the thermal loading by better cooling or using a higher insulation class.

3. **Environmental Conditions**

   Operating environment condition of the motor can lead to degradation of winding insulation. Environmental factors such as high humidity, poor ventilation, chemicals, and sea salt in costal or off-shore installations can cause degradation of insulation, by either corrosion or by deposition on insulation, causing electrical discharge. For example, the presence of dust can lead to reduced heat dissipation, increasing thermal degradation of the winding. Salt along with moisture deposition on winding insulation can cause electrical tracking [12].

4. **Mechanical Stress**

   Mechanical stress on the winding insulation can degrade the winding insulation strength. The electromagnetic force experienced by end-coils is proportional to the square of the motor current can cause pulsating force on the coils. Mechanical stress can also occur due to vibration of the motor, particularly experienced in traction motors.

The gradual degradation of insulation strength leads to the conductors in the winding to come in contact either with other turns or to the ground wall. One of the leading mechanisms of a complete winding failure are inter-turn short-circuit failures (TF) [14] which are especially critical, since the current flowing in the shorted turns can far exceed the rated current of the winding [15], [16]. This can lead to thermal degradation of winding insulation close to the faulted turns and the fault can progressively spread leading to a complete winding fault. The heat generated by the winding fault can cause degradation of not only the coils near it, but also the stator core, leading to costly and lengthy unscheduled maintenance shut down. This is more critical

in permanent magnet (PM) machines since a simple shutdown of the inverter is not enough to mitigate turn faults due to presence of magnets in the rotor, the current continues to flow in the faulted turns until the rotor has stopped spinning. The large circulating current in the faulted turns can also produce irreversible demagnetization of the magnets [17] thereby damaging the rotor as well as the stator if the fault is not checked.

Stator turn fault detection has been under investigation since the early 1980's and many techniques (mainly for induction machines) have been presented in literature. One of the techniques is the use of off-line fault detection. This is done during routine planned maintenance on the machine where the machine is taken off service and tested using techniques like DC winding resistance test, surge test and partial discharge test [12]. However this means that if fault develops in between maintenance periods it will remain undetected and can potentially cause complete winding failure. Therefore an online approach is more suited to inter-turn fault detection. There are several online techniques for inter-turn fault detection in literature, namely using motor current signature analysis (MCSA)) [18]–[20], high frequency (HF) injection [19], [21], [22], measurement of axial leakage flux [23]–[25] and search coil based measurement of flux-linkage unbalance [26]–[28], neutral point voltage measurement [29]–[31], fundamental frequency analysis [32]–[34] and state estimation based methods [35], [36].

1.5 Gaps in Existing Body of Knowledge

Although the topic of fault detection and fault tolerant controls has received increased attention from the research community over the past few decades there are a number of areas where there are gaps in the knowledge.

One such area is the accurate modelling of machines under turn fault. Machine models are crucial in the development of new fault detection and mitigation techniques. However, most models in literature either have simplifying assumptions or are finite-element based models. The former is not sufficiently accurate for representing the fault behaviour while the latter is computationally inefficient and not suitable for system level study and simulation. For surface mounted permanent magnet (SPM) machines, analytical modelling techniques for predicting magnetic field distribution in the air-gap

have been well established, and it should be possible to develop accurate models of a machine under both healthy and fault conditions without the need for FE simulations. This is of potential interest to drive system designers who need to simulate fault conditions to test control and fault detection. However, most of them may not have the necessary expertise or access to finite element analysis software.

Similar gap exists in fault modelling of interior permanent magnet (IPM) machines. It is known that IPM machines have highly non-linear magnetic behaviour even under healthy conditions. Under a fault condition, localised saturation is more pronounced and this behaviour has to be accurately captured in order to have a representative model of the machine. Till now, the models presented in literature are either too simplistic based on assuming linear behaviour or are very time consuming based on time-stepped finite element simulations.

In the area of fault detection, stator inter-turn fault detection for multi-phase machines have not been researched extensively. Some techniques based on analysis performed for 3-phase analysis have been utilised, but most of the techniques cannot perform fast detections in the presence of load or speed disturbances.

In the area of drive controls, there has been an increased interest in developing control techniques for fault tolerant operation. Multi-phase machines due to their higher degree of freedom (number of phases greater than 3) can operate with reduced torque under open and short circuit faults, provided that the short circuit current can be limited to a manageable level. However, most of the proposed control techniques in literature are limited in operation and have been tested only under constant torque operation. Field weakening and control transitioning from healthy to fault operation have received little attention in the literature so far.

The research objectives of this thesis are summarized below:

1. Developing turn fault modelling techniques for permanent magnet (interior and surface mounted) machines.
2. Developing new real time fault detection and identification methods for turn faults and high resistance connection for multi-phase permanent magnet machines.

3. Developing fault tolerant control strategy for open and short circuit faults for multi-phase permanent magnet machine.

1.6 Thesis Outline

The main aim of the thesis is to address these knowledge gaps identified in section 1.5 in order to improve availability of permanent magnet machine drives. The thesis is organised into 8 chapters. The brief summary of each chapter is presented below.

Chapter 1 introduces the global technological trend of electric drives towards more electrification in transportation sector, namely in automotive and aerospace industries as a means to reduce carbon emissions, increased efficiency and safety. The various trends in the two sectors have been described and the need to improve fault diagnosis and fault tolerant controls has been presented.

In order to develop novel fault detection and mitigation strategies a machine model is required. Chapter 2 develops the theory of analytical machine modelling applied to stator turn fault for surface mounted permanent magnet machine. Mathematical modelling presented in this chapter enables designers to quickly assess the impact of machine design and topology on fault currents and can be used to develop machine models for simulation without the need for finite-element simulations.

An important class of permanent magnet machines utilised for traction applications is interior permanent magnet machines. These are characterised by buried magnets in the rotor and typically exhibit non-linear magnetic characteristics. In Chapter 3 an accurate transient model of Interior Permanent Magnet (IPM) machine with stator turn fault with due account of magnetic saturation is developed using flux-linkage map of IPM machine under fault extracted from Finite Element (FE) analysis. The modelling technique is evaluated against FE and experimental results.

In Chapter 4 a semi-analytical model of IPM machine under stator winding inter-turn fault conditions is described. It employs the *dq* flux-linkage map of healthy IPM machine and combines it with analytical equations of turn fault machine in the *dq* frame. The main advantage of this method as opposed to the full FE based model described in Chapter 3 is that no additional FE data is required for the model. Although this modelling technique is not expected to be as accurate as the FE based model, it has

the advantage of requiring much less time and computation resources for implementation. The accuracy of the model is verified against FE and experimental data.

Stator turn fault causes large circulating current in the faulted turns which gives rise to a local hot spot and lead to further insulation failures and ultimately failure of the entire winding. Therefore the fault has to be detected quickly and robustly so that corrective action can be initiated. Turn faults can be detected by applying signal processing online on the controller data, i.e., fundamental voltages and currents. This is investigated in Chapter 5, where an online model based approach is utilised for fault detection. The detection method is purely a software based approach and can be easily incorporated in existing drive controllers. The detection technique is capable of identifying the faulted phase and differentiating between turn fault and high resistance connection.

One interesting effect of turn fault in a winding is the reduction of high frequency winding impedance particularly in the PWM switching frequency range (10 – 20 kHz). This phenomenon is investigated for fault detection in Chapter 6. A hybrid modelling technique is proposed to model the winding high frequency impedance, and a fault detection circuit is designed. This approach is validated against experimental results.

Fault tolerant controls for multi-phase machines under open and short circuit condition is developed in Chapter 7. A novel stationary frame controller capable of controlling unbalanced current and able to operate in field weakening region is presented. Experimental tests are conducted to validate the new control strategy under steady state and under healthy to fault transitioning modes.

Finally, conclusions and recommendations for future work are presented in Chapter 8.

1.7 List of Publications

Most of the research work reported in this thesis has been published in peer-reviewed international conferences and journals. The various publications are listed below.

1. **B. Sen** and J. Wang, "Stator Inter-turn Fault Detection in Permanent Magnet Machines Using PWM Ripple Current Measurement," IEEE Transactions on Industrial Electronics, Accepted for publication, Oct 2015, in press.
2. **B. Sen** and J. Wang, "Stationary Frame Fault Tolerant Current Control of Poly-phase Permanent Magnet Machines under Open-Circuit and Short-Circuit Faults," IEEE Transactions on Power Electronics, Accepted for publication, Aug 2015, in press.
3. **B. Sen**, J. Wang, P. Lazari, "A High Fidelity, Computationally Efficient Transient Model of Interior Permanent Magnet Machine with Stator Turn Fault," IEEE Transactions on Industrial Electronics, Accepted for Publication, Aug. 2015, in press.
4. X. Chen, J. Wang, **B. Sen**, P. Lazari, and T. Sun, "A High-Fidelity, Computationally Efficient Model for Interior Permanent Magnet Machines Considering the Magnetic Saturation, Spatial Harmonics and Iron Loss Effect," IEEE Transactions on Industrial Electronics, vol. 62, no. 7, pp. 4044–4055, Jul. 2015.
5. P. Lazari, **B. Sen**, J. Wang, and X. Chen, "Accurate (d)-(q) Axis Modeling of Synchronous Machines With Skew Accounting for Saturation," IEEE Transactions on Magnetics, vol. 50, no. 11, pp. 1–4, Nov. 2014.
6. P. Lazari, **B. Sen**, J. Wang, and X. Chen, "Accurate d-q axis modelling of Synchronous Machines with Skew accounting for Saturation," presented at the IEEE International Magnetics Conference (INTERMAG - 2014), Dresden, 2014.
7. **B. Sen** and J. Wang, "A fast detection technique for stator inter-turn fault in multi-phase permanent magnet machines using model based approach," in 7th IET International Conference on Power Electronics, Machines and Drives (PEMD 2014), 2014, pp. 1–6.
8. **B. Sen** and J. Wang, "Stator inter-turn fault detection in SPM machines using PWM ripple current measurement," in 7th IET International Conference on Power Electronics, Machines and Drives (PEMD 2014), 2014, pp. 1–6.
9. **B. Sen** and J. Wang, "Analytical modelling of stator turn fault in surface mounted permanent magnet machines," in 2013 IEEE Energy Conversion Congress and Exposition (ECCE), 2013, pp. 4445–4452.

10. **B. Sen**, J. Wang, and P. Lazari, “A detailed transient model of Interior Permanent Magnet motor accounting for saturation under stator turn fault,” in 2013 IEEE Energy Conversion Congress and Exposition (ECCE), 2013, pp. 3548–3555.

Chapter 2

Analytical Modelling of Stator Turn Fault in Surface Permanent Magnet Machines

The main contribution of this chapter is to present a general analytical technique for analysing stator winding inter-turn faults in surface permanent magnet (SPM) machine with arbitrary winding configuration. This approach takes advantage of well-established analytical methods used to analyse behaviour of healthy SPM machines, and applies those techniques for purposes of creating a machine model of SPM machine with turn faults. Concentrated-winding machines as well as distributed winding machines can be analysed using this technique. For purpose of validation, a model of fractional slot wound SPM motor is derived analytically and compared with finite element (FE) simulations. Finally the predictions of the model are compared with standard turn fault model in literature which highlights the need for accurate turn fault modelling.

The developed model can be used to evaluate drive performance under faults, to test novel fault detection algorithms, or can be used by machine designers to analyse the effect of geometry parameters and winding configurations on fault current magnitude. Major contents of this chapter were published by the author in [37].

2.1 Motivation

As explained in Chapter 1, one of the leading causes of winding failure are inter-turn short-circuit failure which is especially critical, since it leads to a large circulating fault current in the faulted turns [15]. This is specially a problem in permanent magnet machine where the magnet field sustains fault current as long as the rotor rotates even after the motor drive has been turned off. This large fault current gives rise to a local hot spot due to ohmic losses in the faulted turns which can cause further insulation

degradation/failures and ultimately leading to a complete failure of the winding as a phase-ground or phase-to-phase fault [38]. The large fault current in the faulted turns can also produce irreversible demagnetization of the magnets [17].

Therefore inter-turn winding faults in permanent magnet machines must be quickly detected and mitigating controls initiated to prevent catastrophic failure of the machine. Such a functionality commonly known as “limp-home” mode [39] is essential for providing high degree of availability, and reliability demanded in safety critical application such as electric vehicles. In order to develop sensitive fault detection algorithms and fault tolerant control strategies, an accurate model of the machine under fault condition is therefore indispensable.

2.2 Literature Review

The modelling of inter-turn short circuit fault, referred to as turn fault, in an SPM machine was treated in [40]–[42] where FE analysis was used to extract circuit parameters of the faulted machine. However, creating an FE model of machine under fault and extraction of individual coil inductances can be time-consuming [43]. In order to derive a fault model without relying on FE analysis, a simplifying assumption of sinusoidal distribution of winding magneto-motive force (MMF) can be used [44], which enables the computation of inductances under fault using a simple scaling factor namely, the fault ratio ‘μ’ which is the ratio of the number of short-circuited turns to the total number of turns in a phase winding as shown in [45], [46]. However, the assumption of sinusoidal distributed winding MMF introduces unnecessary errors in the model, and cannot be applied to a more general class of machine with different winding configurations, in particular fractional slot windings commonly used in SPM motors. In [43] the model of [45], [46] was modified by using local winding fault ratio per stator coil along with FE analysis to compute the inductances of healthy coils, including mutual and leakage and slot mutual inductance and combining it to generate the overall fault model. In [47] winding function theory is used to derive fault inductances, however effect of slot leakage flux is ignored. In [15] an analytical method for computing circuit model of alternate tooth wound SPM machine was presented, wherein the mutual magnetic coupling between phases is negligible and there is only one coil

side per slot. Since the analysis in [15] is restricted to a special class of machine it cannot be readily utilised for analysis of other winding configurations.

The present work extends the approach presented in [15] for a general class of SPM machine, which can have different winding configuration and stator slots can have 2 coil sides.

2.3 Reference FE model of SPM machine

For the purpose of validation of the analytical model, an FE model of a 3-phase, 12-slot, 14-pole SPM machine is taken as reference. Each phase of this example machine has 4 series connected coils with 8 turns in each coil. The machine has a peak power of 10kW at a base speed of 1350 rpm and its design details are given in Table 2-1. Fig. 2-1 shows the geometry of the healthy machine.

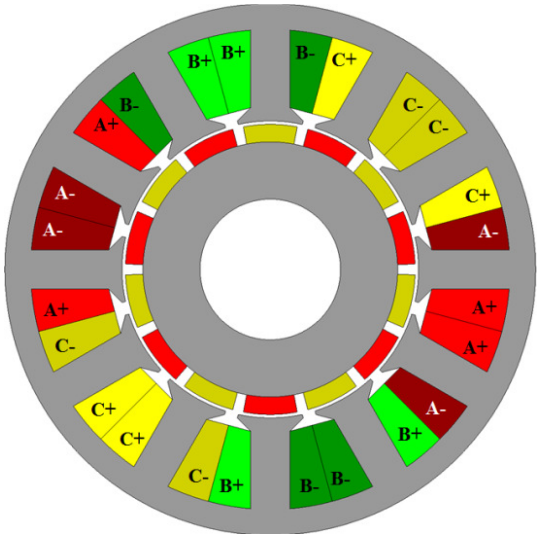

Fig. 2-1: Geometry of 12 slot, 14 pole SPM Machine

In order to validate the analytical fault model, a modified FE model of the machine is created. This is shown in Fig. 2-2, wherein one coil in phase-A has been purposefully subdivided into its constituent 8 turns. This enables creation of faults in these turns and the machine parameters can be extracted and compared against the analytical model.

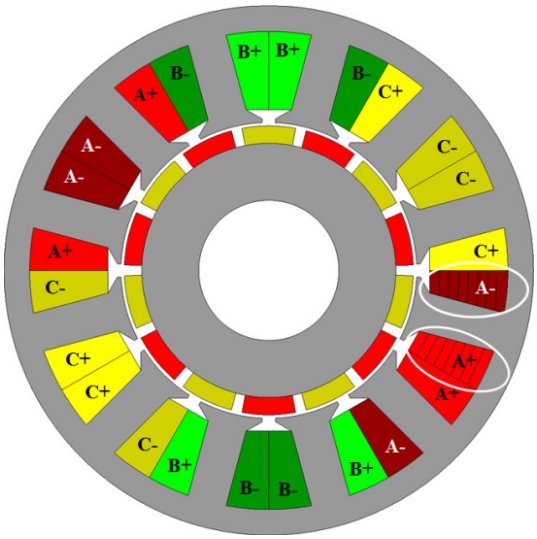

Fig. 2-2: FE model with turn fault (circled) in phase A for model validation

Table 2-1: Machine Specifications

Quantity	**Unit**	**Value**
Torque (peak/rated)	Nm	70/35
Speed (base/max)	r/min	1350/5050
Power (peak/rated)	kW	10/5
Current (peak/continuous)	A (peak)	170/84
Number of pole-pairs	--	7
Number of slots	--	12
Number of turns per coil (N_c)	--	8
Number of coils/phase	--	4
Number of turns/phase (N_t)	--	32
Active stack length (L_{stk})	mm	118
Stator outer diameter	mm	150
Airgap	mm	0.955
Rotor radius (R_r)	mm	41.25
Magnet length (l_m)	mm	5
Magnet pole arc (α_p)	degree	150
Magnet Remanence (B_r)	T	1.12

2.4 Transient and Steady State Model

A general 3-phase SPM machine with turn fault can be represented schematically as shown in Fig. 2-3.

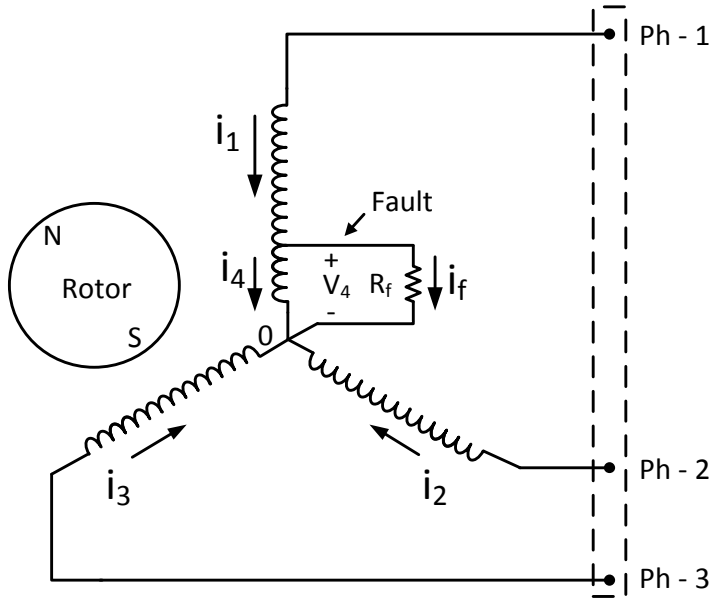

Fig. 2-3: Schematic representation of SPM machine with turn fault on a single phase.

The stator voltage equation can be expressed as (2.1) ,

$$\boldsymbol{v}_s^{\,f} = \boldsymbol{R}_s^{\,f}\boldsymbol{i}_s^{\,f} + \boldsymbol{L}_s^{\,f}\frac{d\boldsymbol{i}_s^{\,f}}{dt} + \boldsymbol{e}_s^{\,f} \tag{2.1}$$

where, $\boldsymbol{v}_s^f$, $\boldsymbol{i}_s^f$, $\boldsymbol{e}_s^f$, $\boldsymbol{R}_s^f$, and $\boldsymbol{L}_s^f$ denotes the voltage, current, back-EMF, resistance and inductance matrices of the system respectively. The faulted winding is considered as a separate winding and denoted as an additional phase (phase-4). For notational convenience, subscripts 1, 2, and 3 denote phases A, B, and C, respectively and superscript *f* denotes fault condition. The matrices can be expressed by (2.2)-(2.3),

$$\begin{aligned}
\boldsymbol{v}_s^{\,f} &= \begin{bmatrix} V_1 & V_2 & V_3 & V_4 \end{bmatrix}^T \\
\boldsymbol{i}_s^{\,f} &= \begin{bmatrix} i_1 & i_2 & i_3 & i_4 \left(= i_1 - i_f\right) \end{bmatrix}^T \\
\boldsymbol{e}_s^{\,f} &= \begin{bmatrix} e_1 & e_2 & e_3 & e_4 \end{bmatrix}^T
\end{aligned} \tag{2.2}$$

$$\begin{aligned}\boldsymbol{R}_s{}^f &= diag\begin{bmatrix}R_1 & R_2 & R_3 & R_4\end{bmatrix}\\ &= diag\begin{bmatrix}R(1-\mu) & R & R & R(\mu)\end{bmatrix}\end{aligned}$$

$$\boldsymbol{L}_s{}^f = \begin{bmatrix}L_{11} & L_{12} & L_{13} & L_{14}\\ L_{21} & L_{22} & L_{23} & L_{24}\\ L_{31} & L_{32} & L_{33} & L_{34}\\ L_{41} & L_{42} & L_{43} & L_{44}\end{bmatrix} \tag{2.3}$$

$$V_4 = i_f R_f \tag{2.4}$$

where R_i, I_i, E_i and L_{ii} (i = 1, 2, 3, and 4) denote the resistance, current, back-EMF and self-inductances of the i^{th} windings. L_{ij} (i, j = 1, 2, 3, 4, $i \neq j$) denotes the mutual inductance between phases i and j, R_f denotes the external fault resistance across the two shorted circuit terminals and 'μ' denotes the winding fault fraction expressed by (2.5).

$$\mu = \frac{\text{No. of Faulted Turns}}{\text{Total No. of Turns/phase}} \tag{2.5}$$

Under sinusoidal steady state condition the equations can be re-written using phasor analysis as (2.6), where j is the imaginary operator and ω_e is the angular frequency in rad/sec, and arrow superscript denotes phasor quantities.

$$\begin{aligned}\vec{V}_4 &= \overrightarrow{I_f} R_f\\ &= \begin{bmatrix}R_4 & 0 & 0\end{bmatrix}\overrightarrow{\boldsymbol{I}_s} + j\omega_e\begin{bmatrix}L_{41}+L_{44} & L_{42} & L_{43}\end{bmatrix}\overrightarrow{\boldsymbol{I}_s}\\ &\quad -R_4\overrightarrow{I_f} - j\omega_e L_{44}\overrightarrow{I_f} + \overrightarrow{E_4}\end{aligned} \tag{2.6}$$

The fault current can then be obtained as given by (2.7),

$$\overrightarrow{I_f} = \frac{\left(R_4\vec{I}_a + j\omega_e\begin{bmatrix}L_{41}+L_{44} & L_{42} & L_{43}\end{bmatrix}\overrightarrow{\boldsymbol{I}_s} + \overrightarrow{E_4}\right)}{R_f + R_4 + j\omega_e L_{44}} \tag{2.7}$$

where, $\boldsymbol{I}s$ is given by (2.8).

$$\overrightarrow{\boldsymbol{I}_s} = \begin{bmatrix}\overrightarrow{I_1} & \overrightarrow{I_2} & \overrightarrow{I_3}\end{bmatrix}^T \tag{2.8}$$

In order to predict the fault currents and voltages, determination of the parameters of machine is essential. This is done by solving analytically the magnetic field equations under fault conditions as detailed in the next few sections.

2.5 Analytical Modelling

For the purpose of deriving a fault model, the following assumptions are made.

- Laminations are infinitely permeable. Magnetic saturation is neglected.
- Slot-leakage flux is parallel to the circumferential direction.
- The coil turns are uniformly distributed along the slot height.
- The shorted turn is treated as the 4^{th} winding while deriving the model.
- Single layer non-overlapped winding is considered for the study.
- Variation of effective airgap permeance due to slot opening is neglected.
- End winding leakage is neglected. The end winding leakage inductance calculated by PC-BDC program is 0.0025mH which is less than 1% of the phase inductance.

To facilitate a general framework for analysing any SPM machine with turn-fault, it is essential to create an easy way of handling different winding configurations. This is done by using a convenient form of coil definition.

2.5.1 Coil Definitions

Coil definition is used for easy handling of coil data for use in computation of flux linkages for back-EMF computation as well as the inductance calculations. Table 2-2 shows the coil definition table with 2 coils as an example.

Table 2-2: Coil Definitions

Coil No.	Ph. No.	Go Slot (a_2)	Return Slot (a_1)	No. Of Turns
1	1	12	1	8
2	1	12	11	8

Here go slot (a_2) refers to the coil side having positive direction of current (out of the sheet of paper) and return slot (a_1) having negative direction of current. The coil definition is performed for all the coils in the machine. The reference for the slot

numbering is arbitrary and can be started from any slot. For the case considered, the slot numbering is as shown in Fig. 2-4.

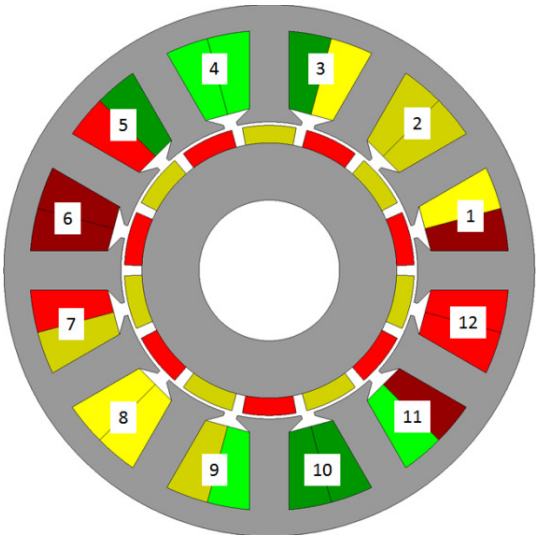

Fig. 2-4: Slot numbering convention

The faulted coils are defined by using the coil number of the original healthy coil as reference. Table 2-3 shows an example faulted coil definition, wherein a 1 turn fault has been assumed in coil 1. Phase number denotes that the faulted coil will be treated as an additional phase (4). The location of the faulted turns may be sandwiched between two parts of the healthy turns, denoted by N_{ha} and N_{hb} with N_{ha} being the number of healthy turns between the fault winding and the bottom of the slot as shown in Fig. 2-5.

Table 2-3: Fault Coil Definition

Coil No.	Phase No.	No. of healthy turns (N_h)	Loc. Of faulted turn in slot (N_{ha})
1	4	7	1

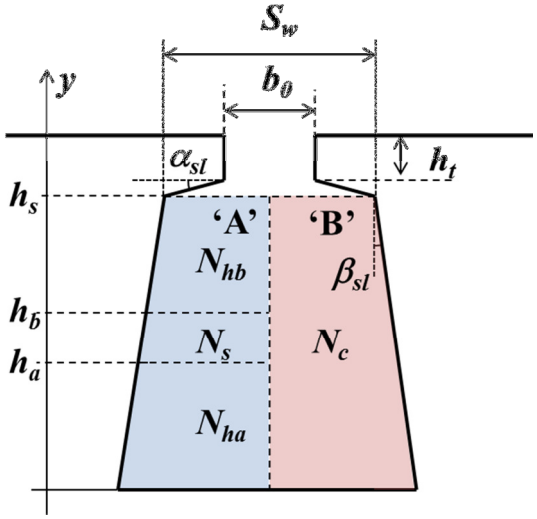

Fig. 2-5: Slot dimension nomenclature. Fault turns are denoted by N_s.

Using the coil and fault coil definition table an augmented coil definition table is created as shown in Table 2-4.

Table 2-4: Augmented Coil Definition

Coil No.	Ph. No.	Go Slot (a_2)	Return Slot (a_1)	No. Of Turns (T_c)
1	1	12	1	**7**
2	1	12	11	8
…	…	…	…	…
13	4	12	1	**1**

The go and return slot numbers, i.e., a_1 and a_2 define the position of the coil in the machine and therefore the analytical equations are derived using these two parameters to predict the flux linkages of a given coil. Since the system has been assumed to be magnetically linear, superposition theorem can be applied to compute overall flux of each winding by adding the flux linkage contribution of each individual coils. The definition of coils performed this way is therefore a useful way of generalizing the code for calculation of parameters.

2.5.2 Open Circuit Back-EMF

Fig. 2-6 shows the rotor geometry of a PM machine, where R_r and R_m are the rotor inner and outer radii, R_{st} is the stator bore radius and M is the magnetisation vector of the rotor magnets shown for the case of parallel magnetisation.

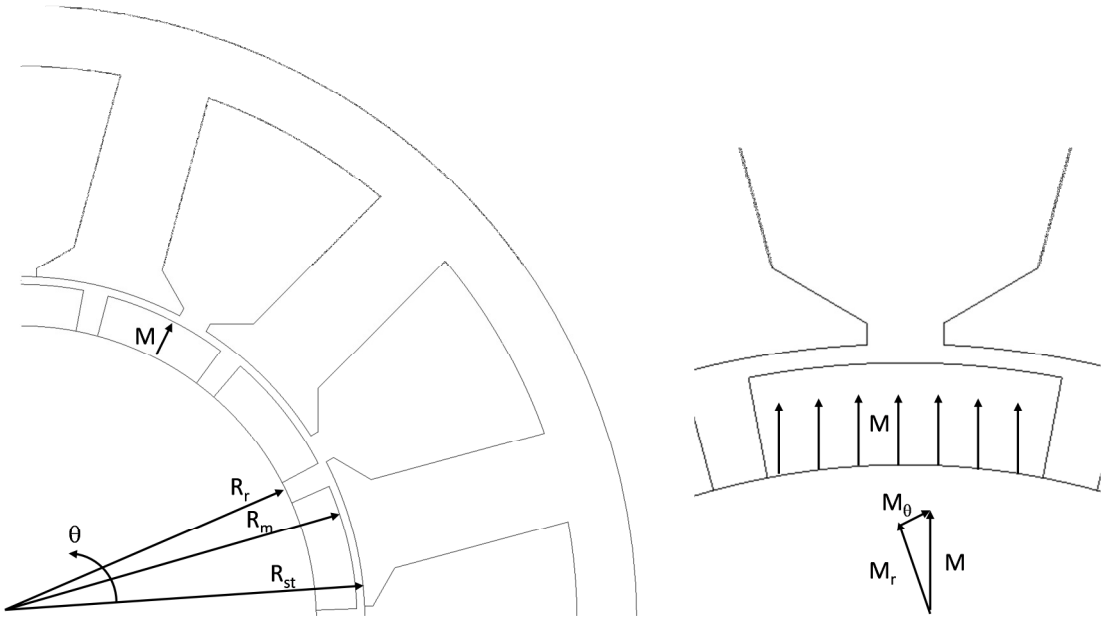

Fig. 2-6: Rotor topology of the machine

In order to compute the back-EMF voltage magnetic field distribution under no load can be derived by solving the Laplace equation (2.9) in air-gap and Poisson's equation (2.10) in magnet [48]–[53] for the magnetic scalar potential φ, where M is the magnetization vector of the magnets defined in (2.12) where M_r and M_θ are the radial and tangential components, a_r and a_θ are unit vectors and r and θ_m are the radius and angle of the point in space under consideration.

$$\frac{\partial^2 \varphi_I}{\partial r^2} + \frac{1}{r}\frac{\partial \varphi_I}{\partial r} + \frac{1}{r^2}\frac{\partial^2 \varphi_I}{\partial \theta_m{}^2} = 0 \quad ; in\, airgap \tag{2.9}$$

$$\frac{\partial^2 \varphi_{II}}{\partial r^2} + \frac{1}{r}\frac{\partial \varphi_{II}}{\partial r} + \frac{1}{r^2}\frac{\partial^2 \varphi_{II}}{\partial \theta_m{}^2} = \frac{1}{\mu_r}\,\mathrm{div}\,\vec{M} \;\; ; \; in\, magnets \tag{2.10}$$

The magnetic field intensity H can be obtained from φ using (2.11).

$$\vec{H} = -\nabla \varphi = -\vec{a}_r \frac{\partial \varphi}{\partial r} - \vec{a}_\theta \frac{1}{r}\frac{\partial \varphi}{\partial \theta_m} \tag{2.11}$$

$$\vec{M} = M_r \vec{a}_r + M_\theta \vec{a}_\theta \tag{2.12}$$

$$\left.\begin{aligned} M_r &= 0 \\ M_\theta &= 0 \end{aligned}\right\} \ \forall -\frac{\pi}{2p} \le \theta_m \le -\alpha_p \frac{\pi}{2p}$$

$$\left.\begin{aligned} M_r &= \frac{B_r \cos\theta_m}{\mu_0} \\ M_\theta &= -\frac{B_r \sin\theta_m}{\mu_0} \end{aligned}\right\} \ \forall -\alpha_p \frac{\pi}{2p} \le \theta_m \le \alpha_p \frac{\pi}{2p}$$

$$\left.\begin{aligned} M_r &= 0 \\ M_\theta &= 0 \end{aligned}\right\} \ \forall \alpha_p \frac{\pi}{2p} \le \theta_m \le \left(2-\alpha_p\right)\frac{\pi}{2p} \tag{2.13}$$

$$\left.\begin{aligned} M_r &= -\frac{B_r \cos\left(\theta_m - \pi/p\right)}{\mu_0} \\ M_\theta &= \frac{B_r \sin\left(\theta_m - \pi/p\right)}{\mu_0} \end{aligned}\right\} \ \forall \left(2-\alpha_p\right)\frac{\pi}{2p} \le \theta_m \le \alpha_p \frac{3\pi}{2p}$$

$$\left.\begin{aligned} M_r &= 0 \\ M_\theta &= 0 \end{aligned}\right\} \ \forall \alpha_p \frac{3\pi}{2p} \le \theta_m \le \frac{3\pi}{2p}$$

For parallel magnetization the radial (M_r) and tangential (M_θ) components of the magnetization vector can be described by (2.13) [52], where, p is the number of pole-pairs, B_r is the magnet remanence field, α_p is the magnet pole arc to pole pitch ratio, and θ_m is the angular position with respect to the centre of magnet pole. Since the magnetization vector is periodic and repeats every pole pair, M_r and M_θ can be expressed as a Fourier series as given by (2.14),

$$\begin{aligned} M_r &= \sum_{n=1,3,5,\ldots}^{\infty} M_{rn} \cos\left(np\theta_m\right) \\ M_\theta &= \sum_{n=1,3,5,\ldots}^{\infty} M_{\theta n} \sin\left(np\theta_m\right) \end{aligned} \tag{2.14}$$

For the case of parallel magnetized magnets, M_{rn} and $M_{\theta n}$ can be expressed by (2.15),

$$M_{rn} = \frac{B_r}{\mu_0}\alpha_p\left(A_{1n} + A_{2n}\right)$$
$$M_{\theta n} = \frac{B_r}{\mu_0}\alpha_p\left(A_{1n} - A_{2n}\right) \tag{2.15}$$

The coefficients A_{1n} and A_{2n} are defined by (2.16),

$$A_{1n} = \frac{\sin\left[\left(np+1\right)\alpha_p\frac{\pi}{2p}\right]}{\left(np+1\right)\alpha_p\frac{\pi}{2p}}$$
$$A_{2n} = \begin{cases} 1 & ;\ \forall\ np = 1 \\ \dfrac{\sin\left[\left(np-1\right)\alpha_p\frac{\pi}{2p}\right]}{\left(np-1\right)\alpha_p\frac{\pi}{2p}} & ;\forall\ np \neq 1 \end{cases} \tag{2.16}$$

The divergence of magnetisation vector can be expressed by (2.17),

$$div\,\vec{M} = \frac{M_r}{r} + \frac{\partial M_r}{\partial r} + \frac{1}{r}\frac{\partial M_\theta}{\partial \theta_m} = \sum_{n=1,3,5,\ldots}^{\infty}\frac{1}{r}M_n\cos\left(np\theta_m\right) \tag{2.17}$$

Where,

$$M_n = M_{rn} + npM_{\theta n} \tag{2.18}$$

The radial and tangential flux density can then be derived as shown in [52], in the air-gap as a function of r and θ_m as given by (2.19)-(2.20).

$$B_r\left(r,\theta_m\right) = \sum_{i=1,3,5,\ldots}^{\infty} K_b\left(n\right) f_{Br}\left(r\right) cos\left(np\theta_m\right) \tag{2.19}$$

$$B_\theta\left(r,\theta_m\right) = \sum_{i=1,3,5,\ldots}^{\infty} K_b\left(n\right) f_{B\theta}\left(r\right) sin\left(np\theta_m\right) \tag{2.20}$$

$K_b(n)$, $f_{Br}(r)$, $f_{B\theta}(r)$ and A_{3n} are given by (2.21)-(2.23) for $np \neq 1$,

$$K_b(n)=\frac{\mu_0 M_n}{\mu_r}\frac{np}{(np)^2+1}\cdot \times\left\{\frac{(A_{3n}-1)+2\left(\frac{R_r}{R_m}\right)^{np+1}-(A_{3n}+1)\left(\frac{R_r}{R_m}\right)^{2np}}{\frac{\mu_r+1}{\mu_r}\left[1-\left(\frac{R_r}{R_{st}}\right)^{2np}\right]-\frac{\mu_r-1}{\mu_r}\left[\left(\frac{R_m}{R_{st}}\right)^{2np}-\left(\frac{R_r}{R_m}\right)^{2np}\right]}\right\} \tag{2.21}$$

$$f_{Br}(r)=\left(\frac{r}{R_{st}}\right)^{np-1}\left(\frac{R_m}{R_{st}}\right)^{np+1}+\left(\frac{R_m}{r}\right)^{np+1}$$
$$f_{B\theta}(r)=-\left(\frac{r}{R_{st}}\right)^{np-1}\left(\frac{R_m}{R_{st}}\right)^{np+1}+\left(\frac{R_m}{r}\right)^{np+1} \tag{2.22}$$

$$A_{3n}=\left(np-\frac{1}{np}\right)\frac{M_{rn}}{M_n}+\frac{1}{np};\forall np\neq 1 \tag{2.23}$$

Here μ_0 is the permeability of vacuum and μ_r is the recoil permeability of the magnet.

In the previous equations, the rotor has been assumed fixed with respect to the stator in order to compute the magnetic field. However, the rotor can rotate and therefore θ_m has to be expressed such that the relative motion of the rotor is accounted for. This can be expressed as (2.24), where, θm_0 is the angular position of the slot with respect to an arbitrary fixed reference and $\omega_m t$ is the angular shift of the centre of magnet pole w.r.t the arbitrary fixed stator reference.

$$\theta_m=\theta_{m0}-\omega_m t \tag{2.24}$$

The no-load flux linkage of a phase coil having T_c turns can be obtained by integrating the magnetic field (B_r) over 1 coil pitch as shown in (2.25) to obtain (2.26).

$$\lambda_c=R_{st}L_{stk}T_c\int_{a_1\beta_s-\omega_m t}^{a_2\beta_s-\omega_m t}\sum_{i=1,3,5,\ldots}^{\infty}K_b(n)f_{Br}(r)\cos(np\theta_m)d\theta_m \tag{2.25}$$

$$\lambda_c=\sum_{n=1,3,\ldots}^{\infty}T_c R_{st}L_{stk}K_b(n)f_{Br}(R_{st})\frac{1}{np}\begin{pmatrix}+\sin\left(np\left(-\omega_m t+a_2\beta_s\right)\right)\\-\sin\left(np\left(-\omega_m t+a_1\beta_s\right)\right)\end{pmatrix} \tag{2.26}$$

where, L_{stk} is the active stator length and β_s is the slot-pitch in radians. The induced EMF can then be calculated by differentiating (2.26) to obtain (2.27).

$$e_c = -\frac{d\lambda_c}{dt}$$
$$= T_c R_{st} L_{stk} \omega_m \sum_{n=1,3,5,\ldots}^{\infty} K_b(n) f_{Br}(R_{st}) \times \begin{pmatrix} +\cos\left(np\left(-\omega_m t + a_2\beta_s\right)\right) \\ -\cos\left(np\left(-\omega_m t + a_1\beta_s\right)\right) \end{pmatrix} \quad (2.27)$$

The EMF calculated is expressed in terms of a_1 and a_2, therefore by iterating through entries of Table 2-4, EMF of all individual coils can be obtained. The induced EMF of a phase can then be calculated by summing EMF's of all individual coils in the phase.

$$e_{ph} = \sum_{phase\,Coils} e_c \quad (2.28)$$

2.5.3 Armature Reaction Field and Airgap Inductance

The armature reaction field in SPM machine can be calculated analytically [48]–[53] using the assumption of smooth stator and rotor core and assuming infinite permeability of stator and rotor cores. Fig. 2-7 shows the current density distribution of a coil assuming the entire ampere-turns to be located in the slot opening area [11], where i is the coil current, T_c is the number of turns of the coil under consideration and b_0 is the slot opening. The go and return slot numbers, i.e., a_1 and a_2 define the position of the coil.

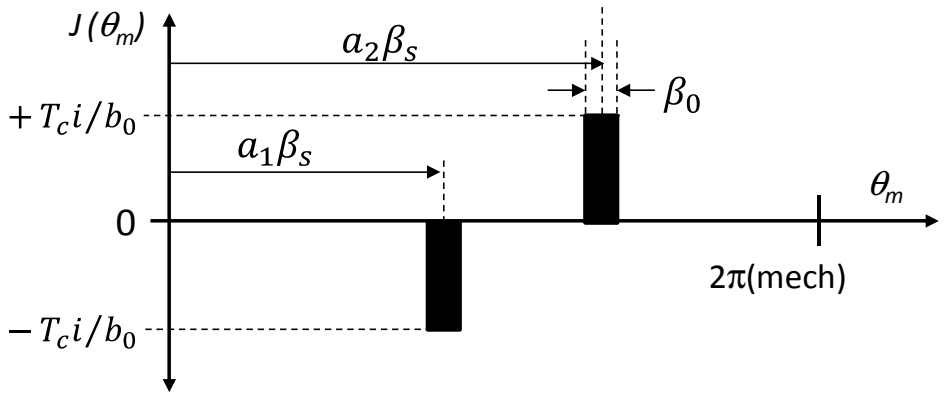

Fig. 2-7: Current density distribution of a coil

The current density distribution (J) can be described by (2.29).

$$J=\begin{cases}0 & \forall\ 0\le\theta_m\le a_1\beta_s-\beta_0/2\\ -T_c i/b_0 & \forall\ a_1\beta_s-\beta_0/2\le\theta_m\le a_1\beta_s+\beta_0/2\\ 0 & \forall\ a_1\beta_s+\beta_0/2\le\theta_m\le a_2\beta_s-\beta_0/2\\ +T_c i/b_0 & \forall\ a_2\beta_s-\beta_0/2\le\theta_m\le a_2\beta_s+\beta_0/2\\ 0 & \forall\ a_2\beta_s+\beta_0/2\le\theta_m\le 2\pi\end{cases} \tag{2.29}$$

The current density distribution can then be written as a Fourier series as given by (2.30)-(2.32).

$$J=\sum_{n=1}^{\infty}J_{an}\cos n\theta_m+J_{bn}\sin n\theta_m \tag{2.30}$$

$$J_{an}=\frac{2T_cI}{n\pi b_0}\sin\frac{n\beta_0}{2}\left[\cos\left(na_2\beta_s\right)-\cos\left(na_1\beta_s\right)\right] \tag{2.31}$$

$$J_{bn}=\frac{2T_cI}{n\pi b_0}\sin\frac{n\beta_0}{2}\left[\sin\left(na_2\beta_s\right)-\sin\left(na_1\beta_s\right)\right] \tag{2.32}$$

The armature reaction components in the airgap can then be obtained by solving the Laplace equation (2.33), subject to the boundary conditions given by (2.34).

$$\frac{\partial^2\varphi}{\partial r^2}+\frac{1}{r}\frac{\partial\varphi}{\partial r}+\frac{1}{r^2}\frac{\partial^2\varphi}{\partial\theta_m{}^2}=0 \tag{2.33}$$

$$\begin{aligned}H_\theta\big|_{r=R_r}&=0\\ H_\theta\big|_{r=R_{st}}&=-J\end{aligned} \tag{2.34}$$

The general solution of (2.33), can be expressed as,

$$\begin{aligned}\varphi=&\sum_{n=1}^{\infty}\left(A_nr^n+B_nr^{-n}\right)\left[\mathrm{C}_n\cos\left(n\theta_m\right)+D_n\sin\left(n\theta_m\right)\right]\\ &+\left(A_0+B_0\ln r\right)\left(C_0+D_0\theta_m\right)\end{aligned} \tag{2.35}$$

The magnetic field intensity can be expressed as (2.36).

$$\begin{aligned}H_\theta=-\frac{1}{r}\frac{\partial\varphi}{\partial\theta_m}=&-\sum_{n=1}^{\infty}\left(A_nr^{n-1}+B_nr^{-n-1}\right)\begin{bmatrix}-n\mathrm{C}_n\sin\left(n\theta_m\right)\\ +nD_n\cos\left(n\theta_m\right)\end{bmatrix}\\ &-\frac{1}{r}\left(A_0+B_0\ln r\right)D_0\end{aligned} \tag{2.36}$$

Applying the stator boundary condition the following can be obtained (2.37),

$$\left.\begin{aligned}\left(A_n {R_{st}}^{n-1} + B_n {R_{st}}^{-n-1}\right) n \mathrm{C}_n &= -J_{bn} \\ \left(A_n {R_{st}}^{n-1} + B_n {R_{st}}^{-n-1}\right) n D_n &= J_{an}\end{aligned}\right\} \Rightarrow C_n, D_n \neq 0$$
$$-\frac{1}{R_s}\left(A_0 + B_0 \ln R_{st}\right) D_0 = 0 \tag{2.37}$$

Applying rotor boundary condition (2.38) can be obtained.

$$\begin{aligned}\left(A_n {R_r}^{n-1} + B_n {R_r}^{-n-1}\right) &= 0 \quad \Rightarrow B_n = -A_n {R_r}^{2n} \\ -\frac{1}{R_r}\left(A_0 + B_0 \ln R_r\right) D_0 &= 0 \quad \Rightarrow \text{either } D_0 = 0 \text{ or } A_0 = B_0 = 0\end{aligned} \tag{2.38}$$

It is also known that without stator excitation H_r =0, and noting that A_n, B_n, C_n and D_n are not equal to zero the following relation can be obtained.

$$\begin{aligned}H_r\big|_{r=R_r} &= -\left.\frac{\partial \varphi}{\partial r}\right|_{r=R_r} = 0 \\ &= -\sum_{n=1}^{\infty}\left(A_n {R_r}^{n-1} - B_n {R_r}^{-n-1}\right)\left(\mathrm{C}_n \cos\left(n\theta_m\right) + D_n \sin\left(n\theta_m\right)\right) \\ &\quad -\frac{B_0}{r}\left(C_0 + D_0 \theta_m\right)\end{aligned} \tag{2.39}$$

$$\Rightarrow -\frac{B_0}{R_r}\left(C_0 + D_0 \theta_m\right) = 0$$

Using the derived constants, the radial magnetic field intensity can be re-written as (2.40).

$$\begin{aligned}H_r &= -\frac{\partial \varphi}{\partial r} \\ &= \sum_{n=1}^{\infty} A_n \left(r^{n-1} - \left(-{R_r}^{2n}\right) r^{-n-1}\right) \frac{\left(J_{bn} \cos\left(n\theta_m\right) - J_{an} \sin\left(n\theta_m\right)\right)}{A_n \left({R_{st}}^{n-1} - {R_r}^{2n} {R_{st}}^{-n-1}\right)} \\ &= \sum_{n=1}^{\infty}\left(\frac{r}{R_{st}}\right)^{n-1} \frac{\left(1 + \left(\frac{R_r}{r}\right)^{2n}\right)}{\left(1 - \left(\frac{R_r}{R_{st}}\right)^{2n}\right)}\left(J_{bn} \cos\left(n\theta_m\right) - J_{an} \sin\left(n\theta_m\right)\right)\end{aligned} \tag{2.40}$$

The magnetic field due to armature reaction can then be obtained as given by (2.41)-(2.42).

$$B_r = \mu_0 H_r = \mu_0 \sum_{n=1}^{\infty} F_{ar} \left(J_{bn} \cos n\theta_m - J_{an} \sin n\theta_m \right) \tag{2.41}$$

$$F_{ar} = \frac{1 + \left(\frac{R_r}{r} \right)^{2n}}{1 - \left(\frac{R_r}{R_{st}} \right)^{2n}} \left(\frac{r}{R_{st}} \right)^{n-1} \tag{2.42}$$

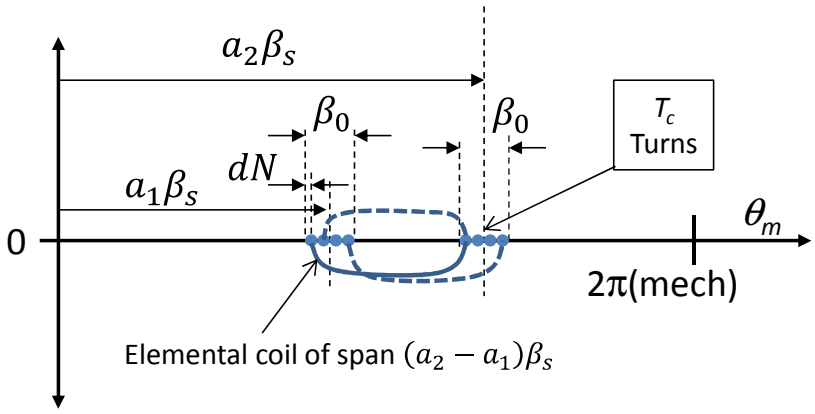

Fig. 2-8: Elemental Coil Diagram

To calculate the total flux linkage of the coil due to armature reaction, the flux ψ_c in the elemental coil of span $(a_2\text{-}a_1)\beta_s$ as shown in Fig. 2-8 is calculated as (2.43)-(2.44) where θ_c is the starting position of the elemental coil.

$$\psi_c(\theta_c) = \int_{\theta_c}^{\theta_c + (a_2 - a_1)\beta_s} B_r L_{stk} R_{st} d\theta_m \tag{2.43}$$

$$\psi_c(\theta_c) = 2\mu_0 L_{stk} R_{st} \cdot \sum_{n=1}^{\infty} \frac{F_{ar}}{n} \sin \frac{n(a_2 - a_1)\beta_s}{2} \times \begin{pmatrix} +J_{bn} \cos\left(n\theta_c + \frac{n(a_2 - a_1)\beta_s}{2} \right) \\ -J_{an} \sin\left(n\theta_c + \frac{n(a_2 - a_1)\beta_s}{2} \right) \end{pmatrix} \tag{2.44}$$

The total flux linkage λ_c can then be obtained by integrating over all elemental coils as given in (2.45).

$$\lambda_c = \int_0^{T_c} \psi_c(\theta_c)\, dN = \int_{a_1\beta_s-\beta_0/2}^{a_1\beta_s+\beta_0/2} \psi_c(\theta_c).\frac{T_c}{\beta_0} d\theta_c$$
$$= \frac{2\mu_0 L_{stk} R_{st} T_c}{\beta_0} \sum_{n=1}^{\infty} \frac{F_{ar}}{n^2} \sin\frac{n\beta_0}{2} \begin{bmatrix} +J_{bn}\{\sin(na_2\beta_s) - \sin(na_1\beta_s)\} \\ -J_{an}\{\cos(na_1\beta_s) - \cos(na_2\beta_s)\} \end{bmatrix} \quad (2.45)$$

The individual flux linkages from coils of a particular phase can be then be summed to obtain the overall flux linkage λ_{ph} of the particular phase as given by (2.46).

$$\lambda_{ph} = \sum_{phase\ Coils} \lambda_c \quad (2.46)$$

Finally, the air-gap inductance L_{ph} of the coil can be obtained using (2.47).

$$L_{ph} = \frac{\lambda_{ph}}{I} \quad (2.47)$$

Fig. 2-9 shows the flowchart for the computation of the air-gap inductance calculations.

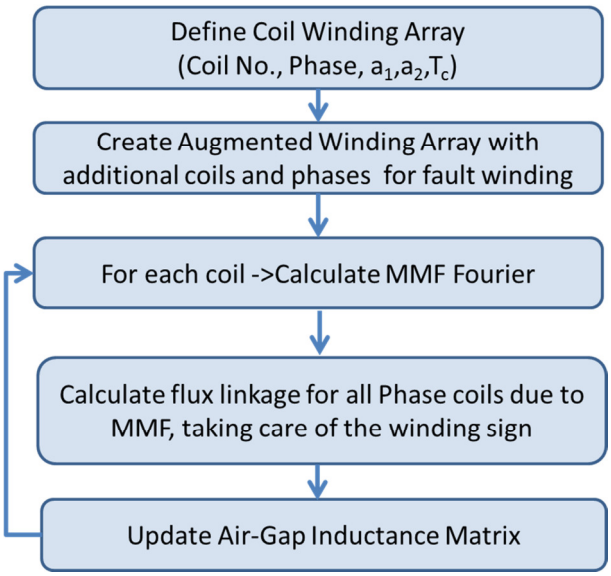

Fig. 2-9: Flowchart for air-gap inductance calculations

2.5.4 Slot Leakage Inductance

To derive analytical formula, for both self and mutual slot leakage inductance, it is assumed that the shorted turns are located at an arbitrary position along the slot height within the coil area in the slot. Fig. 2-5 shows the slot area and the associated turns and its relative position in the slot, assuming that the fault lies in the coil side 'A' for

purpose of illustration. In coil side 'A' N_{ha} and N_{hb} turns correspond to the healthy turns of the coil and N_s corresponds to the shorted turns of the coil. The dimensions of the slot of the machine are given in Table 2-5.

Table 2-5: Slot Specifications

Specification	Symbol	Value
Slot opening	b_o	3.75mm
Opening depth	h_t	1 mm
Height of slot	h_s	22.3mm
Slot opening angle	α_{sl}	30º
Slot angle	β_{sl}	15.35º

The leakage flux linkages can be calculated easily by applying Ampere's circuital law along the flux paths illustrated in Fig. 2-10.

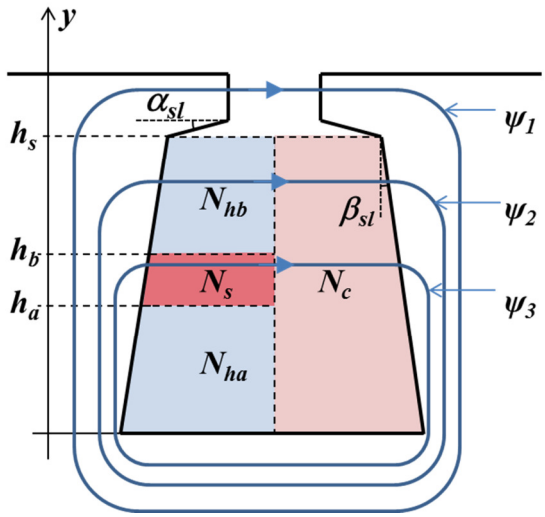

Fig. 2-10: Slot leakage flux paths

2.5.4.1 Flux linkage contribution in the slot opening region due to current in *Ns*

The slot leakage flux due to magnetic field in the slot opening region can be obtained as (2.50) by applying Ampere's law (2.48) in the slot opening region and integrating the magnetic field obtained as given in (2.49), where I denotes the current in the N_s turns.

$$\oint \vec{H}.d\vec{l} = N_s I \tag{2.48}$$

$$\vec{B} = \mu_0 \vec{H}$$
$$\psi = \int \vec{B}.d\vec{s} \tag{2.49}$$

$$B = \frac{\mu_0 N_s I}{b_0}$$
$$\psi = B.h_t.L_{stk} = \frac{\mu_0 N_s h_t L_{stk} I}{b_0} \tag{2.50}$$

Since flux linkages is the product of the flux density times the number of turns in the coil, the flux linkage contribution in the slot opening region can be obtained as (2.51).

$$\lambda = N_s \psi$$
$$\lambda = \frac{\mu_0 N_s{}^2 h_t l_{stk} I}{b_0} \tag{2.51}$$

2.5.4.2 Flux linkage contribution in the wedge area due to current in *Ns*

In the slot wedge area, the effective air-gap length varies with the vertical position as shown in Fig. 2-11 and can be computed using (2.52).

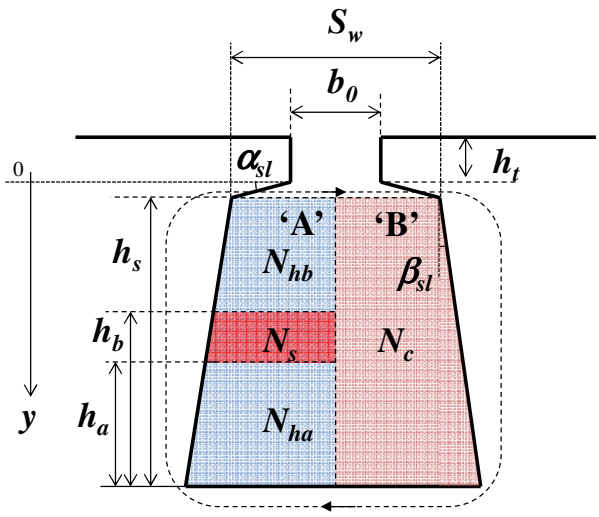

Fig. 2-11: Slot geometry and coordinate system for slot wedge flux calculation

$$g_{eff} = b_0 + \frac{2y}{\tan \alpha_{sl}} \tag{2.52}$$

Applying Ampere's law in the wedge area, flux density can be obtained as (2.53).

$$B.\left(b_0+\frac{2y}{\tan\alpha_{sl}}\right)=\mu_0 N_s I \tag{2.53}$$

The flux can then be computed by integrating the flux density over the entire wedge area as given by (2.54).

$$\psi=\int_0^h \frac{\mu_0 N_s I}{\left(b_0+\frac{2y}{\tan\alpha_{sl}}\right)}dy \tag{2.54}$$

A change of variable can be utilized as shown in (2.55), to simplify the integration in order to obtain (2.56).

$$\begin{aligned} &y'=b_0+\frac{2y}{\tan\alpha_{sl}}\Rightarrow dy'=\frac{2dy}{\tan\alpha_{sl}}\\ &y=0\Rightarrow y'=b_0\\ &y=h\Rightarrow y'=S_w \end{aligned} \tag{2.55}$$

$$\psi=\int_{b_0}^{S_w}\frac{\mu_0 N_s I L_{stk}\tan\alpha_{sl}}{2y'}dy'=\frac{\mu_0 N_s I L_{stk}\tan\alpha_{sl}}{2}\ln\left(\frac{S_w}{b_0}\right) \tag{2.56}$$

The flux linkages can be obtained as (2.57).

$$\lambda=N_s\psi=\frac{\mu_0 {N_s}^2 I L_{stk}\tan\alpha_{sl}}{2}\ln\left(\frac{S_w}{b_0}\right) \tag{2.57}$$

2.5.4.3 Flux linkage contribution in region above the faulted turns due to current in *Ns*

The flux linkage contribution can be computed by integrating flux density above the shorted turns (N_s) as depicted in Fig. 2-12.

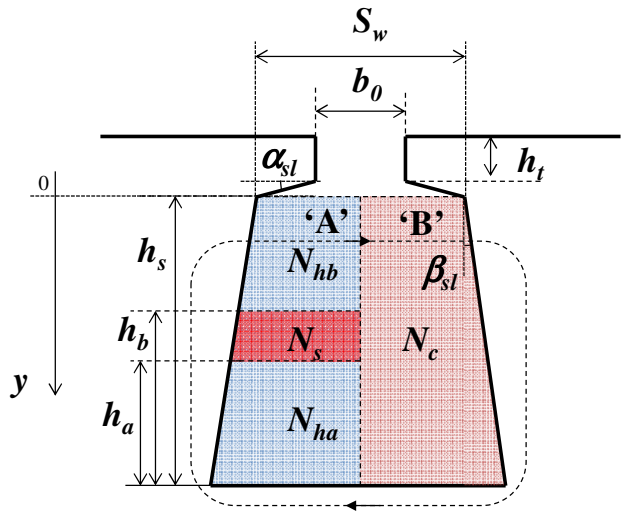

Fig. 2-12: Slot geometry and coordinate system for flux calculation in the winding area

Applying Ampere's law, the magnetic field density can be obtained as (2.58).

$$B\left(S_w + 2y\tan\beta_{sl}\right) = \mu_0 N_s I \tag{2.58}$$

The flux can then be computed by integrating over the area as given by (2.59).

$$\psi = \int_0^{h_s - h_b} \frac{\mu_0 N_s I L_{stk}}{\left(S_w + 2y\tan\beta_{sl}\right)} dy \tag{2.59}$$

Introducing a change of variable given by (2.60) the integration can be simplified to obtain (2.61).

$$\begin{aligned} y' &= \left(S_w + 2y\tan\beta_{sl}\right) \\ y = 0 &\Rightarrow y' = S_w \\ y = h_s - h_b &\Rightarrow y' = S_w + 2\left(h_s - h_b\right)\tan\beta_{sl} \end{aligned} \tag{2.60}$$

$$\begin{aligned} \psi &= \int_{S_w}^{S_w + 2(h_s - h_b)\tan\beta_{sl}} \frac{\mu_0 N_s I L_{stk}}{y'} \frac{dy'}{2\tan\beta_{sl}} \\ &= \frac{\mu_0 N_s I L_{stk}}{2\tan\beta_{sl}} \ln\left(\frac{S_w + 2\left(h_s - h_b\right)\tan\beta_{sl}}{S_w}\right) \end{aligned} \tag{2.61}$$

The flux linkage can be obtained by multiplying the flux with number of turns to obtain (2.62) .

$$\lambda = N_s\psi = \frac{\mu_0 N_s I L_{stk}}{2\tan\beta_{sl}} \ln\left(\frac{S_w + 2\left(h_s - h_b\right)\tan\beta_{sl}}{S_w}\right) \tag{2.62}$$

2.5.4.4 Flux linkage in the region of the faulted turns due to current in *Ns*

The self-flux linkage can be computed by first computing flux of an elemental coil and then integrating over the whole fault region. By applying Ampere's law, the magnetic field density can be obtained as (2.63).

$$B\left(S_w + 2y\tan\beta_{sl}\right) = \mu_0 N_s I\left(-\frac{y-\left(h_s-h_a\right)}{h_b-h_a}\right) \tag{2.63}$$

The flux linkages can then be computed using (2.64).

$$\begin{aligned}\lambda &= \int_{h_s-h_b}^{h_s-h_a} N(y)\,BL_{stk}\,dy \\ &= \mu_0 {N_s}^2 L_{stk}\int_{h_s-h_b}^{h_s-h_a}\left(\frac{y-\left(h_s-h_a\right)}{h_b-h_a}\right)^2\frac{1}{S_w+2y\tan\beta_{sl}}dy\end{aligned} \tag{2.64}$$

Adopting a change of variable as given by (2.65) and substituting it in (2.64), (2.66)-(2.67) can be obtained.

$$\begin{aligned}y' &= \left(S_w + 2y\tan\beta_{sl}\right) \\ y_1 = h_s - h_b &\Rightarrow y_1' = S_w + 2\left(h_s-h_b\right)\tan\beta_{sl} \\ y_2 = h_s - h_a &\Rightarrow y_2' = S_w + 2\left(h_s-h_a\right)\tan\beta_{sl}\end{aligned} \tag{2.65}$$

$$\begin{aligned}\lambda &= \frac{\mu_0 {N_s}^2 L_{stk} I}{2\left(h_b-h_a\right)^2\tan\beta_{sl}}\int_{y_1'}^{y_2'}\left(\frac{y'-S_w}{2\tan\beta_{sl}}-h_s+h_a\right)^2\frac{1}{y'}dy' \\ &= \frac{\mu_0 {N_s}^2 L_{stk} I}{2\left(h_b-h_a\right)^2\tan\beta_{sl}}\int_{y_1'}^{y_2'}\frac{1}{y'}\left(\begin{array}{l}\dfrac{y'^2}{4\tan^2\beta_{sl}}+\left(h_a-h_s-\dfrac{S_w}{2\tan\beta_{sl}}\right)^2 \\ +2\dfrac{y'}{2\tan\beta_{sl}}\left(h_a-h_s-\dfrac{S_w}{2\tan\beta_{sl}}\right)\end{array}\right)dy'\end{aligned} \tag{2.66}$$

$$\lambda = \frac{\mu_0 {N_s}^2 L_{stk} I}{2\left(h_b-h_a\right)^2\tan\beta_{sl}}\left[\begin{array}{l}\dfrac{S_w+\left(2h_s-h_b-h_a\right)\tan\beta_{sl}}{2\tan\beta_{sl}}\left(h_b-h_a\right)+ \\ \left(h_a-h_s-\dfrac{S_w}{2\tan\beta_{sl}}\right)^2\ln\left(\dfrac{S_w+2\left(h_s-h_a\right)\tan\beta_{sl}}{S_w+2\left(h_s-h_b\right)\tan\beta_{sl}}\right) \\ +2\left(h_b-h_a\right)\left(h_a-h_s-\dfrac{S_w}{2\tan\beta_{sl}}\right)\end{array}\right] \tag{2.67}$$

Fig. 2-13 shows the overall algorithm used for calculation of slot leakage inductance. The total inductance of a particular phase can then be obtained simply by adding the air-gap inductance and slot leakage inductance.

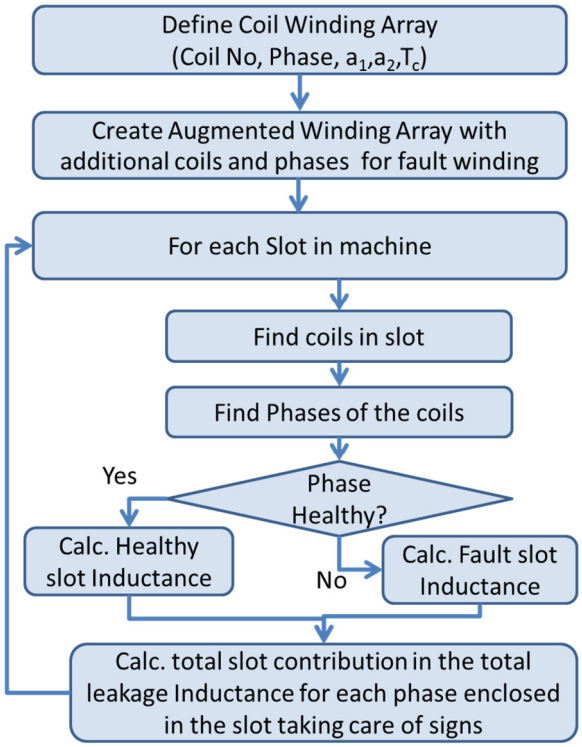

Fig. 2-13: Leakage inductance computation algorithm

2.6 Model Validation

In order to validate the model, the parameters of healthy machine are first computed and compared against FE extracted values. Parameters are then compared against FE for a few cases with differing location of fault winding in the slot for a 1 turn and 3 turn fault. Finally the fault current prediction for 1 turn fault is compared against those obtained from FE, under full load condition.

2.6.1 BEMF Comparison

Table 2-6 shows the comparison of fundamental peak EMF voltage of the analytical model and the FE model at a rotor speed of 1350 r/min. The difference between the analytical and FE is due to the assumption of smooth stator, which ignores

the effect of slot openings on the open circuit field distribution and therefore predicts higher back-EMF.

Table 2-6: Back-EMF Comparison

EMF, fundamental (Analytical)	EMF, fundamental (FE)	% Error
43V	42.37V	1.01%

2.6.2 Airgap Inductance of Healthy Machine

Table 2-7 shows the comparison of analytically predicted and FE calculated air-gap inductance of healthy machine. The FE calculation is performed by making the permeability of slot region very much less than that of air, which leads to suppression of any leakage flux through the slot area. The difference is 1.4% and is attributed to neglecting the slotting effect in the analytical calculation. It can be seen that the mutual coupling via air-gap flux linkage is very small.

Table 2-7: Air-Gap Inductance Comparison

L_{ij}	L(Analytical)	L(FE)	% error
$L_{11}=L_{22}=L_{33}$	0.161mH	0.164mH	-1.7%
$L_{12}=L_{21}$	-5.02μH	-5.0μH	0.36%
$L_{13}=L_{31}$	-5.02μH	-5.0μH	0.36%

2.6.3 Leakage Inductance of Healthy Machine

Table 2-8 shows the comparison of analytically predicted and FE calculated slot-leakage inductance of healthy machine. The FE is performed by making the permeability of rotor, shaft, magnets and air-gap region very much less than that of air, which leads to suppression of any air-gap flux. The difference is 7.9% and is attributed to the fact that leakage flux lines are not strictly parallel to slot bottom in case of non-overlapped winding [54] as illustrated in sub-section 2.6.6.

Table 2-8: Slot Leakage Inductance Comparison

L_{ij}	L(Analytical)	L(FE)	% error
$L_{11}=L_{22}=L_{33}$	0.144mH	0.157mH	-7.9%
$L_{12}=L_{21}$	-24.1µH	-24.7µH	-2.4%
$L_{13}=L_{31}$	-24.1µH	-24.3µH	-1.11%

2.6.4 Overall Healthy Machine Inductance

Table 2-9 compares analytically and FE predicted total inductance of healthy machine. In this and subsequent comparisons, normal material permeability and BH characteristics are used. The difference is 6.1% and is attributed to the discrepancy in the leakage computation as shown in Table 2-8.

Table 2-9: Healthy Machine Inductance Comparison

L_{ij}	L(Analytical)	L(FE)	% error
$L_{11}=L_{22}=L_{33}$	0.305mH	0.325mH	-6.1%
$L_{12}=L_{21}$	-29.1µH	-29.7µH	-2%
$L_{13}=L_{31}$	-29.1µH	-29.7µH	-2%

2.6.5 Faulted Machine Inductance

To limit the number of FE calculations, 3 cases are considered with 1 turn fault. Table 2-10, Table 2-11 and Table 2-12 shows the analytically and FE predicted parameters of 1 turn fault wherein the fault is located at the bottom, mid and top of the slot respectively. All the results show that the difference is between 5-8% which is expected arising out of the difference in leakage inductance calculation. It is to be noted that difference in L_{24} seems to be very large. The absolute value of the inductance is, however, almost three orders of magnitude lower and hence negligible compared with the other inductances in the matrix. It occurs because the coupling between the faulty coil and phase 2 is very small and the error is most likely due to numeric errors in FE. The values in bold is the self-inductance of the faulted turns. It can be seen that the inductance is the least when the faulted turns are located at the top of the slot.

Table 2-10: Inductance Comparison with 1 Turn Fault Located at Bottom of Slot (N_{ha}=0)

L_{ij}	L(Analytical)	L(FE)	% error
L_{11}	0.286mH	0.303mH	-5.65%
L_{12}=L_{21}	-29.1µH	-29.76µH	-1.98%
L_{13}=L_{31}	-27.0µH	-27.2µH	-0.77%
L_{14}=L_{41}	9.11µH	9.46µH	-3.72%
L_{22}	0.305mH	0.325mH	-6.2%
L_{23}=L_{32}	-29.1µH	-29.7µH	-1.92%
L_{24}=L_{42}	-5.89e-10H	-8.91e-9H	-106%
L_{33}	0.305mH	0.325mH	-6.05%
L_{34}=L_{43}	-2.05µH	-2.06µH	-0.65%
L_{44}	**1.12µH**	**1.21µH**	**-7.89%**

Table 2-11: Inductance Comparison with 1 Turn Fault Located in Middle of Slot (N_{ha}=3)

L_{ij}	L(Analytical)	L(FE)	% error
L_{11}	0.286mH	0.303mH	-5.6%
L_{12}=L_{21}	-29.1µH	-29.6µH	-1.98%
L_{13}=L_{31}	-27.1µH	-27.4µH	-0.79%
L_{14}=L_{41}	8.88µH	9.23µH	-3.78%
L_{22}	0.305mH	0.325mH	-6.2%
L_{23}=L_{32}	-29.1µH	-29.7µH	-1.92%
L_{24}=L_{42}	-5.89e-10H	-8.85e-9H	-106%
L_{33}	0.305mH	0.325mH	-6.05%
L_{34}=L_{43}	-1.93µH	-1.94µH	-0.24%
L_{44}	**1.00µH**	**1.07µH**	**-6.1%**

Table 2-12: Inductance comparison with 1 Turn Fault Located At Top of Slot (N_{ha}=7)

L_{ij}	L(Analytical)	L(FE)	% error
L_{11}	0.289mH	0.307mH	-5.65%
$L_{12}=L_{21}$	-29.1µH	-29.7µH	-1.98%
$L_{13}=L_{31}$	-27.7µH	-27.9µH	-0.82%
$L_{14}=L_{41}$	7.41µH	7.66µH	-3.26%
L_{22}	0.305mH	0.325mH	-6.2%
$L_{23}=L_{32}$	-29.1µH	-29.7µH	-1.92%
$L_{24}=L_{42}$	-5.89e-10H	-8.52e-9H	-106%
L_{33}	0.305mH	0.325mH	-6.05%
$L_{34}=L_{43}$	-1.38µH	-1.37µH	0.48%
L_{44}	**0.804µH**	**0.865µH**	**-7.08%**

To further validate the calculation, machine parameters for a 3 turn fault is compared in Table 2-13. It can be seen that the errors are in the same range (5-8%).

Table 2-13: Inductance Comparison with 3 Turn Fault Located in the Middle of the Slot (N_{ha}=3)

L_{ij}	L(Analytical)	L(FE)	% error
L_{11}	0.256mH	0.272mH	-5.89%
$L_{12}=L_{21}$	-29.1µH	-29.7µH	-2.04%
$L_{13}=L_{31}$	-23.6µH	-23.8µH	-0.94%
$L_{14}=L_{41}$	20.3µH	21µH	-3.28%
L_{22}	0.305mH	0.325mH	-6.2%
$L_{23}=L_{32}$	-29.1µH	-29.7µH	-1.92%
$L_{24}=L_{42}$	-1.77e-9H	2.64e-8H	-106%
L_{33}	0.305mH	0.325mH	-6.05%
$L_{34}=L_{43}$	-5.51µH	-5.51µH	0.01%
L_{44}	**8.5µH**	**8.99µH**	**-5.51%**

2.6.6 Leakage Flux Estimation Error Analysis

In order to illustrate the main source of error in the inductance calculation, two winding cases are considered. First case has a current carrying coil which only occupies half of the slot and the other case has the current carrying coil which occupies the whole slot. The field plots obtained by FE are shown in Fig. 2-14. It can be seen that if the coil occupies only half a slot the flux lines are not parallel to the slot bottom compared to the case where coil occupies the whole side. This introduces significant errors in the leakage flux computation [54]. For the sake of simplicity, this is ignored in the analytical computation.

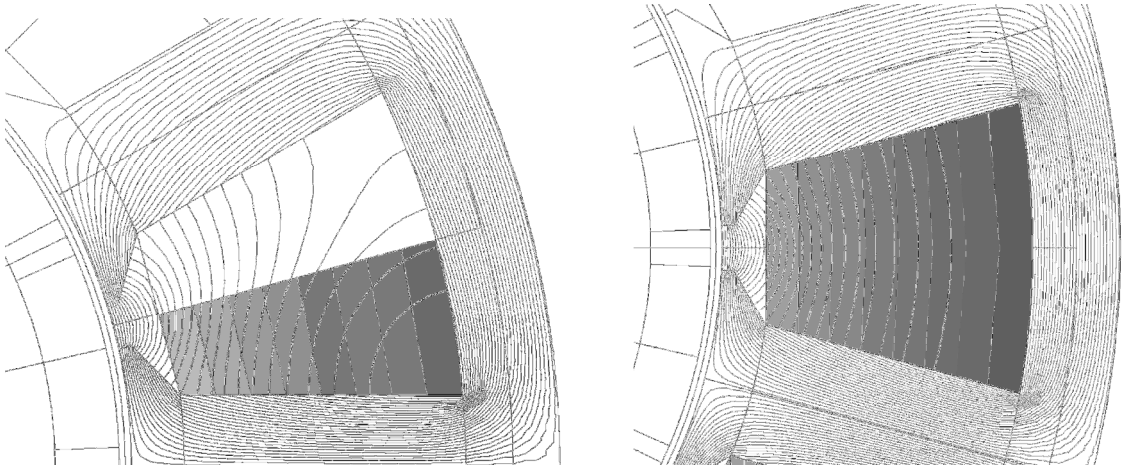

(a) (b)

Fig. 2-14: Comparison of flux iso-lines for (a) half slot coil side and (b) full slot coil side.

2.6.7 Comparison with Classical Models

One established method in literature is the μ-model [44], [55] used for modelling turn fault in machines with distributed winding, such as induction machines. In this model, the mutual and self-inductance is assumed to scale as a product of the number of turns of the two windings and the leakage inductance is assumed to scale linearly with the number of turns. The inductance matrix can then be written as (2.68) where subscript m denotes air-gap inductance. It is to be noted that the model does not distinguish whether the fault is on top, on bottom, or in between of the slot.

$$\mu = \frac{N_s}{N_t}$$

$$L = diag\begin{bmatrix}(1-\mu) & 1 & 1 & \mu\end{bmatrix} L_{ls} + \begin{bmatrix} (1-\mu)^2 L_{11,m} & (1-\mu) L_{12,m} & (1-\mu) L_{13,m} & \mu(1-\mu) L_{11,m} \\ (1-\mu) L_{12,m} & L_{22,m} & L_{23,m} & \mu L_{12,m} \\ (1-\mu) L_{13,m} & L_{23,m} & L_{33,m} & \mu L_{13,m} \\ \mu(1-\mu) L_{11,m} & \mu L_{12,m} & \mu L_{13,m} & \mu^2 L_{11,m} \end{bmatrix} \quad (2.68)$$

Using this technique the predicted inductance is calculated for a 1 turn fault (N_{ha}=7) as given in Table 2-14. It can be seen from L_{14} and L_{44} values that the prediction error for the faulted coil self and mutual inductance is large.

Table 2-14: Comparison of Inductance Predicted by Classical Approach for 1 Turn Fault (N_{ha}=7)

L_{ij}	L(Classical)	L(FE)	% error
L_{11}	0.305mH	0.307mH	-0.47%
L_{12}=L_{21}	-28.7µH	-29.7µH	-3%
L_{13}=L_{31}	-28.7µH	-27.9µH	1.68%
L_{14}=L_{41}	9.8µH	7.66µH	28%
L_{22}	0.322mH	0.325mH	-0.83%
L_{23}=L_{32}	-29.6µH	-29.7µH	0.064%
L_{24}=L_{42}	-0.92µH	-8.52e-9H	-10985%
L_{33}	0.322mH	0.325mH	-0.8%
L_{34}=L_{43}	-0.92µH	-1.37µH	-33%
L_{44}	**0.159µH**	**0.865µH**	**-81%**

2.6.8 Fault Current Prediction

To further confirm the analytical model, fundamental peak fault current predictions are compared with those obtained from FE simulation. Fig. 2-15 shows the results for 1 turn fault in full load condition for varying location of faulted turns inside the slot. The maximum error is 8% which is similar to the error calculated in the inductance comparison. Position 0 denotes that the faulted turn is located on the top of

the slot. It can be observed that the proposed model gives a good match whereas the prediction by the μ- model is off by 56% with respect to the FE predicted current.

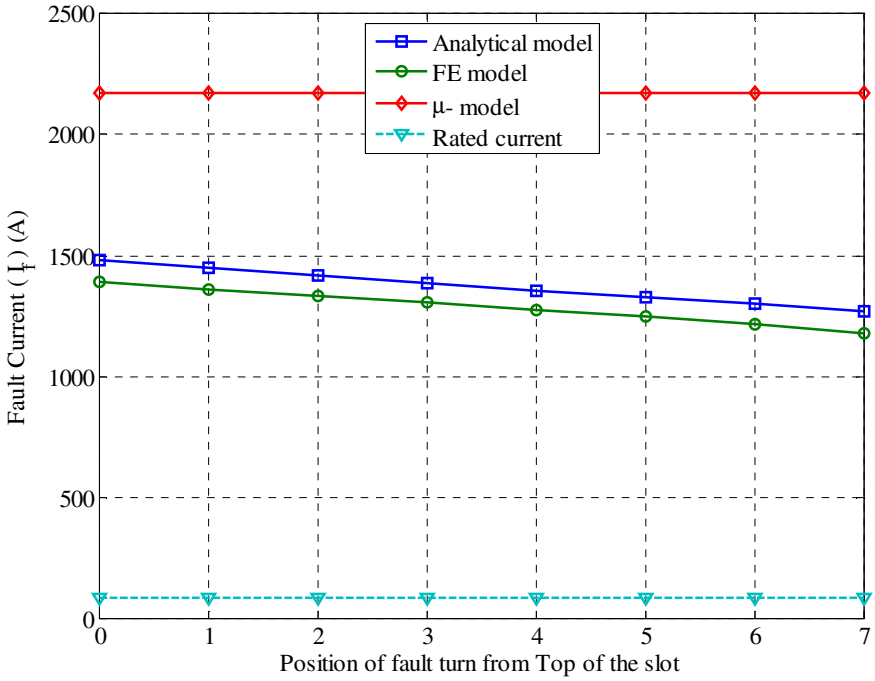

Fig. 2-15: Comparison for peak fault current prediction by proposed and classical model with direct-FE model under 1 turn fault for loaded condition for varying position of fault coil inside the slot (I_q=84A).

2.7 Conclusions

An analytical method of calculating the parameters of a transient SPM machine model under stator turn fault has been described and its utility demonstrated. The performance of the model is confirmed by running validation cases in FE. The model predicts the fault inductances and fault current with a maximum error of 8% compared to FE simulations. This model is general and the method can be extended to any winding configuration SPM machine. The model provides a basis for study of fault behaviour and development of fault detection techniques. If the slot leakage is more accurately predicted analytically by considering distribution of the turn, the accuracy of the model can be greatly improved.

Chapter 3

Transient Modelling of Interior Permanent Magnet Machine with Stator Turn Fault

An accurate transient model of Interior Permanent Magnet (IPM) machine with stator turn fault with due account of magnetic saturation is essential to develop robust and sensitive inter-turn fault detection algorithms and to evaluate drive controller performance and stability under fault conditions. The main contribution of this chapter is a general method of modelling stator turn fault using flux-linkage map of IPM machine under fault extracted from Finite Element (FE) analysis. Simulation results from the proposed fault model are compared against FE and experimental results. The results show that the proposed model matches well with experimental data.

3.1 Motivation

As explained in Chapter 1, inter-turn faults are one of the leading mechanisms to a complete winding failure, which in turn account for 21-37% of faults in electrical machines [7]–[11]. Interior permanent magnet (IPM) machines are increasing being favoured as the machine of choice for electric vehicle application due to their high power density, robustness, large constant power speed range and overall high efficiency [1], [3], [56]–[59]. In order to develop sensitive fault detection algorithms and fault tolerant control strategies, an accurate transient model of the machine under fault condition is indispensable [19], [60], [61] at development stage in order to save time and resources spent on experimental testing. This is because many faults such as inter-turn short-circuit may cause small changes in terminal voltages and currents. Consequently, it is difficult to detect them in an electrically noisy environment. Inaccurate representation of fault behaviour may lead to a detection algorithm working well in simulations, but not effective in real testing.

The previous chapter explored the use of analytical techniques for modelling turn faults in surface permanent magnet (SPM) machines. In deriving the analytical fault model for SPM machines, it was assumed that the laminations of the machine are infinitely permeable. This is a reasonable assumption for SPM machines with a large effective air-gap, however in IPM machines the effect of magnetic saturation cannot be ignored even under healthy condition let alone under fault conditions. This chapter therefore explores a direct FE derived turn fault model which can account for not only magnetic saturation in a healthy machine but also localised saturation caused by turn fault in a faulted machine.

3.2 Literature Review

The modelling of inter-turn short-circuit fault in IPM was treated in [55], where a phase variable model of IPM motor under condition of linear magnetic characteristics was derived, by extending the fault model derived for induction motors in [44]. However, no experimental validation was reported. In [62] a method of extending the IPM model under fault accounting for magnetic saturation was proposed. The self- and mutual-fluxes of the healthy and faulted turns are assumed to be proportional to their number of turns. The phase inductance variation due to saturation described in [62] is obtained by computing first the saturated values of *d*- and *q*- axis inductances, L_d, and L_q, and then performing inverse transformation to *abc* quantities. However, this assumption is not strictly true for most PM machines in which a significant part of the self- and mutual-inductances is contributed by the slot leakage. Moreover, the concept was not tested in simulation or experiments. In [19], [63], [40] an FE time stepping co-simulation transient model of BLDC was used for developing fault detection algorithms. However, time stepped FE simulation is very time consuming and not suitable for computationally efficient simulation studies involving pulse-width modulated (PWM) drives, due to the small time scales involved. Moreover, in case of IPM machine, fault detection needs to be tested at a number of different *dq* currents due to magnetic non-linearity, which will further increase compute time. In [47], [64], a fault model for IPM BLDC was derived using winding function theory (WFT) for single layer magnet rotor, neglecting magnetic saturation effects. The inverse air gap function used in [47] is difficult to derive for more complex rotor geometries common in high

saliency machines. In [65] a permeance network (PN) model for turn faults in saturated PMSMs was proposed. The permeance network model is then used to extract 4-dimensional (4-d) flux/inductance lookup tables needed to formulate the transient model. However no experimental validation was performed. Further derivation of a PN model is very tedious, and compromises accuracy, especially for complex rotor geometries.

In [61] and [36] an inductance based model was proposed for inter-turn fault detection in surface mounted PM machines. However, IPM machines with buried magnets exhibits high level of magnetic saturation and cross-saturation effects and therefore separation of armature reaction flux linkage from the total flux linkage will incur large error and hence compromises model accuracy [66]–[71]. Moreover the method of extraction of inductances reported in [36] and [72] by energy-perturbation is computationally more demanding [70] requiring twice as many FE computations. A hybrid model for wound-rotor synchronous generator reported in [73] assumes that the machine operates in linear region under healthy condition. However, this assumption is not applicable to IPM machines with high level of magnetic saturation [70].

The aim of this chapter is to establish an accurate and computationally efficient model of IPM machines under stator turn fault. This is achieved by extracting flux linkage map of the machine under turn fault conditions using offline static FE analysis and combining it with voltage equations of the machine. The method is not limited to IPM machines and the same technique can be used for modelling stator turn faults in rotor systems including surface PM machines, switched reluctance machines, switched flux machines and, separately excited machines, such as wound field synchronous machines. This approach enables the full representation of spatial harmonics and magnetic saturation under inter-turn fault and all load conditions and therefore is the most accurate representation of the faulted motor behaviour apart from a time stepping FE-coupled analysis [74]. Although the generation of flux map from offline static FE model is computationally expensive, once the lookup tables are established it will have a much faster simulation speed compared to time stepping FE coupled simulation [74]. This is quite advantageous in drive coupled simulation, since the PWM pulses are of small duration, an FE-coupled time stepping simulation is prohibitively expensive in terms of compute time. This method is also advantageous when numerous test cases

under different loads and speeds need to be performed quickly during development of fault detection/mitigation schemes. Simplified models such as that presented in [47], [55] will not be able to represent the phenomena correctly over all load/speed ranges. It also allows speedup of simulation time compared to FE coupled simulation in case where the rotor is skewed, since multi-slice FE simulation has to perform simulation for all the skew slices which results in significant increase in the overall computation time [75]. It should also be noted that although it is possible to neglect saturation characteristics for simulation of turn fault as suggested by some authors [47], [55], the fault model thus obtained will not be useful to check validity of performance of fault detection and fault tolerant algorithms over the entire range of operation of the machine. This may lead to over-simplified fault detection and mitigation methods which work well with the simplified motor model, but may not perform well in actual test conditions. Extensive experimental tests are performed to validate the model over speed and load ranges.

3.3 Transient Machine Modelling under Stator Turn Fault

It is well known that in order to accurately model behaviour of a healthy IPM machine, a mapping of flux-linkages to current is needed [76], [66]. This non-linear flux linkage map can capture most of the behaviour of the machine including the magnetic saturation, spatial saliency and harmonics [66]–[69]. 3-dimensional (3d) effects such as overhang fringe fields, iron losses and rotor eddy currents may also be included. Using the same approach, a model of a machine under stator turn fault can also be extracted in the form of appropriate flux-linkage lookup tables together with voltage governing equations and loss components.

Without loss of generality, the turn fault is assumed to be in 'c' phase winding which is therefore divided into two sub-windings. Sub-winding 'cs1' is the healthy part and sub-winding 'cs2' is the faulty part as shown in Fig. 3-1. 'μ' represents the fault winding fraction, defined as the ratio of number of short-circuited turns in phase c (N_s) to the total number of turns in phase c (N_t) [55]. R_f represents the fault resistance, i_f denotes the current into the fault resistance.

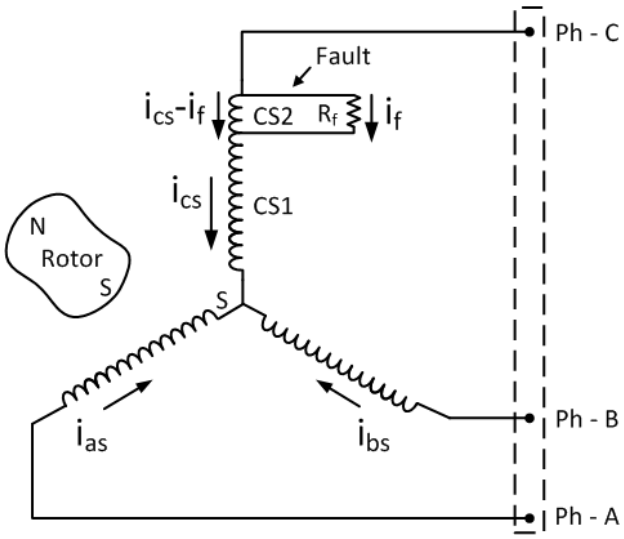

Fig. 3-1: Schematic representation of IPM machine with turn fault in 'C' phase.

3.3.1 Machine Equations in *abc* Frame

The stator equations for IPM machines with turn fault can be expressed as (3.1).

$$\boldsymbol{V_s}^f = \boldsymbol{R_s}^f \boldsymbol{i_s}^f + d\boldsymbol{\lambda_s}^f / dt \tag{3.1}$$

where,

$$\begin{aligned}
\boldsymbol{V_s}^f &= \left[v_{as} \quad v_{bs} \quad v_{cs1} \quad \left(v_{cs2} = v_f\right) \right]^T \\
\boldsymbol{i_s}^f &= \left[i_{as} \quad i_{bs} \quad i_{cs} \quad i_{cs} - i_f \right]^T \\
\boldsymbol{\lambda_s}^f &= \left[\lambda_{as} \quad \lambda_{bs} \quad \lambda_{cs1} \quad \left(\lambda_{cs2} = \lambda_f\right) \right]^T \\
\boldsymbol{R_s}^f &= R_s \, diag\left[1 \quad 1 \quad 1-\mu \quad \mu\right] \\
\mu &= \frac{N_s}{N_t}
\end{aligned} \tag{3.2}$$

Since IPM machine exhibits strong saturation, the flux linkage and torque is a nonlinear function of current and mechanical angular position. This relationship is denoted using function '*g*' as a general non-linearity function between the quantities as shown in,

$$\begin{aligned}
\lambda_{xs} &= g_x\left(i_a, i_b, i_c, i_f, \theta_m\right) \\
T_e &= g_e\left(i_a, i_b, i_c, i_f, \theta_m\right)
\end{aligned} \tag{3.3}$$

where, subscript *x* denotes healthy phases *a*, *b*, and two sub-windings *cs1* or *cs2*(*f*) in phase *c*. Since terminal voltage of phase '*c*' is the sum of voltages of the sub-windings

'*cs1*' and '*cs2*', the last two rows of voltage equation in (3.2) can be added and re-arranged to obtain terminal voltages as shown by (3.4).

$$\boldsymbol{V_s} = R_s \boldsymbol{i}_s + \frac{d\boldsymbol{\lambda_s}}{dt} + \mu \boldsymbol{A}_1 i_f \tag{3.4}$$

where,

$$\begin{aligned}
\boldsymbol{V_s} &= \left[v_{as} \quad v_{bs} \quad \left(v_{cs} = v_{cs1} + v_{cs2} \right) \right]^T \\
\boldsymbol{i_s} &= \left[i_{as} \quad i_{bs} \quad i_{cs} \right]^T \\
\boldsymbol{\lambda_s} &= \left[\lambda_{as} \quad \lambda_{bs} \quad \left(\lambda_{cs} = \lambda_{cs1} + \lambda_{cs2} \right) \right]^T \\
\boldsymbol{A}_1 &= -\left[0 \quad 0 \quad R_s \right]^T
\end{aligned} \tag{3.5}$$

The voltage of the shorted circuited winding '*cs2*' can be written separately as (3.6).

$$V_f = V_{cs2} = R_f i_f = \mu R_s \left(i_{cs} - i_f \right) + \frac{d\lambda_f}{dt} \tag{3.6}$$

3.3.2 Machine Equations in *dq* Frame

The stator equations can be transformed to the *dq* frame using the synchronous frame transformation defined in [77] to obtain (3.7).

$$\begin{aligned}
\boldsymbol{V_{dq}} = \boldsymbol{R_s i_{dq}} + d\boldsymbol{\lambda_{dq}} / dt + \omega_e \left[-\lambda_q \quad \lambda_d \right]^T \\
-\mu \frac{2}{3} R_s \left[\sin\left(\theta_e + 2\pi/3\right) \quad \cos\left(\theta_e + 2\pi/3\right) \right]^T i_f
\end{aligned} \tag{3.7}$$

where,

$$\begin{aligned}
\lambda_d &= g_d \left(i_d, i_q, i_f, \theta_m \right) \\
\lambda_q &= g_q \left(i_d, i_q, i_f, \theta_m \right)
\end{aligned} \tag{3.8}$$

The voltage of the shorted turns can be expressed in terms of the *dq* currents as (3.9).

$$V_f = R_f i_f = \mu R_s \begin{pmatrix} i_d \sin\left(\theta_e + 2\pi/3\right) \\ + i_q \cos\left(\theta_e + 2\pi/3\right) - i_f \end{pmatrix} + \frac{d\lambda_f}{dt} \tag{3.9}$$

where,

$$\lambda_f = \lambda_{cs2} = g_f \left(i_d, i_q, i_f, \theta_m \right) \tag{3.10}$$

The torque of the faulted machine can be calculated by a torque lookup table obtained from static FE using (3.11).

$$T_e = g_T\left(i_d, i_q, i_f, \theta_m\right) \tag{3.11}$$

In order to use the model in dynamic simulations, the equations can be written in its integral form [77].

$$\boldsymbol{\lambda}_{dq} = \int\left(\boldsymbol{V}_{\boldsymbol{dq}} - \boldsymbol{R}_s\boldsymbol{i}_{\boldsymbol{dq}} - \omega_e\begin{bmatrix}-\lambda_q & \lambda_d\end{bmatrix}^T + \mu\frac{2}{3}R_s\begin{bmatrix}\sin\left(\theta_e + 2\pi/3\right)\\ \cos\left(\theta_e + 2\pi/3\right)\end{bmatrix}i_f\right)dt \tag{3.12}$$

$$\lambda_f = \int\left(R_f i_f - \mu R_s\left(i_d\sin\left(\theta_e + 2\pi/3\right) + i_q\cos\left(\theta_e + 2\pi/3\right) - i_f\right)\right)dt \tag{3.13}$$

where, the *d-q* axis currents, i_d and i_q, and the fault current i_f are obtained from the inverses of (3.8) and (3.10).

$$\begin{aligned} i_d &= g_d^{-1}\left(\lambda_d, \lambda_q, \lambda_f, \theta_m\right)\\ i_q &= g_q^{-1}\left(\lambda_d, \lambda_q, \lambda_f, \theta_m\right)\\ i_f &= g_f^{-1}\left(\lambda_d, \lambda_q, \lambda_f, \theta_m\right)\end{aligned} \tag{3.14}$$

Therefore, if the non-linear mapping of the *d*-, *q*-, and *f*- flux linkages to i_d, i_q, i_f and θ_m can be obtained using static FE calculations, it can be used with a differential-algebraic (DAE) capable solver, such as Saber [78] to obtain the solution. Alternatively the current to flux linkage map can be numerically inverted to obtain the inverse mapping functions (3.14) which can be used with an ordinary differential equation (ODE) solver [79].

By way of example, Fig. 3-2 shows schematic of the ODE solver based fault model established using the proposed technique. It should be noted that the temperature effect of the phase resistance can be accounted in the model.

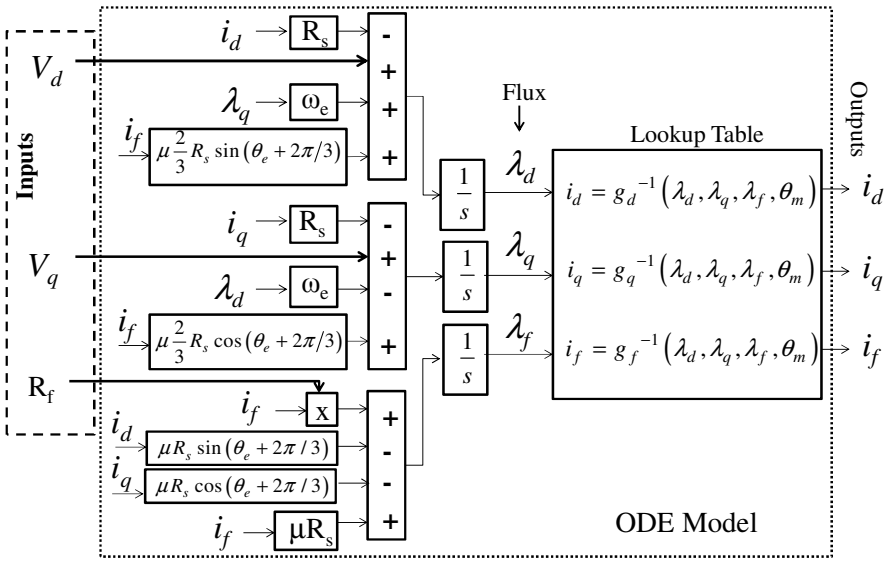

Fig. 3-2: Schematic of ODE solver based fault model.

3.3.3 FE Model

For the purpose of validation of the proposed modelling methodology a transient direct FE model of a 3-phase, 6-pole, 36-slot IPM motor with a two turn fault is generated. The machine is designed to maximize reluctance torque so that a high torque density can be achieved with low grade magnets, such as ferrite or bonded NdFeB. For this reason, it is often called permanent magnet assisted synchronous reluctance machine. The machine has 2 slots per pole per phase and incorporates a 3-step rotor skew of 7º (mech). The main parameters of the machine are listed in Table 3-1.

.

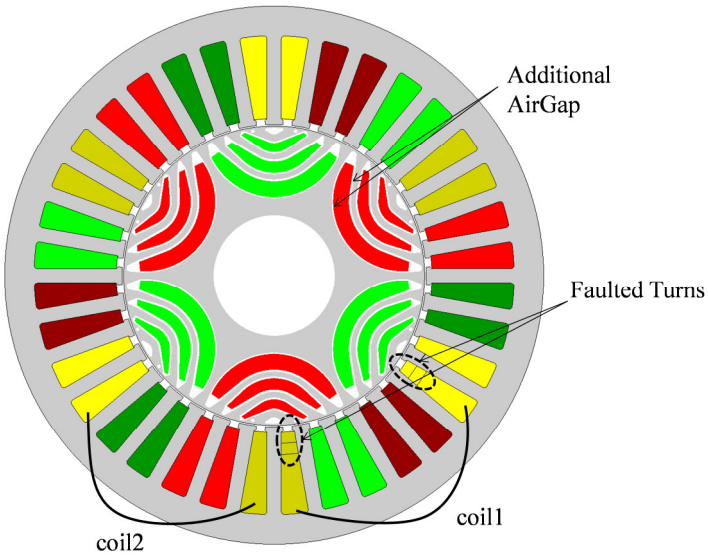

(a)

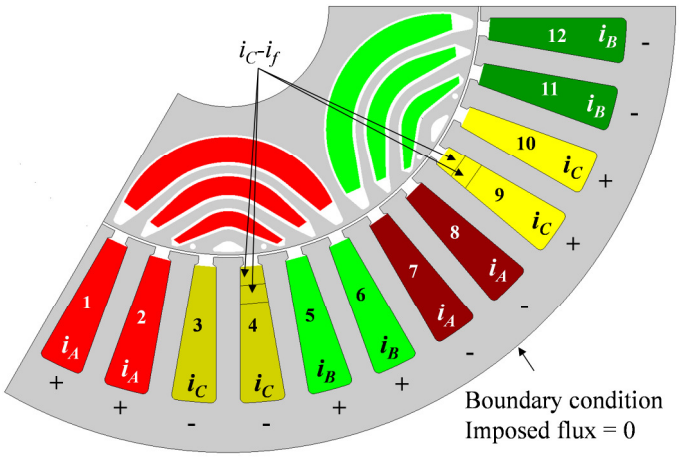

(b)

Fig. 3-3: FE model of 36 slot, 6 pole IPM Machine with 2 turn fault in C phase (a) full FE model, (b) zoomed portion of model containing turn fault showing excitation currents. (+, - signs depicts coil current direction. + represents current direction into the plane of the paper).

Table 3-1: IPM Machine Parameters

Quantity	**Unit**	**Value**
Torque (peak/rated)	Nm	30/17
Speed (base/max)	r/min	2100/8200
Power (peak/rated)	kW	6.6/3.75
Peak current	A	85
Number of pole-pairs (n)	--	3
Number of slots	--	36
Active stator length	mm	105
Stator outer diameter	mm	120
Airgap	mm	0.35
Rotor diameter	mm	67
Rotor skew slices	--	3
Number of turns/phase (N_t)	--	42
Magnet Remanance (B_r)	T	0.56

The laminations of the machine were manufactured by laser cutting and the damage to material property due to the cutting process [80]–[82]. The machine after fabrication was observed to have 22% lower back-EMF due to the damage due to laser cutting [82]. This damage to the laminations was accounted for in the FE model using additional air-gaps in the rotor such that the measured back-EMF matched with the FE model as shown in Fig. 3-16. Fig. 3-3 shows the FE model including the two turn winding fault.

In order to obtain the flux-linkages map of the faulted machine for generating mode of operation magneto-static FE simulations are performed by varying i_q over [-70A, 10A], i_d over [-70A, 10A] in steps of 10A and i_f over [-350A, 350A] in steps of 50A over one complete electrical cycle [0, 120º] (mech) in steps of 2º. To cover both motoring and generating modes of operation, the corresponding d- and q-axis current range of [-70A, 70A] is necessary. Although the coarse steps of 50A for i_f may compromise accuracy of the flux linkage map it was selected to reduce the compute time. It is to be noted that in performing the FE simulations, the current in the 2 short-circuited turns are defined as i_c-i_f as illustrated in Fig. 3-1.

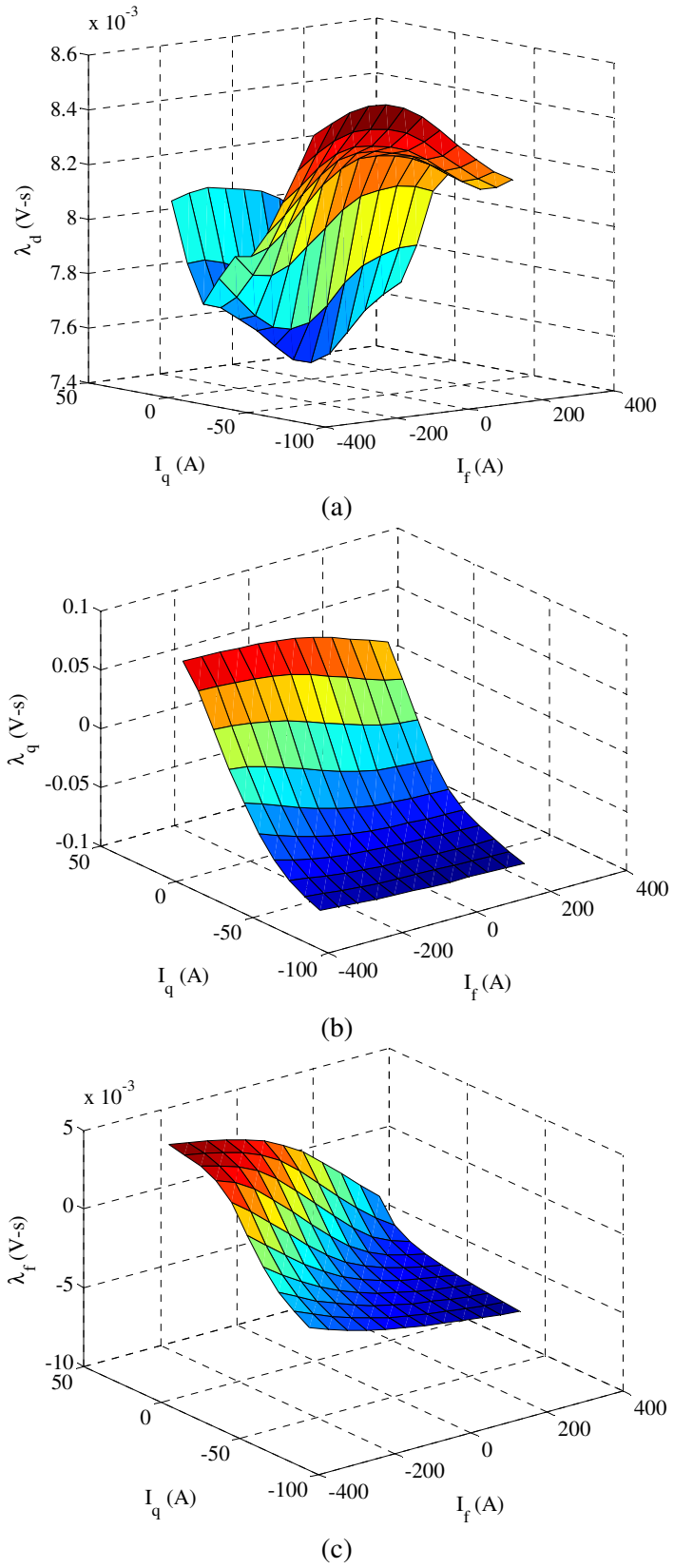

Fig. 3-4: Flux linkage map of machine at a sample case i_d=-30A and θ_m=0. (a) *d*-axis flux linkage. (b) *q*-axis flux linkage (c) *cs2*(*f*) flux linkage

Fig. 3-4 shows the flux-linkage maps of the IPM machine as functions of i_q and i_f at i_d =-30A and θ_m=0º under fault condition. As can be seen from the plots the machine exhibits significant non-linearity as a result of magnetic saturation from the load current and due to fault current. This illustrates the effectiveness of the fault model to capture saturation effects.

Although the faulted phase has been assumed to be in phase 'C', for the development of the model and for extraction of the flux linkage-current lookup tables, fault in any other phase can be simulated without the need to run any further FE computation, since it is simply a shift of electrical/mechanical angle. This can be achieved by modifying θ_e according to (3.15) and accordingly setting $\theta_m = \theta_e/p$ in the lookup tables.

$$\theta_e = \begin{cases} \theta_e - 2\pi/3 & ; \text{Phase A fault} \\ \theta_e - 4\pi/3 & ; \text{Phase B fault} \\ \theta_e & ; \text{Phase C fault} \end{cases} \tag{3.15}$$

3.3.4 Skew Computation

The machine selected for validation of fault modeling incorporates a rotor which consists of 3 identical rotor slices, which are skewed by -3.5º, 0º and +3.5º (mechanical). The rotor slices and shaft are shown in Fig. 3-14(b).

Rotor skew is an effective means of minimizing cogging torque, electro-motive force (EMF) harmonics and output torque ripple [83]. However, this poses a challenge in terms of modeling the behavior of the machine in healthy and faulty condition since each rotor slice will have different saturation levels. Since the machine selected for validation of fault modeling incorporates a 3-step skewed rotor, the problem of skew modeling needs to be addressed. In order to create an accurate flux map, the conventional technique is to perform static FE analysis for all the skew slices and then add the contribution of each slice together to obtain the overall flux/torque map [84]–[86]. However, this is computationally intensive and several methods [87], [88] have been proposed in the literature to obtain the overall flux map from just one set of FE calculations with rotor at 0º skew angle. However, these methods are still not sufficiently accurate specially in capturing spatial harmonic variation and the influence of skew on saturation of the machine [75]. An accurate method to model the effect of

skew in healthy machines was presented in [75]. However, the method in [75] is shown valid for healthy machines and for machine with stator turn fault further refinement of the model needs to be performed. A general case of skew rotor slice is shown in Fig. 3-5 where, d_0, q_0 refers to the reference dq axis of the rotor with 0 skew angle, and d_s, q_s refer to the dq axis of the rotor with β_{sk} mechanical skew angle.

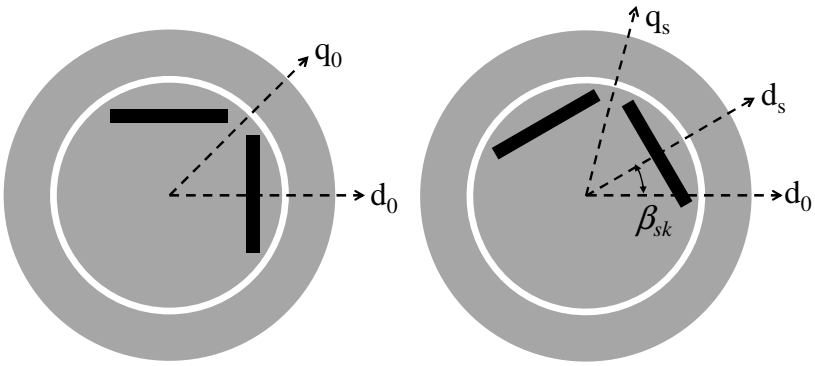

Fig. 3-5: Rotor skew slices at mechanical angle of (a) 0 (rad) skew, (b) β_{sk} (rad) skew

The dq current and flux vector diagram is shown in Fig. 3-6 where, I and λ denotes the stator current and flux linkage space vector respectively. Considering first the case of 0 (rad) rotor skew the current vector projection on d_0, q_0 axis is i_{d0} and i_{q0} as shown in Fig. 6. The flux-linkage and torque can be computed from the lookup tables obtained from magneto-static FE analysis, using the dq current values (i_{d0},i_{q0}) as given by (3.16). It is to be noted that the argument θ_m is necessary in the lookup process, since under fault condition dq flux linkages have a dominant second harmonic corresponding to the unbalance introduced into the machine due to fault.

For the case of rotor slice with skew shift of $+\beta_{sk}$ (mech) angle for a rotor with 'p' pole-pairs, it can be observed from the vector diagram in Fig. 3-6 that the stator current vector is displaced ϕ-$p\beta_{sk}$ with the d_s axis. This is due to the fact that the rotor shift w.r.t. the stator A phase, however, the stator current are still at the same angular displacement w.r.t phase A.

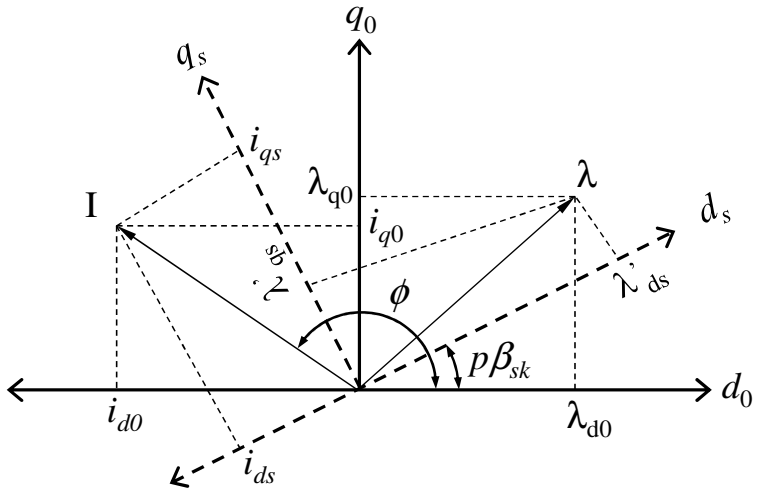

Fig. 3-6: Flux linkage and current vectors for rotor skewed by β_{sk} (mech) angle

$$\begin{aligned}
\vec{I}_{dq0} &= i_{d0} + ji_{q0} = |I| e^{j\phi} \\
\vec{\lambda}_{dq0} &= g_d\left(i_{d0}, i_{q0}, i_f, \theta_m\right) + jg_q\left(i_{d0}, i_{q0}, i_f, \theta_m\right) \\
\lambda_{f0} &= g_f\left(i_{d0}, i_{q0}, i_f, \theta_m\right) \\
T_0(\theta_m) &= T_e\left(i_{d0}, i_{q0}, i_f, \theta_m\right)
\end{aligned} \tag{3.16}$$

Hence, for calculation of the skewed rotor flux-linkage, the projection of the stator current vector I onto d_s-, q_s- axis should be used, to obtain λ_{ds} and λ_{qs} referred to d_s-,q_s- axis as given in (3.17). Further, since the rotor is physically shifted by β_{sk} (mech), the mechanical angle in the lookup process is modified to $\theta_m+\beta_{sk}$, to account for the shift of the rotor. It is also to be noted that the fault current i_f is not modified because it does not change with rotor position. The torque can be similarly computed by using i_{ds}, i_{qs} instead of using i_{d0}, i_{q0} and modifying the θ_m to $\theta_m+\beta_{sk}$ in the torque lookup table.

$$\begin{aligned}
\vec{I}_{dqs} &= i_{ds} + ji_{qs} = \vec{I}_{dq_0} e^{-jp\beta_{sk}} \\
\lambda_{dqs} &= \lambda_{ds} + j\lambda_{qs} \\
\lambda_{ds} &= g_d\left(i_{ds}, i_{qs}, i_f, \theta_m + \beta_{sk}\right) \\
\lambda_{qs} &= g_q\left(i_{ds}, i_{qs}, i_f, \theta_m + \beta_{sk}\right) \\
\lambda_{fs} &= g_f\left(i_{ds}, i_{qs}, i_f, \theta_m + \beta_{sk}\right) \\
T_s(\theta_m) &= T_e\left(i_{ds}, i_{qs}, i_f, \theta_m + \beta_{sk}\right)
\end{aligned} \tag{3.17}$$

However, since the flux-linkage vector in (3.17) is referred to the d_s-, q_s- frame, it has to be transformed back to the d_0, q_0 frame in which the overall machine dq flux-

linkages are referred, to obtain λ_d and λ_q contribution by the skewed rotor slice as given in (3.18). It is to be noted that the faulted coil flux linkages are not rotated since it is not a vector quantity.

$$\begin{aligned} \vec{\lambda}_{dq} &= \left\{ \lambda_{ds} + j\lambda_{qs} \right\} e^{jp\beta_{sk}} \\ \lambda_f &= \lambda_{fs} \end{aligned} \tag{3.18}$$

Finally, the total flux and torque contribution are obtained in (3.19) from all the skewed rotor slices scaled by the axial length of the rotor slice, where l_β is the length of one skewed rotor slice, β_{skew} is the total mechanical skew angle of the rotor and l_{stk} is the total length of the rotor.

$$\begin{aligned} \vec{\lambda}_{dq(total)} &= \sum_{\beta_{sk}} \vec{\lambda}_{dqs} \frac{l_\beta}{l_{stk}}, \quad \lambda_{f(total)} = \sum_{\beta_{sk}} \lambda_{fs} \frac{l_\beta}{l_{stk}} \\ T_{e(total)} &= \sum_{\beta_{sk}} T_s \frac{l_\beta}{l_{stk}} \\ l_\beta &= \frac{l_{stk}}{n}, \quad \beta_{sk} = \begin{cases} \dfrac{\beta_{skew}}{n} y, & y \in \mathbb{N},\ 0 \le y \le n \end{cases} \end{aligned} \tag{3.19}$$

where, n is the number of skewed rotor slices.

An important point to note is that slot leakage flux-linkage should not undergo any change against the skew rotor slice position, i.e., the leakage flux including the slot leakage flux should remain unaffected irrespective of the rotor skew angle. This can be easily proven as shown in (3.20), where λ_m denotes the air-gap flux linkages.

$$\begin{aligned} \vec{\lambda}_{dqs} &= \vec{\lambda}_m \left(i_{ds}, i_{qs} \right) + L_{ls} \vec{I}_{dq_0} e^{-jp\beta_{sk}} \\ \vec{\lambda}_{dq0} &= \vec{\lambda}_{dqs} e^{jp\beta_{sk}} = \vec{\lambda}_m \left(i_{ds}, i_{qs} \right) e^{jp\beta_{sk}} + L_{ls} \vec{I}_{dq_0} \end{aligned} \tag{3.20}$$

In order to verify the proposed skew calculation technique, a test case of (i_d= -40A, i_q= -40A, i_f= -200A) was performed using multi-slice FE simulation and the proposed method, and the results are compared in Fig. 3-7.

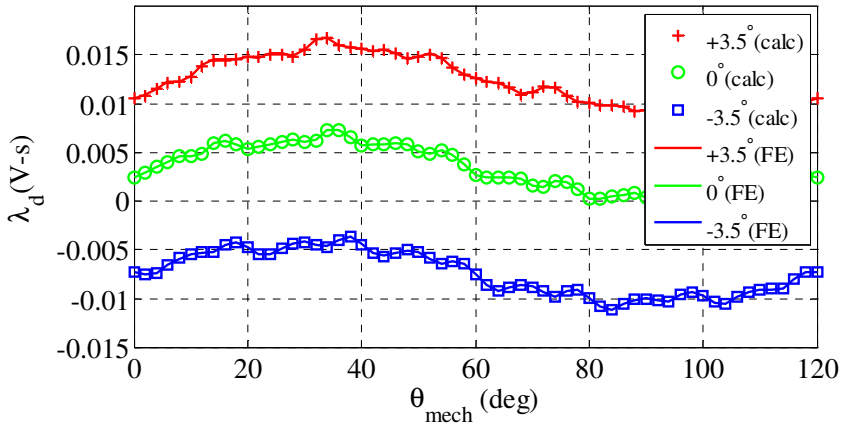
0.015
0.01
0.005
0
-0.005
-0.01
-0.015
0
20
40
60
80
100
120
λd (V-s)
θmech (deg)
+3.5° (calc)
0° (calc)
-3.5° (calc)
+3.5° (FE)
0° (FE)
-3.5° (FE)

(a)

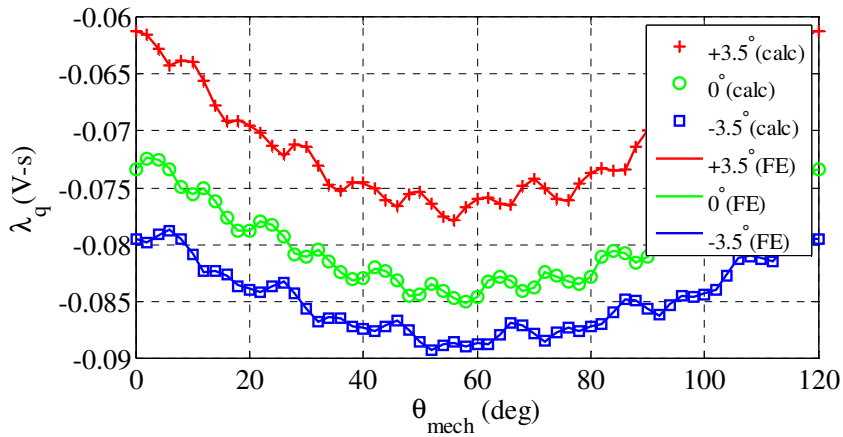
-0.06
-0.065
-0.07
-0.075
-0.08
-0.085
-0.09
0
20
40
60
80
100
120
λq (V-s)
θmech (deg)
+3.5° (calc)
0° (calc)
-3.5° (calc)
+3.5° (FE)
0° (FE)
-3.5° (FE)

(b)

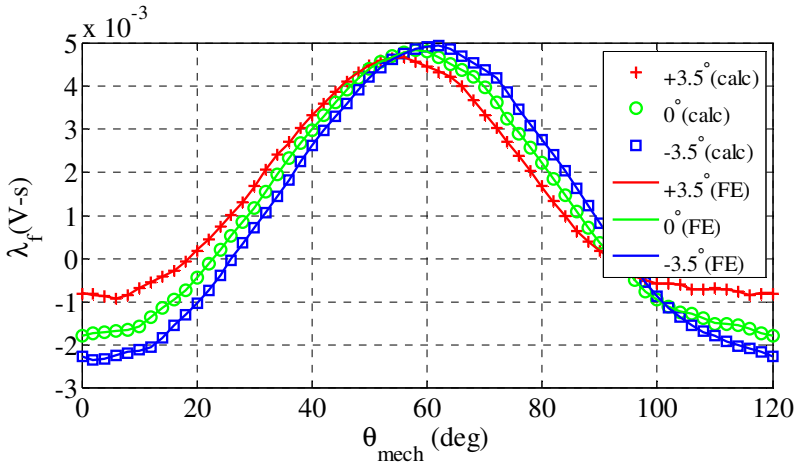
x 10-3
5
4
3
2
1
0
-1
-2
-3
0
20
40
60
80
100
120
λf (V-s)
θmech (deg)
+3.5° (calc)
0° (calc)
-3.5° (calc)
+3.5° (FE)
0° (FE)
-3.5° (FE)

(c)

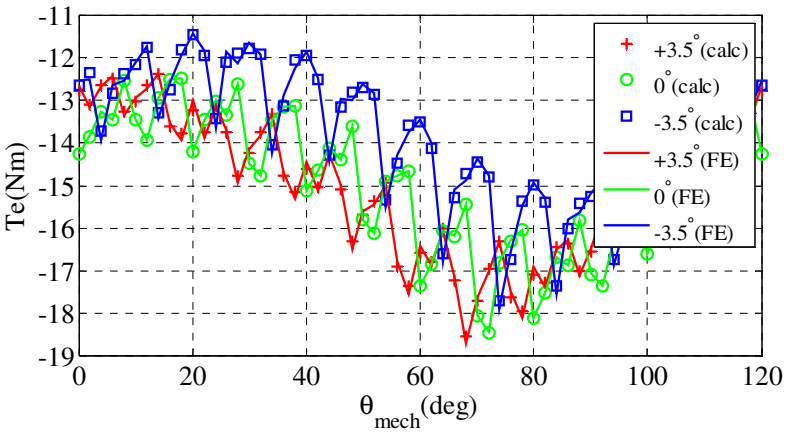

(d)

Fig. 3-7: Comparison between multi-slice FE and proposed method (calc) at (i_d= -40A, i_q= -40A, i_f= -200A) (a) *d*- axis flux linkage, (b) *q*- axis flux linkage, (c) faulted turn flux linkages (d) Torque

It can be seen from Fig. 3-7 that the match is excellent. This algorithm reduces the computation time by a factor of number of skew slices compared to performing static FE calculation for all rotor skew slices. This method is therefore used to generate the flux-linkage lookup tables.

3.3.5 Inverse (Flux-Current) Lookup Algorithm for ODE solvers

In case of ODE solvers, the algebraic loops in the model need to be eliminated. This can be easily achieved if mapping of flux-linkages to current (3.14) can be determined. However this is not a simple process since the lookup tables are 4 dimensional and the relative magnitudes of *dq* flux-linkages are much greater than that of the faulted winding *'f'*. This can cause numerical instability if the data is not properly normalized during the inversion process. In order to create a precise inversion, for each mechanical angle in the lookup table, a minimum and maximum value of λ_d, λ_q, λ_f is obtained and this interval is sub-divided into *m* divisions as given by (3.21). Results are shown with *m*=32.

$$\begin{aligned}
&\lambda_x = \left\{ \lambda_{x,\min} + i\lambda_{x,inc} \;\middle|\; i \in \mathbb{N}, 0 \le i \le m \right\} \\
&\lambda_{x,\min} = \min\left(\lambda_x\left(i_d, i_q, i_f, \theta_m\right)\Big|_{\theta=\theta_0} \right) \\
&\lambda_{x,\max} = \max\left(\lambda_x\left(i_d, i_q, i_f, \theta_m\right)\Big|_{\theta=\theta_0} \right) \\
&\lambda_{x,inc} = \frac{\lambda_{x,\min} + \lambda_{x,\max}}{m} \\
&x \in \{d, q, f\}
\end{aligned} \tag{3.21}$$

The inverse solution can then be obtained by minimization of the root-mean-square (RMS) flux error residual given by (3.22)-(3.23) by varying i_d, i_q, i_f for each $\theta_m = \theta_j$ to minimize the flux prediction error.

$$\lambda_{total}^{\;err} = \sqrt{\sum_{x \in \{d,q,f\}} \lambda_x^{\;err}} \tag{3.22}$$

Where,

$$\begin{aligned}
\lambda_x^{\;err} &= \left(\frac{\left(\lambda_x\left(i_d, i_q, i_f, \theta_j\right) - \lambda_x^{\;*}\right)}{\lambda_{x,mid}\left(\theta_j\right)} \right)^2 \\
\lambda_{x,mid}\left(\theta_j\right) &= \frac{1}{2}\left(\begin{array}{l} \left|\max \lambda_x\left(i_d, i_q, i_f, \theta_j\right)\right| \\ +\left|\min \lambda_x\left(i_d, i_q, i_f, \theta_j\right)\right| \end{array} \right)
\end{aligned} \tag{3.23}$$

The normalization of the flux magnitudes using their mid-range values as given in (3.23) is absolutely essential in the numerical inversion process because if not normalized the RMS error can get swamped by the relative difference in the error magnitudes of the *dq* and fault coil flux linkage magnitudes, resulting in either non-convergence or wrong convergence of the minimizer algorithm. Even then it is possible that some points do not converge to a solution. This happens when the operating flux gets close to the boundary of the flux lookup tables. Usually to avoid non-convergence, the initial current range used to generate the flux linkage map is made much larger than the operating current range so that during the inversion process the operating flux range is well within the current-flux map boundary so that convergence is easily achieved. However, increasing the size of the lookup table increases FE computation time further, so as an acceptable compromise between accuracy and compute time, the non-

convergence points are estimated by linear extrapolation from the neighboring converged points.

Once the inverse flux-current map has been created, a validation of the inversion process can be performed. This is carried out by selecting each set of i_d, i_q, i_f ,θ in the original current-flux linkage map, and using (3.8),(3.10) to compute λ_d, λ_q, λ_f, which are employed in (3.14) to compute a new set of i_d, i_q, i_f. Fig. 3-8 shows the errors in current prediction at a sample operating point of i_d=-50A, and θ=0^o. The maximum errors of the *d*, *q* and fault current prediction are 4%, 4% and 8%, respectively within 80% of the entire current ranges. Although the error can be reduced further by using spline interpolation, increasing the step size and the maximum and minimum bounds of the flux linkage to current map obtained from FE. It was not performed in order to reduce compute time. It is also worth noting that the primary purpose of the inversion calculation is to show a method of solution with ODE solvers which give acceptable prediction performance, however if higher precision is necessary DAE solvers can be used.

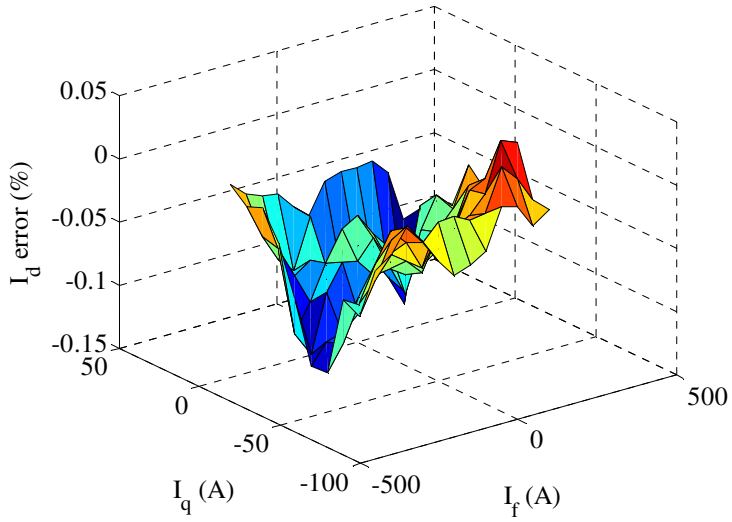

(a)

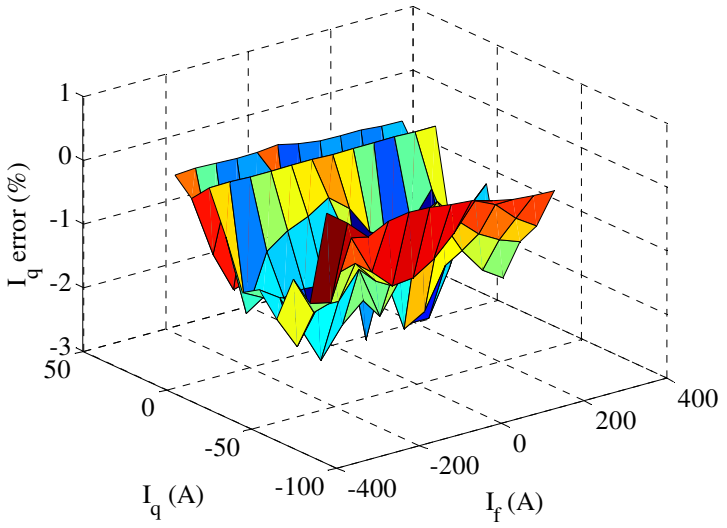

(b)

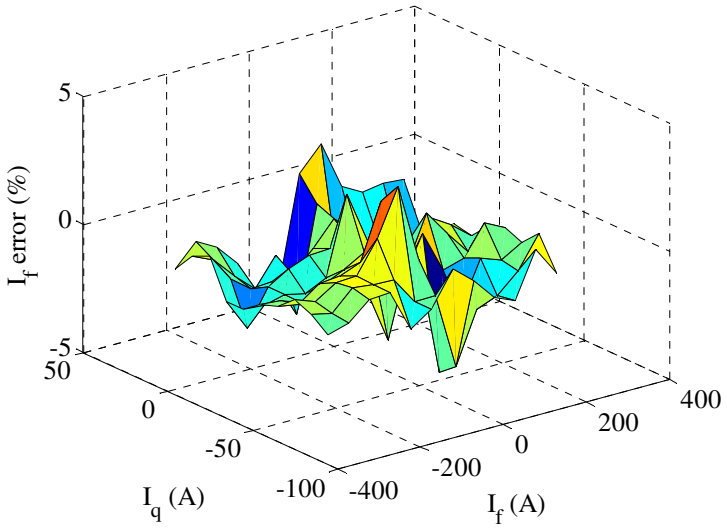

(c)

Fig. 3-8: Current prediction errors due to table inversion at i_d=-50A and θ_m=0 (a) d- axis current error, (b) q- axis current error and (c) fault current error.

3.4 Simulation Validation

To illustrate the utility of ODE and DAE solvers for the proposed fault modeling approach without loss of generality, generator operation of the machine under study with a resistive load of 2.2Ω with two turn short-circuit fault at 3500 r/min and R_f=5.5mΩ is simulated by both the FE model and the proposed model implemented with the inverse lookup tables and ODE23s solver [79], and DAE solver [32]. It is to be

noted that the FE and proposed models are simulated for 1 rotor slice in order to reduce FE computation time, and does not in any way affect model validation as long as the same current-flux linkage relation is maintained in the both models. The comparison of simulation times is shown in Table 3-2. Hardware validations provided in next section uses the current-flux linkage map which accounts for the 3-step skewed rotor.

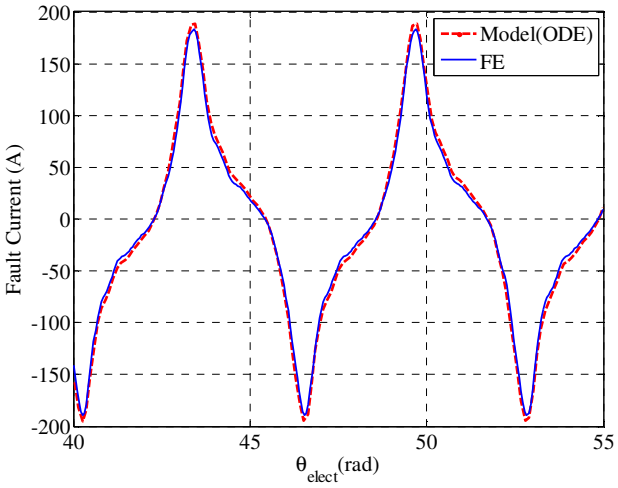

Fig. 3-9: Fault current comparison of FE verses model (ODE) solved by ODE solver at load of 2.2Ω at 3500 r/min

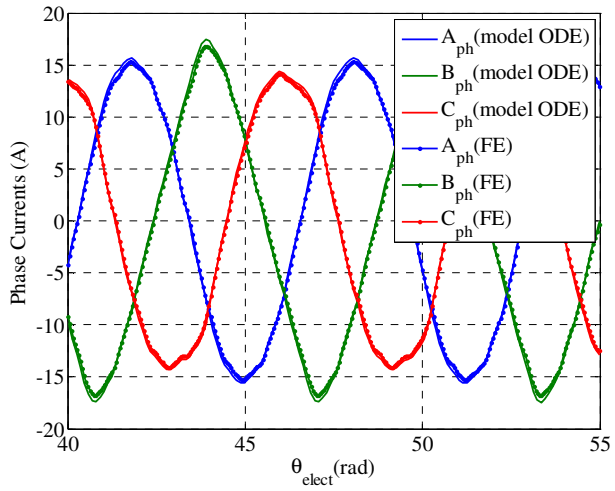

Fig. 3-10: Phase current comparison of FE verses model (ODE) solved by ODE solver at load of 2.2Ω at 3500 r/min

Fig. 3-9 and Fig. 3-10 show the comparison of FE predicted fault current and phase currents with those obtained from the ODE solver based model. As is quite

evident the currents predicted by the proposed model matches very well with the FE results in terms of both peak and wave-shape.

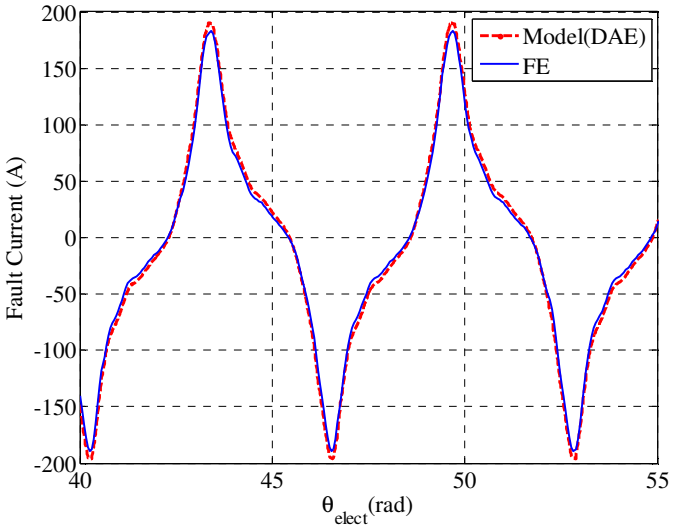

Fig. 3-11: Fault current comparison of FE verses model (DAE) solved by DAE solver at load of 2.2Ω at 3500 r/min

Fig. 3-11 compares the same operating point predicted by the FE and DAE solver based model. It can be observed that the DAE solutions also match the FE prediction very well. It is also to be noted that the errors between the FE and DAE results arises from the coarse steps in i_f selected to generate the lookup table. A finer step size in the lookup tables will improve the model accuracy. The DAE based model is simpler to set up if a DAE solver, such as Saber, Modelica/Dymola, or Simulink/Simscape, etc., is available to the user compared to the ODE based solution which requires numerical inversion of the lookup tables. The numerical inversion with four variables can be time consuming and introduce additional errors in the model.

A comparison of simulation time is shown in Table 3-2 where the time for numerical inversion to build the ODE based model is not included. It is evident that the proposed model dramatically reduces simulation time compared to FE analysis. It is worth noting that healthy machine FE simulation does not require as much time to solve as fault machine simulation, since the symmetry which can be employed in healthy conditions to reduce model size cannot be used in fault conditions, and the model has to be solved for several electrical cycles for the fault currents to reach a steady state.

Transient test is performed by introducing step load of 2.2Ω at θ_{elect}=0.5236 rad and 2 turn fault at θ_{elect}=10.472 rad at 3500 r/min, 2.2 ohm load as shown in Fig. 3-12. It can be observed that the model matches well with the FE prediction. Effect of increase of fault resistance on model prediction is shown in Fig. 3-13 where the fault resistance is increased to 10 times the nominal value assumed in the simulations. It can be observed that there is a good match between FE and model predictions.

Table 3-2: Comparison of simulation times for generator mode operation with resistive load of 2.2Ω at 3500 r/min

Method	Solution Time	Unit
FE	12420	s
ODE solver	62	s
DAE solver	78	s

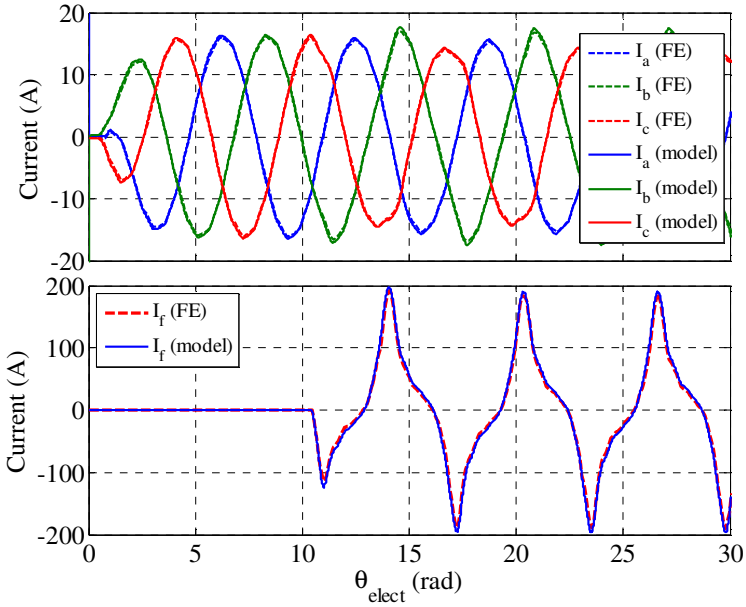

Fig. 3-12: Phase and fault current comparison of FE verses model (ODE) under transient condition at 3500 r/min. Step resistive load (2.2Ω) applied at θ_{elect}=0.5236 rad and 2 turn fault (R_f=5.5mΩ) at θ_{elect}=10.472 rad.

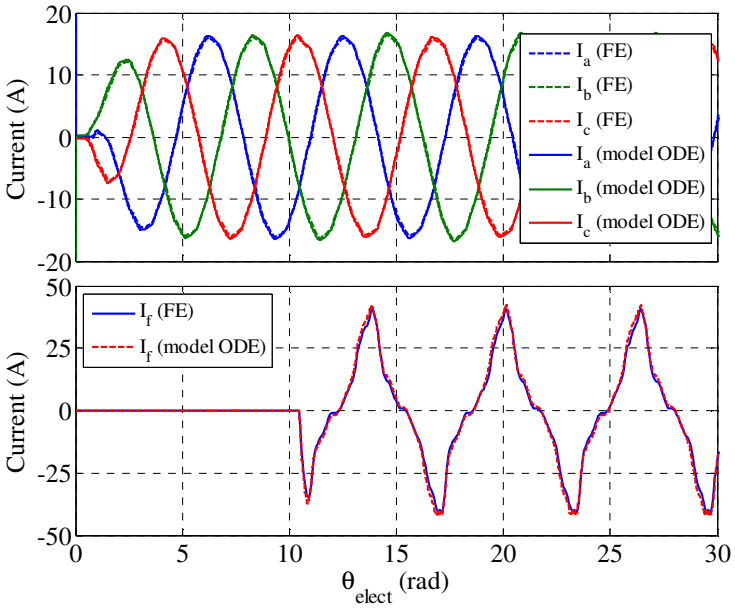

Fig. 3-13: Phase and fault current comparison of FE verses model (ODE) under transient condition at 3500 r/min with 10x nominal fault resistance (R_f=55mΩ). Step resistive load applied at θ_{elect}=0.5236 rad and 2 turn fault at θ_{elect}=10.472 rad.

3.5 Experimental Validation

The prototype 36-slot, 6-pole IPM machine whose specification is given in Table 3-1 was used for the purpose of validation of the fault model. The machine has 2 turns in C phase taken out of the machine for emulating the turn fault (N_s = 2). The machine winding and the fault turns are shown in Fig. 3-14. To test the system under fault, a 3 phase contactor connected to the faulted turns was triggered using a timer circuit to turn on for approximately 500ms. The time is deliberately kept small to prevent any damage to the coils due to prolonged circulating currents. Fig. 3-15 shows the experimental setup. The test machine is driven by a dynamometer and operates in generator mode connected to a 3 phase resistive load bank. Generator mode is chosen specifically to avoid any controller actions from a motor drive from affecting the validation of the faulted machine model. Moreover, creation of fault can cause inverter shutdown especially when fault currents are switched off by the fault timer circuit.

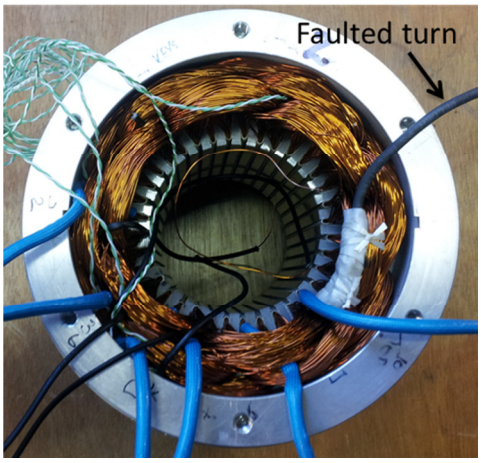

(a)

(b)

Fig. 3-14: (a) Stator winding with 2 turn fault in phase C (b) 3 step rotor and shaft

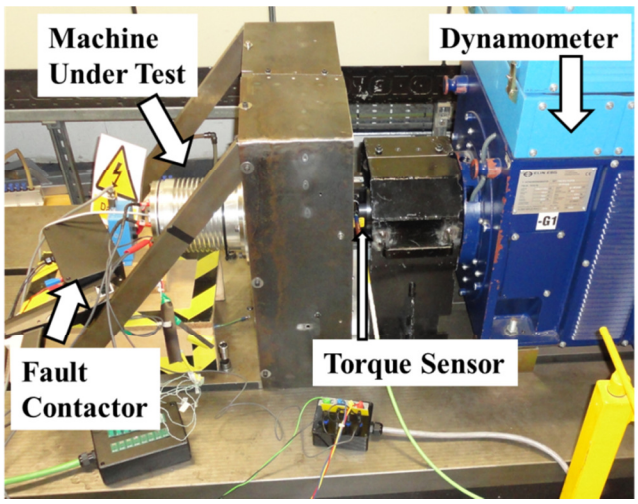

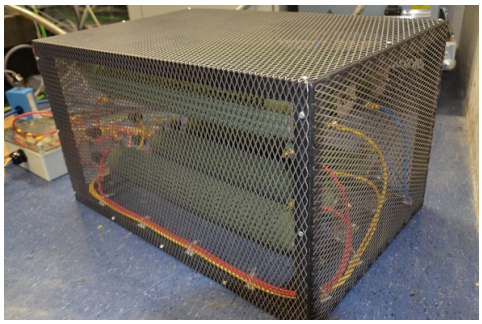

(a) (b)

Fig. 3-15: Experimental Setup (a) Motor Dynamometer setup (b) Resistive load

First no load test under healthy condition was performed and the back-EMF noted and compared against model prediction. Fig. 3-16 shows the match between experiment and model.

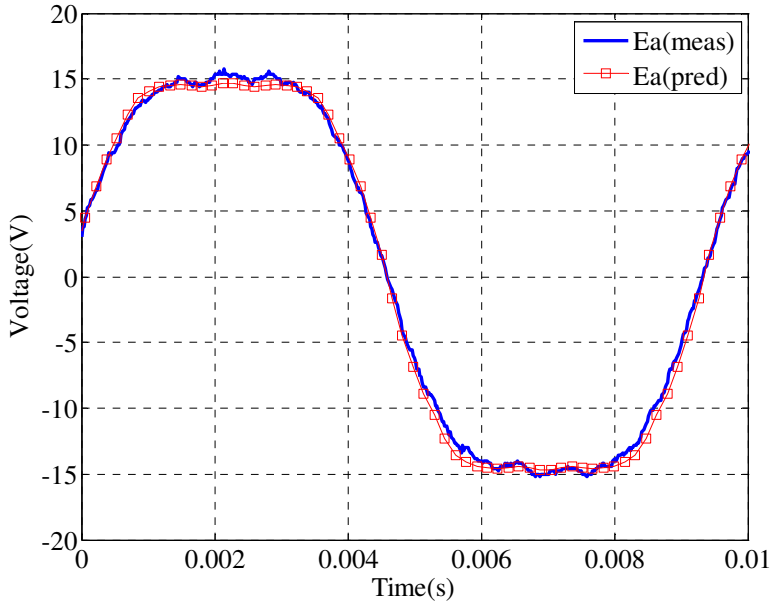

Fig. 3-16: Comparison of measured (meas) and FE model predicted (pred) phase back-EMF at 2100 r/min.

The leakage inductance of the 2 turns was calculated to around 3.76μH using the leakage calculation technique explained in chapter 2. This however, does not account for the end-winding inductance and the inductance introduced due to external connection. When all these effects are accounted, the leakage inductance of the faulted turns was increased to 5.5μH. The contactor resistance was measured to be around 2-2.5mΩ. The extra connection wires from the winding to the contactor introduce an additional resistance of 3mΩ which was also accounted for in the model. To obtain positional alignment of the waveforms w.r.t to rotor position an analog sin/cos encoder was used. Fault tests were performed at four load conditions namely no-load, 1.01Ω, 2.2Ω, and 0.69Ω. For each load condition the speed of the machine is varied from 500r/min to 6500 r/min. Fig. 3-17 shows the comparison of measured and predicted peak and RMS fault current. It can be seen that there is a close match between experiments and simulation both in magnitude and overall trend of the graphs. The maximum error observed is about 20% and occurs at lower rotor speeds and lower load

resistances. It is worth noting that in simulation the contactor resistance is accounted for at a fixed value 2mΩ. However, the contactor resistance has poor repeatability and varies from 2-2.5mΩ (25% variation) at different contactor closures during the experiments. At lower speeds, the resistive component dominates the overall fault impedance compared to higher speeds where dominating contributor is inductance. Consequently, the fault current is particularly sensitive to fault resistance variation at low speeds. It is therefore to be expected that the fault current prediction could be less accurate at low speeds due to contactor resistance variation, and this should not be mistaken as inherent problem with model fidelity. It is also to be noted that FE modeling error, parasitic effects like the extra inductance introduced by the fault emulation set-up and machine construction on lamination BH characteristic all contributes to error. It is difficult to account all these effects in simulation accurately.

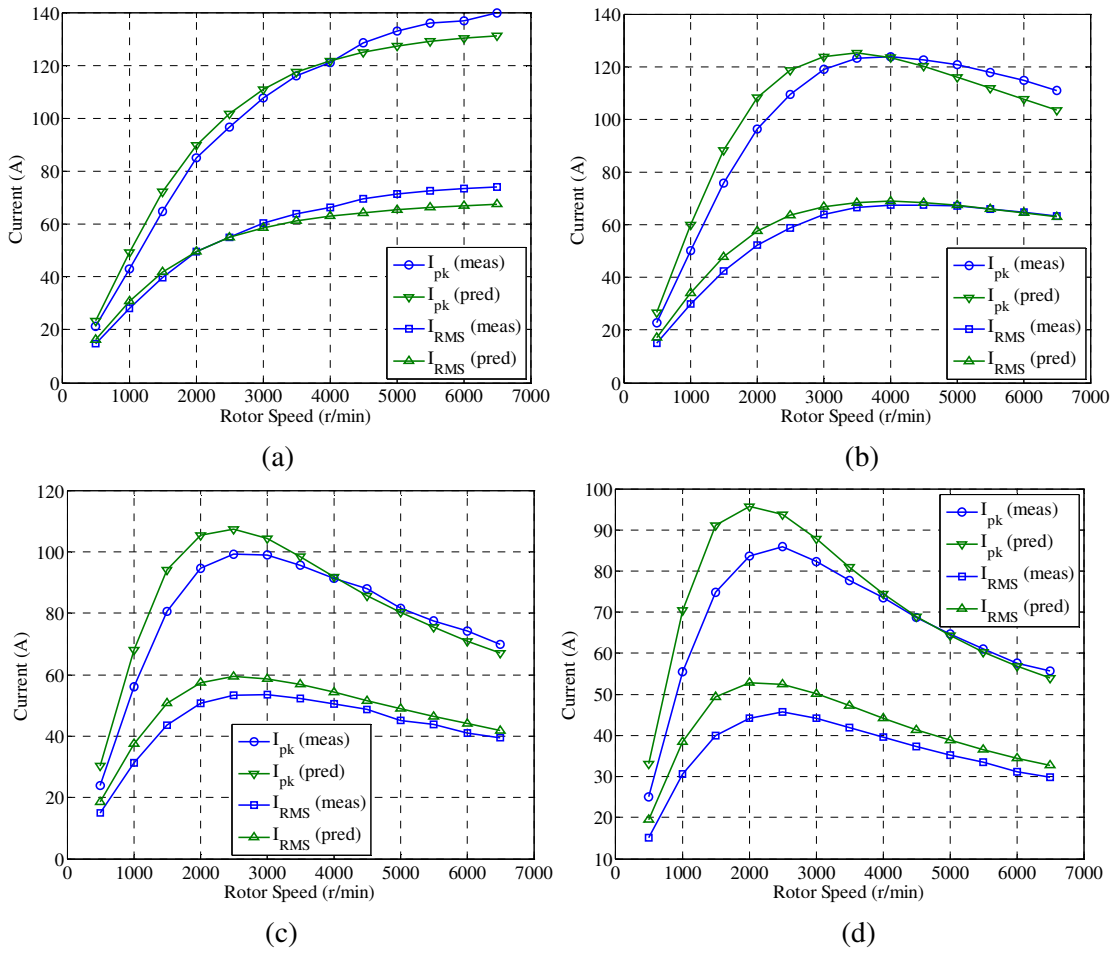

Fig. 3-17: Comparison of measured and predicted fault current variations with speed and load (a) No-load, (b) 2.2Ω load, (c) 1Ω load and (d) 0.69Ω load.

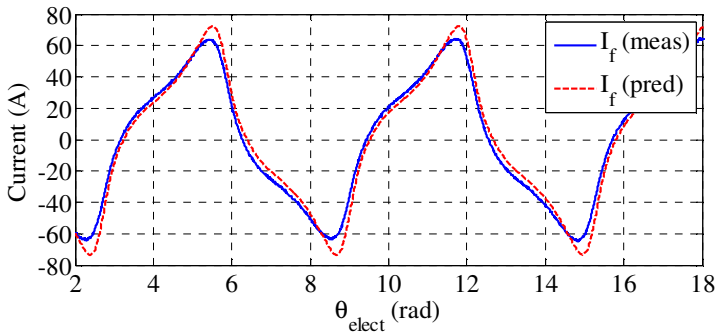

(a)

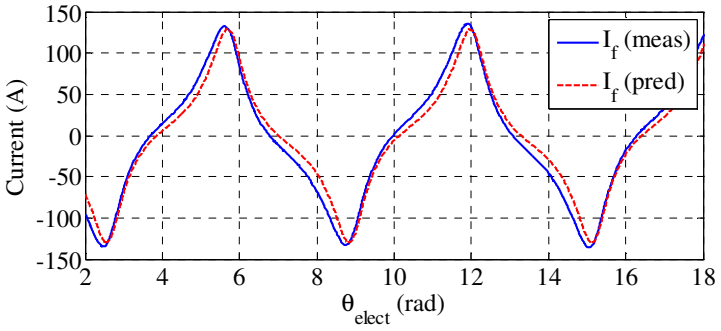

(b)

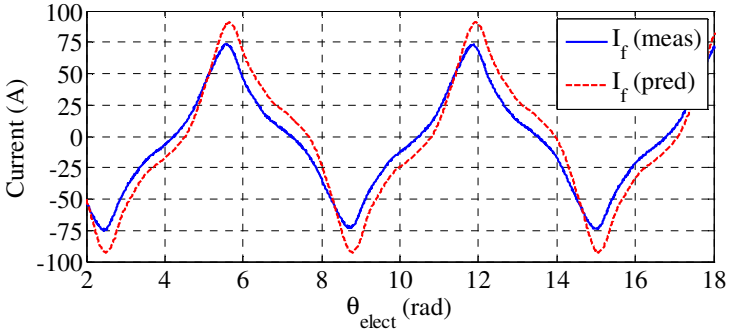

(c)

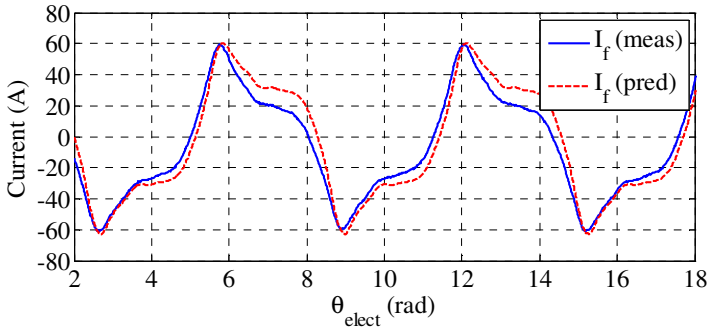

(d)

Fig. 3-18: Comparison of measured (meas) and predicted (pred) fault current at (a) 1500 r/min at no load, (b) 5500 r/min at no-load, (c) 1500 r/min at 0.69 Ω load and (d) 5500 r/min at 0.69 Ω load.

Measured and predicted instantaneous fault current waveforms are compared in Fig. 3-18 at 4 sample test-points at rotor speeds of 1500 r/min and 5500 r/min under no-load and at 0.69Ω load respectively. In all the 4 cases it can be observed that the predicted fault currents match well with the experimental waveforms in terms of both magnitude and shape. Fig. 3-19 shows the performance of the model under a sample transient fault condition at 3500 r/min and 2.2Ω load.

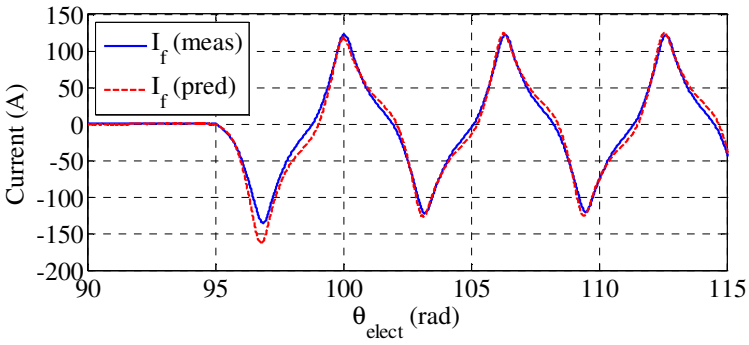

Fig. 3-19: Comparison of measured (meas) and predicted (pred) fault current (I_f) at 3500 r/min and 2.2Ω load. Turn fault initiated at θ_e = 95 rad.

The inter-turn short-circuit fault will give rise to unbalance in the machine operation and hence additional current and voltage ripples. Measured and predicted i_d and i_q ripples are compared in Fig. 3-20 at 3 sample test-points at 5500 r/min with 2.2Ω load and 0.69Ω load, and at 3500 r/min with 2.2Ω load. It can be observed that the predicted ripple matches closely with experiment both in peak and wave-shape. It is to be noted that the voltage ripple is simply a scaled value of the current ripple since the machine is connected to a constant resistive load.

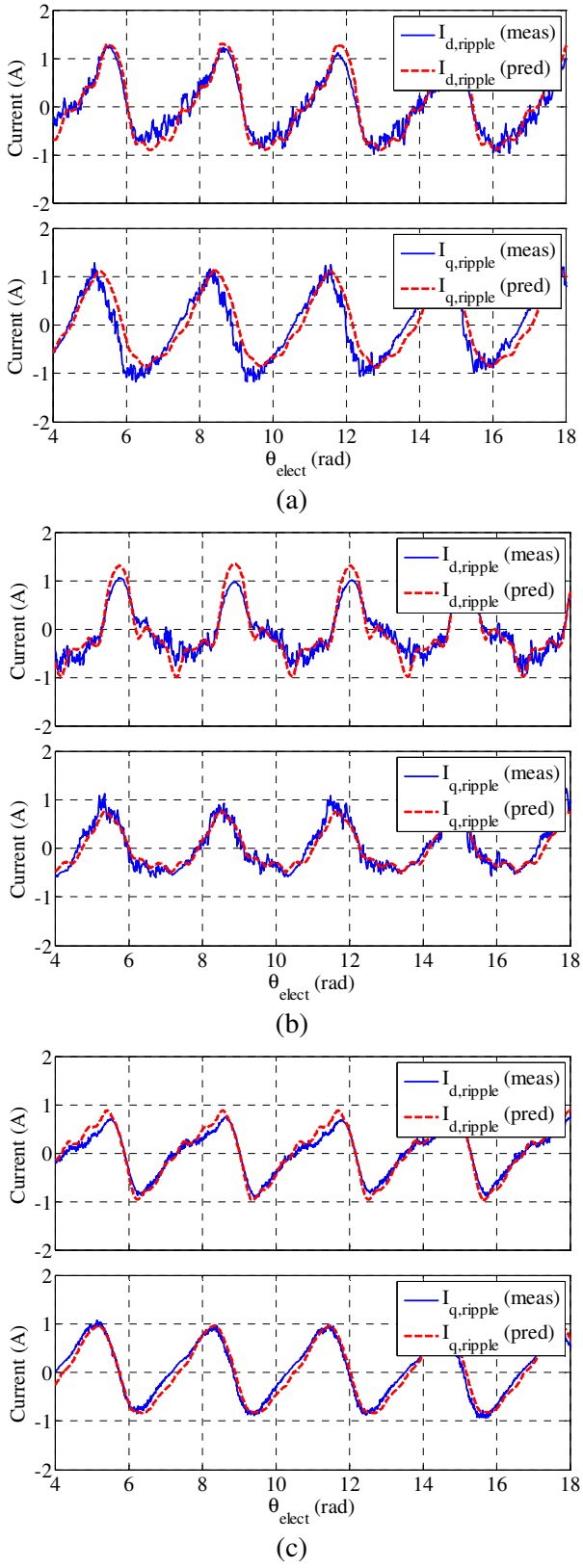

Fig. 3-20: Comparison of measured (meas) and predicted (pred) *dq* current ripple at (a) @5500 r/min and 2.2Ω load, (b) @5500 r/min and 0.69Ω load and @3500 r/min and 2.2Ω load.

3.6 Conclusions

A methodology for derivation of detailed transient model of IPM machine under turn fault has been described. The effects of high level of saturation and rotor skew are accounted. It is shown through simulation and experiments that the model established with the proposed method is accurate and computationally efficient, and is able to capture the harmonics in the fault current and the *dq* current ripple in sufficient detail. The proposed modeling technique can also be used for modeling stator turn faults in other electrical machines exhibiting magnetic non-linearity including surface PM machines, switched reluctance machines, switched flux machines and wound field synchronous machines. The proposed model provides an effective tool for assessing inter-turn short-circuit fault behavior and for evaluation of associated fault detection techniques and mitigation strategies.

It should be noted that the effect of possible partial irreversible demagnetization as a result of inter-turn faults, and influence of temperature variation on permanent magnet field are not accounted in the model. These effects can be the subject of future research.

Chapter 4

Semi-Analytical Model of Interior Permanent Magnet Machine with Stator Turn Fault

The main contribution of this chapter is a semi-analytical model of interior permanent magnet (IPM) machine under stator winding inter-turn fault conditions. The model uses *dq* flux-linkage map of healthy IPM machine and combines it with analytical equations of turn fault machine in the *dq* frame, to derive transient model for the machine with stator turn fault. The main advantage of this method as opposed to the full FE based model presented in the previous chapter, is that no additional FE simulation is required for the model. This is of importance to drive and controls designers as a model of the machine under fault can be generated using only the healthy machine *dq* flux linkage data which is already available to drive/control designers for the control of the IPM machine. Therefore although this modelling technique is not expected to be as accurate as a complete FE based model, it has the advantage of requiring very less time and resources for implementation. The developed model can be used to test drive performance under faults and to down select candidate fault detection algorithms.

Major contents of this chapter were published by author in [89].

4.1 Motivation

As explained in Chapter 1 and 3, inter-turn faults are one of the leading mechanisms to a complete winding failure, which in turn account for 21-37% of faults in electrical machines [7]–[11]. The problem of modelling turn fault in Interior Permanent Magnet (IPM) is a difficult one, owing to its inherent magnetic non-linearity

even under healthy operation. In the chapter 3, finite-element (FE) based model extraction was proposed to generate current to flux linkage lookup tables for creating the fault model of the machine. Although after extraction of the lookup tables, the technique allowed significant time improvement over time stepped FE simulations under fault conditions, generating the lookup tables is a time-consuming process, requiring FE computation of several thousand cases. Therefore, there exists a need for modelling techniques which enable faster creation of fault model.

4.2 Literature Review

The effect of inter-turn short-circuit fault in IPM was first examined in [55], where a phase variable model of IPM motor assuming linear magnetic characteristics was derived, by extending the fault model derived for induction motors in [44]. However, no experimental validation was reported. In [62] a method of extending the IPM model under fault accounting for magnetic saturation was proposed. The self- and mutual inductances of the healthy and faulted turns was assumed to be proportional to their number of turns. The phase inductance variation due to saturation described in [62] is obtained by computing the saturated values of L_d, L_q and then performing transformation to *abc* inductances. However, this assumption is not strictly true for most PM machines in which a significant part of the self- and mutual-inductances is contributed by the slot leakage whose inductance is dependent on location of the turns in the slot [15]. The inductance look-up table also assumes that there is no change in magnetic saturation of the machine due to the fault current itself.

In [19], [63], [40] an FE time stepping co-simulation transient model of BLDC was used for developing fault detection algorithms. However, time stepped FE simulation is very time consuming and not suitable for computationally efficient simulation studies involving pulse-width modulated (PWM) drives, due to the small time scales involved. Moreover, in case of IPM machine, fault detection needs to be tested at a number of different *dq* currents due to magnetic non-linearity, which will further increase compute time.

In [47], [64], a fault model for IPM BLDC was derived using winding function theory (WFT) for single layer magnet rotor, neglecting magnetic saturation effects. The inverse air gap function used in [47] is difficult to derive for more complex rotor

geometries common in high saliency machines. In [65] a permeance network (PN) model for turn faults in saturated PMSMs was proposed. The permeance network model is then used to extract 4-dimensional (4-d) flux/inductance lookup tables needed to formulate the transient model. However no experimental validation was performed. Further derivation of a PN model is very tedious, and compromises accuracy, especially for complex rotor geometries.

In [73] a hybrid model for wound-rotor synchronous generator was reported under the assumption that the machine operates in linear region under healthy condition. However, this assumption is not applicable to IPM machines with high level of magnetic saturation [70].

The aim of this chapter is to create a model of IPM machine under stator turn fault using only the flux-linkage/inductance map of the healthy machine and combining it with analytical model equations of the machine under fault [89]. This enables use of existing FE derived tables employed for drive controls [69], [76], [90] and therefore provides a means to generate quickly a model of the machine with fault without any additional FE computations. Moreover, the proposed model is computationally efficient and capable of capturing key transient behaviour of IPM under inter-turn short circuit conditions. Extensive experiments have been performed to test the validity of the model over speed and load ranges.

4.3 Reference FE Model for IPM Machine

For the purpose of comparison of different transient models an FE model of a 3-phase, 6-pole, 36-slot IPM motor is taken as reference [91]. The machine parameters were detailed in the previous chapter. The machine has 2 coils per pole-pair per phase. The machine incorporates a 3-step rotor skew of 7º (mech). Fig. 4-1 shows the geometry of the healthy machine.

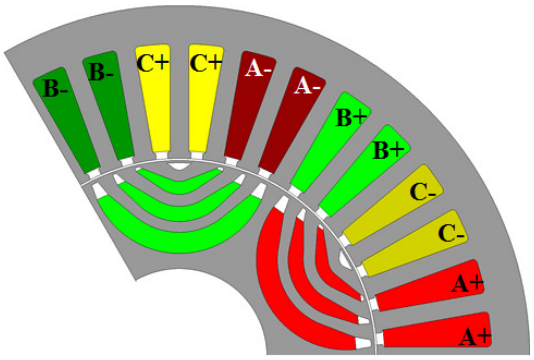

Fig. 4-1: Geometry of 36 slot, 6 pole IPM Machine (1/3rd symmetry model)

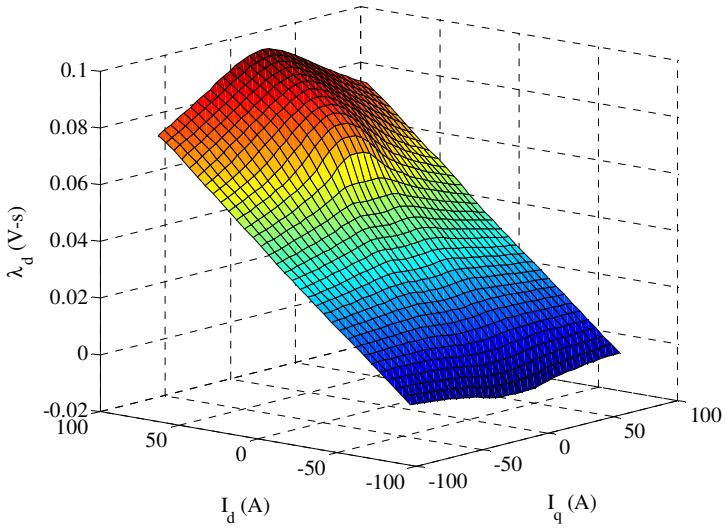

(a)

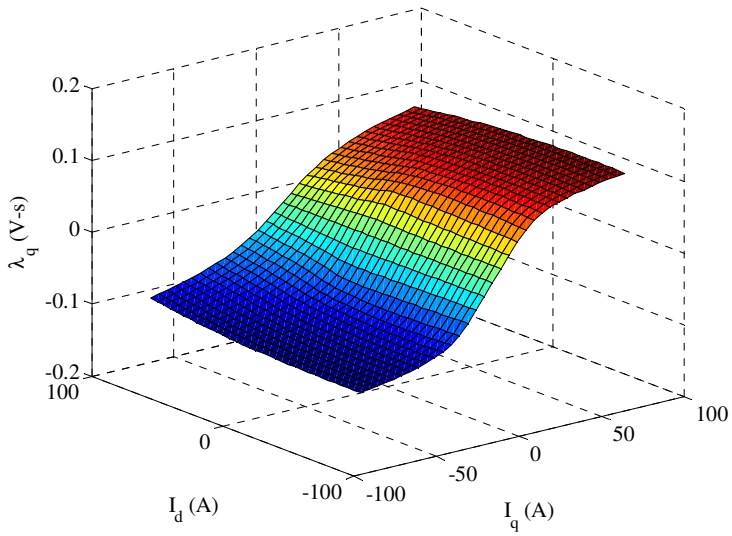

(b)

Fig. 4-2: Flux linkage map of healthy machine. (a) *d*-axis flux linkage. (b) *q*-axis flux linkage

Fig. 4-2 shows the flux map of the healthy IPM machine which is obtained by running a set of static FE simulations by varying i_d and i_q. The dq inductance map can also be obtained from the flux map using (4.1).

$$L_d = \left.\frac{\lambda_d\left(i_d, i_q\right) - \lambda_d\left(i_d = 0, i_q\right)}{i_d}\right|_{i_q = const}, L_q = \left.\frac{\lambda_q\left(i_d, i_q\right)}{i_q}\right|_{i_d = const} \tag{4.1}$$

Fig. 4-3 shows the resultant L_d and L_q variations with d-axis and q-axis currents, which demonstrates that the machine parameters changes significantly due to magnetic saturation under load.

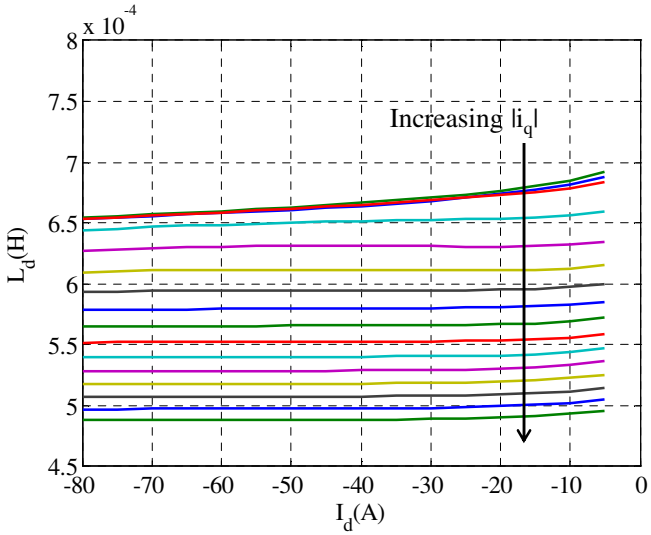

(a)

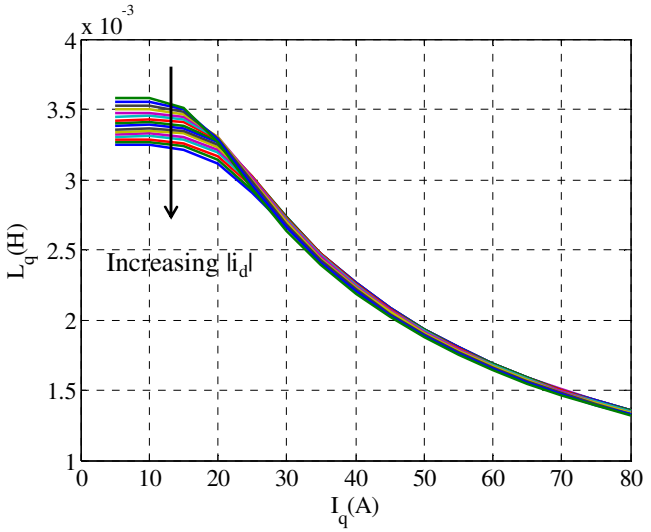

(b)

Fig. 4-3: Inductance map of healthy machine (a) d-axis inductance (b) q-axis inductance

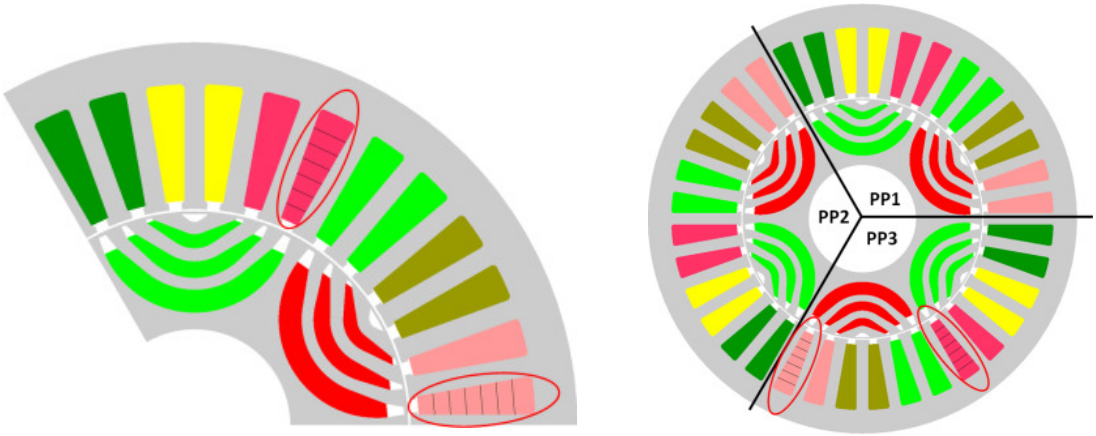

(a) (b)

Fig. 4-4: FE models for fault model validation (fault winding circled)

For the purpose of validation of the fault model, two FE models are generated. Fig. 4-4(a) shows the 1/3rd symmetric fault model of the machine which is used for testing model equations under symmetric fault conditions. Fig. 4-4(b) shows the full model of machine with turn fault. The faulty coil is circled.

4.4 Classical Turn Fault Model for IPM

For the purpose of comparison, the classical fault model is introduced and briefly discussed. The classical fault model referred to in this chapter is a reformulation of the original model proposed in [55] in *dq* frame with non-linear magnetic characteristic of the machine duly accounted as proposed in [62]. Without loss of generality, the turn fault is assumed to be in 'A' phase winding. This is done to simplify angle calculations for the model. Effect of fault in a different phase on the model equations is described in the experimental section (4.7). Phase winding 'A' is therefore divided into two parts. Winding 'AS1' is the healthy part of phase 'A' and winding 'AS2' is the faulty part as shown in Fig. 4-5. 'μ' represents the fault winding fraction, defined as the ratio of number of short-circuited turns in phase A (N_f) to the total number of turns in phase A (N_t) [55]. R_f represents the fault resistance, i_f denotes the current into the fault resistance.

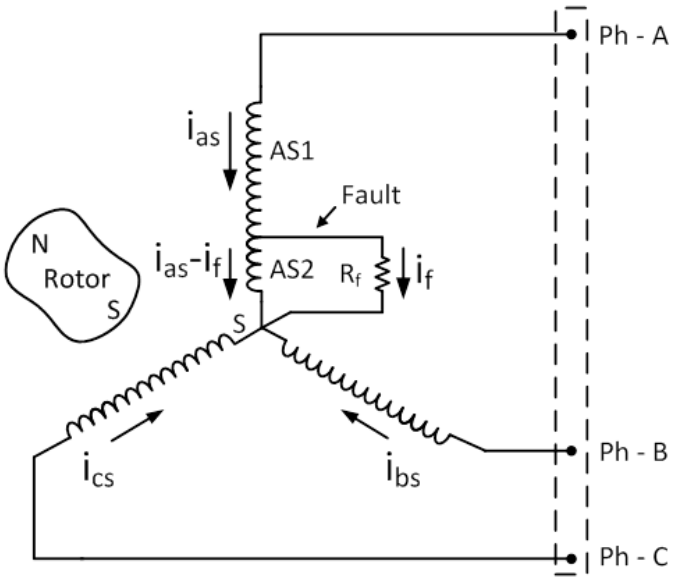

Fig. 4-5: Schematic representation of IPM machine with turn fault in 'A' phase.

4.4.1 Machine Equations in *abc* Frame

The stator equations for IPM machine with turn fault can be expressed as (4.2)-(4.3).

$$\boldsymbol{V}_s^{\,f} = \boldsymbol{R}_s^{\,f}\boldsymbol{i}_s^{\,f} + d\boldsymbol{\lambda}_s^{\,f}/dt \tag{4.2}$$

$$\begin{aligned}
\boldsymbol{V}_s^{\,f} &= \begin{bmatrix} v_{as1} & v_{as2} & v_{bs} & v_{cs} \end{bmatrix}^T \\
\boldsymbol{i}_s^{\,f} &= \begin{bmatrix} i_{as} & i_{as} - i_f & i_{bs} & i_{cs} \end{bmatrix}^T \\
\boldsymbol{\lambda}_s^{\,f} &= \begin{bmatrix} \lambda_{as1} & \lambda_{as2} & \lambda_{bs} & \lambda_{cs} \end{bmatrix}^T \\
\boldsymbol{\lambda}_s^{\,f} &= \boldsymbol{L}_s^{\,f} i_s + \boldsymbol{\lambda}_m^{\,f}
\end{aligned} \tag{4.3}$$

If the machine is not saturated and the permeability of the core is assumed to be infinite, the self- and mutual inductances under the fault condition can be represented by (4.4)-(4.5), where L_A and L_B are the constants for the average and ripple inductance respectively. In the classical model, leakage and air-gap inductance is assumed to scale linearly and as a product of number of turns respectively [55].

$$\boldsymbol{L_s}^{f} = L_{lk} diag\left[1-\mu \quad \mu \quad 1 \quad 1\right] + \begin{bmatrix} (1-\mu)^2 (L_{aa}) & \mu(1-\mu)L_{aa} & (1-\mu)L_{ab} & (1-\mu)L_{ac} \\ \mu(1-\mu)L_{aa} & \mu^2 L_{aa} & \mu L_{ab} & \mu L_{ac} \\ (1-\mu)L_{ba} & \mu L_{ba} & L_{bb} & L_{bc} \\ (1-\mu)L_{ca} & \mu L_{ca} & L_{cb} & L_{cc} \end{bmatrix} \tag{4.4}$$

$$\mu = \frac{N_f}{N_t}$$

$$L_{aa} = L_A - L_B \cos(2\theta_e) \; ; \; L_{bb} = L_A - L_B \cos\left(2\theta_e - \frac{4\pi}{3}\right)$$

$$L_{cc} = L_A - L_B \cos\left(2\theta_e + \frac{4\pi}{3}\right) \tag{4.5}$$

$$L_{ab} = -0.5L_A - L_B \cos\left(2\theta_e - \frac{2\pi}{3}\right) ; \; L_{ac} = -0.5L_A - L_B \cos\left(2\theta_e + \frac{2\pi}{3}\right)$$

$$L_{bc} = -0.5L_A - L_B \cos(2\theta_e)$$

Since terminal voltage of 'A' phase is sum of voltage across sub-winding 'AS1' and 'AS2', the first two rows of voltage equation in (4.3) can be added and re-arranged to obtain (4.6).

$$\boldsymbol{V_s} = R_s \boldsymbol{i_s} + \frac{d\boldsymbol{\lambda_s}}{dt} + \mu \boldsymbol{A}_1 i_f \tag{4.6}$$

where,

$$\begin{aligned} \boldsymbol{V_s} &= \left[(v_{as1} + v_{as2}) \quad v_{bs} \quad v_{cs}\right]^T \\ \boldsymbol{i_s} &= \left[i_{as} \quad i_{bs} \quad i_{cs}\right]^T \\ \boldsymbol{\lambda_s} &= \left[(\lambda_{as1} + \lambda_{as2}) \quad \lambda_{bs} \quad \lambda_{cs}\right]^T \end{aligned} \tag{4.7}$$

The flux vector can be rewritten as (4.8),

$$\boldsymbol{\lambda_s} = \boldsymbol{L_s} i_s + \boldsymbol{\lambda_m} - \mu i_f \boldsymbol{A}_2 \tag{4.8}$$

where,

$$\begin{aligned}
\boldsymbol{A}_1 &= -\begin{bmatrix} R_s & 0 & 0 \end{bmatrix}^T \\
\boldsymbol{A}_2 &= -\begin{bmatrix} L_{lk} + L_A - L_B\cos(2\theta_e) \\ -0.5L_A - L_B\cos\left(2\theta_e - \dfrac{2\pi}{3}\right) \\ -0.5L_A - L_B\cos\left(2\theta_e + \dfrac{2\pi}{3}\right) \end{bmatrix} \\
\boldsymbol{L_s} &= L_{lk}\,diag\begin{bmatrix} 1 & 1 & 1 \end{bmatrix} + \begin{bmatrix} L_{aa} & L_{ab} & L_{ac} \\ L_{ba} & L_{bb} & L_{bc} \\ L_{ca} & L_{cb} & L_{cc} \end{bmatrix}
\end{aligned} \tag{4.9}$$

The voltage equation of the short-circuited winding can be written as (4.10),

$$V_{as2} = R_f i_f = \mu R_s\left(i_{as} - i_f\right) + \frac{d\lambda_{as2}}{dt} \tag{4.10}$$

where,

$$\lambda_{as2} = -\mu \boldsymbol{A}_2{}^T i_s + \mu\lambda_m \sin\theta_e - \mu i_f\left[L_{lk} + \mu\left(L_A - L_B\cos 2\theta_e\right)\right] \tag{4.11}$$

4.4.2 Machine Equations in *dq* Frame

The stator equations can be transformed to the *dq* frame using synchronous frame transformation defined in (4.12) [77] to obtain (4.13).

$$T_{abc\to qd0} = \frac{2}{3}\begin{bmatrix} \cos(\theta_e) & \cos\left(\theta_e - \dfrac{2\pi}{3}\right) & \cos\left(\theta_e + \dfrac{2\pi}{3}\right) \\ \sin(\theta_e) & \sin\left(\theta_e - \dfrac{2\pi}{3}\right) & \sin\left(\theta_e + \dfrac{2\pi}{3}\right) \\ \dfrac{1}{2} & \dfrac{1}{2} & \dfrac{1}{2} \end{bmatrix} \tag{4.12}$$

$$\boldsymbol{V_{qd}} = \boldsymbol{R_s i_{qd}} + d\boldsymbol{\lambda_{qd}} / dt + \omega_e\begin{bmatrix} \lambda_d & -\lambda_q \end{bmatrix}^T - \mu\frac{2}{3}R_s\begin{bmatrix} \cos\theta_e & \sin\theta_e \end{bmatrix}^T i_f \tag{4.13}$$

where,

$$\begin{aligned}
\boldsymbol{\lambda_{qd}} &= diag\begin{bmatrix} L_q & L_d \end{bmatrix}\boldsymbol{i_{qd}} - \mu\frac{2}{3}\begin{bmatrix} L_q\cos\theta_e & L_d\sin\theta_e \end{bmatrix}^T i_f + \begin{bmatrix} 0 & \lambda_m \end{bmatrix}^T \\
L_q &= L_{lk} + \frac{3}{2}\left(L_A - L_B\right) \\
L_d &= L_{lk} + \frac{3}{2}\left(L_A + L_B\right)
\end{aligned} \tag{4.14}$$

The equation for the short-circuited turns is given by (4.15),

$$V_{as2} = R_f i_f = \mu R_s\left(i_q\cos\theta_e + i_d\sin\theta_e - i_f\right) + \frac{d\lambda_{as2}}{dt} \tag{4.15}$$

where,

$$\begin{aligned}
\lambda_{as2} = &-\mu\begin{bmatrix} L_q\cos\theta_e & L_d\sin\theta_e \end{bmatrix} i_{qd} \\
&+\mu\lambda_m\sin\theta_e - \mu i_f\left[L_{lk} + \mu\left(L_A - L_B\cos 2\theta_e\right)\right]
\end{aligned} \tag{4.16}$$

It is known that IPM machine exhibits non-linear magnetic saturation. This is quite evident in Fig. 4-3. In order to account for saturation as suggested in [62], the *dq* inductances and the magnet flux linkage are no longer treated as constants but they are updated with changing i_q and i_d using lookup tables as given by (4.17).

$$\begin{aligned}
L_q &= L_q\left(i_d, i_q\right); \lambda_q = f_q\left(i_d, i_q\right) \\
L_d &= L_d\left(i_d, i_d\right); \lambda_d = f_d\left(i_d, i_q\right) \\
\lambda_m &= \lambda_m\left(i_q\right)
\end{aligned} \tag{4.17}$$

The model is tested by simulation with R_f = 0.1mΩ, V_d = -65V, and V_q=13V which corresponds to i_d = -50A and i_q = 50A under healthy condition. Fig. 4-6 compares the fault current with 1 turn short-circuit predicted by the classic fault model and by the full FE model. As is clearly evident the classical model predicts 41% less fault current than that predicted by FE.

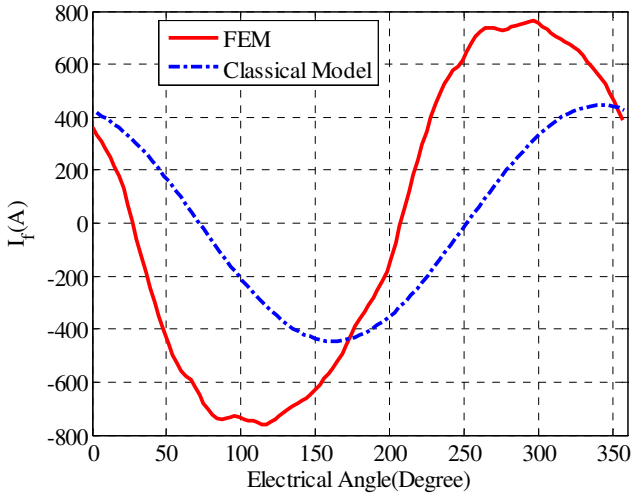

Fig. 4-6: Comparison of fault current prediction by FEM simulation and classical model at R_f = 0.1mΩ, V_d = -65V, and V_q=13V

4.5 Proposed Fault Model

The classical model has several assumptions listed below.

- L_d, L_q is considered only dependent on (i_d,i_q) and does not depend on i_f. However, i_f can affect the operating point of the magnetic field considerably since i_f >> (i_d,i_q).
- Leakage inductance is assumed to scale linearly with number of turns which leads to incorrect prediction of leakage inductance in the faulty winding.
- Fault winding is assumed to have same winding distribution as that of the entire phase. It does not take into account the fact that phase A may be composed of many series connected coils which are in turn distributed and phase shifted with each other.

It is to be noted that the aforementioned assumptions in the classical fault model are needed if no information about the winding configuration or mechanical dimensions of the machine is available. However, if the dimensions and winding configuration are available some of the limitations can be overcome. Therefore several modifications are proposed to improve the model.

4.5.1 MMF Distribution of the Fault Winding with Reference to Complete Phase Winding

First the effect of fault current is analysed under the affected pole-pair region. Since fault occurs in only one coil of a phase winding which may comprise of several distributed coils connected in series, as shown in Fig. 4-7 the distribution needs to be properly accounted in the calculation. This is done by representing the magneto-motive force (MMF) of the phase winding and faulted turns as space vectors and calculating their combined effect.

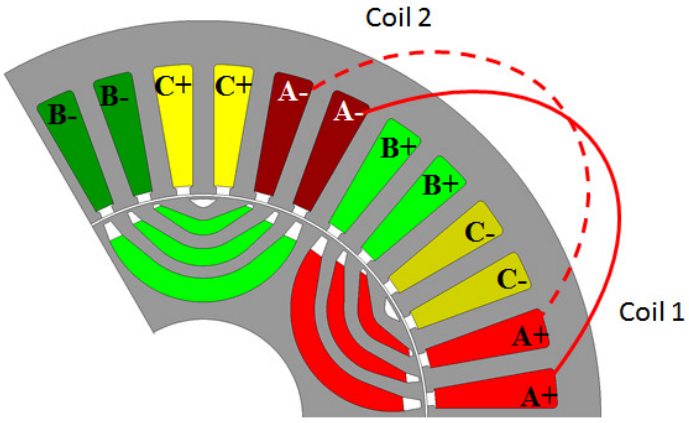

Fig. 4-7: Series connected coils of phase-A

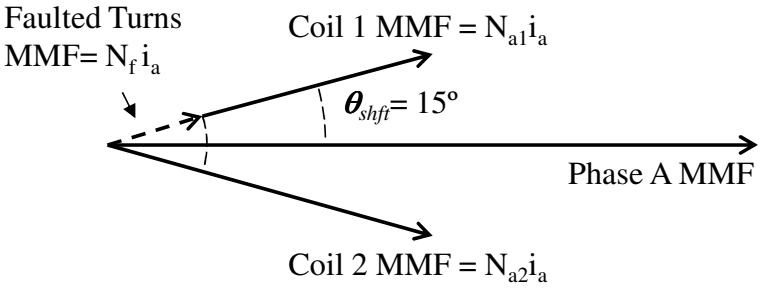

Fig. 4-8: MMF Phasor diagram of two coils in Phase A in healthy condition

Fig. 4-8 shows the phase shift between the two MMF vectors of the two coils in phase A, where coil 1 is the coil containing the faulted turns N_f. The instantaneous MMF space vector can then be written in complex domain as (4.18) taking into account the fact that the two coils of phase A (a_1 and a_2) are shifted ±15° = π/12 rad, denoted by θ_{shft} w.r.t the Phase A axis.

$$\left.\begin{aligned} N_{a1}i_a &= \left(N - N_f\right)i_a e^{j\left(\theta_e+\theta_{shft}\right)} \\ N_f\left(i_a - i_f\right) &= N_f\left(i_a - i_f\right)e^{j\left(\theta_e+\theta_{shft}\right)} \end{aligned}\right\} a_1\ coil$$
$$\left.\begin{aligned} N_{a2}i_a &= Ni_a e^{j\left(\theta_e-\theta_{shft}\right)} \end{aligned}\right\} a_2\ coil \tag{4.18}$$

N is the number of turns in one coil and faulted coil is assumed to be in coil a_1. Similarly the MMF of other phase can also be written. The combined MMF contribution of all the three phases in PP3 can then be written as (4.19).

$$\begin{aligned} MMF &= N_{a1}i_a + N_{a2}i_a + N_{b1}i_b + N_{b2}i_b + N_{c1}i_c + N_{c2}i_c + N_f\left(i_a - i_f\right) \\ MMF &= \frac{3}{2}N\left(2\cos\left(\theta_{shft}\right)\right)\left(i_q + ji_d\right) + N_f\left(-i_f\right)e^{j\left(\theta_e+\theta_{shft}\right)} \\ i_q &= \tfrac{2}{3}\left(i_a\cos\left(\theta_e\right) + i_b\cos\left(\theta_e - 2\pi/3\right) + i_c\cos\left(\theta_e + 2\pi/3\right)\right) \\ i_d &= \tfrac{2}{3}\left(i_a\sin\left(\theta_e\right) + i_b\cos\left(\theta_e - 2\pi/3\right) + i_c\cos\left(\theta_e + 2\pi/3\right)\right) \end{aligned} \tag{4.19}$$

From (4.19), it is clear that under fault condition the MMF of the machine changes. This leads to the definition of $i_{d,f}$ and $i_{q,f}$ which is obtained by normalizing (4.19) to obtain (4.20), where $cos(\theta_{shft})$ is the winding distribution factor.

$$i_{q,f} + ji_{d,f} = \left(i_q + ji_d\right) + \frac{2}{3}\frac{N_f}{N\left(2cos\left(\theta_{shft}\right)\right)}\left(-i_f\right)e^{j\left(\theta_e+\theta_{shft}\right)} \tag{4.20}$$

This relationship is used in the next section to generate the flux map under fault condition.

4.5.2 MMF Flux Mapping

Under healthy machine condition, the flux map of the machine is determined by varying i_d and i_q and averaging the flux linkage obtained over one electrical cycle. Any change in MMF due to the fault, should be accounted to calculate the flux linkage under fault condition. Thus, instead of using (4.17) in the classical model, the flux-linkages in fault conditions are determined by (4.21),

$$\lambda_{d,f} = f_d\left(i_{d,f}, i_{q,f}\right); \lambda_{q,f} = f_q\left(i_{d,f}, i_{q,f}\right) \tag{4.21}$$

where, f_d and f_q are the d- and q-axis flux linkage maps under healthy conditions as shown in Fig. 4-2. By computing the d- and q-axis currents, $i_{d,f}$ and $i_{q,f}$ under fault conditions according to (4.20), the d- and q-axis flux linkages under fault condition can

be obtained. In the classical model, it is assumed that the fault current does not affect the flux look-up table, however, this leads to an error since it is known that the fault will affect the overall MMF and hence the operating point in the machine.

To test this concept, a flux map of healthy machine with the slot leakage flux suppressed was created. This is done so that only the influence of fault on air-gap flux can be studied. This enables testing the modified *dq* current references to validate its performance without leakage flux affecting the results. The first test is with the 1/3rd symmetric model, Fig. 4-4(a). Fig. 4-9 shows the comparison of the flux linkages predicted by the model and by FE simulation, with i_d =-50A, i_q= 50A, i_f = 300A (DC) with 1 turn fault. It should be noted that the high frequency ripple seen in the FE prediction is due mainly to the slotting effect which is not accounted in the analytical model. Fig. 4-10 shows the comparison of the flux linkages predicted by the model and by FE simulation, with i_d =-50A, i_q= 50A, i_f = 150A (DC) with 3 turn fault. It can be seen that the model and FE results match well under both the fault conditions.

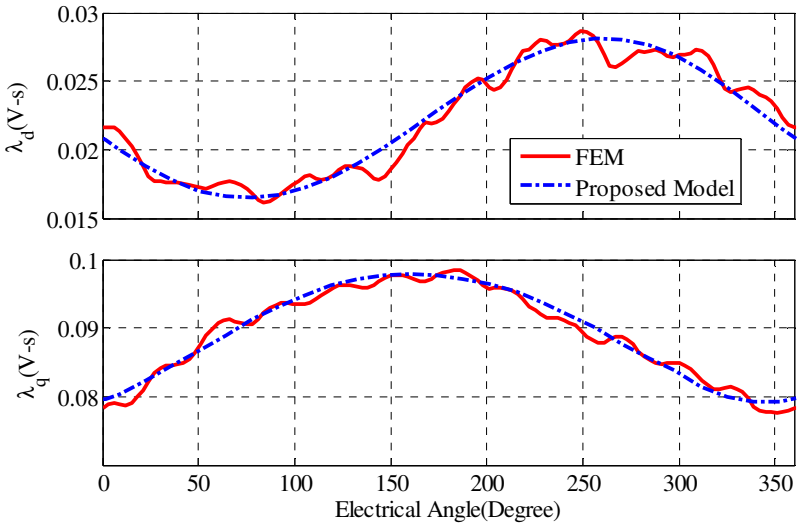

Fig. 4-9: Comparison of flux linkages predicted by proposed model and by FE 1/3 symmetric Model, No leakage. (i_d = -50A, i_q = 50A, i_f = 300A) under 1 turn fault.

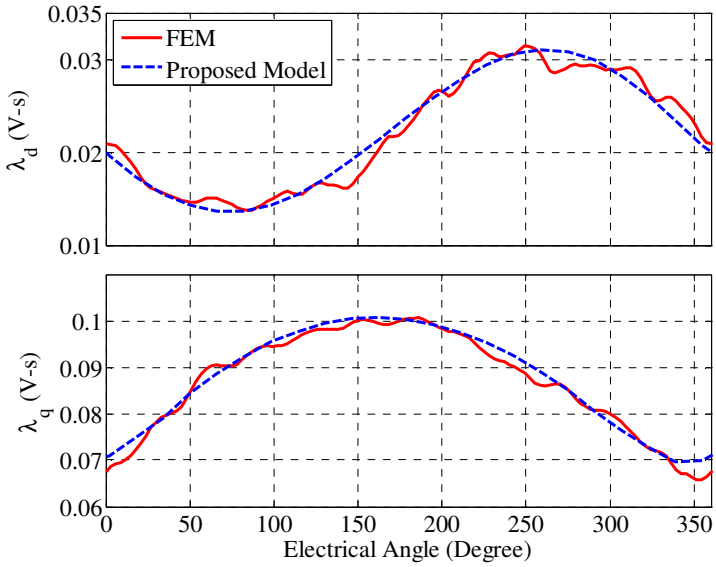

Fig. 4-10: Comparison of flux linkages predicted by proposed model and by FE 1/3 symmetric Model, No leakage. (i_d = -50A, i_q = 50A, i_f = 150A) under 3 turn fault.

A second test with the full FE model, Fig. 4-4(b), is then performed. Fig. 4-11 compares the predicted flux linkages of the coils in PP3 (pole-pair 3) by the proposed fault model and by FE simulation. The match is reasonably good; however, is not as good as the 1/3rd symmetry model. This is because there remain small interactions between pole-pairs, which are not accounted for in the analytical model. Fig. 4-12 compares the prediction verses FE model for a 3 turn fault. It can be observed that in both these fault conditions the prediction is good.

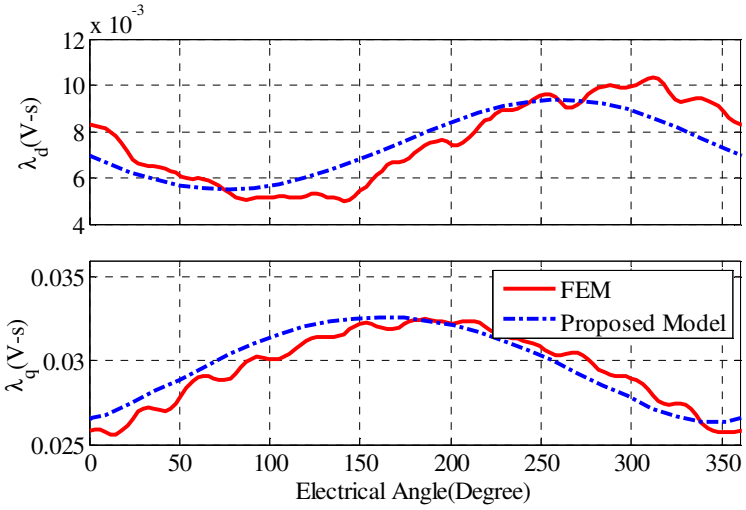

Fig. 4-11: Comparison of predicted flux linkages of faulted pole-pair (PP3) by proposed model and by FE, Full Model, No leakage. (i_d = -50A, i_q = 50A, i_f = 300A) under 1 turn fault.

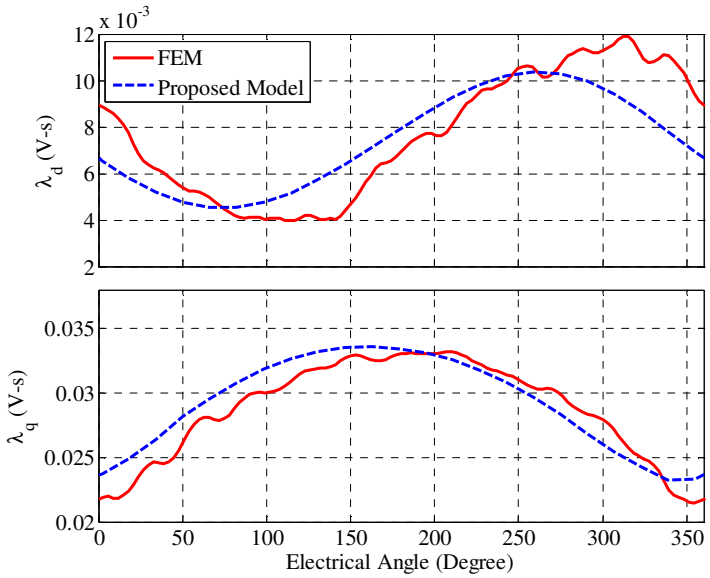

Fig. 4-12: Comparison of predicted flux linkages of faulted pole-pair (PP3) by proposed model and by FE, Full Model, No leakage. (i_d = -50A, i_q = 50A, i_f = 150A) under 3 turn fault.

4.5.3 Fault Winding Interaction with Pole-Pair Winding Groups

In Fig. 4-4(b) the fault winding is shown under only one pole-pair group denoted as PP3. Its interaction with the phase windings under the other two pole-pairs (PP1-2) can be represented using extended winding function theory [92]. Fig. 4-13 shows the turn function plot. Defining the inverse air-gap function as (4.22),

$$\frac{1}{g_{air}(\theta_m, \theta_{rm})} = a + b\cos\{2p(\theta_m - \theta_{rm})\} \tag{4.22}$$

where, θ_{rm} is the angle of the rotor d-axis w.r.t. phase-A axis. Mutual flux linkage can then be calculated by (4.23) [92],

$$\lambda_{AF} = \mu_0 R_{st} l_{stk} i_f \int_0^{2\pi} \frac{1}{g_{air}(\theta_m, \theta_{rm})} n_A(\theta_m) N_f(\theta_m) d\theta_m$$

$$= \mu_0 R_{st} l_{stk} \left(\frac{6\alpha_s}{2\pi} N_f i_f \right) \left[\begin{array}{l} \int_{\alpha_s/2}^{13\alpha_s/2} N\left[a + b\cos\left\{ 2p(\theta_m - \theta_{rm}) \right\} \right] d\theta_m \\ + \int_{3\alpha_s/2}^{15\alpha_s/2} N\left[a + b\cos\left\{ 2p(\theta_m - \theta_{rm}) \right\} \right] d\theta_m \end{array} \right] \quad (4.23)$$

$$\because \alpha_s = \frac{2\pi}{36}$$

$$\lambda_{AF} = \frac{36\mu_0 R_{st} l_{stk} i_f N N_f a \alpha_s^{\,2}}{\pi} = \frac{\mu_0 R_{st} l_{stk} i_f N N_f a \pi}{9} = \lambda_{BF} = -\lambda_{CF}$$

where α_s is the slot angle, i is the current in the fault winding, R_{st} is the stator bore radius, l_{stk} is the effective length of the stator core, n_A is the turn function of phase A and N_f is the winding function [92] of fault winding, and λ_{AF} is the flux linkage induced in Phase A in pole pair 1, due to current in fault winding 'f'. The same results apply to coils of pole-pair 2 as well. Turn function is the sum of MMF contribution of all coil sides of a particular phase in consideration. Positive direction is arbitrarily chosen as into the plane of the paper. Winding function is the zero averaged turn function [92]. The slight DC shift in the winding function N_f as seen in Fig. 4-13 will induce a slight DC MMF shift for all coils in PP1.

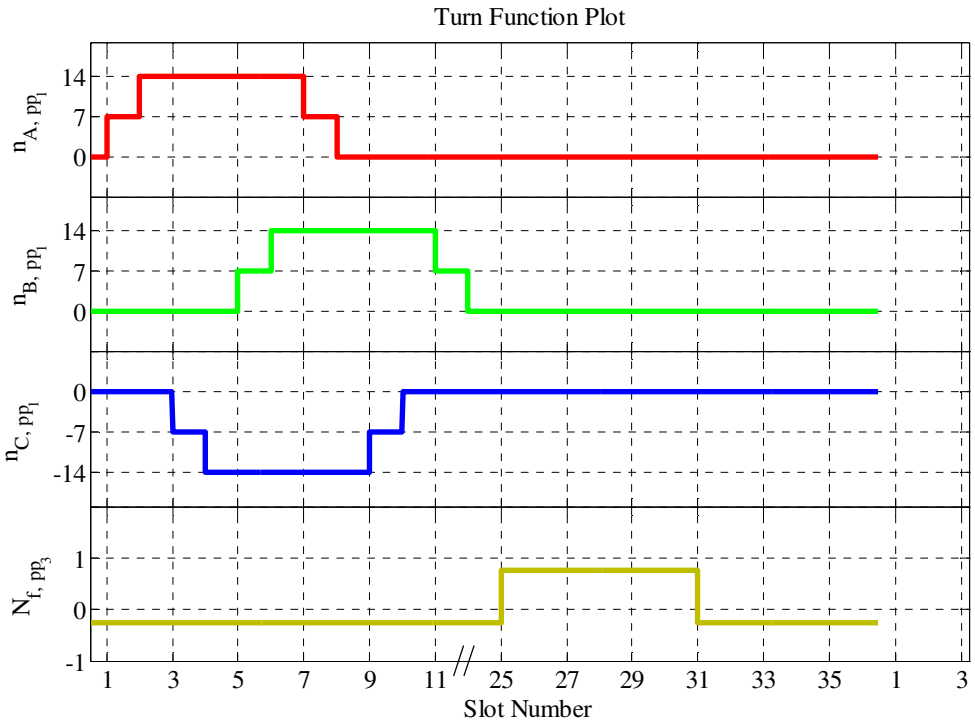

Fig. 4-13: Turn functions (n) of phase A, B, C coils (located in pole pair 1) and winding function (N_f) of fault winding (located in pole-pair 3)

The contribution of this fault MMF is expected to be small on the coils under the healthy pole-pairs. This condition is cross-checked with FE simulation by injecting a constant DC fault current (i_f =300A) in the fault winding (1 turn) with i_d = -50A, and i_q =50A, and then computing the *dq* flux for individual pole pairs. Fig. 4-14 compares the *dq* flux linkages of each pole-pair under the healthy and fault conditions. For the purpose of comparison, slot leakage flux was suppressed by setting the permeability of the slot region to be less than air in the FE model. This suppression of slot leakage flux enables the study of only the air gap flux in order to check the validity of the winding function analysis. It is shown that the flux under PP3 where the fault takes place is most affected as compared to that under the healthy condition. In contrast, the fluxes under PP1 and PP2 are less affected and hence their changes due to the fault under PP3 may be neglected.

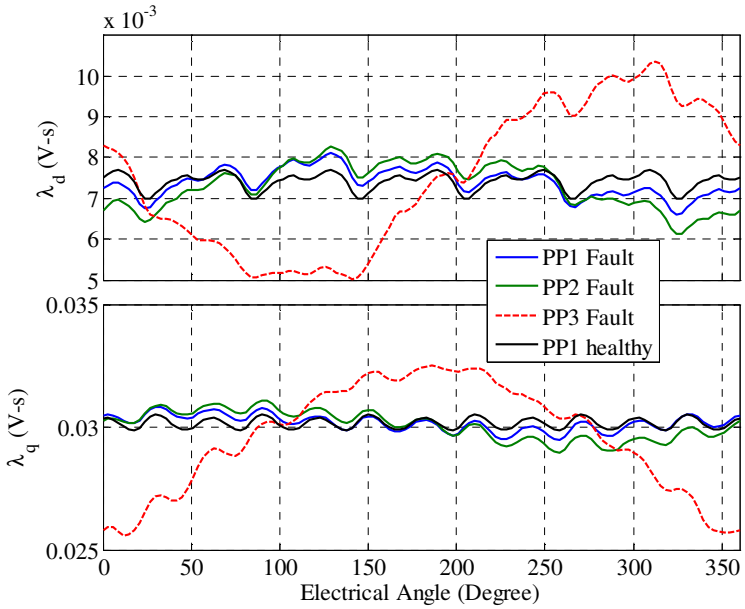

Fig. 4-14: Flux linkage comparison under different pole pairs (FE) with i_d = -50A, i_q=50A and fault current (i_f =300A) in the fault winding (1 turn)

From Fig. 4-13 and Fig. 4-14 it is clear that the MMF due to the fault winding is small for the healthy pole-pairs. One possible solution to modelling this is to ignore the small effect of fault MMF on the healthy pole-pairs. This is expressed as (4.24).

$$\lambda_{d,pp1} = \lambda_{d,pp2}\,; \lambda_{q,pp1} = \lambda_{q,pp2}\,; \tag{4.24}$$

Since, the flux lookup table shown in Fig. 4-2 is for the healthy machine, to compute the flux linkages for the healthy and faulted windings under different pole-pairs it needs to be scaled. It is known that under healthy condition each pole-pair contributes the same amount of flux. Thus, the following is true.

$$\begin{aligned} \lambda_d &= p\lambda_{d,pp1} = p\lambda_{d,pp2} = p\lambda_{d,pp3} \\ \lambda_q &= p\lambda_{q,pp1} = p\lambda_{q,pp2} = p\lambda_{q,pp3} \end{aligned} \tag{4.25}$$

From the foregoing assumption that the flux linkage under PP1 and PP2 are unaffected and equal to healthy flux linkage value, the following can be written as (4.26).

$$\begin{aligned} \lambda_{d,pp1} = \lambda_{d,pp2} &= \frac{1}{p} f_d\left(i_d, i_q\right) \\ \lambda_{q,pp1} = \lambda_{q,pp2} &= \frac{1}{p} f_q\left(i_d, i_q\right) \end{aligned} \tag{4.26}$$

A more accurate model can also be derived which does not involve the approximation as in (4.26). This is required when the number of faulted turns or the fault current is higher and consequently the fault MMF contribution is difficult to ignore. The effect of fault can be accounted for the coils under the healthy pole-pairs by using the fact that for 'a' and 'b' phases the flux contribution is equal whereas for c phase it is opposite phase as given in (4.23) and using the MMF contribution of the faulted turns on the coils to modify the *dq* currents for flux lookup under the healthy pole-pairs. Therefore, using the same technique as shown in sub-section 4.5.1, the effective *dq* axis currents for the healthy pole pairs can be expressed as (4.27).

$$\begin{bmatrix} i_q \\ i_d \\ i_0 \end{bmatrix}_h = \begin{bmatrix} i_q \\ i_d \\ i_0 \end{bmatrix} + T_{abc\to qd0} \frac{\left(6N_f i_f/36\right)}{\left(2N_c \cos\left(\theta_{shft}\right)\right)} \begin{bmatrix} 1 \\ 1 \\ -1 \end{bmatrix}$$
$$\lambda_{d,\mathrm{h}} = \lambda_{d,\mathrm{pp1}} = \lambda_{d,\mathrm{pp2}} = f_d\left(i_{d,\mathrm{h}}, i_{q,\mathrm{h}}\right); \tag{4.27}$$
$$\lambda_{q,\mathrm{h}} = \lambda_{q,pp1} = \lambda_{q,pp2} = f_q\left(i_{d,\mathrm{h}}, i_{q,\mathrm{h}}\right)$$

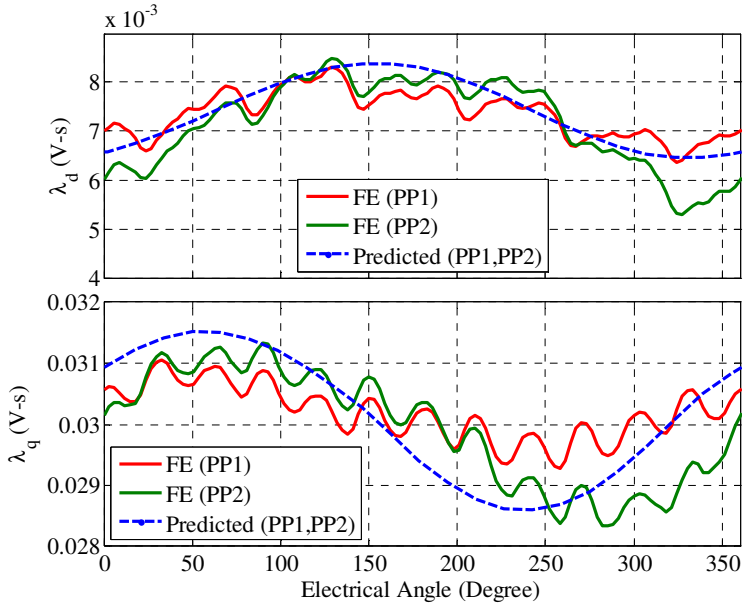

Fig. 4-15: Comparison of *dq* flux linkages of FE simulation verses model for healthy pole pair (PP1,PP2) flux linkages without slot leakage flux (i_d = -50A, i_q = 50A, i_f = 150A) under 3 turn fault.

To illustrate this method, a 3 turn fault case is compared in Fig. 4-15. It can be seen that the match is good. Therefore, it is a design choice to either use (4.26) for

simplicity or use (4.27) for more accurate representation. For low turn fault or low fault currents (4.26) can be utilized without much compromise in fidelity of the simulation.

The total flux linkage equation for the machine under fault can then be written as (4.28).

$$\lambda_{d,total} = \left(\lambda_{d,pp1} + \lambda_{d,pp2}\right) + \lambda_{d,pp3}$$
$$\lambda_{d,total} = \frac{p-1}{p}\lambda_{d,h} + \lambda_{d,pp3} \; ; \; \lambda_{q,total} = \frac{p-1}{p}\lambda_{q,h} + \lambda_{q,pp3} \tag{4.28}$$

This sum of flux linkages is not affected by the fact that the system is nonlinear, since the total flux is the sum of flux linkages contribution by all the coils in all the pole pairs.

4.5.4 Combined Flux-Linkages of All Pole-Pairs

Fig. 4-16 shows the comparison of the total *dq* flux-linkages of all the coils under all the pole-pairs, predicted by the classical model, the proposed model and the FE model with no slot leakage flux present. It can be observed that the flux linkages predicted by the proposed model match close to that predicted by the FE model.

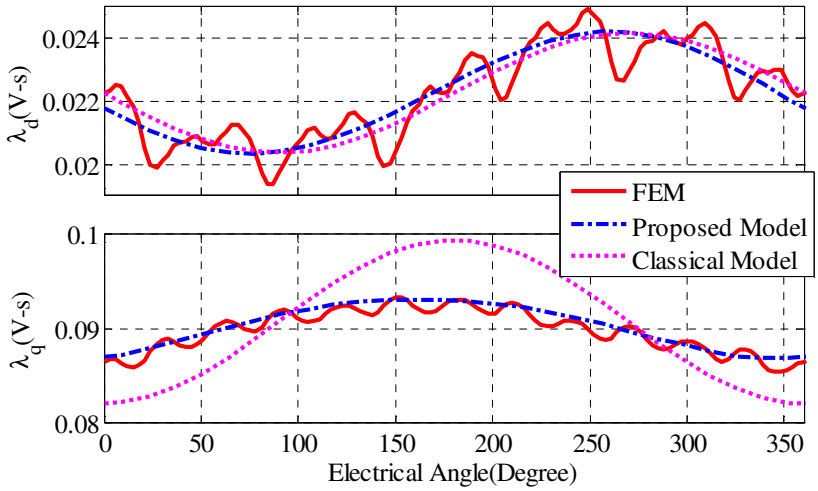

Fig. 4-16: Comparison of predicted *dq* flux linkages of classical and proposed model verses FE simulation of full model without slot leakage flux (i_d = -50A, i_q = 50A, i_f = 300A) under 1 turn fault.

To check performance of the method a further comparison with FE simulation is performed under a 3 turn fault as shown in Fig. 4-17. It can be observed that the match is good.

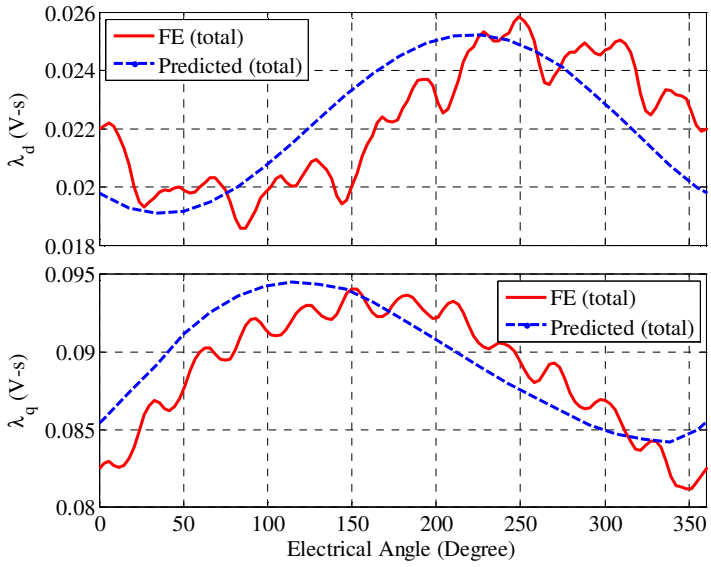

Fig. 4-17: Comparison of predicted *dq* flux linkages of proposed model verses FE simulation of full model without slot leakage flux (i_d = -50A, i_q = 50A, i_f = 150A) under 3 turn fault.

4.5.5 Leakage Flux Calculation and Flux Linkage of Faulted Turns

In the previous section influence of fault on air-gap flux linkage was investigated, which involved using a flux-linkage map of the machine with leakage flux suppressed. However, a real machine has slot leakage flux which has to be accounted for in the model. Therefore, the true flux linkage map of the machine without suppressing the leakage flux is used for calculating the *dq* flux linkages under fault. Since the air-gap flux linkage is still required for modelling it is assumed that the leakage flux is not affected by saturation in the machine and can be subtracted from the total flux linkages to obtain air-gap flux linkages. By method of example the *q*- axis air-gap flux linkages can be computed by first computing the air gap flux by subtracting the leakage flux and then the total leakage flux is added to obtain (4.29).

$$\begin{aligned}\lambda_{q,pp3} &= \frac{1}{p}\left(\lambda_{q,h}\left(i_{d,f}, i_{q,f}\right) - L_{lk} i_{q,f}\right) \\ \lambda_{q,total} &= \frac{p-1}{p}\left(\lambda_{q,h}\left(i_d, i_q\right) - L_{lk} i_q\right) + \lambda_{q,pp3} + L_{lk} i_q\end{aligned} \tag{4.29}$$

Fig. 4-18 and Fig. 4-19 shows the comparison of the prediction of *dq* flux linkages verses FE model under 1 and 3 turn fault respectively when the slot leakage is

taken into account. It can be seen the flux linkages predicted by the proposed model match close to those predicted by the FE model.

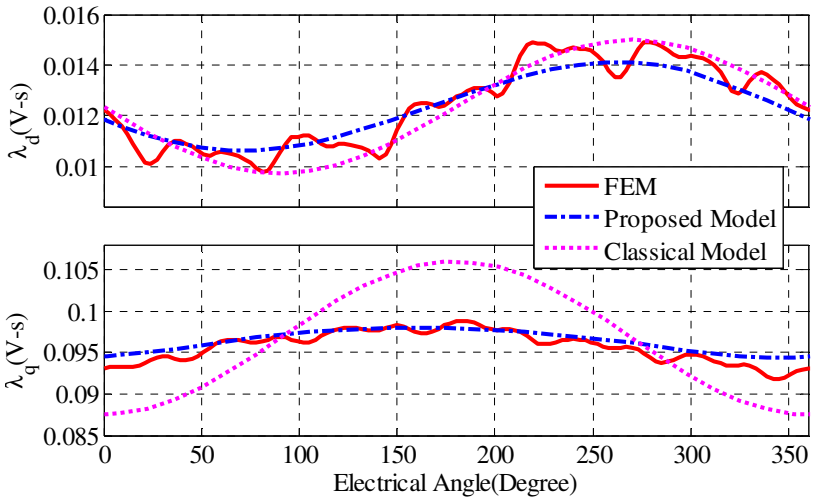

Fig. 4-18: Comparison of *dq* flux linkage prediction of classical and proposed model verses FE simulation of full model with slot leakage flux (i_d = -50A, i_q = 50A, i_f = 300A) under 1 turn fault

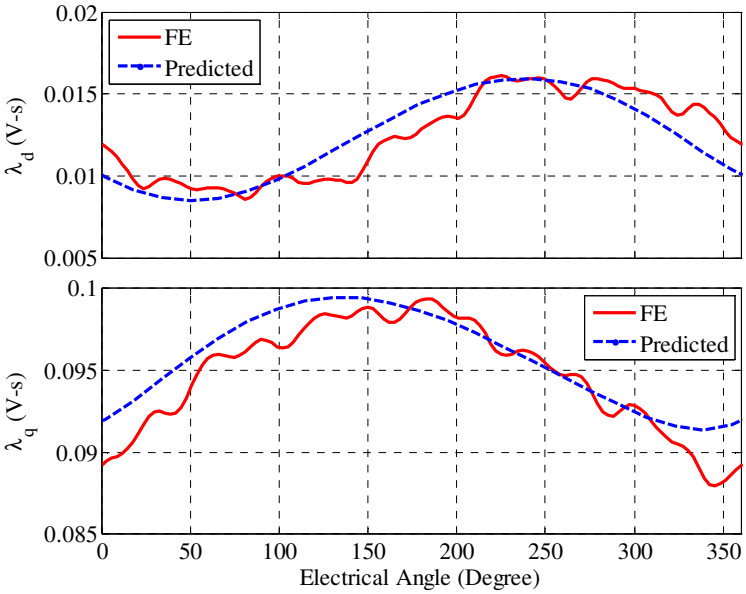

Fig. 4-19: Comparison of *dq* flux linkage prediction of classical and proposed model verses FE simulation of full model with slot leakage flux (i_d = -50A, i_q = 50A, i_f = 150A) under 3 turn fault

The air-gap flux linkages of the faulted turns is then calculated from the phase flux linkage using the *dq* flux linkages of the pole pair under fault (PP3) with due account of the distribution factor (phase shift) and the number of faulted turns as shown

in (4.30). The flux linkage vector diagram is similar to the MMF vector diagram as illustrated in Fig. 4-8.

$$\lambda_{as2} = \frac{N_f}{N_c}\frac{1}{2\cos\left(\theta_{shft}\right)}\left[\lambda_{d,pp3}\sin\left(\theta+\theta_{shft}\right)+\lambda_{q,pp3}\cos\left(\theta+\theta_{shft}\right)\right] \tag{4.30}$$

The self-leakage inductance ($L_{lk,f}$) of the faulty turns and its mutual leakage inductance ($M_{lk,fh}$) with the healthy winding in the same slot can be calculated using the method described in [15] instead of scaling the leakage inductance as in the classical model. The leakage flux can then be added to the air-gap flux linkages to obtain the total flux linkages of the faulted turns as given in (4.31).

$$\lambda_{as2} = \frac{N_f}{N_c}\frac{1}{2\cos\left(\theta_{shft}\right)}\lambda_{as}+\left(i_a-i_f\right)L_{lk,f}+i_aM_{lk,fh} \tag{4.31}$$

Fig. 4-20 and Fig. 4-21 shows the comparison of prediction verses FE model for the flux linkage of the faulted turns for 1 turn and 3 turn fault respectively. It can be seen that the proposed model matches close to the FE model prediction.

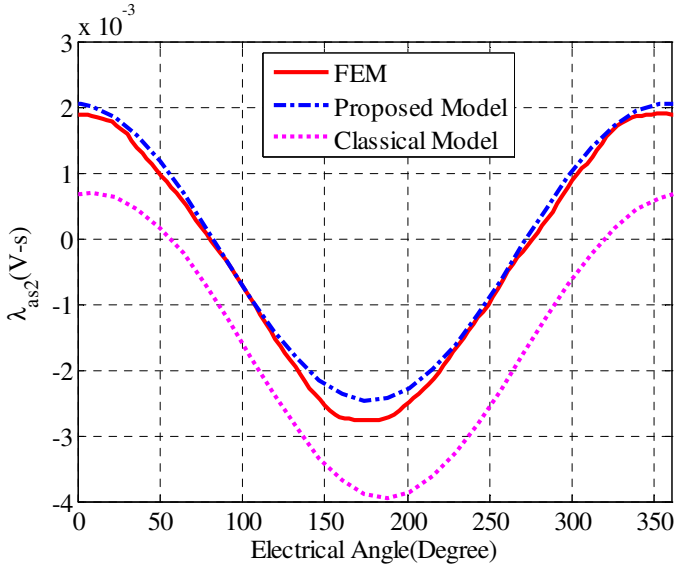

Fig. 4-20: Comparison of faulted coil flux linkage prediction of classical and proposed model verses FE simulation of full model with slot leakage flux (i_d = -50A, i_q = 50A, i_f = 300A) under 1 turn fault

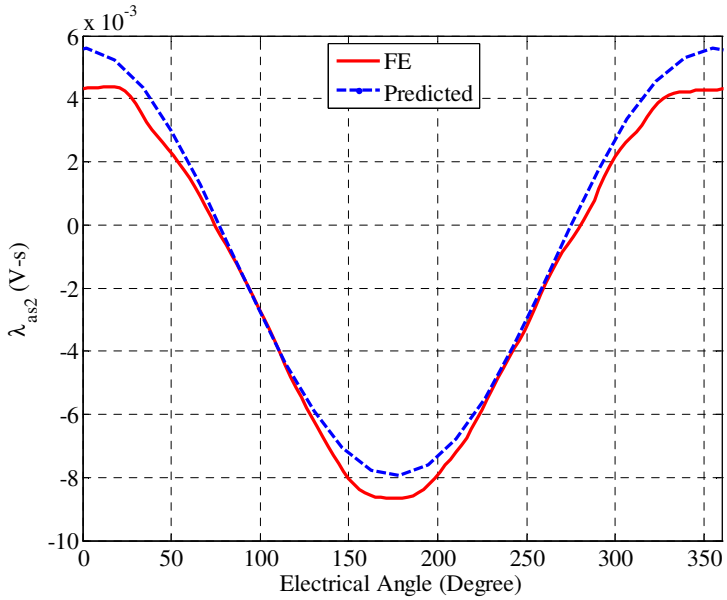

Fig. 4-21: Comparison of faulted coil flux linkage prediction of classical and proposed model verses FE simulation of full model with slot leakage flux (i_d = -50A, i_q = 50A, i_f = 150A) under 3 turn fault

In order to compute the total leakage flux linkage contribution in all the phases, the leakage flux contribution must be added and is given by (4.32).

$$\begin{aligned} \lambda_{a,lk} &= L_{lk} i_a - \left(L_{lk,f} + M_{lk,fh}\right) i_f \\ \lambda_{b,lk} &= L_{lk} i_b \\ \lambda_{c,lk} &= L_{lk} i_c \end{aligned} \tag{4.32}$$

4.5.6 Complete Turn Fault Model

Based on the foregoing sections the governing equations under an inter-turn short circuit fault are summarized in (4.33)-(4.43).

$$V_q = R_s i_q + \frac{d\lambda_q}{dt} + \omega_e \lambda_d - \frac{2}{3}\mu R_s i_f \cos\theta_e \tag{4.33}$$

$$V_d = R_s i_d + \frac{d\lambda_d}{dt} - \omega_e \lambda_q - \frac{2}{3}\mu R_s i_f \sin\theta_e \tag{4.34}$$

$$R_f i_f = V_{as2} = \mu R_s \left(i_q \cos\theta_e + i_d \sin\theta_e - i_f\right) + \frac{d\lambda_{as2}}{dt} \tag{4.35}$$

$$\lambda_q = \frac{p-1}{p}\left(\lambda_{q,h}\left(i_d, i_q\right) - L_{lk} i_q\right) + \lambda_{q,pp3} + L_{lk} i_q - \left(L_{lk,f} + M_{lk,fh}\right) i_f \cos\theta_e \tag{4.36}$$

$$\lambda_d = \frac{p-1}{p}\left(\lambda_{d,h}\left(i_d, i_q\right) - L_{lk} i_d\right) + \lambda_{d,pp3} + L_{lk} i_d - \left(L_{lk,f} + M_{lk,fh}\right) i_f \sin\theta_e \quad (4.37)$$

$$\lambda_{q,pp3} = \frac{1}{p}\left(\lambda_{q,h}\left(i_{d,f}, i_{q,f}\right) - L_{lk} i_{q,f}\right) \quad (4.38)$$

$$\lambda_{d,pp3} = \frac{1}{p}\left(\lambda_{d,h}\left(i_{d,f}, i_{q,f}\right) - L_{lk} i_{d,f}\right) \quad (4.39)$$

$$\lambda_{as2} = \frac{N_f}{N_c}\frac{1}{2\cos\theta_{shft}}\begin{bmatrix}\lambda_{d,pp3}\sin\left(\theta_e + \theta_{shft}\right) \\ +\lambda_{q,pp3}\cos\left(\theta_e + \theta_{shft}\right)\end{bmatrix} + \left(i_a - i_f\right) L_{lk,f} + i_a M_{lk,fh} \quad (4.40)$$

$$i_{d,f} = i_d - \frac{2}{3}\frac{N_f}{N_c}\frac{1}{2\cos\left(\theta_{shft}\right)} i_f \sin\left(\theta_e + \theta_{shft}\right) \quad (4.41)$$

$$i_{q,f} = i_q - \frac{2}{3}\frac{N_f}{N_c}\frac{1}{2\cos\left(\theta_{shft}\right)} i_f \cos\left(\theta_e + \theta_{shft}\right) \quad (4.42)$$

Where,

$$\theta_{shft} = \pi / 12 \quad (4.43)$$

The model equations can be easily implemented in any simulation environment, such as Matlab/Simulink [79] or circuit simulator like Synopsys/Saber [78], to perform system simulations in a computationally efficient manner.

4.6 Model Comparison with FE

To validate the model, a constant V_d and V_q which represent a given operating condition are applied to the model and the resulting *dq* and fault currents at a speed of 2100 r/min are then compared in steady state.

Fig. 4-22 and Fig. 4-23 show the comparison of the resultant currents predicted by the proposed and the classical models, and by the FE model. As is clearly evident the currents predicted by the proposed model match much closer to the FE predictions than those of the classical model. Fig. 4-23 particularly shows that the proposed model is able to predict the current wave-shape close to that predicted by FE. It is to be noted that as the fault ampere turn becomes higher local saturation effects due to the turn fault makes the prediction worse than lower fault ampere-turns.

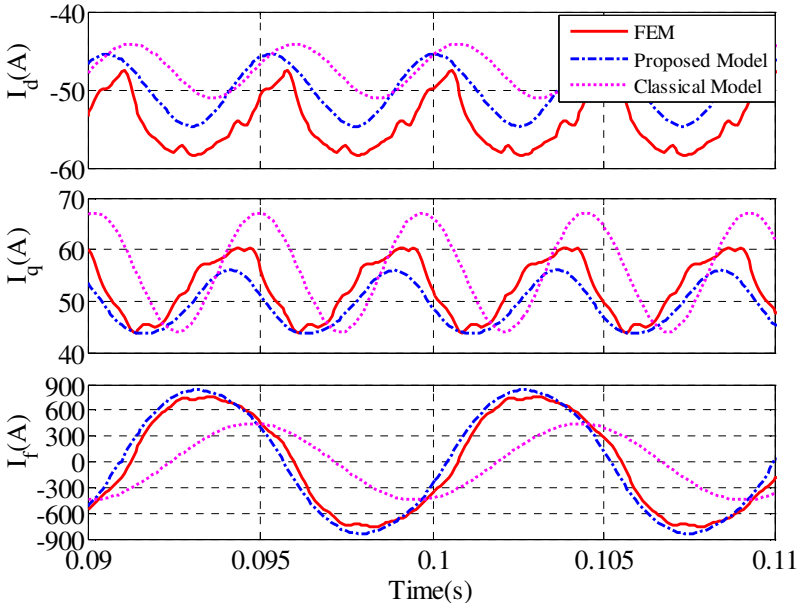

Fig. 4-22: Comparison of current prediction of classical and proposed model verses FE simulation under 1 turn fault (V_d = -65V, V_q= 13V, R_f = 0.1mΩ) (operating point i_d ~= -50A, i_q ~= 50A)

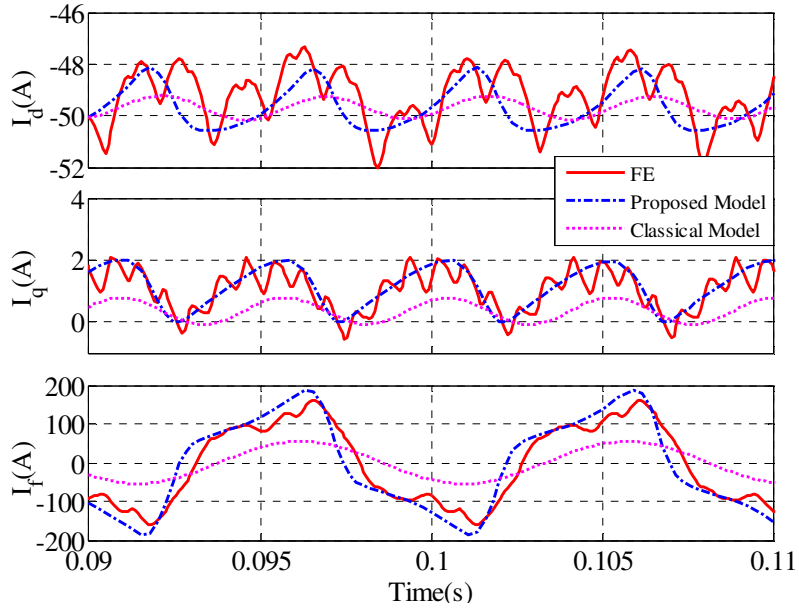

Fig. 4-23: Comparison of current prediction of classical and proposed model verses FE simulation under 1 turn fault (V_d = -3.485V, V_q= 7.33V, R_f = 0.1mΩ) (operating point i_d ~= -50A, i_q ~=0A).

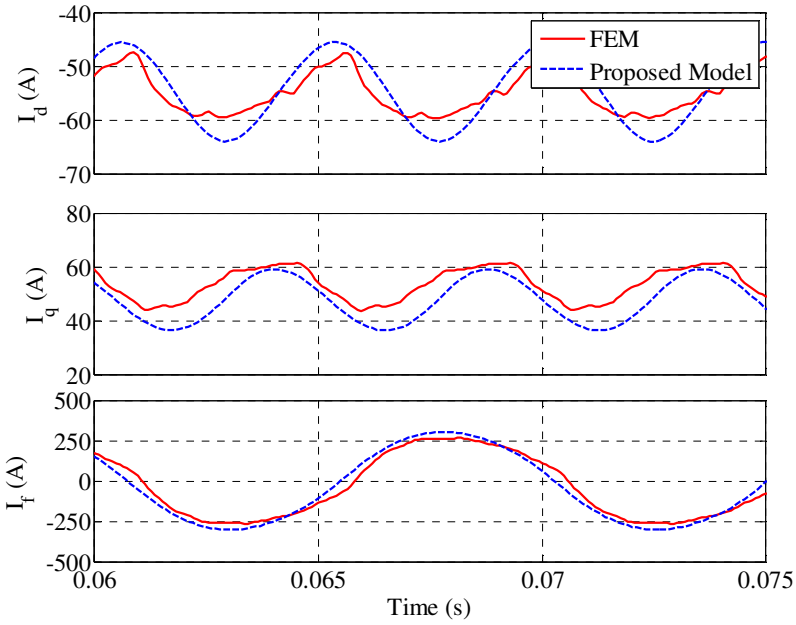

Fig. 4-24: Comparison of current prediction of classical and proposed model verses FE simulation under 3 turn fault (V_d = -65V, V_q= 13V, R_f = 10mΩ) (operating point i_d ~= -50A, i_q ~= 50A)

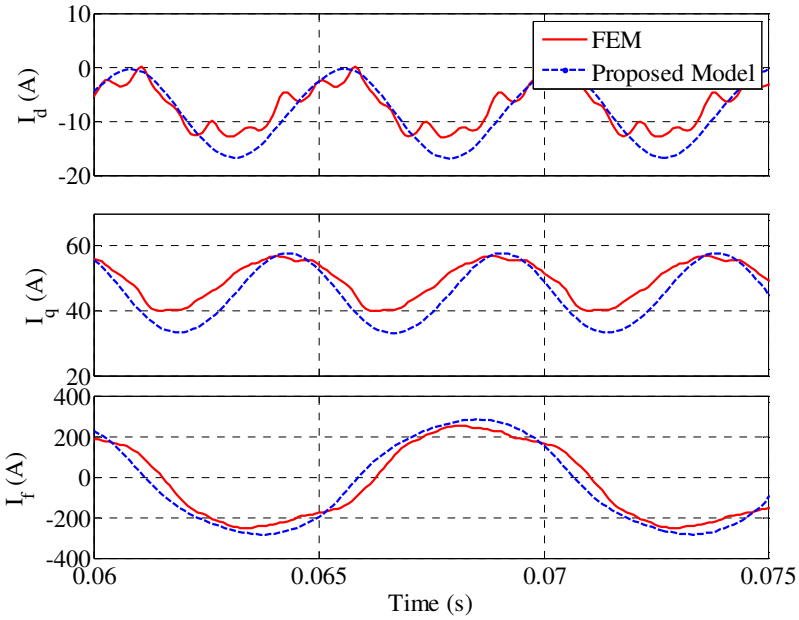

Fig. 4-25: Comparison of current prediction of classical and proposed model verses FE simulation under 3 turn fault (V_d = -57V, V_q= 30V, R_f = 10mΩ) (operating point i_d ~= 0A, i_q ~= 40A)

A further validation run is performed under a 3 turn fault with R_f = 10mΩ is shown in Fig. 4-24 and Fig. 4-25 for different operating conditions. It can be observed that the model matches well with FE prediction.

It is to be noted again that the model involves some simplifying assumptions in order to enable use of only the healthy machine data for prediction of the machine behaviour under fault condition. Therefore some error is to be expected. The purpose of the comparisons in this section was to highlight that although the match is not perfect, it is a close approximation.

4.7 Experimental Validation

The same test-rig as shown in Chapter 3 is utilised for validation of the proposed model. It is to be noted again that due to damage to the rotor laminations during laser cutting process [80], extra air-gaps near all cut edges of the lamination is utilised to account for the reduced magnetic properties of the material in the adjusted FE model. Since the motor consists of 3 step skewed rotor, the flux map is run for zero skew rotor case and subsequently the overall flux for the 3 step skew rotor is computed using method described in [75] to reduce the computation time.

The flux linkage lookup tables under healthy condition were generated using this adjusted FE model. The prototype machine is constructed with short-pitched coils, i.e., coil span is 5 slots instead of 6 as shown in Fig. 4-26. To account for the effect of short pitch factor sin(5π/12), the equivalent $i_{d,f}$ and $i_{q,f}$ is modified accordingly, as shown in (4.44). The vector angle is shifted by 2π/3 since the fault is in phase-C, instead of phase-A. It is also to be noted that θ_{shift} does not appear in the exponential term in (4.44) since the MMF of the short pitched coil is centred w.r.t the phase C flux linkage.

$$i_{q,f} + ji_{d,f} = \left(i_q + ji_d\right) + \frac{2}{3}\frac{N_f \sin\left(5\pi/12\right)}{N\left(2cos\left(\theta_{shft}\right)\right)}\left(-i_f\right)e^{j(\theta_e + 2\pi/3)} \tag{4.44}$$

To avoid any controller from introducing errors in model validation, the machine prototype was run in generator mode with a resistive load. To obtain positional alignment of the waveforms w.r.t to rotor position an analog sin/cos encoder was used.

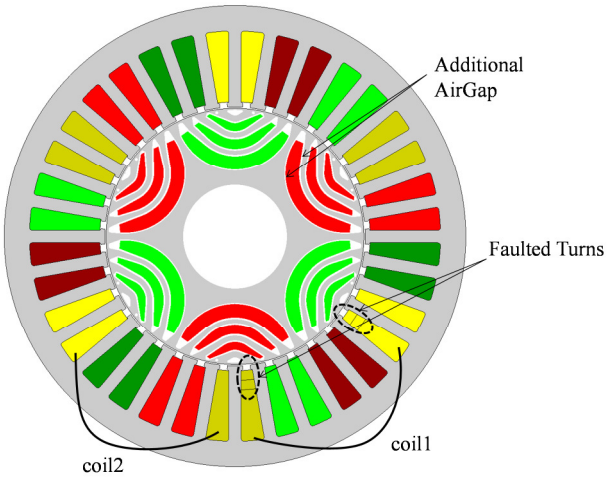

Fig. 4-26: Geometry of the test machine, including additional air-gaps and short pitched coils.

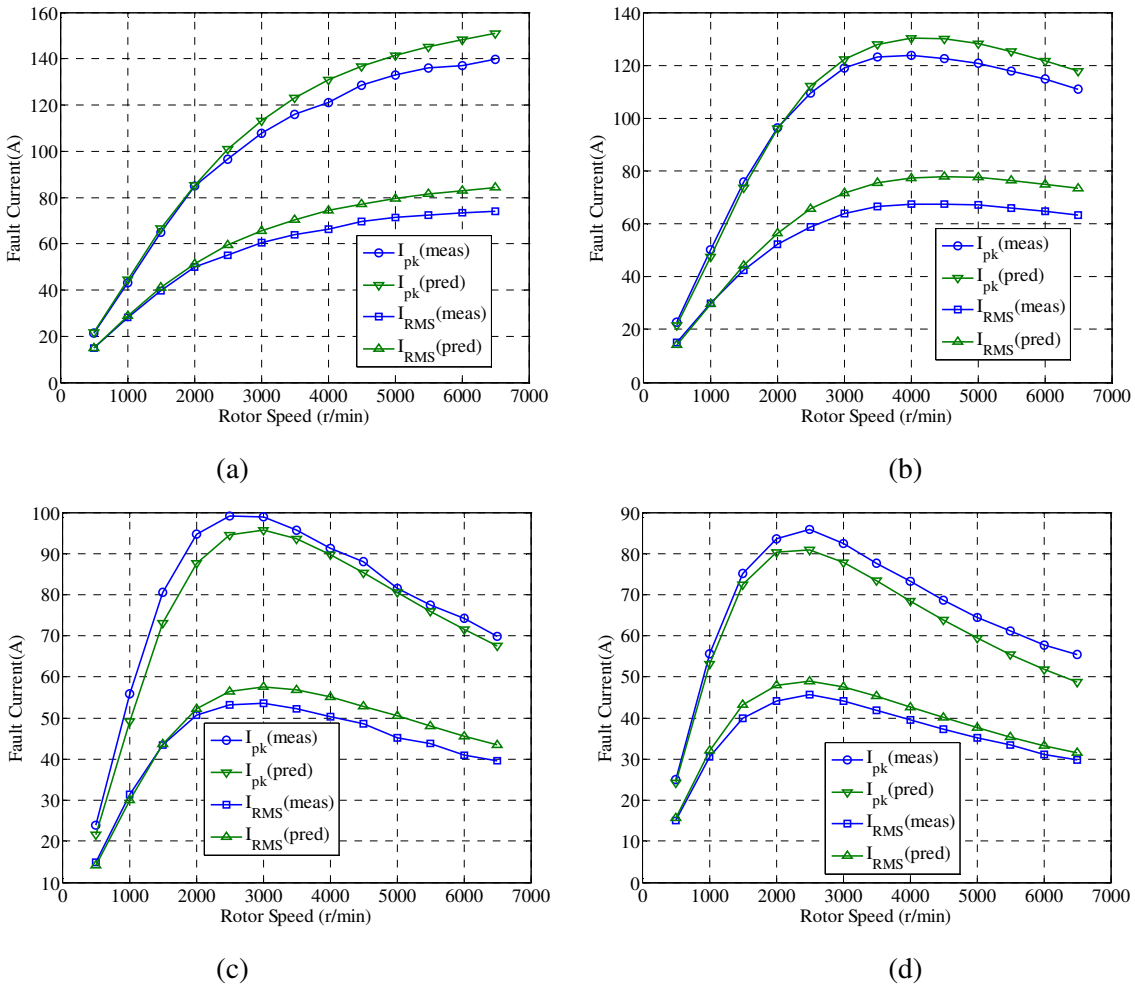

Fig. 4-27: Comparison of measured and predicted fault current variations with speed and load (a) No-load, (b) 2.2Ω load, (c) 1.01Ω load and (d) 0.69Ω load.

Fault tests were performed at four load conditions namely no-load, 0.69Ω, 1.01Ω, and 2.2Ω. For each load condition the rotor speed of the machine is varied from 500 r/min to 6500 r/min. Fig. 4-27 shows the comparison of measured and predicted peak and RMS fault currents. The maximum error observed is about 12%.

Measured and predicted instantaneous fault current waveforms are compared in Fig. 4-28 at 4 sample test-points at rotor speed of 1500 r/min and 5500 r/min under no-load and at 0.69Ω load respectively. In all the 4 cases it can be observed that the predicted fault currents match closely to the experimental waveforms in terms of both magnitude and shape.

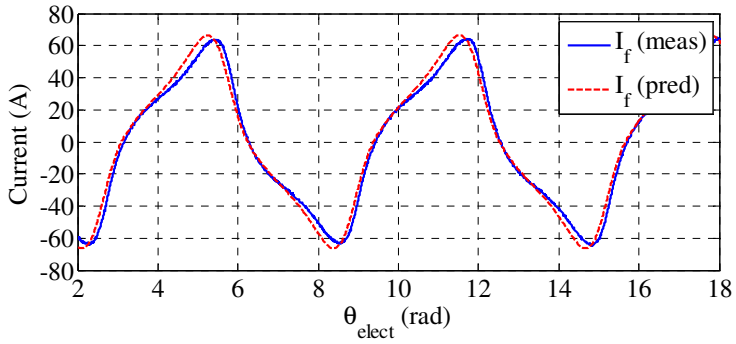

(a)

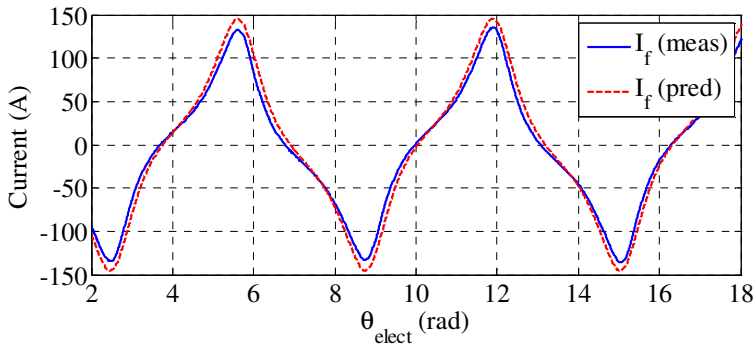

(b)

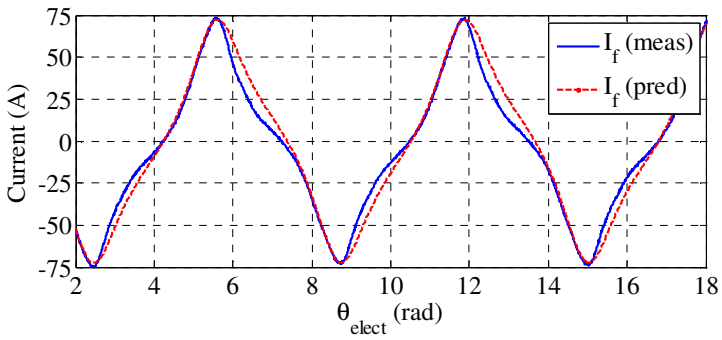

(c)

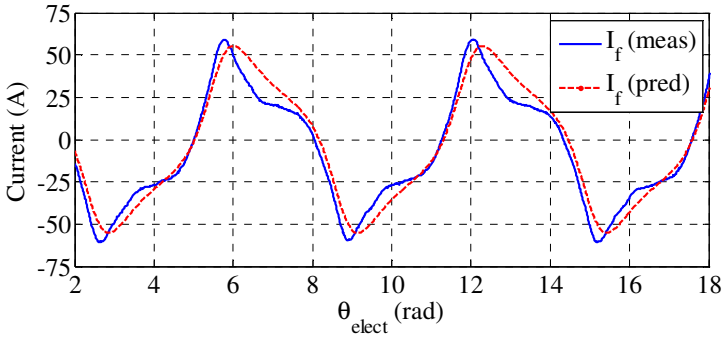

(d)

Fig. 4-28: Comparison of measured (meas) and predicted (pred) fault current at (a) 1500 r/min at no load, (b) 5500 r/min at no-load, (c) 1500 r/min at 0.69 Ω load and (d) 5500 r/min at 0.69 Ω load

Current/voltage ripple at the terminals of the machine is an important indicator of unbalance in the machine caused due to the fault. Measured and predicted i_d and i_q ripple are compared in Fig. 4-29 at 3 sample test-points at 5500 r/min with 2.2Ω load and 0.69Ω load and at 3500 r/min with 2.2Ω load. It can be observed that the predicted ripple matches closed with experiment both in peak and wave-shape. It is to be noted that the voltage ripple is simply a scaled value of the current ripple since the machine is connected to a constant resistive load.

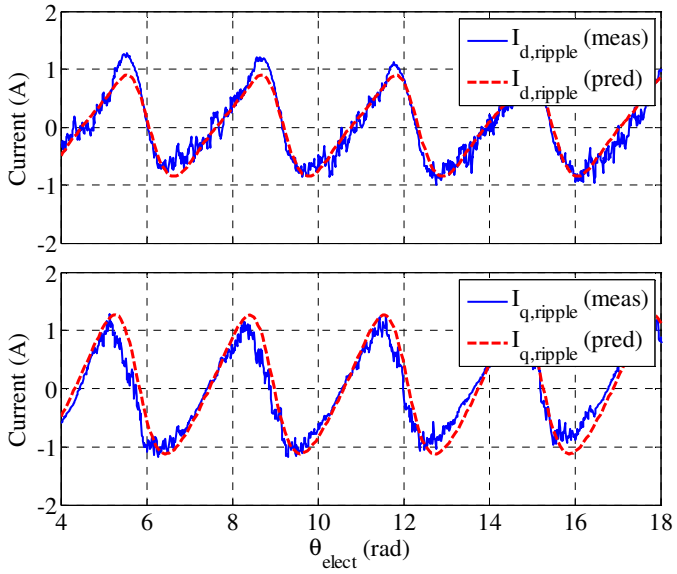
I d,ripple (meas)
I d,ripple (pred)
Current (A)
I q,ripple (meas)
I q,ripple (pred)
Current (A)
θ elect (rad)

(a)

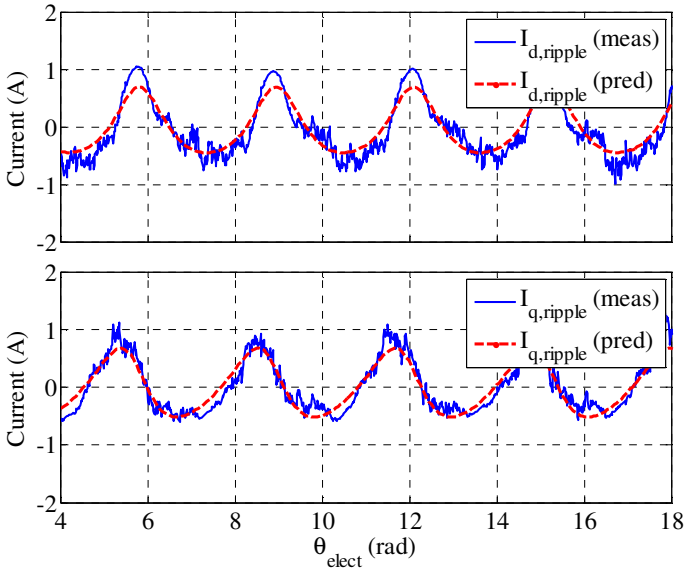
I d,ripple (meas)
I d,ripple (pred)
Current (A)
I q,ripple (meas)
I q,ripple (pred)
Current (A)
θ elect (rad)

(b)

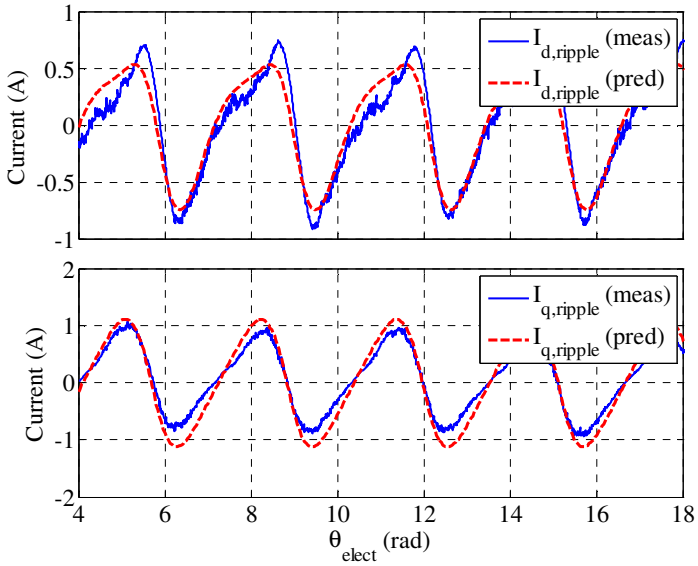

(c)

Fig. 4-29: Comparison of measured (meas) and predicted (pred) *dq* current ripple at (a) @5500 r/min and 2.2Ω load, (b) @5500 r/min and 0.69Ω load and (c) @3500 r/min and 2.2Ω load.

4.8 Comparison of Simulation Setup Time with Direct FE Model

The main advantage of the semi-analytical approach is the reduced simulation setup time required compared to the direct FE derived method proposed in Chapter 3. The simulation setup time is defined as the amount of time required to generate the current to flux linkage lookup tables. Table 4-1 shows the comparison of the two approaches on a computer with an Intel Xeon quad core processor running at 3.1 GHz with 16GB RAM using Cedrat/Flux 11.1 software. The reduction is due to the fact that the FE model required for the semi-analytical model is a 1/3rd symmetry healthy machine model running only a sweep of i_d and i_q, whereas the direct-FE derived model is a full machine model running a sweep of i_d, i_q and i_f. It is therefore clear that using the semi-analytical model the fault model can be setup much quicker than the direct-FE approach at the cost of simplifying assumptions required to derive the model which can reduce the fidelity of the model.

Table 4-1: Comparison of Simulation Setup Time

Method	Simulation Setup Time	Unit
Direct FE Derived (Chapter 3)	16	Days
Semi-Analytical	0.8	Days

4.9 Conclusions

A computationally efficient transient model of IPM machine under stator inter-turn fault conditions has been described. The model can be established using the flux linkage map of the machine under healthy conditions. It is shown through simulation and experiments that the model is able to capture the harmonics in the fault current and the dq currents in sufficient detail, even though the model uses only average *dq* flux linkages. The model can be used for developing fault detection and mitigation techniques for IPM machines.

Chapter 5

Online Stator Fault Detection Using Residual Currents

The main contribution of this chapter is a fast online fault detection scheme for stator turn fault (TF) and high resistance connection (HRC) using only the drive current controller inputs such as motor currents (*dq* frame) and rotor position along with current controller output such as inverter voltage command (*dq* frame) to achieve fault detection. No external sensor(s) or high speed sampling of currents/voltages are needed in this technique. The fault detection algorithm is implemented in real-time in DSP and executes in parallel to the drive current controller. The detector is based on an internal motor model which utilises the command voltages to predict the motor currents. The predicted currents are subtracted from the measured currents to obtain residual currents which show significant change between healthy and faulted operation. In addition the fault detection algorithm can identify the faulted phase enabling appropriate fault mitigation algorithms to be applied. This is particularly useful in multi-phase machines which due to its higher degree of control freedom enabling fault tolerant operation of machine without the need to shut down the machine. Extensive simulation and experimental results are presented as validation for the proposed strategy.

Major contents of this chapter were published by the author in [93].

5.1 Motivation

As explained in chapter 1 and 2, inter-turn faults are one of the leading mechanisms to a complete winding failure, which in turn accounts for 21-37% of faults in electrical machines [7]–[11]. In chapters 2-4 different turn fault modelling techniques were explored. These turn fault models form the basis on which this chapter develops turn fault detection schemes. Fundamental signal based fault detection is among the

most commonly used techniques in literature [94]. However, since fundamental fault detection relies on unbalance detection other faults especially high resistance connection (HRC) can be picked up and classified incorrectly as turn faults. Therefore this chapter includes analysis and detection of HRC fault along with turn fault to obtain more robust fault detection and classification method.

High resistance connection (HRC) [29] can occur due to loosening of any electrical joint between the drive and the motor. HRC can occur due to thermal cycling, vibration or corrosion. It can lead to open circuit condition due to failure of joint due to overheating. Thermal over heating of the joint can also cause insulation damage that can eventually lead to short-circuit failure and may also cause electrical fire. However, HRC progresses slower than TF as the circulating current in TF is many times greater than the rated current of the machine and causes a higher rate of thermal heating. Therefore, compared to a TF which requires immediate mitigation measures to reduce the circulating current, HRC does not require an immediate corrective measure [29].

In this chapter and the next chapter, a low power 5-phase permanent magnet machine is utilised to experimentally test fault detection techniques under relatively low fault currents. The knowledge gained by the experiments is then utilised to extend the technique(s) in simulation for a high power IPM prototype as part of the MotorBrain project deliverables.

5.2 Literature Review

5.2.1 Offline Fault Detection

Offline fault detection can only be performed on motors that are disconnected from service. However, these are accurate methods and have been long used in industry as part of scheduled maintenance and testing. Some of the major classes of offline turn fault detection are DC winding resistance test, surge test and partial discharge test [12].

DC winding resistance as the name suggests is measurement of the winding resistance under standstill condition. Turn fault can show up as reduction in DC resistance of a winding. Although easy to perform the test, the sensitivity of the method is affected by ambient temperature and resolution of small changes particularly in low voltage automotive motors with low winding resistance.

Surge test and frequency response testing involves application of transient voltage across the winding. If a turn fault is present, this can be observed in the current response of the winding in either frequency or magnitude. This has been in use for industrial motors and the recommended test procedure is given in IEEE 522 [95].

Partial discharge measurement is based on measurement of small leakage currents that flow when a high voltage is applied to the winding. Partial discharge can be detected analysing the frequency components of the leakage currents. This recommended test procedure is detailed in IEEE1434 [96]. However, this method is not readily applicable to low voltage machines.

5.2.2 Online Detection

Online detection is performed while machine is in operation. Online methods are preferred to off-line methods for stator turn fault detection as turn fault creates a local hotspot that if left unchecked can damage the entire winding of the machine in a very short period of time (1-2s). [16], [94], [97]. In available literature the techniques for stator turn fault detection can be grouped into 6 major categories.

The first group of techniques is motor current signature analysis (MCSA)) [18]–[20]. Stator turn fault causes changes in the stator magneto-motive force (MMF) spectrum and therefore modifies specific higher order harmonics in motor current/voltage and the changes in their magnitude or phase of these harmonics can be used for fault detection. However, in case of variable speed drives this is complicated by the fact that speed of the motor can change and therefore advanced signal processing such as short time fourier transform (STFT), continuous wavelet transform (CWT), and Hilbert-Huang transform [98], [99] transformation have been proposed to overcome these issues. However, these algorithms are computationally expensive and have only been implemented using advanced platforms like Labview or dSpace or implemented off-line using measured data. Similar methods have also been proposed on mechanical measurements like vibration and torque signals [100]–[103] but are expensive to implement due to high cost of the sensors.

The second group of techniques is based on high frequency (HF) injection based methods. These require injection of HF signal (1-2kHz) in the modulation signal of the inverter [19], [21], [22]. The current due to the HF signal extracted from the motor

currents is a function of the winding impedance and can therefore be used as fault indicator. However injection of HF is not preferred due to increase of acoustic noise from the machine. To overcome this ripple current due to PWM of the inverter was proposed in [104] as a means of fault detection utilising the modulation as inherent HF source. However an external circuit was needed to extract the PWM ripple current.

The third group of techniques is based on electromagnetic measurements such as axial leakage flux [23]–[25], search coil based methods [26]–[28]. The voltage sensed by the search coil acts as an indicator of magnetic unbalance in the machine and can be used for fault detection. However, this is an invasive technique requiring additional winding in stator/rotor, and therefore not widely used.

The fourth group of techniques is based on neutral point voltage measurement [29]–[31]. The voltage between motor neutral point and inverter artificial neutral point changes under fault conditions and can be used as an indicator for turn fault. This technique requires additional circuitry to sense the neutral voltage and connection to the neutral point of the machine which in many cases is not readily accessible.

The fifth group of techniques is based on fundamental frequency analysis. This includes negative sequence voltage [32], negative sequence currents [33] and cross-coupled impedance [34]. This technique can be implemented in parallel with controller and needs no additional sensors. Most of the methods are based on negative sequence analysis, however in multi-phase machines there are additional sequence components which also contain the fault signature and needs to be properly accounted for in the detection. In [105], a product of two inverter voltage command space vectors was proposed for fault detection in multi-phase machines.

Finally the sixth group of techniques is based on state estimation based methods, estimating equivalent resistance and inductance [35] and back-EMF [36] of the machine and utilising any changes as fault indicator. In [106], [107] state estimation was utilised to reject most of the healthy signal using an internal motor model. The method has benefit of fast load and speed disturbance rejection. In [108] third harmonic frame was proposed for HRC detection which can identify the faulted phase.

HRC detection methods are based on signal injection [109], neutral voltage measurements [110], sequence component based [111] and detection in higher order harmonic frames [108]. Most of the methods however, are focused on HRC connection

alone, however since turn fault can also cause unbalance in the machine most methods cannot distinguish the two faults. In [29] a fault classification algorithm for 3 phase induction machines was proposed which could classify turn fault and HRC faults using neutral voltage measurement and phase angles of the negative sequence currents.

In multi-phase machines [112], the number of sequence components is higher than that of 3 phase machines, which implies that the fault signature is distributed across many more sequence components compared to a 3-phase machine. Therefore, using just negative sequence components [93] will lead to degradation of fault detectability. In addition it is not only important to detect that a fault has occurred in the machine, but also to detect which phase has the turn fault. This is due to the fact that in case of multi-phase machine, it is possible to operate the machine with the fault if the faulted phase is properly identified [113].

This chapter contributes to the body of knowledge in the following aspects:

1. Fast detection (<1.5 electrical cycle) of fault using an online motor model. The detector is able to reject load and speed disturbances.
2. Identification of faulted phase.
3. Classification of a fault as TF or HRC based on angle calculation.

5.3 Transient Machine Modelling under Stator Turn Fault

The machine under consideration is a 10-slot 12-pole, 5-phase surface permanent magnet (SPM) machine. This machine was selected as a low power platform to test fault detection techniques as part of the MotorBrain project. The fault detection techniques experimentally tested on this prototype is then extended to 3-phase high power IPM machine described in section 5.12. Fig. 5-1 shows the geometry of the machine. The 5 phase SPM machine with a turn fault can be represented schematically as shown in Fig. 5-2. The parameters of the machine and inverter are given in Table 5-1.

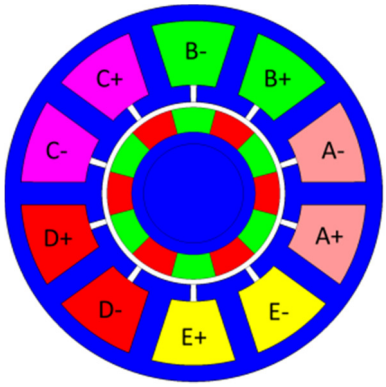

Fig. 5-1: Five phase fault tolerant SPM machine

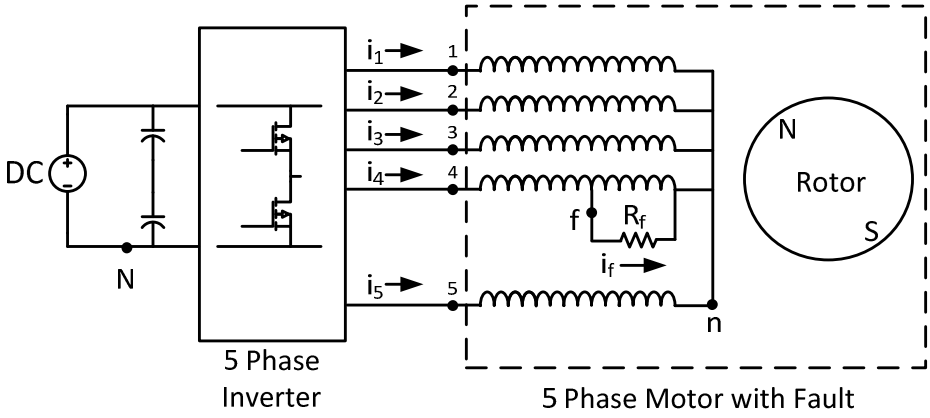

Fig. 5-2: Schematic representation of 5 phase SPM machine with turn fault on phase-4

Table 5-1: Specification of the Prototype Five-Phase Fault-Tolerant PM Machine

Parameter	**Value**
Rated Torque	1.86 Nm
Maximum Speed	3000 r/min
Phase Inductance	2.8mH
Phase Resistance	380 mΩ
Cable Resistance	300 mΩ
Number of pole pairs	6
Number of phases	5
Total Number of turns / phase (N_t)	62
Rated RMS current	6.5/√2A
Fundamental flux linkage (Ψ_{m1})	19.1mVs
Third harmonic flux linkage (Ψ_{m3})	416uVs

The machine with fault can be modelled by (5.1) considering the faulted winding as a separate winding. For notational convenience, subscripts 1, 2, 3, 4 and 5 denote phases A, B, C, D and E respectively and superscript *f* denotes the fault node. All voltages are referred to the motor neutral '*n*', except for V_{4f} which is referred to node '*f*'.

$$\boldsymbol{v}_s{}^f = \boldsymbol{R}_s{}^f \boldsymbol{i}_s{}^f + \boldsymbol{L}_s{}^f \frac{d\boldsymbol{i}_s{}^f}{dt} + \boldsymbol{e}_s{}^f \tag{5.1}$$

Where,

$$\begin{aligned} \boldsymbol{v}_s^f &= \begin{bmatrix} V_1 & V_2 & V_3 & V_{4f} & V_5 & V_{fn} \end{bmatrix}^T \\ \boldsymbol{i}_s^f &= \begin{bmatrix} i_1 & i_2 & i_3 & i_4 & i_5 & i_4 - i_f \end{bmatrix}^T \end{aligned} \tag{5.2}$$

$$\begin{aligned} \boldsymbol{R}_s{}^f &= diag\begin{bmatrix} R_1 & R_2 & R_3 & R_{4f} & R_5 & R_{fn} \end{bmatrix} \\ &= R_s diag\begin{bmatrix} 1 & 1 & 1 & (1-\mu) & 1 & (\mu) \end{bmatrix} \end{aligned}$$

$$\boldsymbol{L}_s{}^f = \begin{bmatrix} L_{1n} & 0 & 0 & 0 & 0 & 0 \\ 0 & L_{2n} & 0 & 0 & 0 & 0 \\ 0 & 0 & L_{3n} & 0 & 0 & 0 \\ 0 & 0 & 0 & L_{4f} & 0 & M_{4f} \\ 0 & 0 & 0 & 0 & L_{5n} & 0 \\ 0 & 0 & 0 & M_{4f} & 0 & L_{fn} \end{bmatrix} \tag{5.3}$$

$$\begin{aligned} \boldsymbol{e}_s{}^f &= \begin{bmatrix} e_1 & e_2 & e_3 & e_{4f} & e_5 & e_{fn} \end{bmatrix}^T \\ e_j &= \omega_e \Psi_{m1} \sin\left(\theta - (j-1)2\pi/5\right) + 3\omega_e \Psi_{m3} \sin 3\left(\theta - (j-1)2\pi/5\right) \\ e_{4f} &= (1-\mu) e_4 \\ e_{fn} &= \mu e_4 \\ V_{fn} &= i_f R_f \end{aligned} \tag{5.4}$$

R_s, i_j, e_j and L_{jj} (j = 1, 2, 3, 4 and 5) denote the resistance, current, back-EMF and self-inductances of the j^{th} winding, respectively, R_f denotes the external resistance across the faulted turns, ω_e denotes the electrical frequency in rad/sec and 'μ' denotes the winding fault fraction given by the ratio of the number of faulted turn to the total number of turns [55]. For the particular SPM topology considered L_{ij} (i, j = 1, 2, 3, 4, 5, $i \neq j$) is zero [114]. Table 5-2 shows the parameter of the winding under turn fault

condition. The parameters are derived using a similar procedure outlined in Chapter 2 using parameters listed in Table 5-3 .

Table 5-2: Machine Parameters under Turn fault

Parameter	**Fault Condition**	
N_f	2 turn fault	20 turn fault
R_{4f}	0.65Ω	0.46Ω
R_{fn}	0.021Ω	0.21Ω
L_{4f}	2.6mH	1.3mH
L_{fn}	2.8μH	0.28mH
M_{4f}	83μH	0.6mH

Table 5-3: Machine Geometry Data

Parameter	**Value**
Air-gap length	1.0 mm
Stator outer diameter	70 mm
Bore diameter ($2*R_{st}$)	34 mm
Slot opening (b_0)	1.1 mm
Slot opening depth (h_t)	3.1 mm
Height of slot (h_s)	11.9 mm
Magnet Thickness	4.5 mm
Axial length	70 mm
Slot opening angle (α_{sl})	7.7º
Slot angle (β_{sl})	4.98º

Since in (5.1) phase-4 is divided into two coils, healthy (V_{4f}) and faulty (V_{fn}), (5.1) can be re-arranged by adding the 4th and the 6th row of (5.1) to obtain the motor terminal voltages, $\boldsymbol{v}_s$ (5.5).

$$\boldsymbol{v}_s = R_s \boldsymbol{i}_s + L_s \frac{d\boldsymbol{i}_s}{dt} + \boldsymbol{e}_s + \mu \boldsymbol{A}_1 i_f + \boldsymbol{A}_2 \frac{di_f}{dt} \tag{5.5}$$

Where,

$$\begin{aligned}
\boldsymbol{i}_s &= \begin{bmatrix} i_1 & i_2 & i_3 & i_4 & i_5 \end{bmatrix}^T \\
\boldsymbol{v}_s &= \begin{bmatrix} V_1 & V_2 & V_3 & V_4 & V_5 \end{bmatrix}^T \\
\boldsymbol{e}_s &= \begin{bmatrix} e_1 & e_2 & e_3 & e_4 & e_5 \end{bmatrix}^T \\
\boldsymbol{A}_1 &= \begin{bmatrix} 0 & 0 & 0 & -R_s & 0 \end{bmatrix}^T \\
\boldsymbol{A}_2 &= \begin{bmatrix} 0 & 0 & 0 & -\left(M_{4f} + L_{fn}\right) & 0 \end{bmatrix}^T
\end{aligned} \tag{5.6}$$

Since the motor is fed by an inverter, and the machine neutral terminal '*n*' is floating as shown in Fig. 5-2, the applied inverter phase voltage vector $\boldsymbol{v}_i$, w.r.t node '*N*', i.e., the negative terminal of the DC supply, can be re-formulated in terms of the motor phase voltage vector $\boldsymbol{v}_s$ as given by (5.7) where, V_{nN} is the voltage between node '*n*' and '*N*'.

$$\boldsymbol{v}_i = \boldsymbol{v}_s + V_{nN} \tag{5.7}$$

$$\sum i_j = 0 \tag{5.8}$$

By adding all the rows of (5.7) and applying Kirchhoff's current law (5.8), V_{nN} can be obtained as given by (5.9). V_{nN} can be eliminated by substituting (5.9) in (5.7), to obtain (5.10).

$$V_{nN} = \frac{\sum \boldsymbol{v}_i + \mu R i_f + \left(M_{4f} + L_{fn}\right)\dfrac{di_f}{dt}}{5} \tag{5.9}$$

$$\boldsymbol{v}_{cmd} = \boldsymbol{v}_i - \frac{\sum \boldsymbol{v}_i}{5} = R_s \boldsymbol{i}_s + \boldsymbol{L}_s \frac{d\boldsymbol{i}_s}{dt} + \boldsymbol{e}_s + \mu \boldsymbol{A}_3 i_f + \boldsymbol{A}_4 \frac{di_f}{dt} \tag{5.10}$$

The left hand side of (5.10), is the command voltage $\boldsymbol{v}_{cmd}$ generated by the current controller. $\boldsymbol{A}_3$ and $\boldsymbol{A}_4$ are given by (5.11).

$$\begin{aligned}
\boldsymbol{A}_3 &= R_s \begin{bmatrix} 1/5 & 1/5 & 1/5 & -4/5 & 1/5 \end{bmatrix}^T \\
\boldsymbol{A}_4 &= \left(M_{4f} + L_{fn}\right) \begin{bmatrix} 1/5 & 1/5 & 1/5 & -4/5 & 1/5 \end{bmatrix}^T
\end{aligned} \tag{5.11}$$

5.4 Steady State Voltage Analysis under Turn Fault

It can be observed from (5.10) that the voltage equation of the machine under fault condition is different from that of a healthy machine model as given by (5.12). Therefore, by processing the inverter command voltages through signal processing to

extract only the terms containing i_f, turn fault could be detected. In order to derive a fault indicator first the sinusoidal steady state behaviour is analysed.

$$\boldsymbol{v}_{cmd} = \boldsymbol{v}_i - \frac{\sum \boldsymbol{v}_i}{5} = R_s \boldsymbol{i}_s + \boldsymbol{L}_s \frac{d\boldsymbol{i}_s}{dt} + \boldsymbol{e}_s \tag{5.12}$$

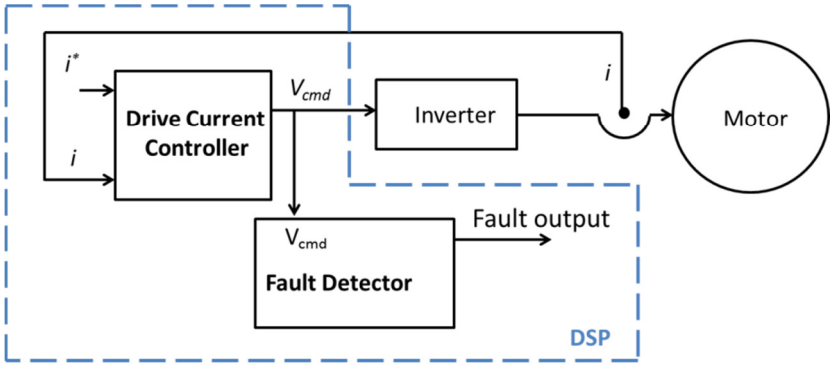

Fig. 5-3: Voltage Based Detector Structure

5.4.1 Phasor Analysis

Under sinusoidal steady state, the time domain equation (5.10) can be expressed as complex variables (phasors) by replacing d/dt with $j\omega_e$, to obtain (5.13). Phasor voltage command in case of a healthy machine is given by (5.14). Superscript $\rightarrow$ denotes phasor quantities.

$$\begin{aligned} \vec{\mathbf{V}}_{cmd} &= \left(R_s + j\omega_e L_s\right)\vec{\mathbf{I}}_s + \vec{\mathbf{E}}_s + \frac{1}{5}\boldsymbol{A}_5\left(\mu R_s + j\omega_e\left(M_{4f} + L_{fn}\right)\right)\vec{I}_f \\ \boldsymbol{A}_5 &= \begin{bmatrix}1 & 1 & 1 & -4 & 1\end{bmatrix}^T \end{aligned} \tag{5.13}$$

$$\vec{\mathbf{V}}_{cmd,healthy} = \left(R_s + j\omega_e L_s\right)\vec{\mathbf{I}}_s + \vec{\mathbf{E}}_s \tag{5.14}$$

Comparing the phasor voltage equation of machine under fault (5.13) and the phasor voltages expected from a healthy machine (5.14) the following observations can be made:

1. Phasor voltages consist of a vectorial sum of terms due to stator current, back-EMF and terms due to fault current i_f.
2. Fault current influences different phase voltages differently as can be observed from terms of $\mathbf{A}_5$ with the faulted phase having the highest coefficient. The phasor voltages are therefore unbalanced.

Although the fault current influences the inverter command voltages the overall magnitude of the voltages will only differ by a tiny amount due to the large influence of the terms associated with the stator current and back-EMF. An effective method of resolving small unbalances is by using sequence components.

5.4.2 Sequence Component Analysis

Unbalance can be analysed using Fortescue transformation [115] for 5-phase system given by (5.15) and applying it to (5.13)-(5.14) to obtain (5.16)-(5.17), where superscript * denotes sequence component phasors. F_j in (5.15) denotes phasor values of j^{th} phase, subscript 0, +, --, ++ and - denotes the different sequence components. Fig. 5-4 shows the individual sequence components and the angular relationship of the individual phasors. It is to be noted that -- and - are the reverse rotation sequence components of ++ and + respectively.

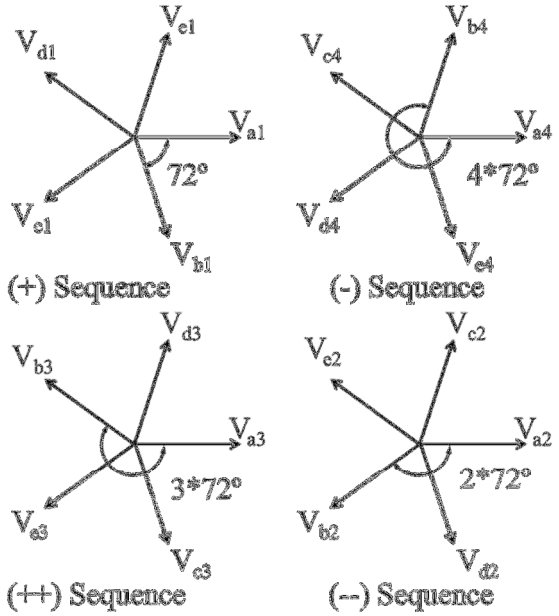

Fig. 5-4: Sequence components and the phase relationship.

$$\vec{\mathbf{F}}^{*}=\begin{bmatrix}\vec{F}_{0}^{*}\\ \vec{F}_{+}^{*}\\ \vec{F}_{--}^{*}\\ \vec{F}_{++}^{*}\\ \vec{F}_{-}^{*}\end{bmatrix}=\frac{1}{5}\begin{bmatrix}1 & 1 & 1 & 1 & 1\\ 1 & \alpha & \alpha^{2} & \alpha^{3} & \alpha^{4}\\ 1 & \alpha^{2} & \alpha^{4} & \alpha & \alpha^{3}\\ 1 & \alpha^{3} & \alpha & \alpha^{4} & \alpha^{2}\\ 1 & \alpha^{4} & \alpha^{3} & \alpha^{2} & \alpha\end{bmatrix}\begin{bmatrix}\vec{F}_{1}\\ \vec{F}_{2}\\ \vec{F}_{3}\\ \vec{F}_{4}\\ \vec{F}_{5}\end{bmatrix} \tag{5.15}$$

$$\alpha=e^{j\frac{2\pi}{5}};\quad |\alpha|=1$$

$$\begin{aligned}&\vec{\mathbf{V}}_{\mathbf{cmd}}^{*}=\left(R_s+j\omega_e L_s\right)\vec{\mathbf{I}}_{\mathbf{s}}^{*}+\vec{\mathbf{E}}_{\mathbf{s}}^{*}+\frac{1}{5}\left(\mu R_s+j\omega_e\left(M_{4f}+L_{fn}\right)\right)\mathbf{B}_1\vec{i}_f\\ &\mathbf{B}_1=-\begin{bmatrix}0 & \alpha^{3} & \alpha & \alpha^{4} & \alpha^{2}\end{bmatrix}^{T}\end{aligned} \tag{5.16}$$

$$\vec{\mathbf{V}}_{\mathbf{cmd},healthy}^{*}=\left(R_s+j\omega_e L_s\right)\vec{\mathbf{I}}_{\mathbf{s}}^{*}+\vec{\mathbf{E}}^{*} \tag{5.17}$$

In (5.16) the voltage component consists of a healthy part and fault part related to i_f component. Assuming perfect current control by the drive and balanced back-EMF of a healthy machine the sequence components of current and back-EMF are given by (5.18).

$$\begin{aligned}&\vec{\mathbf{I}}_{\mathbf{s}}^{*}=\begin{bmatrix}0 & \vec{I}_{+} & 0 & 0 & 0\end{bmatrix}^{T}\\ &\vec{\mathbf{E}}_{\mathbf{s}}^{*}=\begin{bmatrix}0 & \vec{E}_{+} & 0 & 0 & 0\end{bmatrix}^{T}\end{aligned} \tag{5.18}$$

From (5.16) and using (5.18) several observations can be made.

1. Zero sequence component in the command voltage is zero (V_0^{*}=0) under healthy and faulted conditions. This however does not imply that V_{nN} is zero.
2. Under fault condition (5.16) the --, ++ and – sequence components are non-zero and are of same absolute magnitude, whereas under healthy conditions (5.17) these components are zero.
3. The + sequence component comprises of terms expected from the healthy + sequence component and also terms due to 'i_f' terms which has the same magnitude as the other sequence components.
4. The fault information is spread out in all the sequence components (except zero sequence) equally in terms of magnitude as can be deduced

from $\mathbf{B}_1$, therefore fault signature from all sequence components should be extracted to maximise the detection signature.

Since --, ++ and – sequence voltage components consists only of terms comprising of fault current, an effective detection can be achieved simply by summing up the absolute values of the real and imaginary terms of these sequence voltages as given by (5.19). Since the + sequence component contains both healthy and fault terms and the fault terms cannot be separated out, the + sequence voltage is ignored for the computation of the detector.

$$\begin{aligned}\text{detector} = &\left|\text{Re}\left(\vec{V}^*_{--}\right)\right| + \left|\text{Im}\left(\vec{V}^*_{--}\right)\right| + \left|\text{Re}\left(\vec{V}^*_{++}\right)\right| + \left|\text{Im}\left(\vec{V}^*_{++}\right)\right| \\ &+ \left|\text{Re}\left(\vec{V}^*_{-}\right)\right| + \left|\text{Im}\left(\vec{V}^*_{-}\right)\right|\end{aligned} \tag{5.19}$$

In addition to fault detection, in order to enable effective fault mitigation controls, the faulted phase has to be identified. However since the + sequence component contains healthy terms which are dominant, in order to achieve faulted phase identification the voltage phasors are re-constructed by removing the + sequence component in (5.16) to obtain (5.20). By applying inverse Fortescue transformation (5.21) on (5.20) the residual voltage phasors ($\boldsymbol{V}_{res}$) can be obtained as (5.22).

$$\begin{aligned}\vec{\mathbf{V}}^*_{res} &= \frac{1}{5}\left(\mu R_s + j\omega_e\left(M_{4f} + L_{fn}\right)\right)\mathbf{B}_2\vec{I}_f \\ \mathbf{B}_2 &= -\begin{bmatrix}0 & 0 & \alpha & \alpha^4 & \alpha^2\end{bmatrix}^T\end{aligned} \tag{5.20}$$

$$\begin{bmatrix}\vec{F}_1\\ \vec{F}_2\\ \vec{F}_3\\ \vec{F}_4\\ \vec{F}_5\end{bmatrix} = \begin{bmatrix}1 & 1 & 1 & 1 & 1\\ 1 & \alpha^4 & \alpha^3 & \alpha^2 & \alpha\\ 1 & \alpha^3 & \alpha & \alpha^4 & \alpha^2\\ 1 & \alpha^2 & \alpha^4 & \alpha & \alpha^3\\ 1 & \alpha & \alpha^2 & \alpha^3 & \alpha^4\end{bmatrix}\begin{bmatrix}\vec{F}^*_0\\ \vec{F}^*_+\\ \vec{F}^*_{--}\\ \vec{F}^*_{++}\\ \vec{F}^*_-\end{bmatrix} \tag{5.21}$$

$$\begin{aligned}\vec{\mathbf{V}}_{res} &= \frac{1}{5}\left(\mu R_s + j\omega_e\left(M_{4f} + L_{fn}\right)\right)\mathbf{A}_6\vec{I}_f \\ \mathbf{A}_6 &= \begin{bmatrix}1+\alpha^3 & 1+\alpha^2 & 1+\alpha & -3 & 1+\alpha^4\end{bmatrix}^T\end{aligned} \tag{5.22}$$

$$\left|\mathbf{A}_6\right| \approx \begin{bmatrix}0.618 & 0.618 & 1.618 & 3 & 1.618\end{bmatrix}^T \tag{5.23}$$

From (5.22) and (5.23) the following observations can be made:

1. Comparing $\mathbf{A}_5$ in (5.13) with $\mathbf{A}_6$ in (5.22) it can be observed that even if the positive sequence is neglected the reconstructed residual voltage phasor of the faulty phase (phase-4) still retains the same angular information of the fault current i_f as in the original voltage equation (5.13). However for the other healthy phases it gets modified as given by $\mathbf{A}_6$.
2. The ratio between faulted and healthy phases voltage residual is (3/1.618=1.85) for the two closest healthy phases and (3/0.618=4.85) for the other two healthy phases as given by (5.23). This implies that a determination about the fault location can be made, however the faulted phase residual is only 85% higher than the closest healthy phase residuals. Presence of noise and harmonics and non-ideal control can reduce this theoretical ratio and may cause mis-identification of the faulted phase.

Therefore in conclusion using just the inverter command voltages, determination of fault and localisation of fault can be done in steady state. However, since inverter command voltages are subject to changes under transient conditions such as load and speed changes, it needs to be filtered in order to extract the phasor data. This will increase response time of the detector. This approach may be suitable for industrial drives running under steady load conditions, however is unsuitable from traction/EV application due to dynamic loading. However the benefit of using voltage based detection is that no machine parameter is required by the detector making it machine-parameter independent.

5.5 Steady State Residual Current Analysis under Turn Fault

It can be appreciated from the previous section that residual voltages can be used for fault detection. However, under transient conditions the extraction of voltage sequence components is difficult and requires filtering to reduce the effect of transients. If however, the nominal response of the healthy machine can be predicted and removed using a state observer, the detection will be faster and more robust to load and speed changes. This is because the state observer can predict the same transient response as that expected from a healthy machine and by subtracting the output of the observer from

the actual machine response, any load or speed transient can be theoretically eliminated. However, machine voltage prediction is difficult especially under transient conditions such as load and speed changes due to presence of current derivatives in (5.13) which are difficult to compute due to presence of switching noise in the feedback current.

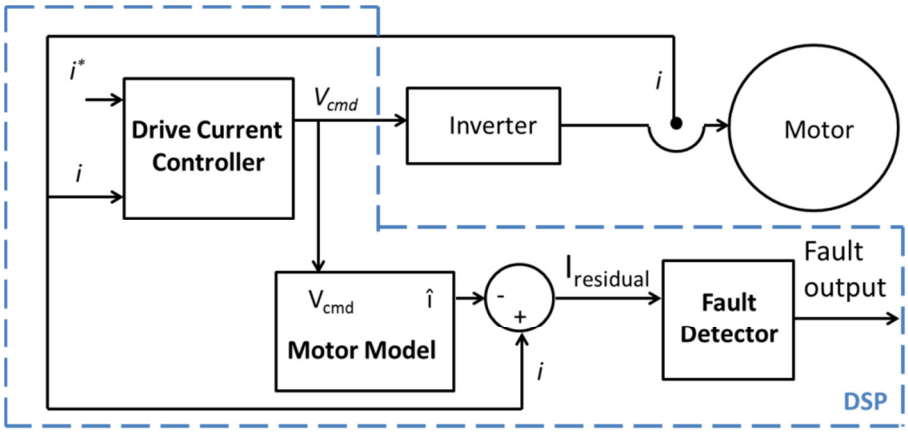

Fig. 5-5: Simplified residual current detector structure

Current however being an integrated quantity is ideal for state estimation. Therefore an internal state estimator to predict nominal motor current using the inverter command voltages can be utilised to extract only the fault signature. Fig. 5-5 shows the simplified detector structure. To analyse the implications steady state analysis similar to that presented in the previous section is performed.

5.5.1 Phasor Analysis

Under sinusoidal steady state, as was shown in the previous section the faulted motor model is given by (5.24).

$$\vec{\mathbf{V}}_{cmd} = \left(R_s + j\omega_e L_s\right)\vec{\mathbf{I}}_s + \vec{\mathbf{E}}_s + \frac{1}{5}\boldsymbol{A}_5\left(\mu R_s + j\omega_e\left(M_{4f} + L_{fn}\right)\right)\vec{I}_f$$
$$\boldsymbol{A}_5 = \begin{bmatrix}1 & 1 & 1 & -4 & 1\end{bmatrix}^T \tag{5.24}$$

The model predicted phasor current using the same voltage command is given by (5.25) where superscript ^ denotes predicted quantities. It is to be noted here that it is assumed that model parameter matches exactly with the actual machine parameters under healthy conditions.

$$\vec{\mathbf{V}}_{cmd} = \left(R_s + j\omega_e L_s\right)\hat{\vec{\mathbf{I}}}_s + \vec{\mathbf{E}}_s \tag{5.25}$$

Since the voltage in (5.24)-(5.25) are equal they can be equated to obtain residual current as shown by (5.26).

$$\vec{\mathbf{I}}_{res} = \vec{\mathbf{I}}_s - \hat{\vec{\mathbf{I}}}_s = -\frac{1}{5}\boldsymbol{A}_5 \frac{\left(\mu R_s + j\omega_e\left(M_{4f} + L_{fn}\right)\right)}{\left(R_s + j\omega_e L_s\right)}\vec{I}_f \tag{5.26}$$

By way of example, from (5.26) the residual currents of the faulted phase (phase-4) and a healthy phase (phase-2) can be extracted and is given by (5.27)-(5.28) and their ratio is given by (5.29).

$$\overrightarrow{I_4} - \overrightarrow{\hat{I}_4} = +\frac{4}{5}\frac{\left(\mu R_s + j\omega_e\left(M_{4f} + L_{fn}\right)\right)}{\left(R_s + j\omega_e L_s\right)}\overrightarrow{I_f} \tag{5.27}$$

$$\overrightarrow{I_2} - \overrightarrow{\hat{I}_2} = -\frac{1}{5}\frac{\left(\mu R_s + j\omega_e\left(M_{4f} + L_{fn}\right)\right)}{\left(R_s + j\omega_e L_s\right)}\overrightarrow{I_f} \tag{5.28}$$

$$\frac{\overrightarrow{I_4} - \overrightarrow{\hat{I}_4}}{\overrightarrow{I_2} - \overrightarrow{\hat{I}_2}} = -\frac{4}{1} \tag{5.29}$$

From (5.26)-(5.29) the following observations can be made:

1. The residual currents are proportional to the fault current 'i_f'.
2. The residual current magnitudes of the healthy phases are equal.
3. The residual current in the faulted phase is in opposite phase with, and 4 times larger than, that of the healthy phases. This enables easy determination of the faulted phase. In presence of system noise the ratio is expected to decrease however, a ratio of 4.0 is an excellent signal-to-noise ratio. The relationship can be further generalised to an N phase SPM machine which has zero mutual inductance as given by (5.30).

$$\frac{\overrightarrow{I_{fault,ph}} - \overrightarrow{\hat{I}_{fault,ph}}}{\overrightarrow{i_{nofault,ph}} - \overrightarrow{\hat{I}_{nofault,ph}}} = -\frac{N-1}{1} \tag{5.30}$$

This property of large residual ratio between the faulted and healthy phase can be exploited to determine the faulted phase by extracting the residual phasor magnitudes and comparing the relative magnitudes. Since the ratio is large it also provides a good signal-to-noise ratio for phase identification against model errors. It is to be noted that in the voltage phasor analysis the ratio between faulted phase and healthy phases varied

with the minimum ratio being 1.85. Therefore the residual current method offers higher signal-to-noise ratio than that possible with voltage based detection.

5.5.2 Sequence Component Analysis

Unbalance can also be analysed using Fortescue transformation (5.15) and applying it to (5.26), (5.31) can be obtained, where superscript * denotes sequence component phasors.

$$\vec{\mathbf{I}}_{res}^{*} = \vec{\mathbf{I}}_{s}^{*} - \vec{\hat{\mathbf{I}}}_{s}^{*} = \frac{1}{5}\frac{\left(\mu R_s + j\omega_e\left(M_{4f} + L_{fn}\right)\right)}{\left(R_s + j\omega_e L_s\right)}\mathbf{B}_1\vec{i}_f$$
$$\mathbf{B}_1 = \begin{bmatrix} 0 & \alpha^3 & \alpha & \alpha^4 & \alpha^2 \end{bmatrix}^T \tag{5.31}$$

Several key observations can be made using (5.31):

1. Under fault condition the residual current sequence components are non-zero and are of the same absolute magnitude, whereas under healthy conditions these components are zero.
2. The fault information is spread out equally in magnitude in all the sequence components, therefore fault signature from all sequence components should be extracted to maximise the detection.
3. The assumption of perfect current control is no longer necessary for residual current analysis, compared to that needed for voltage analysis. This is because, the state estimator uses the same voltage command and any non-ideality of control affects the machine and the model equally and thus gets cancelled. Therefore, this method can accommodate low bandwidth current controller without loss of precision.

Since in practical conditions it is not possible to have an exact match of motor model parameters to the actual machine, it is quite possible that small mismatches may result in a small residual component in healthy operation. This can easily be removed by only considering the --, ++ and – sequence component for fault detection and ignoring the + sequence for fault detection. An effective detection can be achieved by summing up the absolute values of the real and imaginary terms of these sequence voltages using the same detector as given by (5.32).Ignoring the + sequence component does not

however imply that the model can be far off from actual machine behaviour since that will negate the benefit of having a model based detection.

$$\begin{aligned}\text{detector} = &\left|\text{Re}\left(\vec{I}^{*}_{res,--}\right)\right| + \left|\text{Im}\left(\vec{I}^{*}_{res,--}\right)\right| + \left|\text{Re}\left(\vec{I}^{*}_{res,++}\right)\right| + \left|\text{Im}\left(\vec{I}^{*}_{res,++}\right)\right| \\ &+ \left|\text{Re}\left(\vec{I}^{*}_{res,-}\right)\right| + \left|\text{Im}\left(\vec{I}^{*}_{res,-}\right)\right|\end{aligned} \tag{5.32}$$

5.6 Transient Machine Modelling under HRC

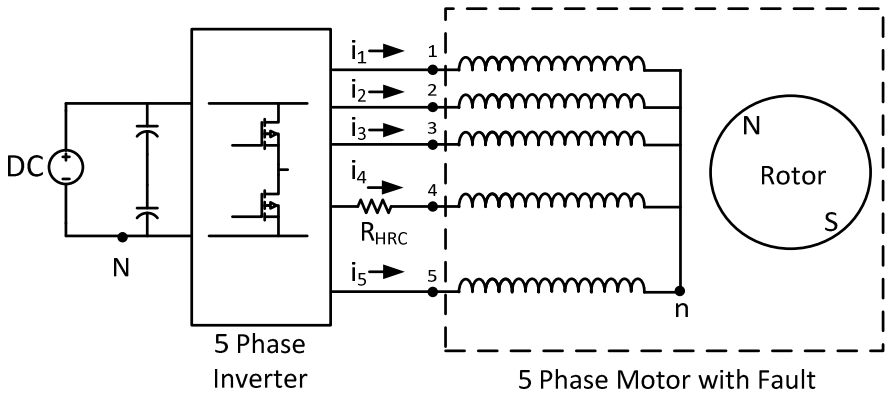

Fig. 5-6: Schematic of machine with high resistance connection in phase-4

Fig. 5-6 shows the schematic of the machine with HRC fault in phase-4. The excess resistance introduced due to the faulty connection is denoted by R_{HRC}. The faulted machine can be modelled by (5.33).

$$\boldsymbol{v}_s{}^f = \boldsymbol{R}_s{}^f \boldsymbol{i}_s + \boldsymbol{L}_s \frac{d\boldsymbol{i}_s}{dt} + \boldsymbol{e}_s \tag{5.33}$$

where,

$$\begin{aligned}\boldsymbol{v}_s^f &= \begin{bmatrix} V_1 & V_2 & V_3 & V_5 \end{bmatrix}^T \\ \boldsymbol{i}_s^f &= \begin{bmatrix} i_1 & i_2 & i_3 & i_4 & i_5 \end{bmatrix}^T\end{aligned} \tag{5.34}$$

$$\begin{aligned}\boldsymbol{R}_s{}^f &= diag\begin{bmatrix} R_s & R_s & R_s & R_s + R_{HRC} & R_s \end{bmatrix} \\ \boldsymbol{L}_s &= L_s diag\begin{bmatrix} 1 & 1 & 1 & 1 & 1 \end{bmatrix} \\ \boldsymbol{e}_s{}^f &= \begin{bmatrix} e_1 & e_2 & e_3 & e_4 & e_5 \end{bmatrix}^T \\ e_j &= \omega_e \Psi_{m1} \sin\left(\theta - (j-1)2\pi/5\right) + 3\omega_e \Psi_{m3} \sin 3\left(\theta - (j-1)2\pi/5\right)\end{aligned} \tag{5.35}$$

Since the motor is fed by an inverter, and the machine neutral terminal '*n*' is floating as shown in Fig. 5-6, the applied inverter phase voltage vector $\boldsymbol{v}_i$, w.r.t node '*N*', i.e., the negative terminal of the DC supply, can be re-formulated in terms of the motor phase voltage vector $\boldsymbol{v}_s$ as given by (5.36) where, V_{nN} is the voltage between node '*n*' and '*N*'.

$$\boldsymbol{v}_i = \boldsymbol{v}_s + V_{nN} \tag{5.36}$$

By adding all the rows of (5.33) and noting that the sum of phase currents equals zero, V_{nN} can be obtained as given by (5.37). By substituting (5.37) in (5.36), V_{nN} can be eliminated from the voltage equation as given by (5.38).

$$V_{nN} = \frac{\sum \boldsymbol{v}_i - R_{HRC} i_4}{5} \tag{5.37}$$

$$\boldsymbol{v}_{cmd} = \boldsymbol{v}_i - \frac{\sum \boldsymbol{v}_i}{5} = R_s \boldsymbol{i}_s + \boldsymbol{L}_s \frac{d\boldsymbol{i}_s}{dt} + \boldsymbol{e}_s + \boldsymbol{A}_7 i_4 \tag{5.38}$$

The left hand side of (5.38), is the command voltage v_{cmd} generated by the current controller. $\boldsymbol{A}_7$ is given by (5.39).

$$\boldsymbol{A}_7 = R_{HRC}\begin{bmatrix} -1/5 & -1/5 & -1/5 & 4/5 & -1/5 \end{bmatrix}^T \tag{5.39}$$

5.7 Steady State Voltage Analysis under HRC

Using the similar approach as in the turn fault analysis the steady state command voltages is first analysed. Comparing (5.38) to the healthy motor model (5.12), it can be noted that the two equations differ only by the terms containing the resistance 'R_{HRC}'. Therefore, by processing the inverter command voltages through signal processing to extract only the terms containing R_{HRC}, fault could be detected. In order to derive a fault indicator first the sinusoidal steady state behaviour is analysed.

5.7.1 Phasor Analysis

Under sinusoidal steady state, the time domain equation (5.38) can be expressed as complex variables (phasors) by replacing *d/dt* with $j\omega_e$, to obtain (5.40). Phasor voltage command in case of a healthy machine is given by (5.41).

$$\begin{aligned} \vec{\mathbf{V}}_{cmd} &= \left(R_s + j\omega_e L_s\right)\vec{\mathbf{I}}_s + \vec{\mathbf{E}}_s + \frac{1}{5}\boldsymbol{A}_8 R_{HRC}\vec{I}_4 \\ \boldsymbol{A}_8 &= \begin{bmatrix} -1 & -1 & -1 & 4 & -1 \end{bmatrix}^T \end{aligned} \tag{5.40}$$

$$\vec{\mathbf{V}}_{cmd,healthy} = \left(R_s + j\omega_e L_s\right)\vec{\mathbf{I}}_s + \vec{\mathbf{E}}_s \tag{5.41}$$

From the phasor voltage equation of machine under HRC (5.40) the following observations can be made:

1. Phasor voltages of the machine under the HRC are similar to the ones obtained for the turn fault (5.13). The extra terms in the voltage phasors are due to the extra resistance whereas in turn fault case it is due to the fault current i_f.
2. The magnitude of the **A** matrix which is a measure of effect of fault on different phases is same as that obtained in the turn fault case, However the sign of the **A** vector has been reversed.
3. The terms in (5.40) due to the HRC fault are proportional to R_{HRC} and Phase-4 current I_4. This implies that the influence of the HRC fault decreases as motor current decreases. At zero load current the terms vanish. Therefore the HRC fault detection at no loads or light loads is not possible. This is quite different from turn fault case where the fault terms are present even in no-load conditions.
4. HRC fault influences different phase voltages differently as can be observed from terms of $\mathbf{A}_8$ with the faulted phase having the highest coefficient. The phasor voltages are therefore unbalanced.

5.7.2 Sequence Component Analysis

Unbalance can be analysed using Fortescue transformation (5.15) and applying it to (5.40)-(5.41) to obtain (5.42)-(5.43) where superscript * denotes sequence component phasors.

$$\begin{aligned}\vec{\mathbf{V}}^*_{\mathbf{cmd}} &= \left(R_s + j\omega_e L_s\right)\vec{\mathbf{I}}^*_{\mathbf{s}} + \vec{\mathbf{E}}^*_{\mathbf{s}} + \frac{1}{5}R_{HRC}\mathbf{B}_3\vec{I}_4 \\ \mathbf{B}_3 &= \begin{bmatrix} 0 & \alpha^3 & \alpha & \alpha^4 & \alpha^2 \end{bmatrix}^T\end{aligned} \tag{5.42}$$

$$\vec{\mathbf{V}}^*_{\mathbf{cmd},healthy} = \left(R_s + j\omega_e L_s\right)\vec{\mathbf{I}}^*_{\mathbf{s}} + \vec{\mathbf{E}}^* \tag{5.43}$$

Assuming perfect current control by the drive and balanced back-EMF of a healthy machine the sequence components of current and back-EMF can be represented by (5.44).

$$\vec{\mathbf{I}}_{\mathbf{s}}^{*} = \begin{bmatrix} 0 & \vec{I}_{+} & 0 & 0 & 0 \end{bmatrix}^{T}$$
$$\vec{\mathbf{E}}_{\mathbf{s}}^{*} = \begin{bmatrix} 0 & \vec{E}_{+} & 0 & 0 & 0 \end{bmatrix}^{T} \quad (5.44)$$

From (5.42) and using (5.44) several observations can be made:

1. Zero sequence voltage in the command voltages is zero under healthy and faulted conditions. This however does not imply that V_{nN} is zero.
2. Under fault condition, the --, ++ and – sequence components are non-zero and are of same absolute magnitude, whereas under healthy conditions these components are zero. This is similar to that obtained for the turn fault case.
3. The + sequence component comprises of terms expected from the healthy + sequence component and also terms due to R_{HRC} which also has the same magnitude as that in the other sequence components.
4. The fault information is spread out in all the sequence components equally in terms of magnitude as can be deduced from $\mathbf{B}_3$, therefore fault signature from all sequence components should be extracted to maximise the detection.

Since --, ++ and – sequence voltage components consists only of terms comprising of fault resistance, an effective detection can be achieved by summing up the absolute values of the real and imaginary terms of these sequence voltages as given by (5.19). Since the + sequence component consists of both healthy and faulty terms and cannot be separated out the + sequence voltage is consequently ignored.

However since the + sequence component contains healthy terms which are dominant, in order to achieve faulted phase identification the voltage phasors are re-constructed by ignoring the + sequence component in (5.42) to obtain (5.45). By applying inverse Fortescue transformation (5.21) on (5.45) the residual voltage phasors ($\boldsymbol{V}_{res}$) can be obtained as (5.46).

$$\vec{\mathbf{V}}_{res}^{*} = \frac{1}{5} R_{HRC} \mathbf{B}_4 \vec{i}_4$$
$$\mathbf{B}_4 = \begin{bmatrix} 0 & 0 & \alpha & \alpha^4 & \alpha^2 \end{bmatrix}^{T} \quad (5.45)$$

$$\vec{\mathbf{V}}_{res} = \frac{1}{5} R_{HRC} \mathbf{A}_9 \vec{i}_4$$
$$\mathbf{A}_9 = -\begin{bmatrix} 1+\alpha^3 & 1+\alpha^2 & 1+\alpha & -3 & 1+\alpha^4 \end{bmatrix}^T \quad (5.46)$$

$$\left|\mathbf{A}_9\right| \approx \begin{bmatrix} 0.618 & 0.618 & 1.618 & 3 & 1.618 \end{bmatrix}^T \quad (5.47)$$

From (5.46) and (5.47) the following observations can be made:

1. The residual voltage in the faulted phase (phase-4) is in phase with the phase current. This implies that even if the positive sequence is neglected, the reconstructed residual voltage phasor of the faulty phase is still in phase with the phase current. This is quite different from the result from the turn fault analysis where the residual phasor voltage is 180º out of phase with the scaled fault current. This distinction in angles can therefore be utilised to distinguish the two faults.
2. The ratio between the faulted and healthy phases is (3/1.618=1.85) for the two closest healthy phases and (3/0.618=4.85) for the other two healthy phases. This implies that a determination about the fault location can be made, however the separation ratio is just 1.85. This is the same result as that obtained in turn fault conditions.

It can therefore be concluded that the fault behaviour under HRC is very similar to that due to turn fault. The residual voltages have the same ratios and the fault detector will show a similar response. However, since the residual voltage of the HRC faulted phase is in phase with the phase current, HRC and turn faults can be distinguished, by comparing the angle of the residual voltage to the phase current.

5.8 Steady State Residual Current Analysis under HRC

Using similar arguments as presented in the case of the turn fault, a state estimator can be used in order to remove the influence of the terms due to healthy machine operation and thereby allow for a more sensitive detection which can reject load and speed disturbances. Detection structure as shown in Fig. 5-5 is evaluated under steady state conditions.

5.8.1 Phasor Analysis

Under sinusoidal steady state the phasor voltage command is given by (5.40). The model predicted phasor current using the same voltage command is given by (5.48) where superscript ^ denotes predicted quantities. It is to be noted here that it is assumed that model parameter matches exactly with the actual machine parameters under healthy conditions.

$$\vec{\mathbf{V}}_{cmd} = \left(R_s + j\omega_e L_s\right)\hat{\vec{\mathbf{I}}}_s + \vec{\mathbf{E}}_s \tag{5.48}$$

Since the voltage in (5.40) and (5.48) are equal they can be equated to obtain residual current as given by (5.49).

$$\vec{\mathbf{I}}_{res} = \vec{\mathbf{I}}_s - \hat{\vec{\mathbf{I}}}_s = -\frac{1}{5}\boldsymbol{A}_8 \frac{R_{HRC}}{\left(R_s + j\omega_e L_s\right)}\vec{I}_4 \tag{5.49}$$

By way of example the residual currents of the faulted phase (phase-4) and a healthy phase (phase-2) is given by (5.50) and (5.51) and their ratio is given in (5.52).

$$\overrightarrow{I_4} - \overrightarrow{\hat{I}_4} = -\frac{4}{5}\frac{R_{HRC}}{\left(R_s + j\omega_e L_s\right)}\overrightarrow{I_4} \tag{5.50}$$

$$\overrightarrow{I_2} - \overrightarrow{\hat{I}_2} = \frac{1}{5}\frac{R_{HRC}}{\left(R_s + j\omega_e L_s\right)}\overrightarrow{I_4} \tag{5.51}$$

$$\frac{\overrightarrow{I_4} - \overrightarrow{\hat{I}_4}}{\overrightarrow{I_2} - \overrightarrow{\hat{I}_2}} = -\frac{4}{1} \tag{5.52}$$

From (5.50)-(5.52) the following observations can be made:

1. The residual currents are proportional to the faulted phase current I_4.
2. The residual current magnitudes of all the healthy phases are equal.
3. The residual current of the faulted phase in (5.50) is in phase with $-I_4/Z_s$. This is different from the turn fault case. By comparing the phase angle of the faulted residual and comparing it to the angle of the faulted phase current, HRC and turn fault can be distinguished.
4. The residual current in faulted phase is in opposite phase with, and 4 times larger than, that of the healthy phases. This is the same as that obtained for the turn fault case. It implies that the same technique that can distinguish the faulted phase under turn fault condition can also work under the HRC fault. The

relationship can be extended for any N phase SPM machine and is given by (5.53).

$$\frac{\overrightarrow{I_{fault,ph}} - \overrightarrow{\hat{I}_{fault,ph}}}{\overrightarrow{i_{nofault,ph}} - \overrightarrow{\hat{I}_{nofault,ph}}} = -\frac{N-1}{1} \tag{5.53}$$

Therefore it can be concluded from phasor analysis that most of the properties of residual current are similar to that obtained under the turn fault with one major exception of the angle relationship of the faulted phase residual to the phase current. This enables to utilise the same detection structure and yet achieve ability to distinguish between turn fault and HRC.

5.8.2 Sequence Component Analysis

Unbalance can be analysed using Fortescue transformation (5.15) and applying it to (5.49), (5.54) is obtained where subscript * denotes sequence component phasors.

$$\begin{aligned} \vec{\mathbf{I}}^*_{res} &= \vec{\mathbf{I}}^*_s - \vec{\hat{\mathbf{I}}}^*_s = -\frac{1}{5}\boldsymbol{B}_3 \frac{R_{HRC}}{\left(R_s + j\omega_e L_s\right)} \vec{I}_4 \\ \mathbf{B}_3 &= \begin{bmatrix} 0 & \alpha^3 & \alpha & \alpha^4 & \alpha^2 \end{bmatrix}^T \end{aligned} \tag{5.54}$$

Several key observations can be made on (5.54):

1. Under HRC fault condition the residual current sequence components are non-zero and are of same absolute magnitude, whereas under healthy conditions these components are zero.
2. The HRC fault information is spread out equally in magnitude in all the sequence components, therefore fault signature from all sequence components should be extracted to maximise the detection signature.
3. The assumption of perfect current control is not necessary for residual current analysis, compared to that needed for voltage analysis. Therefore, this method can accommodate low bandwidth current controller without loss of precision.

Since in practical conditions it is not possible to have an exact match of motor model parameters to the actual machine, it is quite possible that small mismatches may

result in a residual component in healthy operation. This however can easily be removed by only considering the --, ++ and – sequence component for fault detection and ignoring the + sequence for fault detection. An effective detection can be achieved by summing up the absolute values of the real and imaginary terms of residual current sequence components as given by (5.32).

5.9 Fault Detection

Based on the analysis of the previous section(s), it is clear that both voltage and residual current based methods can achieve fault detection. However, there are some differences between the two methods.

Although both methods can detect turn fault and HRC, and can classify the faults, the sensitivity of the voltage based method in identification of the faulted phase is lower than that obtain by the residual current method. Moreover, the voltage based method needs near perfect current control under fault conditions to obtain the theoretical sensitivities; the residual current method does not pose such requirements. In the residual current method the use of a real-time motor model for prediction of motor currents, implies that under healthy conditions the residuals will not be affected by load and speed changes. This is important advantage of the residual current method since any load and speed disturbances will affect the voltage based method and will thereby need more filtering and increase detection time. However, the benefit of the voltage based method is that it needs no prior knowledge of the machine parameters and therefore can be used where no parameter of the machine is available. Most PMSM drive however can easily determine parameters of the machine by running a self-commissioning algorithm such as those implemented by Control Techniques drives [116].

Regardless, of the method there are some common signal processing requirements. Both methods require an extraction of phasor data and sequence components. Both methods require the same algorithm for classification and localisation of fault by calculation of phasor angles and phasor magnitude ratios. The residual current method requires an additional state estimator to predict motor currents.

In the previous sections, steady state fault behaviour was evaluated, based on phasor and sequence component analysis. However, in real-time only instantaneous voltage and current data is available. Therefore, the phasor and sequence component

data needs to be extracted using the instantaneous data. In this section, real-time signal processing is discussed.

Based on the analysis of the previous section that residual currents allow effective turn fault detection, a real time residual current detection algorithm is needed. However, extraction of residual current using state estimation does not immediately yield a fault indicator. This is because the residual currents are themselves time varying quantities and using just the instantaneous values will not result in an effective detector. Therefore, the time varying residuals needs to be converted to DC quantity which will serve as a fault indicator. It is well known that *dq* transformation allow for conversion of time-varying quantities to DC for controls, similar technique can then be used for detection purpose as well.

During fault, the residual currents are as such unbalanced which implies they contain both positive and negative sequence components, applying *dq* transformation will result in the transformed quantities to contain DC as well as time varying values. This is well known since the negative sequence components will appear as time varying quantity with frequency of $2\omega_e$ in the positive rotating *dq* frame and vice-versa. This will again pose a challenge in obtaining a steady fault indicator. Therefore, it is necessary to separate out the positive and negative rotating components from the *dq* frame using two reference frames, one with positive rotation and the other with negative rotation. In order to remove the $2\omega_e$ components from the individual reference frames, low pass filter can be used [32], however this will lead to sluggish response of the detector due to use of large time constant to achieve sufficient attenuation, therefore a more elegant method of sequence component extraction is required.

5.9.1 Extraction of Sequence Components

In order to extract the sequence components, Fortescue transformation is usually utilised. However, Fortesque transformation can only be applied to phasor quantities. Under transient conditions, the sequence components can be extracted using multiple rotating *dqxy* transformation given by (5.55), where *s()* and *c()* are sine and cosine functions respectively. Fig. 5-7 shows the 4 sequence components and the related *dqxy* frames. To take an example, positive sequence component can be extracted using

positive rotating *dqxy* quantities and negative sequence from negative rotating *dqxy* quantities.

$$T_{dqxy0}(\theta)=\frac{2}{5}\begin{bmatrix} \mathrm{s}(\theta) & \mathrm{s}(\theta-2\pi/5) & \mathrm{s}(\theta-4\pi/5) & \mathrm{s}(\theta-6\pi/5) & \mathrm{s}(\theta-8\pi/5) \\ \mathrm{c}(\theta) & \mathrm{c}(\theta-2\pi/5) & \mathrm{c}(\theta-4\pi/5) & \mathrm{c}(\theta-6\pi/5) & \mathrm{c}(\theta-8\pi/5) \\ \mathrm{s}(\theta) & \mathrm{s}(\theta-6\pi/5) & \mathrm{s}(\theta-2\pi/5) & \mathrm{s}(\theta-8\pi/5) & \mathrm{s}(\theta-4\pi/5) \\ \mathrm{c}(\theta) & \mathrm{c}(\theta-6\pi/5) & \mathrm{c}(\theta-2\pi/5) & \mathrm{c}(\theta-8\pi/5) & \mathrm{c}(\theta-4\pi/5) \\ 1/2 & 1/2 & 1/2 & 1/2 & 1/2 \end{bmatrix} \tag{5.55}$$

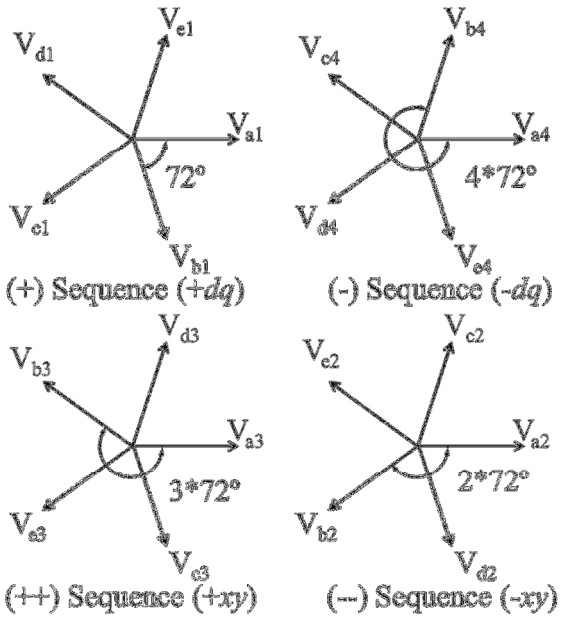

Fig. 5-7: Relationship between *dqxy* and sequence components

In order to establish the frequency components induced due to unbalance, a test vector given by (5.56) is transformed by (5.55), to obtain (5.57).

$$\begin{aligned} F_{1,abcde} = {} & A_{1,+}\begin{bmatrix} \cos(\theta-\varphi_{+}) \\ \cos(\theta-\varphi_{+}-\alpha) \\ \cos(\theta-\varphi_{+}-2\alpha) \\ \cos(\theta-\varphi_{+}-3\alpha) \\ \cos(\theta-\varphi_{+}-4\alpha) \end{bmatrix} + A_{1,-}\begin{bmatrix} \cos(-\theta-\varphi_{-}) \\ \cos(-\theta-\varphi_{-}-\alpha) \\ \cos(-\theta-\varphi_{-}-2\alpha) \\ \cos(-\theta-\varphi_{-}-3\alpha) \\ \cos(-\theta-\varphi_{-}-4\alpha) \end{bmatrix} \\ & + A_{1,++}\begin{bmatrix} \cos(\theta-\varphi_{++}) \\ \cos(\theta-\varphi_{++}-3\alpha) \\ \cos(\theta-\varphi_{++}-6\alpha) \\ \cos(\theta-\varphi_{++}-9\alpha) \\ \cos(\theta-\varphi_{++}-12\alpha) \end{bmatrix} + A_{1,--}\begin{bmatrix} \cos(-\theta-\varphi_{++}) \\ \cos(-\theta-\varphi_{++}-3\alpha) \\ \cos(-\theta-\varphi_{++}-6\alpha) \\ \cos(-\theta-\varphi_{++}-9\alpha) \\ \cos(-\theta-\varphi_{++}-12\alpha) \end{bmatrix} \end{aligned} \tag{5.56}$$

$$F_{1,dqxy0} = T_{dqxy0}(\theta) F_{1,abcde} = \begin{bmatrix} A_{1,+}\sin(\varphi_+) + A_{1,-}\sin(2\theta+\varphi_-) \\ A_{1,+}\cos(\varphi_+) + A_{1,-}\cos(2\theta+\varphi_-) \\ A_{1,++}\sin(\varphi_{++}) + A_{1,--}\sin(2\theta+\varphi_{--}) \\ A_{1,++}\cos(\varphi_{++}) + A_{1,--}\cos(2\theta+\varphi_{--}) \\ 0 \end{bmatrix} \tag{5.57}$$

It is known that the back-EMF of a five phase machine has a third harmonic component, an unbalanced third harmonic test vector (5.58) is transformed by substituting θ by 3θ in (5.55), to obtain (5.59).

$$\begin{aligned} F_{3,abcde} = {} & A_{3,+}\begin{bmatrix} \cos(3\theta-\varphi_+) \\ \cos(3(\theta-\alpha)-\varphi_+) \\ \cos(3(\theta-2\alpha)-\varphi_+) \\ \cos(3(\theta-3\alpha)-\varphi_+) \\ \cos(3(\theta-4\alpha)-\varphi_+) \end{bmatrix} + A_{3,-}\begin{bmatrix} \cos(-3\theta-\varphi_-) \\ \cos(3(-\theta-\alpha)-\varphi_-) \\ \cos(3(-\theta-2\alpha)-\varphi_-) \\ \cos(3(-\theta-3\alpha)-\varphi_-) \\ \cos(3(-\theta-4\alpha)-\varphi_-) \end{bmatrix} \\ & + A_{3,++}\begin{bmatrix} \cos(3\theta-\varphi_{++}) \\ \cos(3(\theta-3\alpha)-\varphi_{++}) \\ \cos(3(\theta-6\alpha)-\varphi_{++}) \\ \cos(3(\theta-9\alpha)-\varphi_{++}) \\ \cos(3(\theta-12\alpha)-\varphi_{++}) \end{bmatrix} + A_{3,--}\begin{bmatrix} \cos(-3\theta-\varphi_{--}) \\ \cos(3(-\theta-3\alpha)-\varphi_{--}) \\ \cos(3(-\theta-6\alpha)-\varphi_{--}) \\ \cos(3(-\theta-9\alpha)-\varphi_{--}) \\ \cos(3(-\theta-12\alpha)-\varphi_{--}) \end{bmatrix} \end{aligned} \tag{5.58}$$

$$F_{3,dqxy0} = T_{dqxy0}(3\theta) F_{3,abcde} = \begin{bmatrix} -A_{3,--}\sin(2\theta+\varphi_{--}) - A_{3,++}\sin(-4\theta+\varphi_{++}) \\ A_{3,--}\cos(2\theta+\varphi_{--}) + A_{3,++}\cos(-4\theta+\varphi_{++}) \\ A_{3,+}\sin(-2\theta+\varphi_+) + A_{3,-}\sin(4\theta+\varphi_-) \\ A_{3,+}\cos(-2\theta+\varphi_+) + A_{3,-}\cos(4\theta+\varphi_-) \\ 0 \end{bmatrix} \tag{5.59}$$

It is therefore clear from (5.57) and (5.59) that under unbalance condition each of the *dqxy* components will contain *0*, $2\omega_e$ and $4\omega_e$ frequency components. The frequency components have to be suppressed in order to extract only the DC components. Two different approaches to this problem are explored.

1. Cross-coupled filter.
2. Multiple notch filter.

5.9.1.1 Cross Coupled Filter

The cross-coupled filter block diagram is shown in Fig. 5-8. The concept of the cross coupled filter [117] is based on extraction of space vector components in each rotating reference frame and subtracting out from the inputs of the other reference frames. To take an example if the residual currents are a combination of negative and positive sequence quantities then in the negative rotating *dqxy* frame the positive sequence components appear as $2\omega_e$ time varying disturbance and vice versa.

If the filtered positive sequence components are subtracted from the signal before applying the negative rotation *dqxy* transformation, ripple cancellation will occur and the disturbance will eventually disappear from both the frames as the system settles to steady state. The problem is complicated by the presence of 3rd harmonic in a five phase system necessitating the use of two more sequence extractions in positive and negative third harmonic reference frame. In Fig. 5-8 each unit cell corresponds to a particular rotating reference frame. There are four reference frames corresponding each to positive and negative sequence of fundamental and positive and negative sequence of third harmonic.

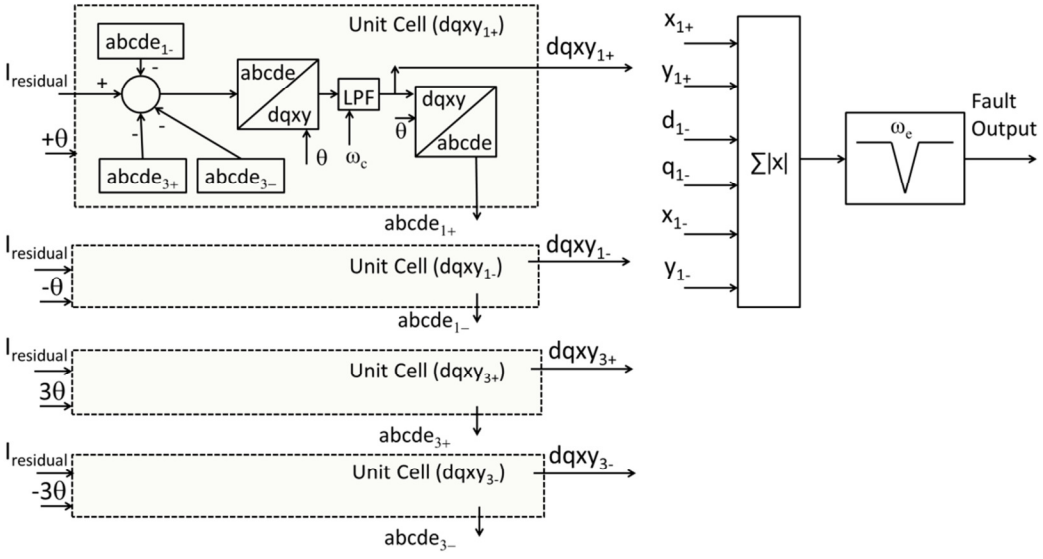

Fig. 5-8: Cross coupled detector structure

A low pass filter (LPF) used in each unit cell is a simple first order filter given by (5.60) [117]. The LPF removes any residual ripple in the *dqxy* frame to obtain

filtered *dqxy* quantities. The filter corner frequency is varied as a function of electrical frequency. The detector is the absolute sum of all unbalanced quantities in fundamental frequency, given by (5.61). An additional notch filter given by (5.62) is inserted in series to attenuate the effect of slight DC drift in current sensors, which when transformed to the *dqxy* frame converts to frequency of ω_e.

$$LPF(s) = \frac{1}{\frac{s}{\omega_c} + 1}; \omega_c = k_f \omega_e \tag{5.60}$$

$$\text{detector} = |x_+| + |y_+| + |d_-| + |q_-| + |x_-| + |y_-| \tag{5.61}$$

$$H_{notch}(s) = \frac{s^2 + \omega_e^{\,2}}{s^2 + 2\xi\omega_e s + \omega_e^{\,2}}; \xi = 0.7 \tag{5.62}$$

As can be clearly seen from Fig. 5-8 the filter is a multi-input multi-output (MIMO) system. Therefore, to select proper corner frequency of the LPF filter in (4.60), numerical simulation is performed to determine optimal range of k_f.

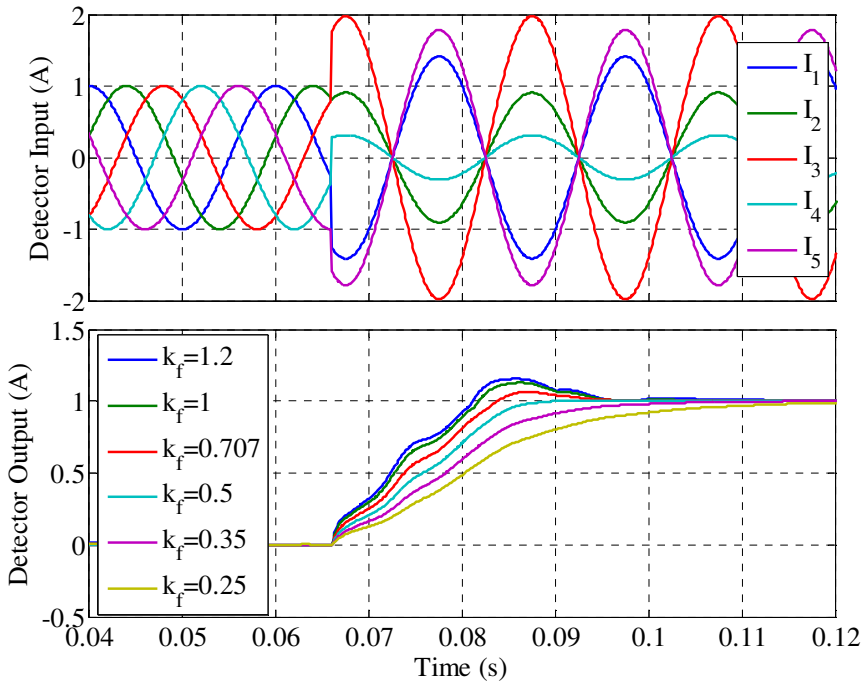

Fig. 5-9: Negative sequence step response of the cross coupled filter to varying k_f.

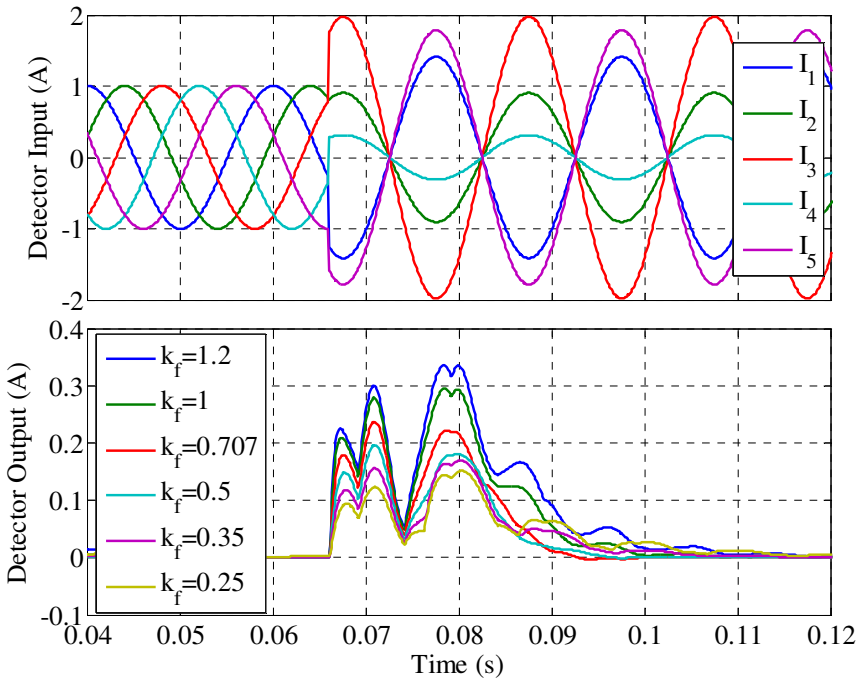

Fig. 5-10: Positive sequence disturbance step rejection response of the cross-coupled filter to varying k_f.

Fig. 5-9 shows the response of the detector to a unit step change in negative sequence component at 0.066s at a fundamental frequency of 50Hz. k_f is varied from 1.2 to 0.25. It should be noted that a steady positive sequence component present in the waveform does not reflect in the detector output which is desirable since small positive sequence components may be present in the residual currents due to mismatch between model and actual machine in healthy conditions and should not be flagged as a fault. It can be observed from Fig. 5-9 that at higher k_f values the response becomes more under damped. Fig. 5-10 shows the disturbance response to unit positive sequence step for varying k_f. It can be observed that as k_f decreases the rejection performance improves, which is expected since lower k_f implies lower corner frequency and therefore greater attenuation.

A range of k_f between [0.5-0.707] is therefore suitable for this application. The recommended value for critically damped response of cross-coupled 3 phase filter in [117] is 0.707, however for 5-phase cross-coupled filter k_f=0.5 is a better choice from point of view of damped response. However, since the rise time is slightly faster and the overshoot is small (6% higher) for k_f =0.707, this value is chosen for detection. It can

be seen that the detector clearly picks up the negative sequence and settles to the new value within 1.5 electrical cycles.

5.9.1.2 Multi-Notch filter Approach

Multi-notch filters can be used for same purpose as the cross-coupled filter. Fig. 5-11 shows the detector structure. It is known that both fundamental and third harmonic will become unbalanced during fault. Therefore to take an example negative sequence and third harmonic will appear as 2nd and 4th harmonic in positive *dqxy* frame. Therefore 2 notch filters are needed, one at $2\omega_e$ and the other at $4\omega_e$. In addition, a low pass filter is required to filter any higher frequency noise from the signal. Fig. 5-12 shows the bode plot of the filter for varying ξ, where $2\omega_e$ and $4\omega_e$ are the notch frequencies, and $2\xi(\omega_f)$ defined the -3dB width of the notch filter(s).

$$H(s)=\frac{s^2+(2\omega_e)^2}{s^2+2\xi(2\omega_e)s+(2\omega_e)^2}\cdot\frac{s^2+(4\omega_e)^2}{s^2+2\xi(4\omega_e)s+(4\omega_e)^2}\cdot\frac{1}{s/\omega_e+1} \qquad (5.63)$$

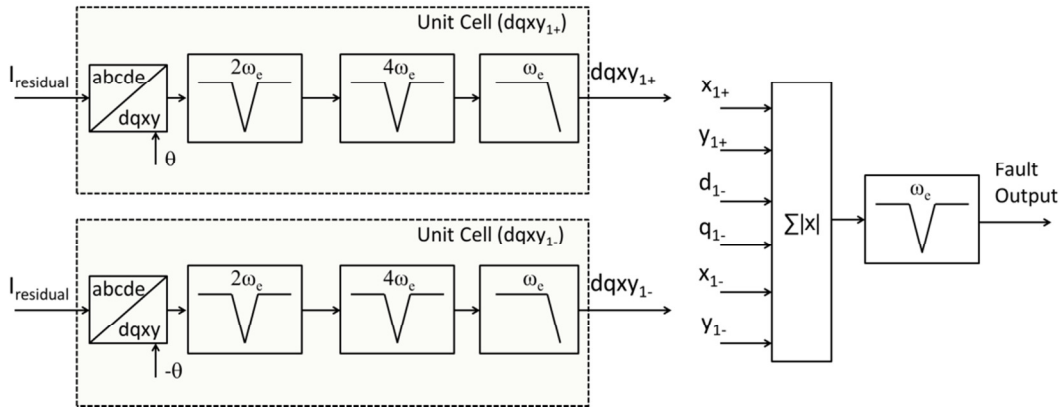

Fig. 5-11: Multi-notch filter based detector

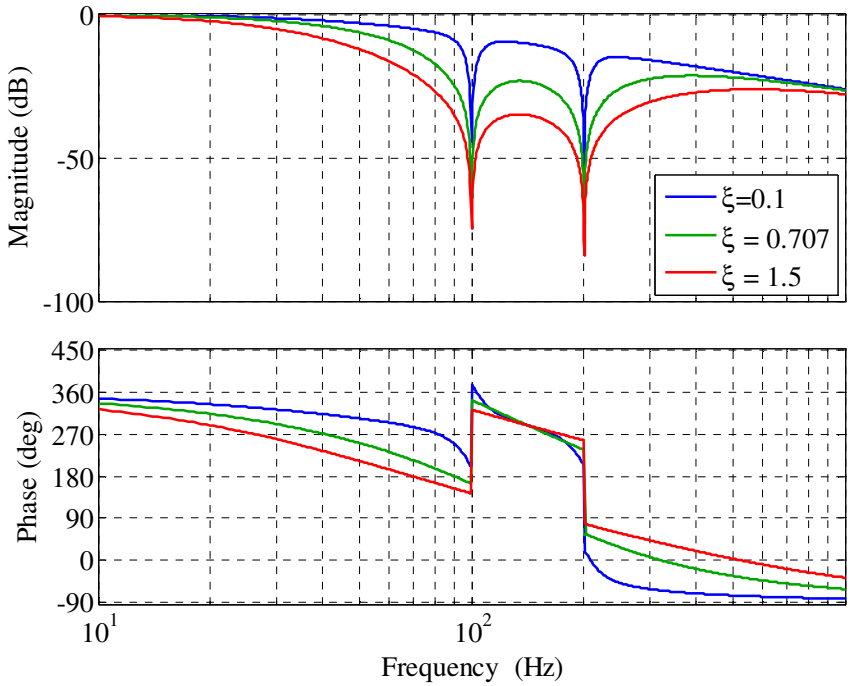

Fig. 5-12: Bode plot of multi-notch filter

Fig. 5-13 shows the response of the multi-notch filter to a unit step change in negative sequence component at 0.066s at a fundamental frequency of 50Hz. ξ is varied from 1.5 to 0.3. It can be observed from Fig. 5-13 that at higher ξ values the response becomes slower, which is to be expected due to increase in the damping. Fig. 5-14 shows the disturbance response to unit positive sequence step for varying ξ. It can be observed that as ξ decreases the rejection performance decreases, which is expected since lower ξ implies lower damping. Therefore an optimal value of ξ can be selected between [0.5-1], which optimises both response time and disturbance rejection.

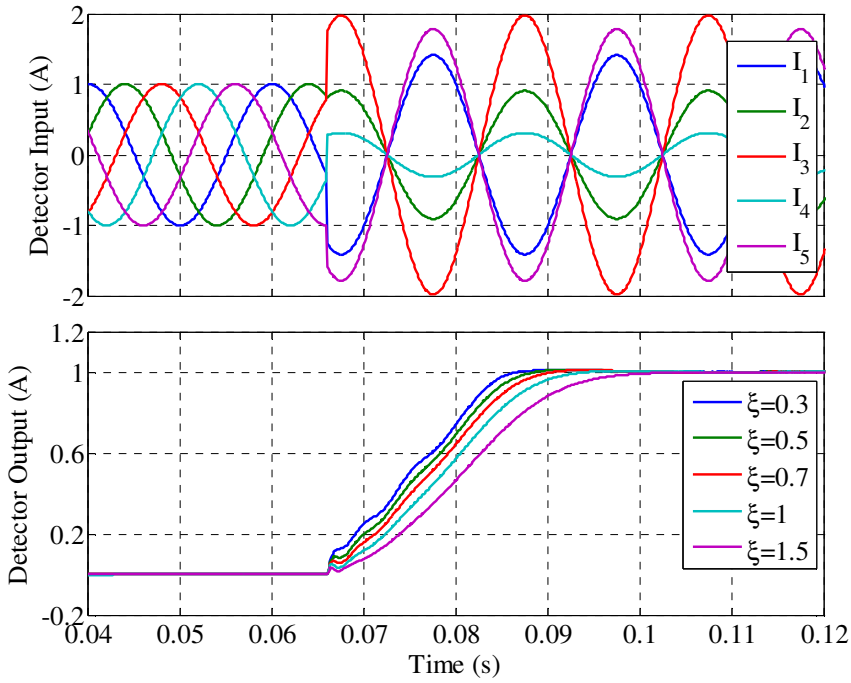

Fig. 5-13: Negative sequence step response of the cross coupled filter to varying ξ.

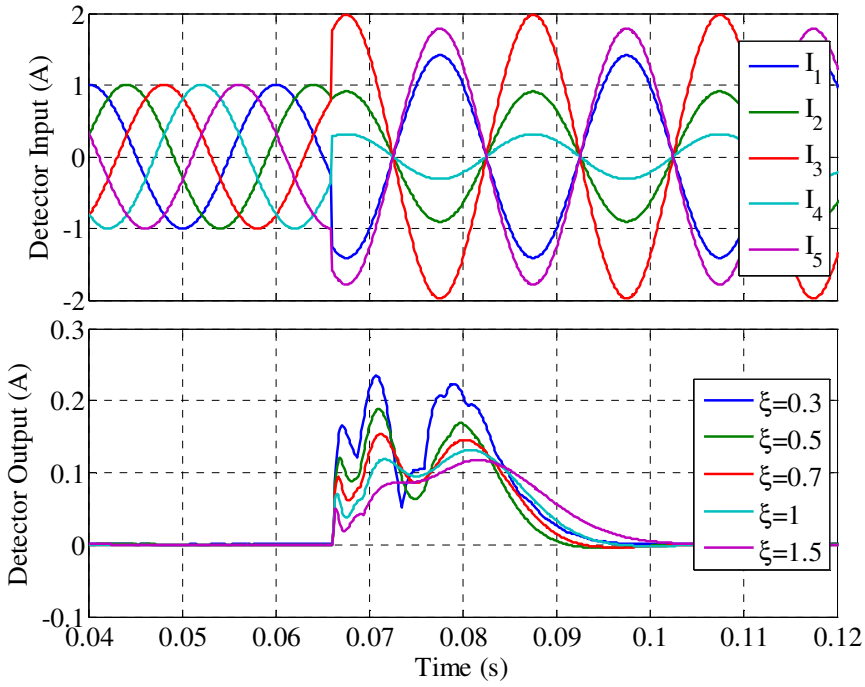

Fig. 5-14: Positive sequence disturbance step rejection response of the cross-coupled filter to varying ξ.

5.9.1.3 Comparison of Cross-Coupled Filter to Multi-Notch Filter

To compare the performance of the multi-notch filter and the cross-coupled filter, both filters are designed with the same rise and settling time (k_f =0.5 and ξ=0.5) and are fed with the same negative sequence step change and a positive sequence step change to determine the step response and disturbance response respectively. Fig. 5-15 shows the comparison of the responses of the two filters. It can be seen that it is possible to design the two filters with same response times, and they exhibit similar disturbance rejection characteristics.

Although Fig. 5-11 looks decidedly simpler than Fig. 5-8, the cross-coupled filter offers computation time advantage compared to multiple notch filter if both fundamental and third harmonic components are to be extracted. This is selected to enable extraction of the third harmonic in hardware to enable maximum flexibility in design of the fault detector. Table 5-4 compares major computing elements of the two approaches. The cross-coupled filter requires more *dq* transformations whereas the multiple notch filter approach requires 32 more notch filters compared to the cross-coupled filter approach.

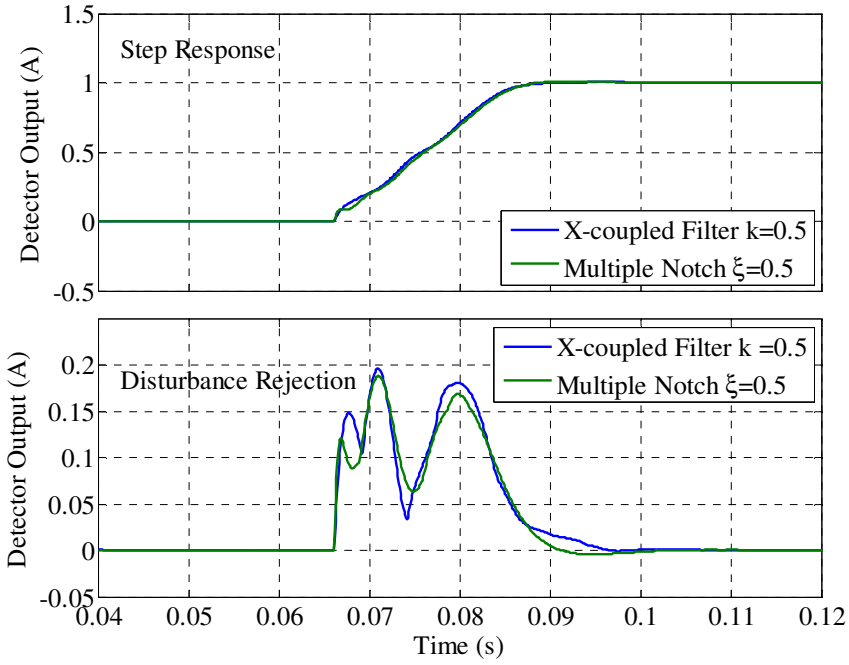

Fig. 5-15: Comparison of cross-coupled filter and multi-notch filter

Table 5-4: Comparison of Computational Requirements for Cross-coupled and Multiple Notch Filter

Filter elements	Cross-coupled filter	Multiple notch filter
No. of 1st order LPF filters	16	16
No. of 2nd order notch filters	1	33
dq transformations	8	4

5.9.1.4 Implementation of LPF and notch Filters

In order to implement the filter structures in real time, the low pass and the notch filter is discretised using Tustin transformation (5.64) to obtain (5.65)-(5.66).

$$s = \frac{2}{T_s}\frac{1-z^{-1}}{1+z^{-1}} \tag{5.64}$$

$$H_{LPF}(z) = \frac{y(z)}{u(z)} = \frac{b_0\left(1+z^{-1}\right)}{1+a_1 z^{-1}}$$
$$b_0 = \frac{\frac{\omega_c T_s}{2}}{\left(1+\frac{\omega_c T_s}{2}\right)};\ a_1 = \frac{\left(1-\frac{\omega_c T_s}{2}\right)}{\left(1+\frac{\omega_c T_s}{2}\right)} \tag{5.65}$$

$$Hnotch(z) = \frac{\beta_0 + \beta_1 z^{-1} + \beta_2 z^{-2}}{1+\alpha_1 z^{-1} + \alpha_2 z^{-2}}$$
$$\beta_0 = \beta_2 = \frac{1+\frac{{\omega_0}^2 {T_s}^2}{4}}{1+\frac{{\omega_0}^2 {T_s}^2}{4}+\xi\omega_0 T_s}$$
$$\beta_1 = \frac{\frac{{\omega_0}^2 {T_s}^2}{2}-2}{1+\frac{{\omega_0}^2 {T_s}^2}{4}+\xi\omega_0 T_s};\quad \alpha_1 = \beta_1; \tag{5.66}$$
$$\alpha_2 = \frac{1+\frac{{\omega_0}^2 {T_s}^2}{4}-\xi\omega_0 T_s}{1+\frac{{\omega_0}^2 {T_s}^2}{4}+\xi\omega_0 T_s}$$

Notch filter is implemented in DSP using direct-form II (DF-II) structure. Fig. 5-16 shows the structure. DF-II has benefit of reducing the data storage requirement from 4 variables for a conventional implementation to 2 variables and therefore is a more optimal structure to implement.

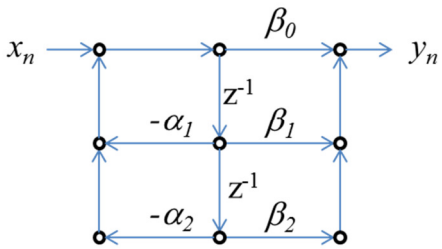

Fig. 5-16: Direct form II implementation of notch filter

5.9.1.5 Implementation of *dqxy* transformation

In order to implement in DSP, it is important that the number of calls to sin and cos functions be restricted to minimum, since they use up a lot of processor clock cycles. The *dqxy* transformation given by (5.55) can be easily separated into a stationary transformation and rotating transformation matrices as given by (5.67)-(5.70) where s() and c() represent sin and cos functions. It can be observed that the Clarke transformation is a constant matrix and the park transformation only requires *sin(θ)* and *cos(θ)* values which are available since these are also required by the current controller.

$$T_{clarke} = \frac{2}{5}\begin{bmatrix} 0 & -\mathrm{s}(2\pi/5) & -\mathrm{s}(4\pi/5) & -\mathrm{s}(6\pi/5) & -\mathrm{s}(8\pi/5) \\ 1 & \mathrm{c}(2\pi/5) & \mathrm{c}(4\pi/5) & \mathrm{c}(6\pi/5) & \mathrm{c}(8\pi/5) \\ 0 & -\mathrm{s}(6\pi/5) & -\mathrm{s}(2\pi/5) & -\mathrm{s}(8\pi/5) & -\mathrm{s}(4\pi/5) \\ 1 & \mathrm{c}(6\pi/5) & \mathrm{c}(2\pi/5) & \mathrm{c}(8\pi/5) & \mathrm{c}(4\pi/5) \\ 1/2 & 1/2 & 1/2 & 1/2 & 1/2 \end{bmatrix} \tag{5.67}$$

$$T_{park} = \begin{bmatrix} \cos(\theta) & \sin(\theta) & 0 & 0 & 0 \\ -\sin(\theta) & \cos(\theta) & 0 & 0 & 0 \\ 0 & 0 & \cos(\theta) & \sin(\theta) & 0 \\ 0 & 0 & -\sin(\theta) & \cos(\theta) & 0 \\ 0 & 0 & 0 & 0 & 1 \end{bmatrix} \tag{5.68}$$

$$F_{dqxy0} = T_{park} T_{clarke} F_{abcde} \tag{5.69}$$

$$F_{abcde} = T_{clarke}^{-1} T_{park}' F_{dqxy0} \tag{5.70}$$

5.9.1.6 Implementation of cross coupled filter

It can be noted from Fig. 5-8 that the output of unit cell is feedback to the input of other unit cells. This means that the filter is inherently cross-coupled and the discretised equations need to be solved simultaneously for correct implementation. This is not an issue in case of high performance controllers like dSpace, however in DSP this will become overly complicated and a simpler implementation is required. One approach to solving this issue is to insert a unit delay at an appropriate location, which does not affect overall performance of the filter. There are many potential sites for insertion of unit delay as shown in Fig. 5-17. However, sites 1 and 3 will introduce un-desirable phase delay. The most appropriate location for unit delay location is at the input of LPF at site 2 after the *dqxy* transformation. Since in *dqxy* the quantities are DC, a delay does not cause phase shift and has minimal effect on the filter performance.

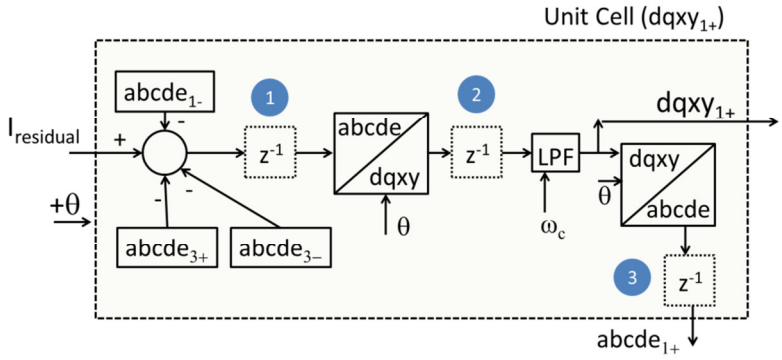

Fig. 5-17: Potential sites for delay insertion

5.9.2 Residual Current extraction

Fig. 5-18 shows the block diagram of the residual current algorithm. It employs a current estimation block which implements a SPM motor model in *dq1dq3* frame (5.71)-(5.72) with the command voltages generated by the controller as its inputs. A star-connected 5-phase machine, has 4 components, denoted as *d1*, *q1*, *d3*, and *q3* in the *dq1* and *dq3* reference frames to account for the influence of fundamental and third harmonic components [118]. The model predicted current is subtracted from the measured currents to obtain the residual currents denoted by $I_{residual}$ in Fig. 5-18. The

residual currents in *dq1dq3* frame is converted to *abcde* frame and then passed to a sequence component extraction block to obtain the fault indicator.

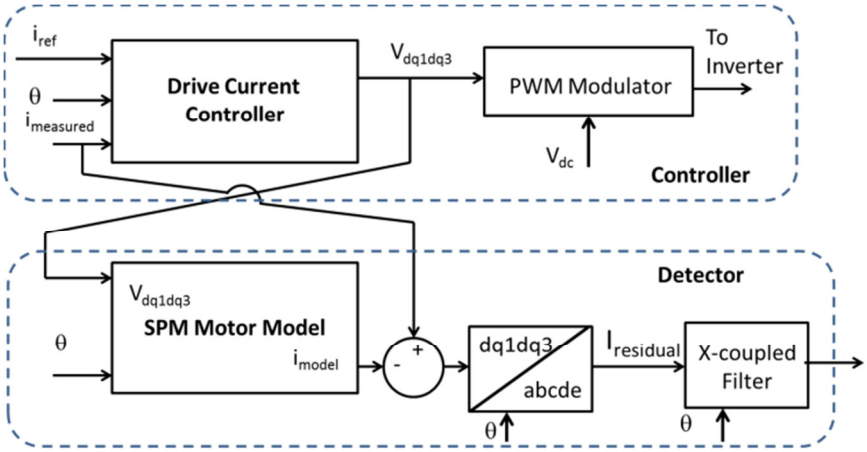

Fig. 5-18: Residual Current block diagram

$$\begin{aligned}
\boldsymbol{V_{dq1}} &= \boldsymbol{R_s i_{dq1}} + \frac{d\boldsymbol{\lambda_{dq1}}}{dt} + \omega_e \begin{bmatrix} -\lambda_{q1} & \lambda_{d1} \end{bmatrix}^T \\
\boldsymbol{V_{dq3}} &= \boldsymbol{R_s i_{dq3}} + \frac{d\boldsymbol{\lambda_{dq3}}}{dt} + 3\omega_e \begin{bmatrix} -\lambda_{q3} & \lambda_{d3} \end{bmatrix}^T
\end{aligned} \tag{5.71}$$

$$\begin{aligned}
\lambda_{d1} &= \Psi_{m1} + L_s i_{d1} \\
\lambda_{q1} &= L_s i_{q1} \\
\lambda_{d3} &= \Psi_{m3} + L_s i_{d3} \\
\lambda_{q3} &= L_s i_{q3}
\end{aligned}$$

$$T_{dq1dq3,0} =$$

$$\frac{2}{5}\begin{bmatrix}
\mathrm{s}(\theta) & \mathrm{s}(\theta-2\pi/5) & \mathrm{s}(\theta-4\pi/5) & \mathrm{s}(\theta-6\pi/5) & \mathrm{s}(\theta-8\pi/5) \\
\mathrm{c}(\theta) & \mathrm{c}(\theta-2\pi/5) & \mathrm{c}(\theta-4\pi/5) & \mathrm{c}(\theta-6\pi/5) & \mathrm{c}(\theta-8\pi/5) \\
\mathrm{s}(3\theta) & \mathrm{s}(3\theta-6\pi/5) & \mathrm{s}(3\theta-2\pi/5) & \mathrm{s}(3\theta-8\pi/5) & \mathrm{s}(3\theta-4\pi/5) \\
\mathrm{c}(3\theta) & \mathrm{c}(3\theta-6\pi/5) & \mathrm{c}(3\theta-2\pi/5) & \mathrm{c}(3\theta-8\pi/5) & \mathrm{c}(3\theta-4\pi/5) \\
1/2 & 1/2 & 1/2 & 1/2 & 1/2
\end{bmatrix} \tag{5.72}$$

5.9.2.1 Motor Model Discretisation

Motor model has to be discretised for real-time implementation. The simplest approach is by using Euler integration. The more accurate approach is 4th order Runge-Kutta (RK4) method.

In order to discretise using Euler method, (5.73) is substituted in model equation (5.71) to obtain (5.74). The equation (5.74) can then be solved for $i_{d1}(k)$, $i_{q1}(k)$ resulting in (5.75)-(5.76) and i_{d3} and i_{q3} can be similarly obtained by replacing ω_e by $3\omega_e$ and Ψ_{m1} by Ψ_{m3} in (5.76)-(5.77).

$$s = \frac{\left(1 - z^{-1}\right)}{T_s} \tag{5.73}$$

$$\begin{aligned} V_{d1}(k) &= \left(R_s + \frac{L_s}{T_s}\right)\hat{i}_{d1}(k) - \frac{L_s}{T_s}\hat{i}_{d1}(k-1) - \omega_e L_s \hat{i}_{q1}(k) \\ V_{q1}(k) &= \left(R_s + \frac{L_s}{T_s}\right)\hat{i}_{q1}(k) - \frac{L_s}{T_s}\hat{i}_{q1}(k-1) + \omega_e L_s \hat{i}_{d1}(k) + \omega_e \Psi_{m1}(k) \end{aligned} \tag{5.74}$$

$$\hat{i}_{d1}(k) = \frac{\left(R_s + \frac{L_s}{T_s}\right)\left[V_{d1}(k) + \frac{L_s}{T_s}\hat{i}_{d1}(k-1)\right] + \omega_e L_s\left[V_{q1}(k) + \frac{L_s}{T_s}\hat{i}_{q1}(k-1) - \omega_e \Psi_{m1}(k)\right]}{\left(R_s + \frac{L_s}{T_s}\right)^2 + (\omega_e L_s)^2} \tag{5.75}$$

$$\hat{i}_{q1}(k) = \frac{\left(R_s + \frac{L_s}{T_s}\right)\left[V_{q1}(k) + \frac{L_s}{T_s}\hat{i}_{q1}(k-1) - \omega_e \Psi_{m1}(k)\right] + (\omega_e L_s)\left[V_{d1}(k) + \frac{L_s}{T_s}\hat{i}_{d1}(k-1)\right]}{\left(R_s + \frac{L_s}{T_s}\right)^2 + (\omega_e L_s)^2} \tag{5.76}$$

The 4th order Runge-Kutta (RK4) is a more accurate implementation for solving the motor model. Runge-Kutta methods are implicit, implying that there is no need to solve linear equations after discretisation as required in the Euler method. RK4 is ideal for solving IPM motor model wherein the current-to-flux linkage map is non-linear and therefore require better solver for accurate estimation. However, compared to Euler

method RK4 is computationally more expensive. RK4 equations for *d*- axis are given by (5.77). Equations for other axis can be similarly derived.

$$\frac{d\boldsymbol{\lambda_{dq1}}}{dt}=\begin{bmatrix} f_{d1} \\ f_{q1} \end{bmatrix}=\boldsymbol{V_{dq1}}-\boldsymbol{R_s i_{dq1}}-\omega_e\begin{bmatrix} -\lambda_{q1} & \lambda_{d1} \end{bmatrix}^T$$

$$\begin{aligned}
k_{d1} &= T_s f_{d1}\left(t(k-1),\lambda_{\mathrm{d1}}(k-1),\lambda_{q1}(k-1)\right) \\
k_{d2} &= T_s f_{d1}\left(t(k-1)+\frac{\mathrm{T_s}}{2},\lambda_{\mathrm{d1}}(k-1)+\frac{k_{d1}}{2},\lambda_{q1}(k-1)+\frac{k_{q1}}{2}\right) \\
k_{d3} &= T_s f_{d1}\left(t(k-1)+\frac{\mathrm{T_s}}{2},\lambda_{\mathrm{d1}}(k-1)+\frac{k_{d2}}{2},\lambda_{q1}(k-1)+\frac{k_{q2}}{2}\right) \\
k_{d4} &= T_s f_{d1}\left(t(k-1)+\mathrm{T_s},\lambda_{\mathrm{d1}}(k-1)+k_{d3},\lambda_{q1}(k-1)+k_{q3}\right) \\
\lambda_{\mathrm{d1}}(k) &= \lambda_{\mathrm{d1}}(k-1)+\frac{k_{d1}}{6}+\frac{k_{d2}}{3}+\frac{k_{d3}}{3}+\frac{k_{d4}}{6} \\
i_d(k) &= \frac{\lambda_{\mathrm{d1}}(k)-\Psi_{m1}}{L_{d1}}
\end{aligned} \tag{5.77}$$

To compare the two solvers a step load change at 1200 r/min is performed in simulation, which includes the discrete current controller and switching inverter. Fig. 5-19 and Fig. 5-20 show the simulation result with the Euler and RK4 method respectively.

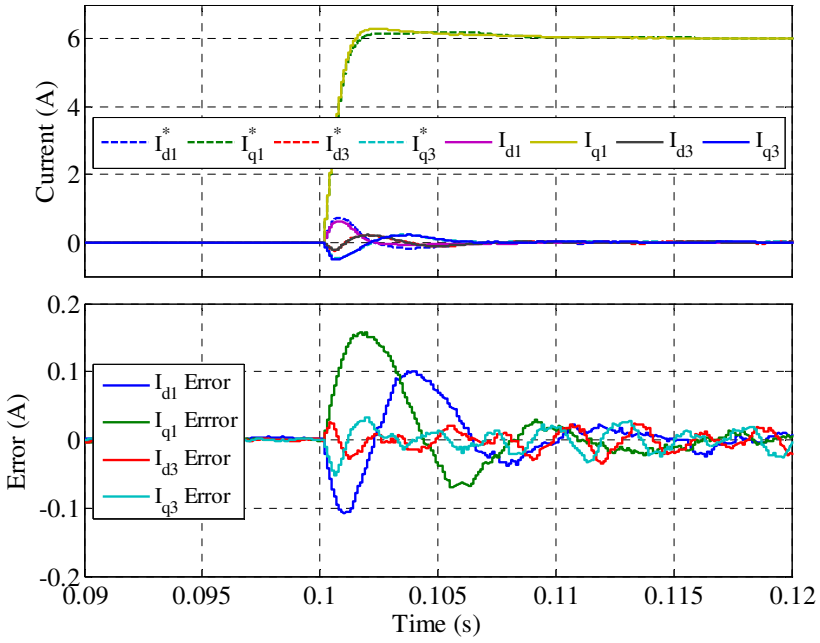

Fig. 5-19: Euler solver (dashed) verses motor current

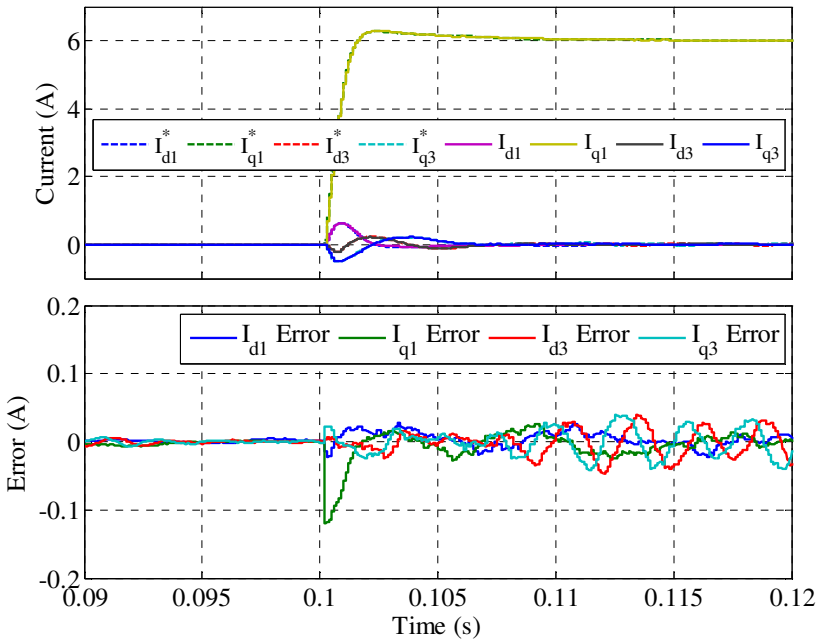

Fig. 5-20: RK4 solver (dashed) verses motor current

It can be observed from the error plots that the RK4 yields lower error in transient and can give better results. However, due to computation time restriction using the TMS320F28335 DSP, the Euler method is implemented in hardware at the sampling rate of 10kHz.

5.9.2.2 Delay Compensation

In a digital implementation of current controller, computation of current controller and PWM duty cycle update introduces compute time delay of one sampling time (T_s). Moreover PWM itself introduces delay in application of the correct voltage vector to the motor terminal. This is commonly approximated at half the switching time. Fig. 5-21 shows the time sequence diagram of the instant of current sampling, control computation, and PWM output. Due to the zero order hold behaviour of the current controller and compute as well as PWM delay, the voltage vector actually applied to the motor terminal is different from that at the output of the current controller. Usually this difference is small and hence neglected, however in case of model based method this delay needs to be accounted in the model. This difference can be calculated analytically by method proposed in [119] and is given by (5.78). The compensation of *dq3* components can be similarly derived by replacing ω_e by $3\omega_e$.

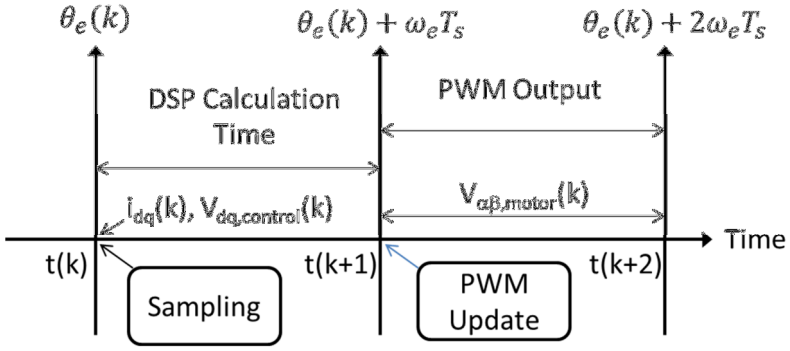

Fig. 5-21: Timing Diagram of sampling, computation and PWM output

$$V_{dq1,motor} = V_{dq1,control}\frac{2}{\omega_e T_s}\sin\left(\frac{\omega_e T_s}{2}\right)e^{-j1.5\omega_e T_s} \tag{5.78}$$

In order to evaluate the effect of delay compensation, simulation results of residual currents under a step change of i_{q1} is plotted with and without compensation under healthy machine operation as shown in Fig. 5-22. It can be seen that without using delay compensation there is a constant residual current in steady state, which implies that even under healthy condition with the same motor parameters the motor model will predict different current than actual and will therefore adversely affect the performance of the detector. Delay compensation is therefore implemented in DSP to compensate for the PWM and calculation time delay.

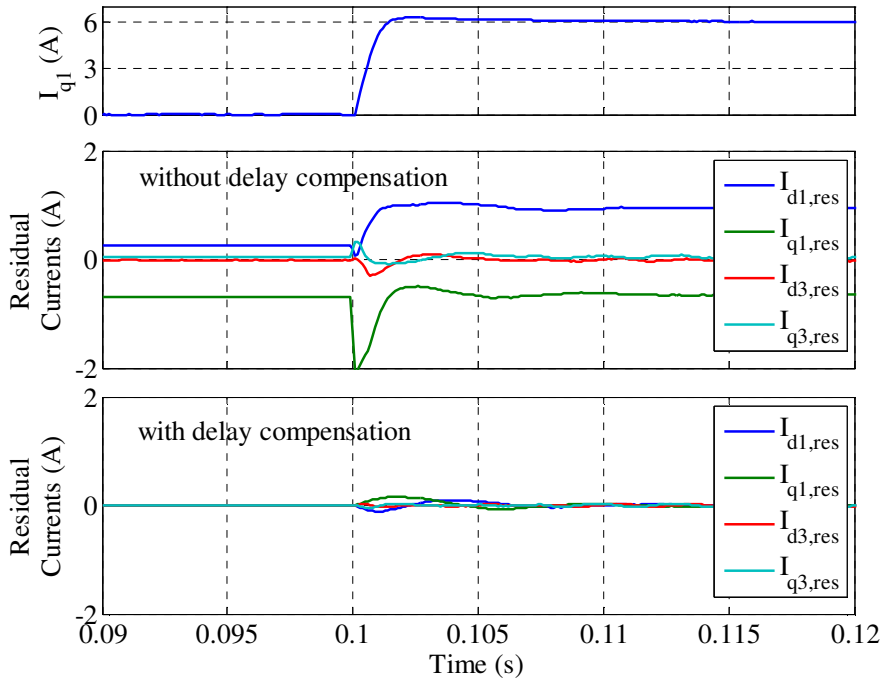

Fig. 5-22: Effect of delay compensation on residual currents

5.9.3 Faulted Phase Detection

The phasor magnitude of the residual currents for the j^{th} phase can be extracted from the filtered fundamental *dqxy* components using (5.79), where α_j = 0, -2π/5, -4π/5, -6π/5 and -8π/5, for phases 1, 2, 3, 4 and 5 respectively.

$$\begin{aligned}
\overrightarrow{i_{res,j}} &= \mathrm{Re}\left(\overrightarrow{i_{res,j}}\right) + i\,\mathrm{Im}\left(\overrightarrow{i_{res,j}}\right) \\
\left|\overrightarrow{i_{res,j}}\right| &= \sqrt{\left(\mathrm{Re}\left(\overrightarrow{i_{res,j}}\right)\right)^2 + \left(\mathrm{Im}\left(\overrightarrow{i_{res,j}}\right)\right)^2} \\
\angle\overrightarrow{i_{res,j}} &= \tan^{-1}\left(\mathrm{Im}\left(\overrightarrow{i_{res,j}}\right) \Big/ \mathrm{Re}\left(\overrightarrow{i_{res,j}}\right)\right) \\
\mathrm{Re}\left(\overrightarrow{i_{res,j}}\right) &= -\left(i_{res,d+} + i_{res,d-}\right)\sin\left(\alpha_j\right) + \left(i_{res,q+} + i_{res,q-}\right)\cos\left(\alpha_j\right) \\
&\quad -\left(i_{res,x+} + i_{res,x-}\right)\sin\left(3\alpha_j\right) + \left(i_{res,y+} + i_{res,y-}\right)\cos\left(3\alpha_j\right) \\
\mathrm{Im}\left(\overrightarrow{i_{res,j}}\right) &= +\left(i_{res,q+} - i_{res,q-}\right)\sin\left(\alpha_j\right) + \left(i_{res,d+} - i_{res,d-}\right)\cos\left(\alpha_j\right) \\
&\quad +\left(i_{res,y+} - i_{res,y-}\right)\sin\left(3\alpha_j\right) + \left(i_{res,x+} - i_{res,x-}\right)\cos\left(3\alpha_j\right)
\end{aligned} \tag{5.79}$$

5.9.4 Fault Classification

Based on fault analysis the phasor angle derived can be used for fault classification. From (5.49) it can be noted that during an HRC fault the residual current is in phase with $-i_4/Z_s$. Therefore, using the phasor angle and adding the impedance angle and comparing it with the command current angle of the faulted phase as given by (5.80) fault classification can be made.

$$classifier = \left|\sin\left(\angle\overrightarrow{i_{res,j}} + \angle Z_s - \angle\overrightarrow{i_j}\right)\right| \tag{5.80}$$

Since the angle at an HRC fault is expected to be close to zero and for a turn fault closer to 90º, if an HRC fault occurs the value of fault classifier is expected to be close to 0, whereas for a turn fault it will be close to 1.

5.10 Simulation Results

To test the performance of the new detector, a speed ramp from 300 RPM to 1200RPM, with pulse load steps applied on the motor model as shown in Fig. 6. A 20 turn fault is applied on phase 4 at 1.0 sec and cleared at 1.1 sec. The fault indicator response shown in Fig. 5-24 shows good rejection of load and speed disturbance and

picks up only when the fault occurs. Fig. 5-25 shows the residual currents and the residual phasor magnitudes calculated by the algorithm. It shows clearly that the residual current in phase 4 is approximately 4 times larger and in phase opposition to that of the residuals of the other healthy phases, thus validating the analytical results. The extracted phasor magnitudes show smooth transition to final DC value.

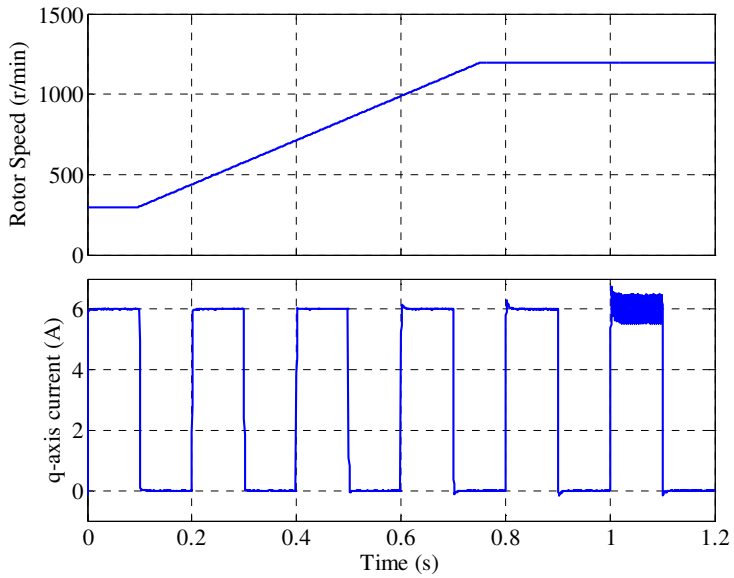

Fig. 5-23: Speed ramp and pulse load test. 20 turn Fault is initiated at 1s and removed at 1.1s.

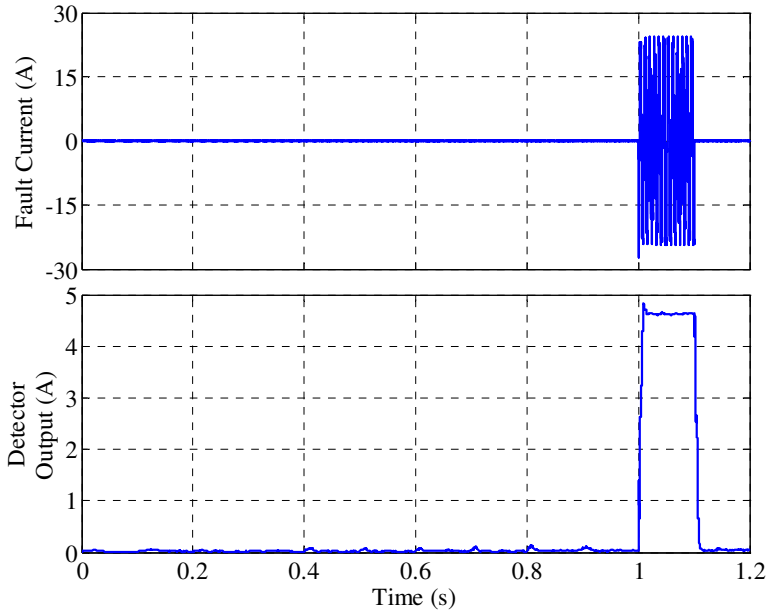

Fig. 5-24: Speed ramp and pulse loading test of fault detector. 20 turn Fault is initiated at 1s and removed at 1.1s.

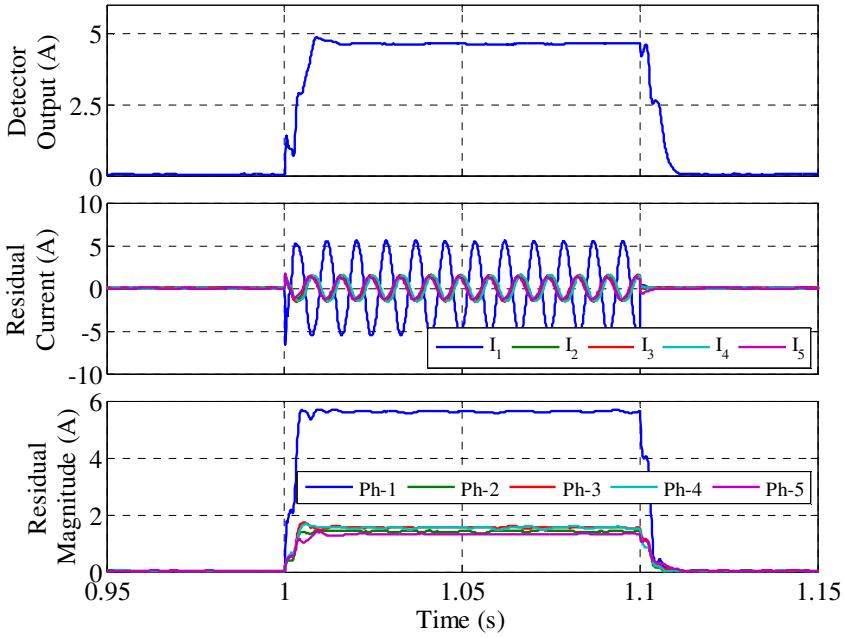

Fig. 5-25: Speed ramp and pulse loading test response of residual magnitude extraction. 20 turn Fault is initiated at 1s and removed at 1.1s.

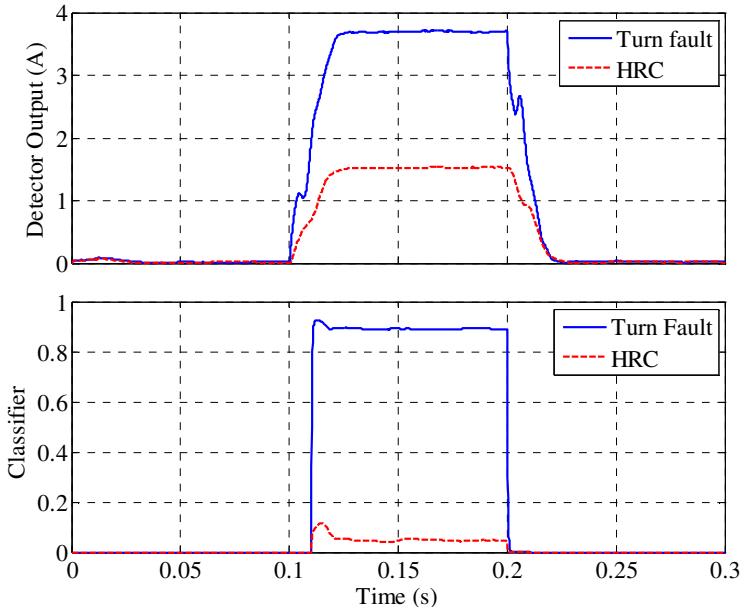

Fig. 5-26: Comparison of classifier output to a 20 turn fault and HRC connection (+60% R) at 500 r/min and i_q=6A. Fault initiated at 0.1s and removed at 0.2s.

Fig. 5-26 shows the response of the classifier output to 20 turn fault and a HRC fault (+60% R) at a rotor speed of 500 r/min and i_q=6A. It can be observed that in case

of HRC fault the classifier is close to zero and turn fault is close to 1. Therefore the classifier can successfully identify HRC or turn fault.

5.11 Experimental Validations

To validate the developed fault detection algorithm, a 5 phase PM machine fed by 5 phase custom inverter was designed and fabricated. The test-rig shown in Fig. 5-28(a) comprises of a Lenz dynamometer connected to the 5- phase test-motor. The stator of the 5 phase machine is shown in Fig. 5-27. An incremental encoder is used for rotor position feedback. A five phase custom built MOSFET inverter is used to control the test motor as shown in Fig. 5-28(b). The inverter is controlled through a floating point TI DSP board (TMS320F28335 EzDSP). Commands to the DSP board is issued using either CAN interface using LabView or through the USB connection via the TI Code Composer studio. Standard *dq* based current control as employed in [118] is utilized to vary the current loading of the test machine. Details of controller can be found in the Appendix.

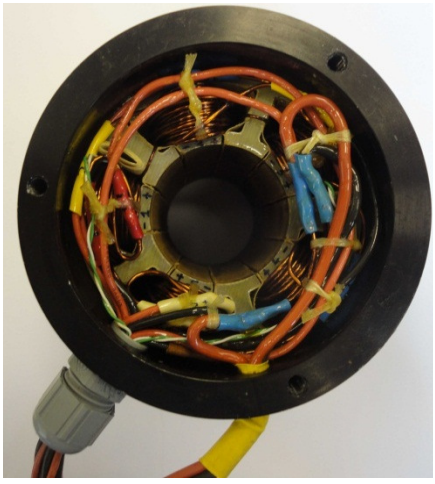

Fig. 5-27: Motor stator winding with fault taps

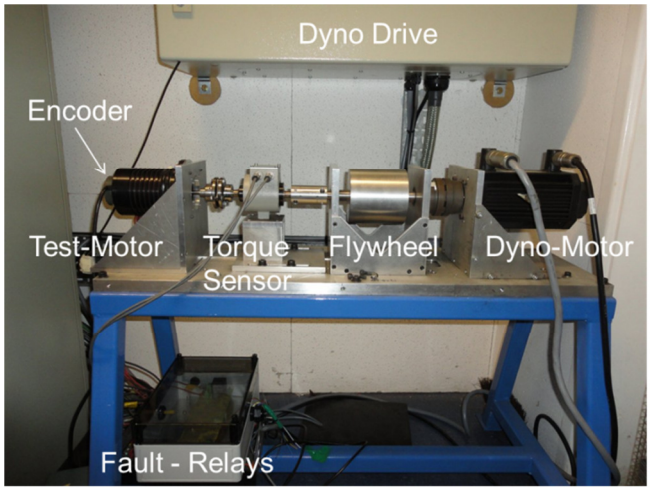

(a)

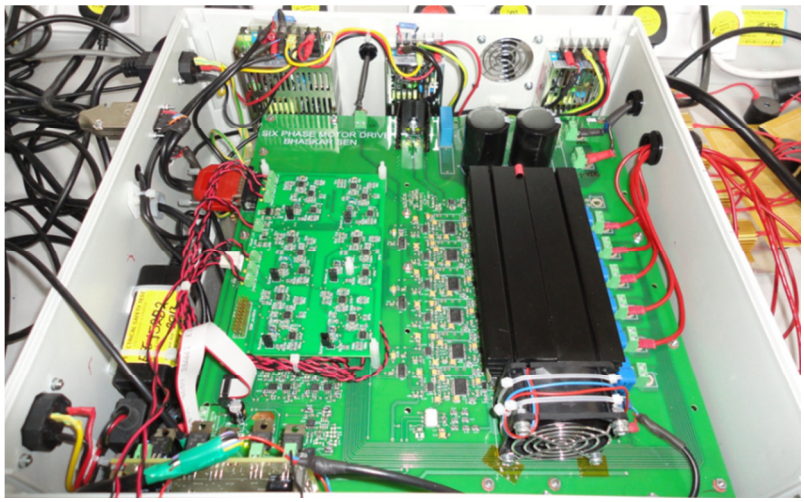

(b)

Fig. 5-28: (a) Dynamometer setup with test machine with fault relays and (b) 5 phase inverter board

5.11.1 Machine Back-EMF

Back EMF of a healthy machine is usually assumed to be constant when transformed to *dq1dq3* frame. This implies that in equation (5.74), $\Psi_m(k)$ does not vary with $\theta(k)$. However, actual machine suffer from fabrication issues like, angular displacement of the magnet poles during assembly and non-uniform magnetisation of the poles. Fig. 5-29 shows the measured back- EMF of the machine at 800 r/min transformed to the *dq1dq3* frame for two mechanical cycles. It can be observed that the

back-EMF is periodic with every mechanical cycle (0.075s) which is expected, however within each mechanical cycle the back-EMF shows variations.

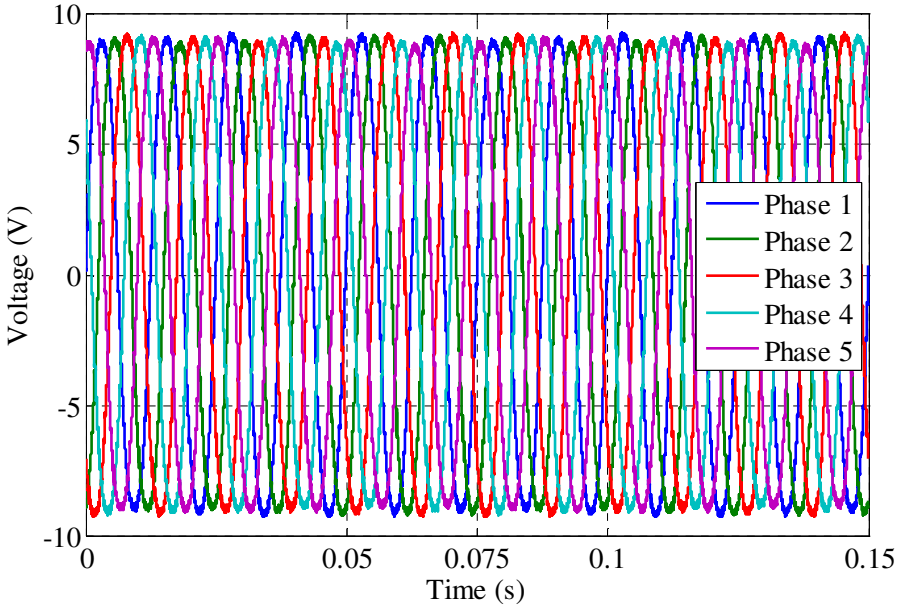

(a)

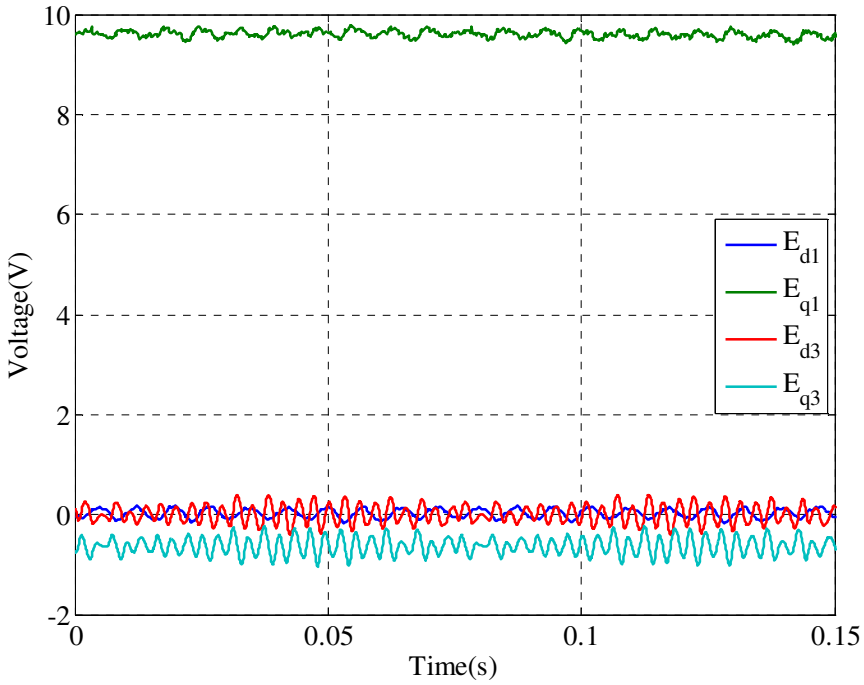

(b)

Fig. 5-29: Back-EMF of the machine at 800 r/min in (a) stationary frame and (b) in *dq1dq3* frame

Usually this variation is ignored in control design since the controller can compensate for these non idealities. However, for fault detection it is important that

back-EMF variation be properly compensated to achieve good sensitivity. Since under low turn faults the signature is small, the variation in back-EMF can easily mask the signature leading to problems in detection. One approach can be to ignore this effect resulting in only detection of higher number of faulted turns. Another approach can be to filter out these harmonics using notch filters. However, since the frequencies are a function of mechanical frequency which is lower than the electrical frequency ($f_m=f_e/6$) a filter will introduce delay and is also not a good solution. Therefore, a lookup table is generated by equally diving one mechanical cycle into 512 points for each phase back-EMF as given by (5.81), where $e_{lk,j}$ refers to the j^{th} phase back-EMF lookup table as a function of the rotor mechanical angle, θ_m. The phase back-EMF is then transformed to *dq1dq3* frame and utilised in the motor model equations given by (5.71)-(5.76).

$$\begin{aligned} \boldsymbol{e}_s &= \frac{\omega_e}{\omega_{e,nom}}\left[e_{lk,1}(\theta_m) \quad e_{lk,2}(\theta_m) \quad e_{lk,3}(\theta_m) \quad e_{lk,4}(\theta_m) \quad e_{lk,5}(\theta_m) \right]^T \\ \omega_e \boldsymbol{\lambda}_{dq1dq3}(k) &= T_{dq1dq3}\boldsymbol{e}_s \end{aligned} \tag{5.81}$$

In order to appreciate the importance of using the lookup table verses using constant values, a test is performed with the residual current detector at 800 r/min and I_{q1}=6A as shown in Fig. 5-30. 2 turn fault is initiated at 0.07s and removed at 0.21s. It can be observed that without using the back-EMF lookup the variation in the fault detector output is high and is not desirable for stable fault detection.

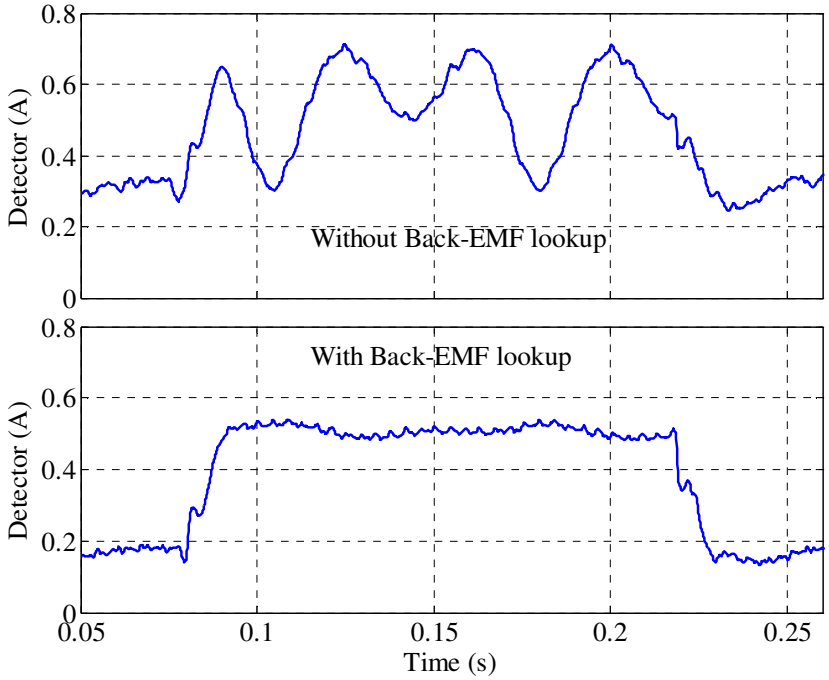

Fig. 5-30: Effect of back-EMF lookup method on 2 turn fault detection at 800 r/min, i_{q1}=6A. Fault is initiated at 0.07s and removed at 0.21s.

5.11.2 Plant Fitting

In order to match the internal motor model (implemented in the DSP) to the physical motor, two test currents { i_{q1} = 6A, i_{d1}=i_{d3}=i_{q3}=0} and { i_{d1} = -3A, i_{q1}=i_{d3}=i_{q3}=0} are commanded at two different rotor speeds (500 and 800 r/min) and the delay compensated controller command voltage is used to extract the equivalent inductance and resistance of the motor. In order to check the fitting different command currents are different speeds is tested. Fig. 5-31 shows the comparison of the predicted voltage using the fitted parameters verses actual voltage command. The voltage error can be observed to be small and therefore the extracted parameters are a good fit with the actual machine.

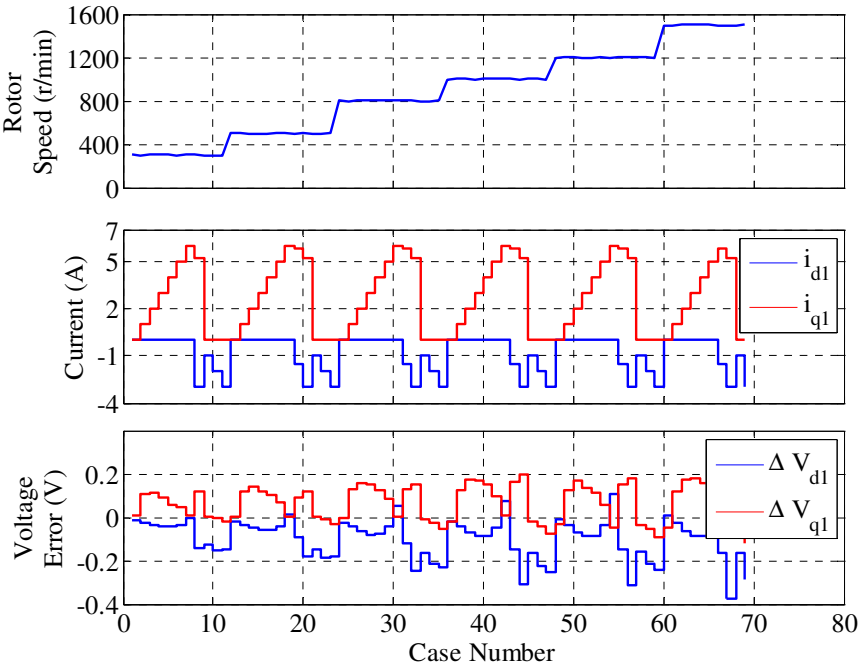

Fig. 5-31: Parameter fitting result.

5.11.3 Healthy Machine Transient Response

Fig. 5-32 and Fig. 5-33 show the response of the calibrated internal motor model to step commands to *dq1* current references at 800 r/min.

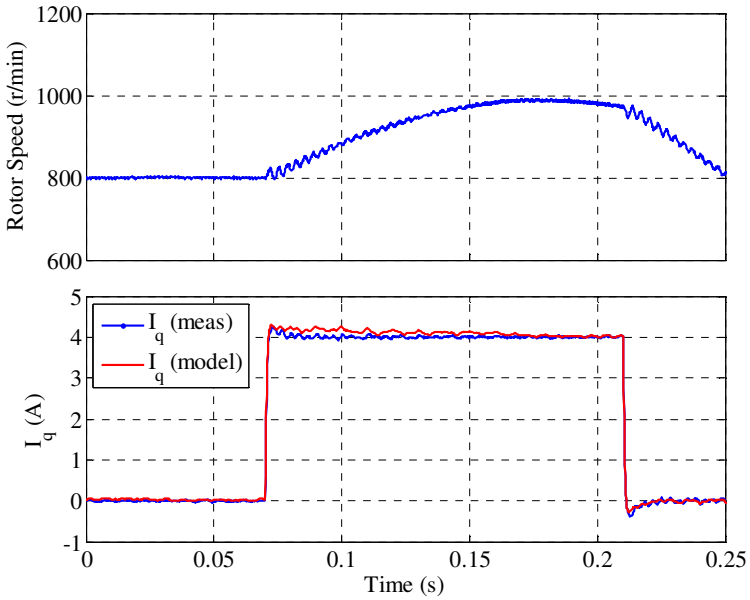

Fig. 5-32: Measured model response to step changes to i_q current (0 to 4A step) at 800 r/min. i_d=0A.

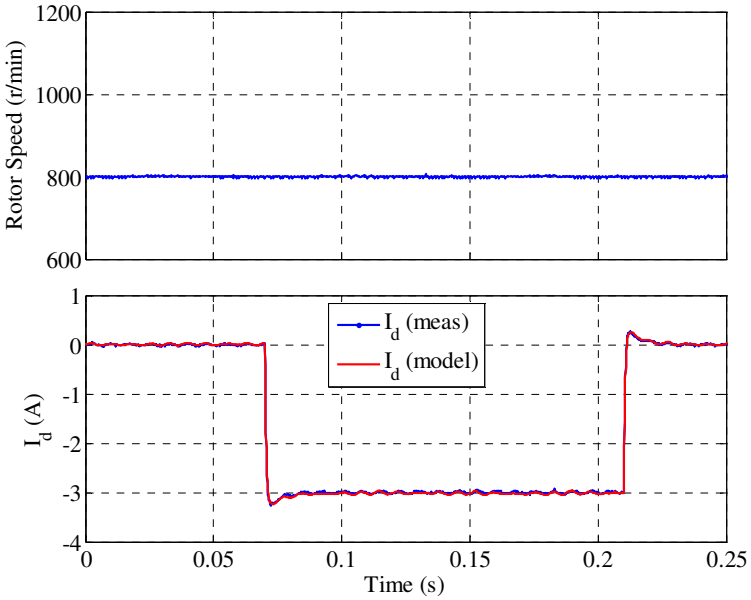

Fig. 5-33: Measured model response to step changes to i_d current (0 to -3A step). i_q=0A.

It can be observed from Fig. 5-32 and Fig. 5-33 that the internal model tracks the actual current response quite well. It is to be noted though that at lower speeds this response is slightly degraded since lower modulation voltages causes errors between actual voltages at inverter output compared to command voltages.

5.11.4 Turn Fault Detection

For testing turn fault, a tap of 2 turn and 20 turn on phase-4 winding is shorted externally using a controlled relay. The measured external resistance including lead wires and contactor resistance is ~8mΩ. First, the variation of fault current for a 2 turn fault is shown in Fig. 5-34. Since the rated RMS current of the winding is 4.24Arms it is evident from the plot that in order to prevent further damage to winding, the detector should detect faults above 400 r/min rotor speed. The linear increase in fault current is due to the fact that the total resistance is the dominating factor in the total impedance. Since back-EMF increases linearly and inductance is negligible compared to the overall resistance, the fault current increases linearly.

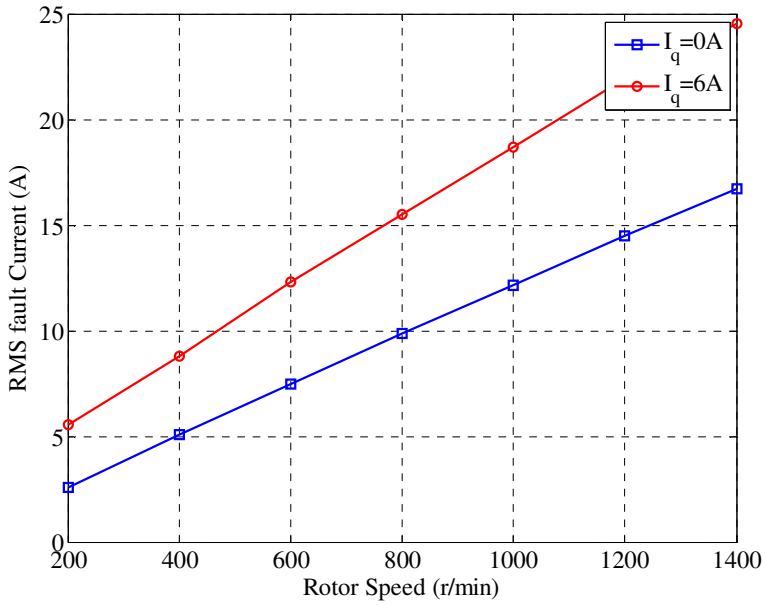

Fig. 5-34: Measured variation of steady state fault current due to 2 turn fault to loading and speed.

In order to appreciate the difficulty in detecting small inter-turn fault the raw data (voltage and current) to the detector is shown in Fig. 5-35 at rotor speed of 600 r/min and i_{q1}=3A. The data point selected is an operating point at a low speed where the detector can easily pick up the turn fault. It can be seen from the raw data that there exists a lot of noise even under healthy condition and the change in current is almost negligible whereas in the voltage it is barely noticeable. For the sake of brevity, i_{q1} and i_{d1} are simply referred to as i_q and i_d in the rest of the chapter since i_{d3} and i_{q3} current commands are set to zero for the experiments.

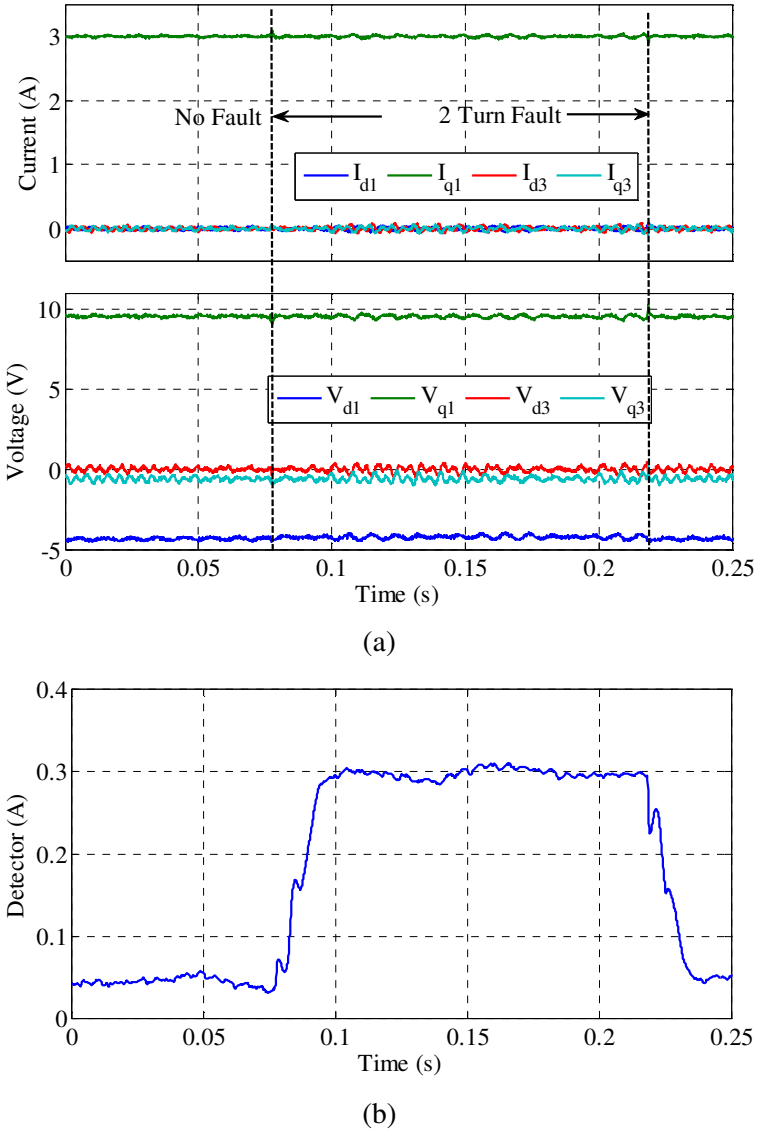

Fig. 5-35: (a) Controller command voltage and feedback current plots and (b) detector output, at 600 r/min and i_{q1}=3A under a 2 turn fault. Fault initiated at 0.07s and removed at 0.21s

Fig. 5-36 and Fig. 5-37 show the response of the detector to a sudden turn fault at 1000 r/min and i_q=6A for 2 turn and 20 turn fault captured using an oscilloscope. It can be observed that the fault detection reaches steady state within 1.5 electrical cycle of fault initiation. It can be seen that less than 2 turn fault the line current post fault remain same as the pre-fault current, however, for a 20 turn fault the currents become unbalanced. This is an expected result, since 20 turn fault causes more un-balance and the current controller is not able to reject the disturbance. It should be further noted from Fig. 5-36 that the current ripple in the fault current is much higher than that

observed in the phase currents. This change of high frequency ripple current and its implication for fault detection is explored in detail in the next chapter.

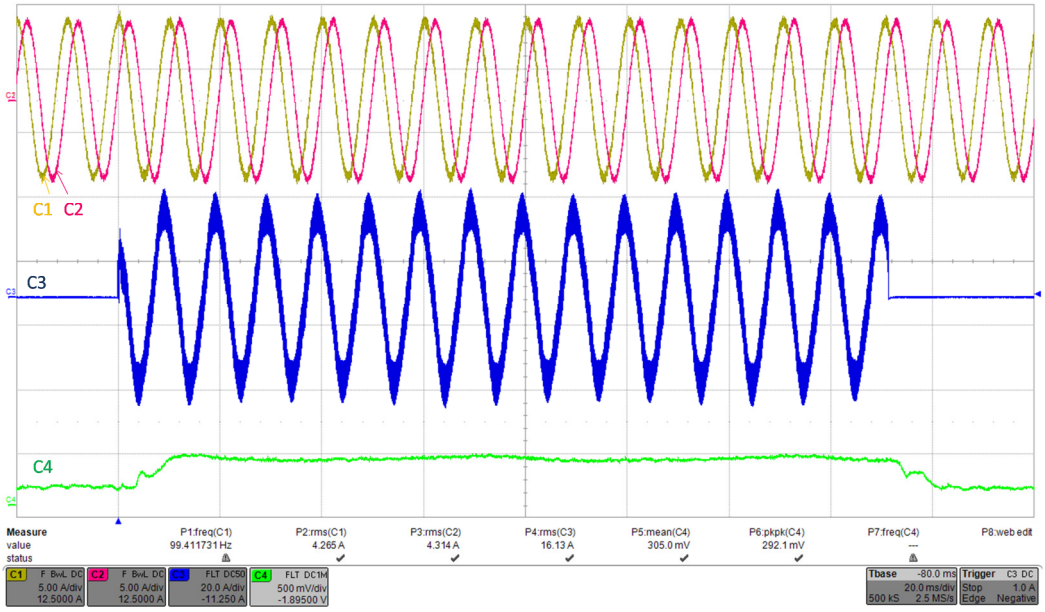

Fig. 5-36: Detector response to 2 turn fault at 1000 r/min. C1, C2 current in phase-4 and 5 respectively (5A/div), C3 is fault current (20A/div) and C4 is detector output, 0.5V/div. Ph-4 is the faulted phase.

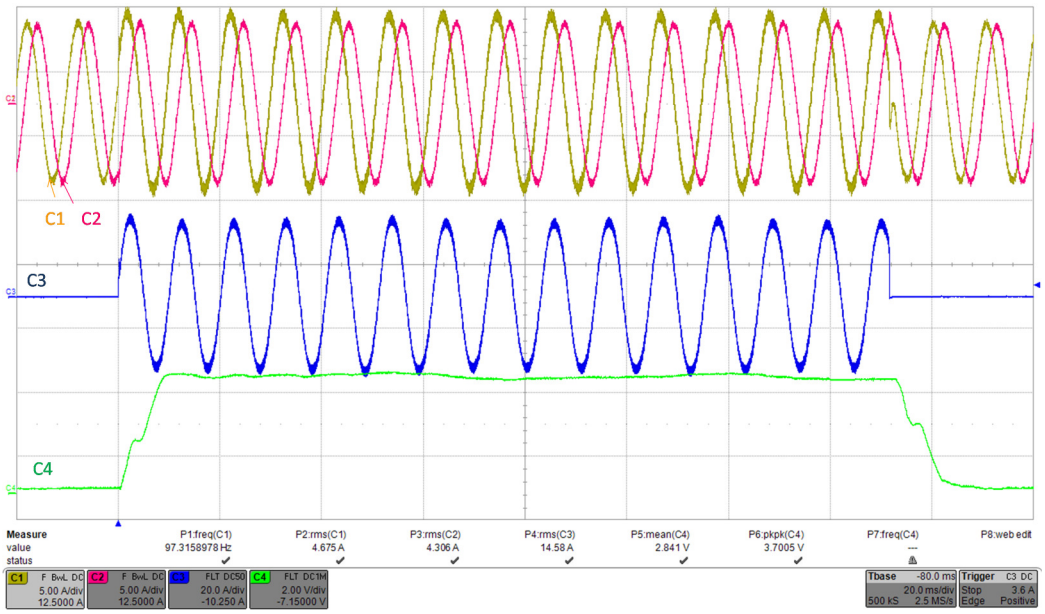

Fig. 5-37: Detector response to 20 turn fault at 1000 r/min. C1, C2 current in phase-4 and 5 respectively (5A/div), C3 is fault current (20A/div) and C4 is detector output, 2V/div. Ph-4 is the faulted phase.

It is to be noted that the detector output is converted using an on-board SPI-DAC for oscilloscope capture. Due to limited number of DAC and oscilloscope channels, the operation of detector is analysed further using the DSP to record the detector parameters at the sample rate of 10 kHz before, during and after the fault. This data is utilised in the rest of the figures for analysis.

Fig. 5-38 and Fig. 5-39 shows the detector response to a 2 and 20 turn fault initiated at 0.07s and removed at 0.21s at various steady current loading at 1000 r/min. The step load response of the detector is shown to provide a comparison of detector response to transient condition under healthy condition to that under fault condition, and it can be appreciated that the detector peak value under healthy transient condition is far below that under fault condition. It can be also observed from Fig. 5-39 that the fault detector response for 20 turn fault is higher than 2 turn fault case. It shows that the detector is responsive to severity of fault and higher fault turn results in higher detector response. The change of magnitude of detector with load current is also expected since the fault current is affected by the load current due to the mutual coupling between the healthy and faulted turns.

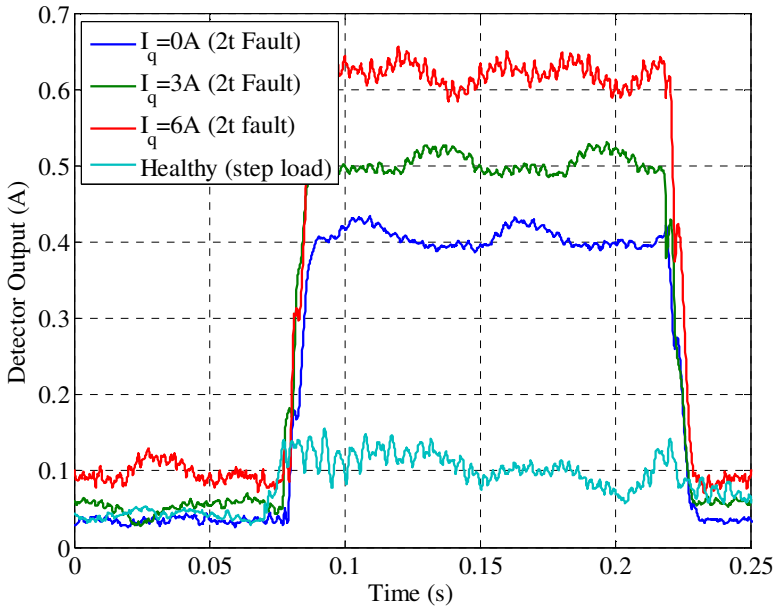

Fig. 5-38: Detector response to turn faults at 1000 r/min under various steady load currents to 2 turn fault. Step i_q (0-4A) response of detector under healthy condition is added for comparison. Fault and load step transient initiated at 0.07s and removed at 0.21s.

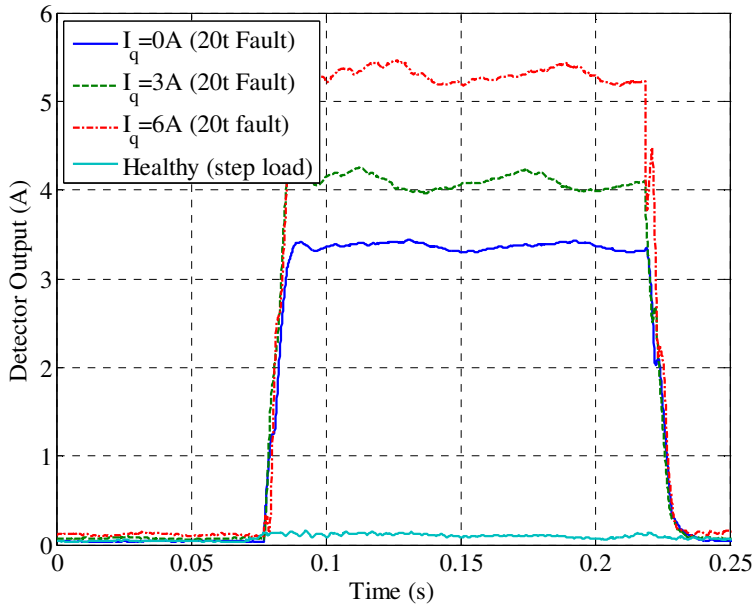

Fig. 5-39: Detector response to turn faults at 1000 r/min under various steady load currents to 20 turn fault. Step i_q (0-4A) response of detector under healthy condition is added for reference. Fault and load step transient initiated at 0.07s and removed at 0.21s.

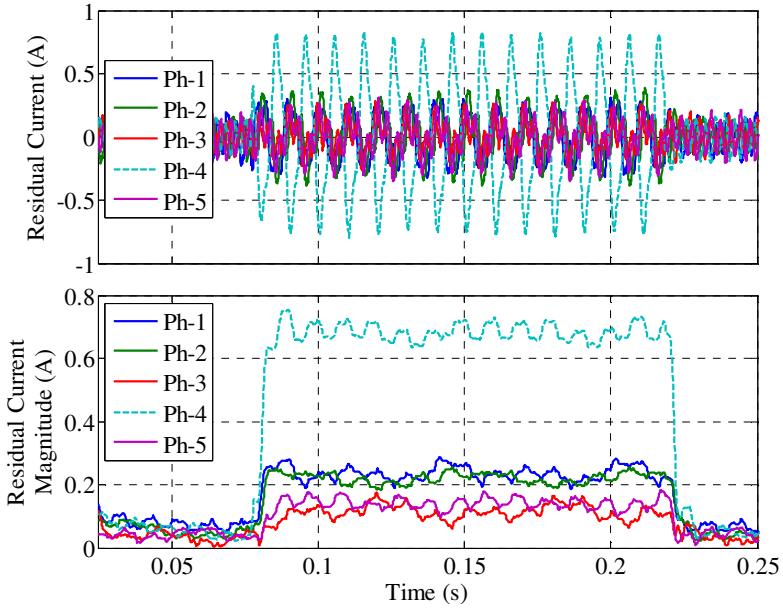

Fig. 5-40: Residual Current magnitude extraction for fault localisation at i_q =6A at 1000 r/min for 2 turn fault. Ph-4 has the turn fault.

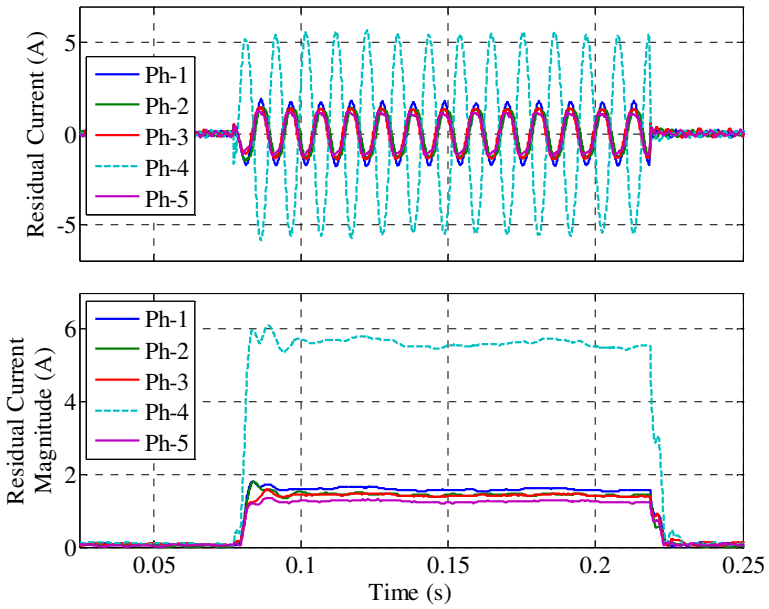

Fig. 5-41: Residual Current magnitude extraction for fault localisation at i_q =6A at 1000 r/min for 20 turn fault. Ph-4 has the turn fault.

Fig. 5-40 and Fig. 5-41 show the residual currents of each phase under 2 and 20 turn fault respectively initiated at 0.07s and removed at 0.21s. It can be seen that the residual currents clearly identify the faulty phase (Ph-4). The magnitude extraction also shows a clear distinction between the faulty phase and healthy phases.

The average ratio of the residual current magnitude is 3 and 3.52 for 2 turn and 20 turn case respectively. The residual current ratio is less than theoretically prediction of 4.0, due to existing unbalance between phases in healthy machine, but is sufficient to allow for clear distinction between the faulty and healthy phases.

5.11.5 HRC Fault Detection

Fig. 5-42 and Fig. 5-43 shows the detector response to an HRC fault of 0.22Ω (+32% increase) and 0.66Ω (+95% increase) respectively initiated in phase-4 at 0.07s and removed at 0.21s. It can be observed that the detector is fast and responsive to the fault. It can also be appreciated that the detector is responsive to the severity of fault i.e., a higher HRC fault results in a higher value. It should also be noted that the detector value changes with the load current which is expected from the theoretical analysis and that the detector can only detect HRC fault when there is load current.

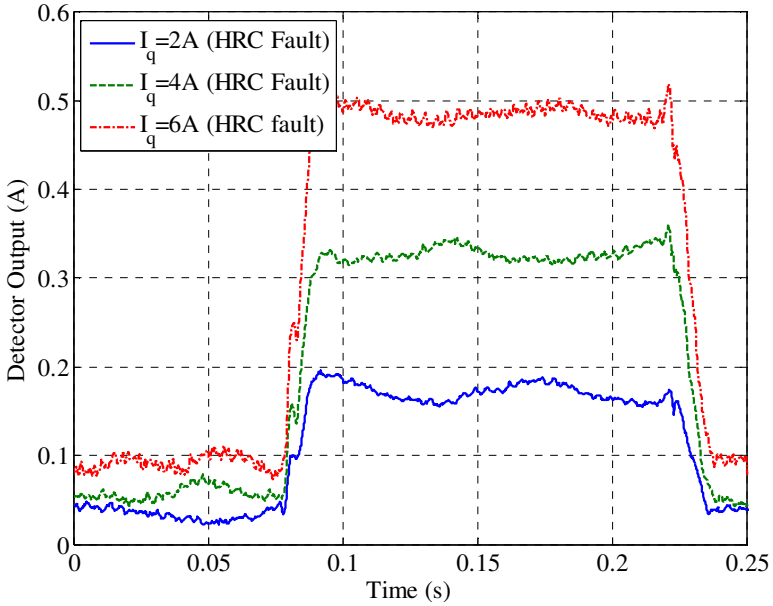

Fig. 5-42: Detector response under various load currents at 800 r/min with HRC fault initiated in phase-4 at 0.07s and removed at 0.21s with 0.22 Ω HRC.

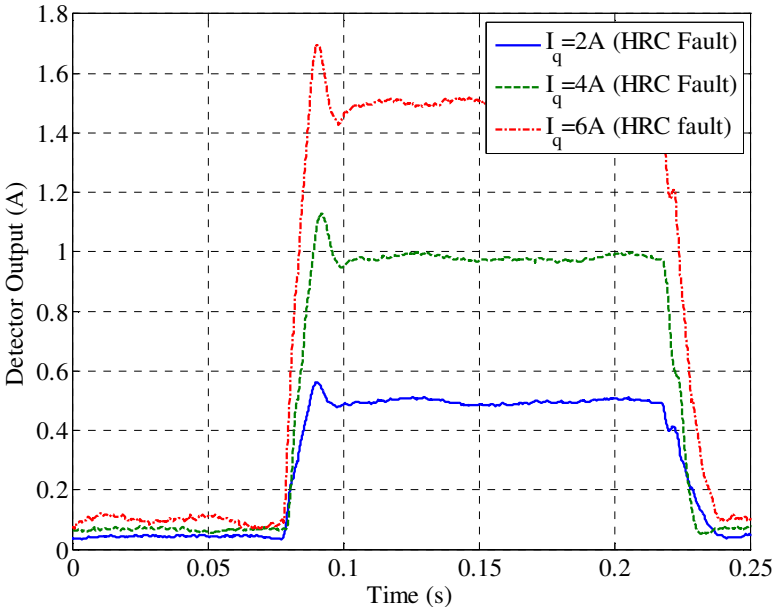

Fig. 5-43: Detector response under various load currents at 800 r/min with HRC fault initiated in phase-4 at 0.07s and removed at 0.21s with 0.66 Ω HRC.

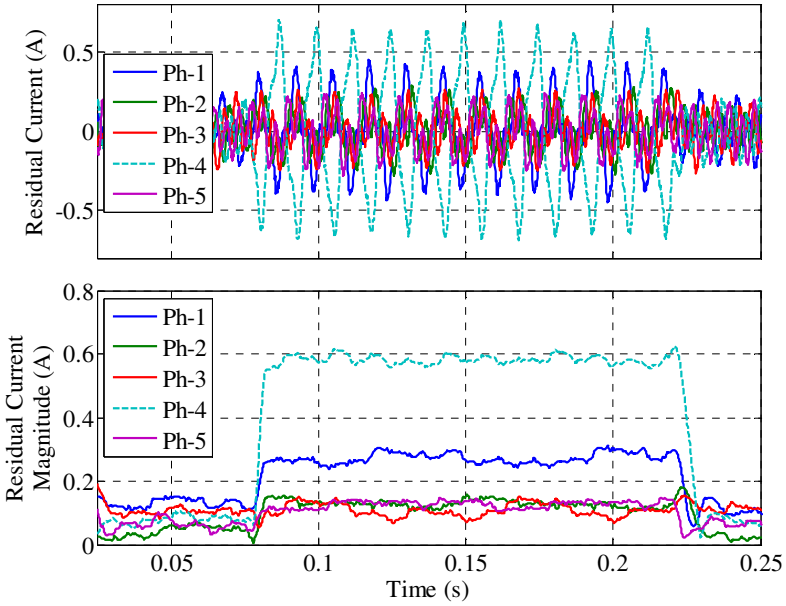

Fig. 5-44: Residual Current magnitude extraction for fault localisation at i_q =6A at 800 r/min with HRC fault initiated in phase-4 at 0.07s and removed at 0.21s with 0.22 Ω HRC. Ph-4 is the phase with HRC.

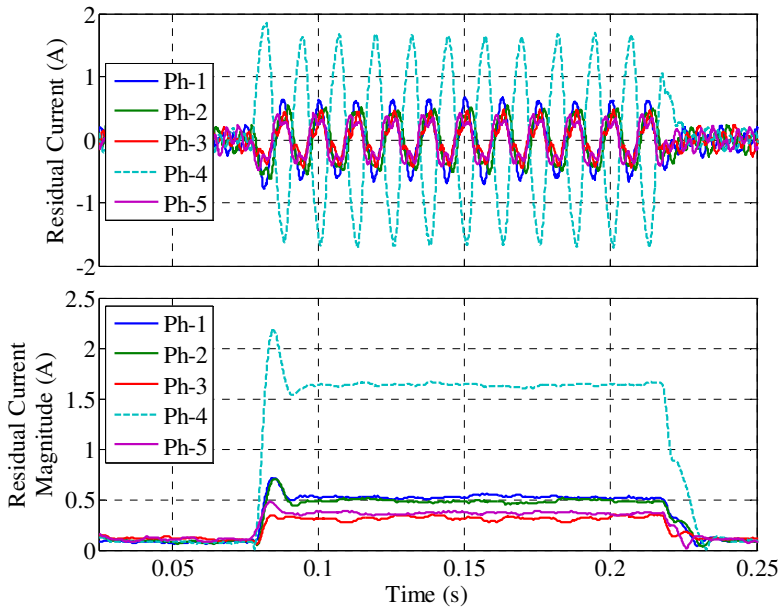

Fig. 5-45: Residual Current magnitude extraction for fault localisation at i_q =6A at 800 r/min with HRC fault initiated in phase-4 at 0.07s and removed at 0.21s with 0.66Ω HRC. Ph-4 is the phase with HRC.

Fig. 5-44 and Fig. 5-45 shows the residual current waveforms under the HRC fault of 0.22Ω (+32% increase) and 0.66Ω (+95% increase) respectively initiated in

phase-4 at 0.07s and removed at 0.21s. It can be seen that the residual currents clearly identify the faulty phase. The magnitude extraction also shows a clear distinction between the faulty phase and healthy phases. The average ratio of the residual current magnitude is 2.14 and 3.13 for 0.22Ω turn and 0.66Ω HRC fault case respectively. The residual current ratio is less than theoretically predicted of 4.0, due to existing unbalance in healthy machine, but is sufficient to allow for clear distinction between the faulty and healthy phases.

5.11.6 Fault Classification

Fig. 5-46 shows the response of the fault classification technique to a 2 turn and HRC (0.22Ω) fault initiated at 0.07s and removed at 0.21s. It can be observed that in the HRC fault case the expected angle deviation from i_4/Z_s is small resulting in value close to zero, compared to that from turn fault.

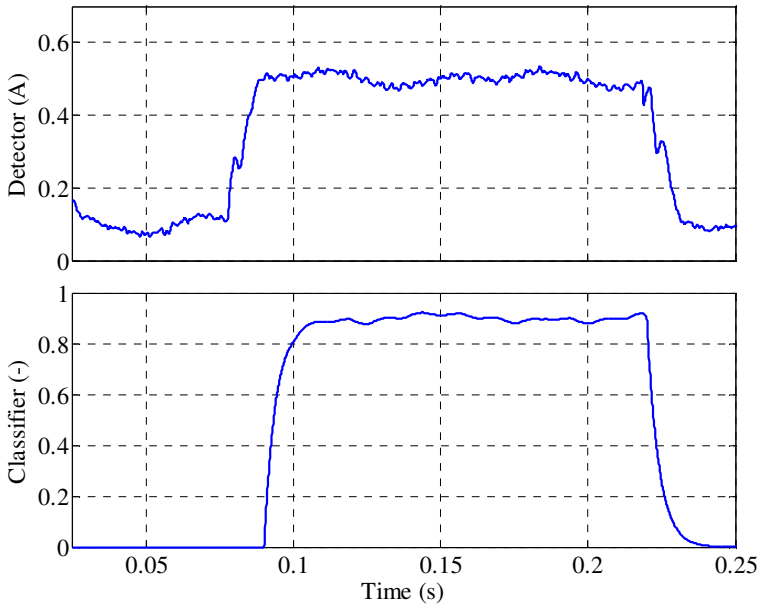

(a)

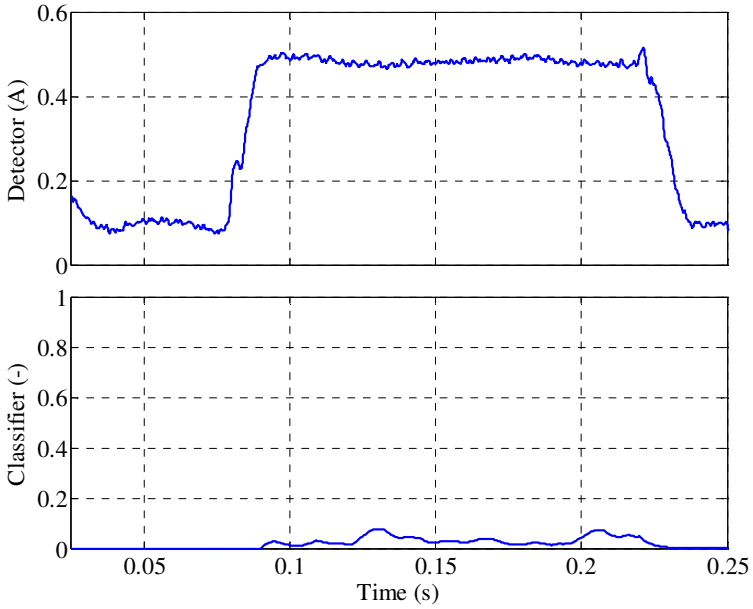

(b)

Fig. 5-46: Residual Current fault classification at i_q =6A at 800 r/min (a) 2 turn fault (b) High resistance fault (0.22Ω).

5.11.7 Comparison of Detector Output in Steady State

In order to understand the efficacy of fault detector at various fault, speed and load conditions, the average detector output is now compared. Fig. 5-47(a) shows the effect of rotor speed and current loading on fault detection for 2 turn fault case, under steady conditions. It can be observed that at lower speeds (<400 r/min) although there is a change of the detector value from healthy to fault case, a bit of overlap exists between healthy signal at high current and fault signature at low current loading. This is because the signal due to inherent healthy motor imbalances is close to the detector output under fault condition at low speeds where the fault current is also lower. Therefore at lower speeds a lookup table maybe utilized to store healthy data at various current loading to differentiate healthy from fault condition. At higher speed (>400 r/min) as can be observed from the plot a simple threshold based detection is sufficient. Fig. 5-47(b) shows the effect of speed on load variation on fault detection at 20 turn fault. Since the fault ratio is higher, fault can very easily be detected using a simple threshold.

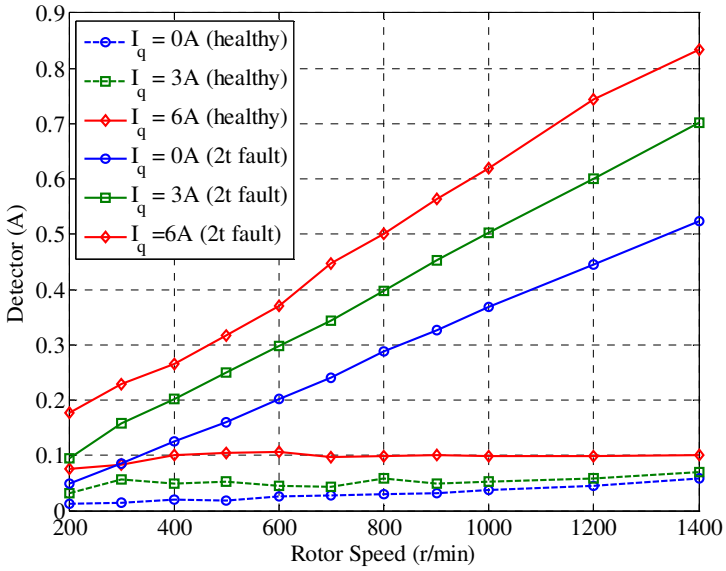

(a)

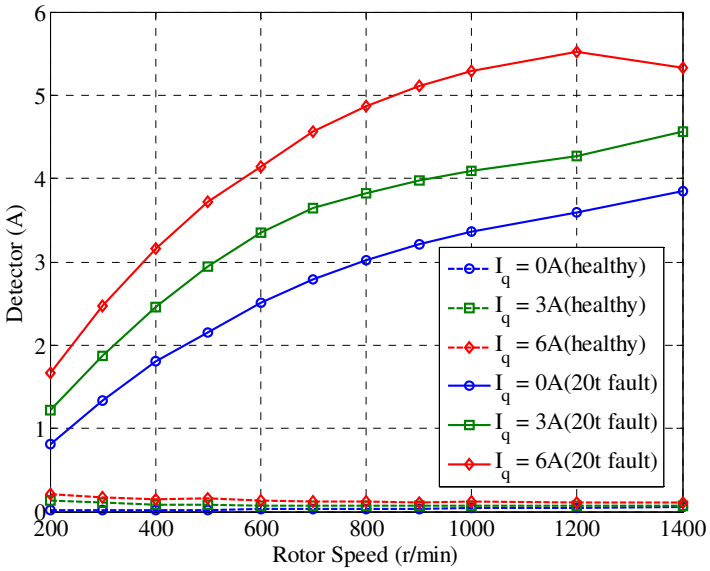

(b)

Fig. 5-47: Variation of fault detector output (measured) to varying loads and speeds (a) 2 turn fault, (b) 20 turn fault

Fig. 5-48(a) shows the residual current magnitudes under 2 turn fault at i_q =0A loading with varying speed. This is the worst case scenario for fault detection because line current is zero. It can be observed that at speeds >400 r/min it is possible to clearly detect the faulted phase (ph-4) by quantifying the maximum of all the residual magnitudes. Fig. 5-48(b) shows the residual current magnitudes under 20 turn fault at i_q

=0A loading with varying speed. It can be observed that at higher fault (20 turn) the faulted phase can be clearly identified even at very low speeds.

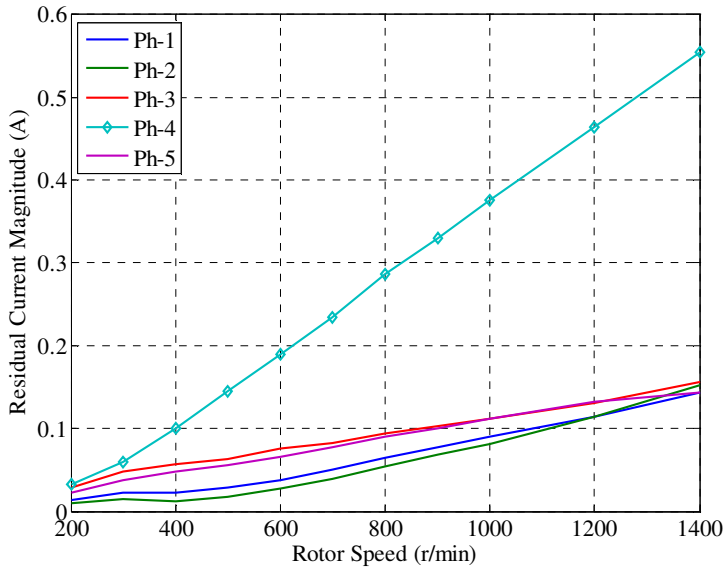

(a)

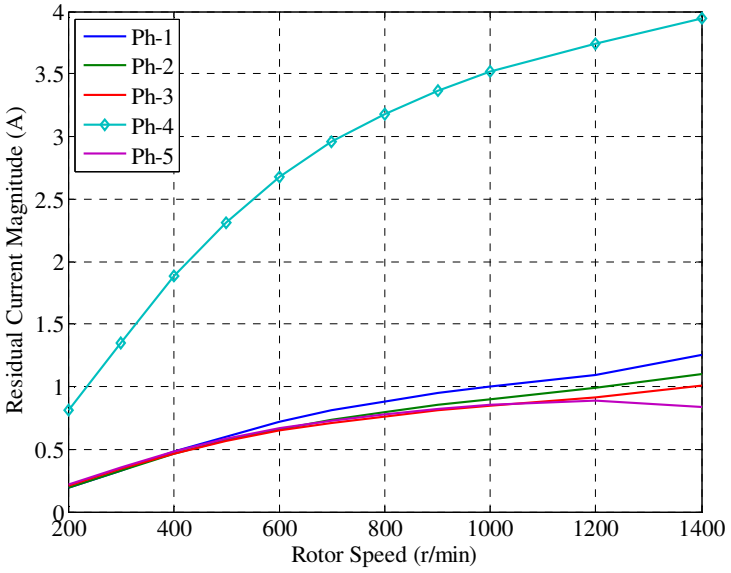

(b)

Fig. 5-48: Variation of residual current magnitude at i_q=0A and varying speed (a) 2 turn fault, (b) 20 turn fault. Ph-4 is the faulted phase.

Fig. 5-49(a) shows the effect of rotor speed and current loading on fault detection for HRC fault of 0.22Ω (+32% increase), in phase-4 under steady conditions. It can be observed that the output of the detector is highest at high load currents. This is expected result since the degree of unbalance is directly proportional to the current

flowing in the HRC fault. The other important aspect to note is that as rotor speed increases the detector output decreases. This is also an expected result, since the residual current analysis in (5.49) indicates an inverse relation to healthy motor impedance which increases with rotor speed/electrical frequency. Fig. 5-49(b) shows the effect of rotor speed and current loading on fault detection for HRC fault of 0.66Ω (+95% increase), in phase-4 under steady conditions. Since the fault resistance is higher it generates a higher signature, and consequently is easier to detect.

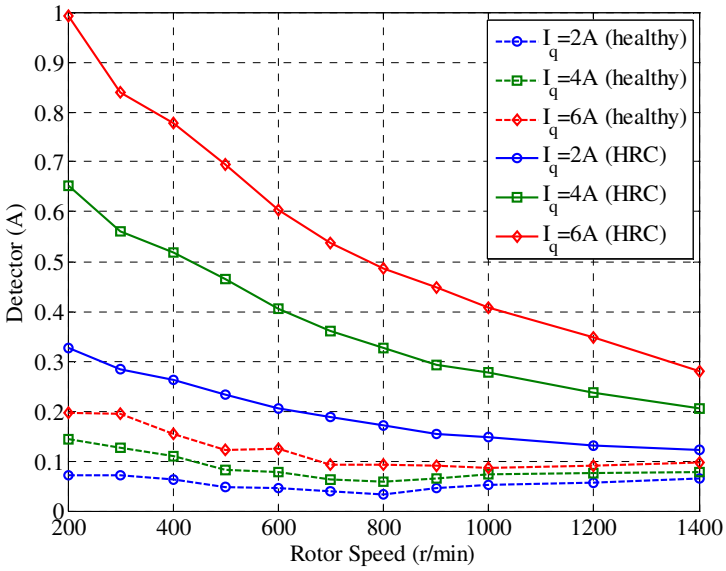

(a)

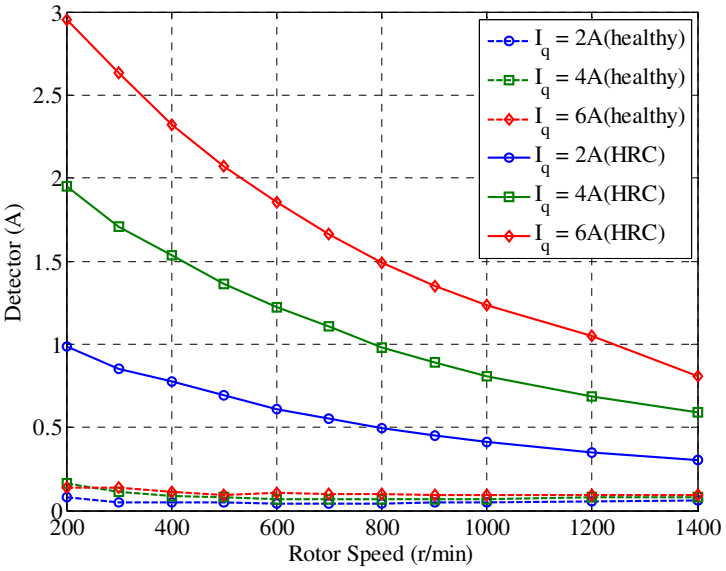

(b)

Fig. 5-49: Variation of fault detector output (measured) to varying loads and speeds (a) 0.22Ω HRC, (b) 0.66Ω HRC.

From Fig. 5-47 and Fig. 5-49 it can be concluded that fault signature increases with rotor speed for a turn fault and decreases for an HRC fault. This implies that the turn fault detection is sensitive at higher speeds and the HRC detection at lower speeds. Since HRC is not a critical fault demanding immediate action from the controller, the reduced sensitivity at high speed is acceptable.

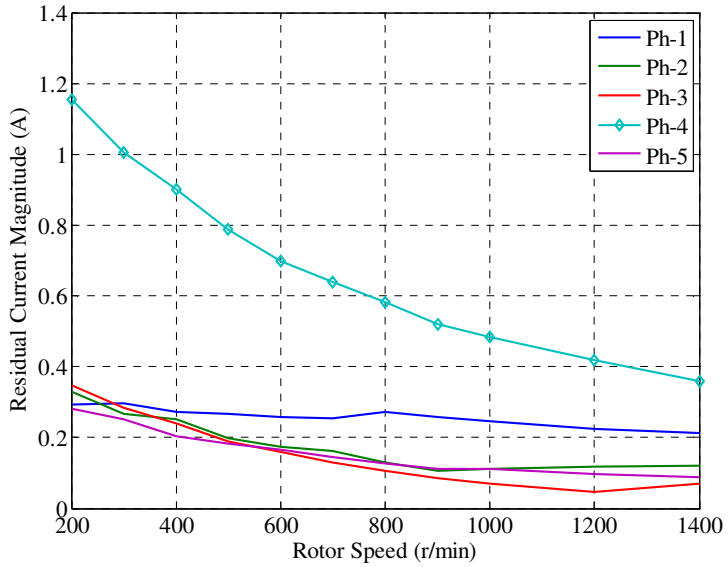

(a)

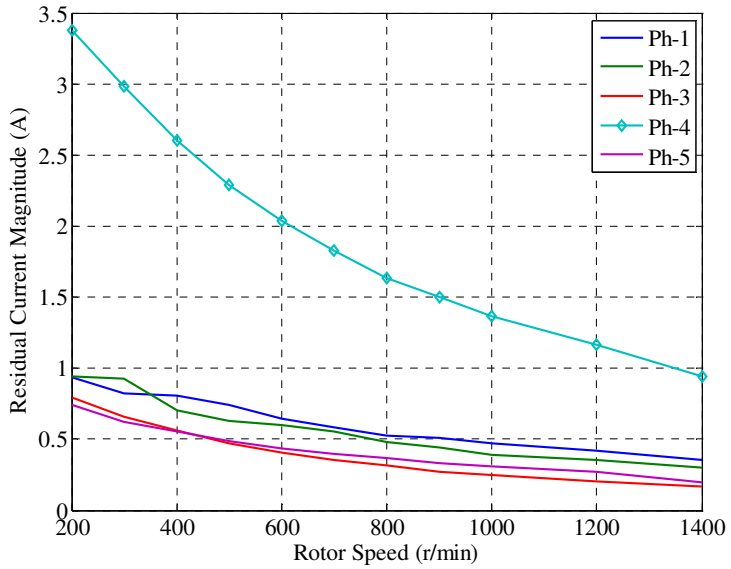

(b)

Fig. 5-50: Variation of residual current magnitude at i_q=6A and varying speed (a) 0.22Ω HRC, (b) 0.66Ω HRC. Ph-4 is the faulted phase

Fig. 5-50 (a) and Fig. 5-50 (b) shows the residual current magnitudes variation with i_q=6A under varying rotor for HRC fault of 0.22Ω (+32% increase), and 0.66Ω (+95% increase) in phase-4. It can be observed that the faulted phase (ph-4) can be clearly identified by quantifying the maximum of all the residual magnitudes and the detection is best at lower speed.

Fig. 5-51 shows the classifier output variation with loading and speed for 2 turn fault and 0.22Ω HRC fault. It can be seen that there exists a clear difference between 2 turn fault (close to 1) and HRC fault (close to 0). Therefore the classifier can distinguish turn fault and HRC fault enabling application of appropriate fault mitigation strategies.

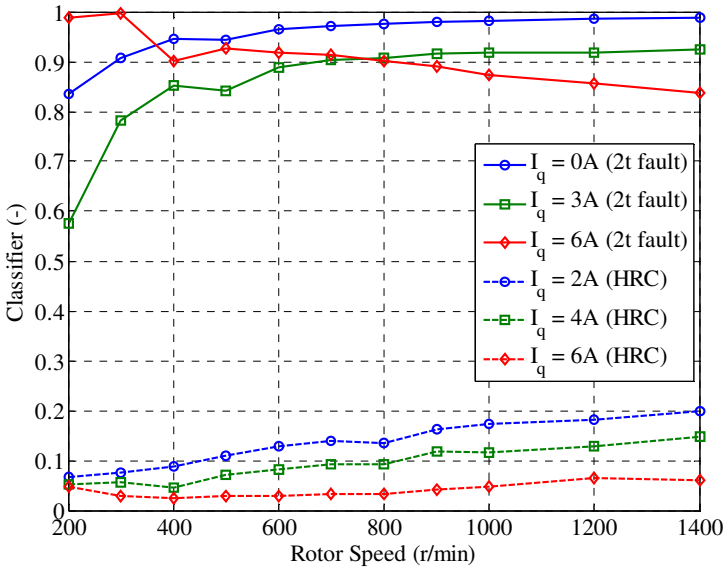

Fig. 5-51: Comparison of classifier output at different loading and speed with 2 turn fault and 0.22Ω HRC fault.

5.12 Extension to 3-phase IPM machines

As part of MotorBrain project, the turn fault detection for a triplex 3-phase 18slot 16-pole IPM machine was investigated in simulation. Fig. 5-52 shows the FE model of the machine with the faulted turn circled. The schematic of the one faulted phase set of the machine is shown in Fig. 5-53 and the parameters of the machine are given in Table 5-5.

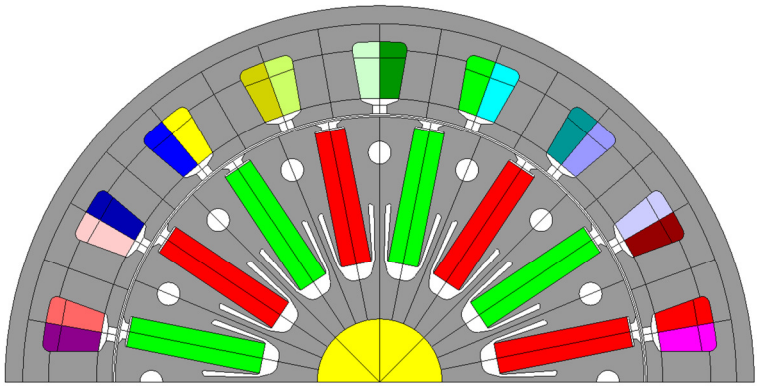

Fig. 5-52: 18-slot 16-pole spoke type IPM machine

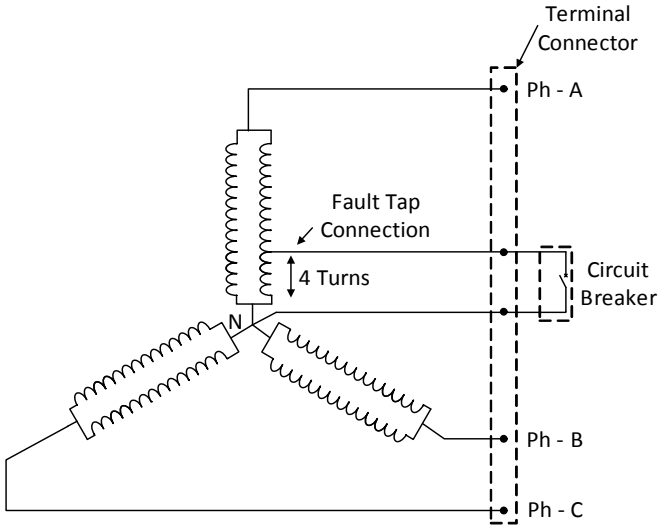

Fig. 5-53: Schematic of the 18-slot 16-pole IPM machine showing winding configuration for the faulted set.

Table 5-5: 18-slot, 16-pole IPM Machine Nominal Parameters

Parameter	**Value**	**Parameter**	**Value**
Rated Torque	92 Nm	Number of poles	16
Peak Torque	154 Nm	Number of phases	3x3
Base Speed	4000 r/min	Phase resistance	0.017Ω
Maximum Speed	11300 r/min	L_d (nominal)	0.47mH
Rated current	85A	L_q (nominal)	0.58mH
BEMF at max speed	467V	Total number of turns / coil	15

The machine is modelled using the similar technique as given in Chapter 3. The current to flux linkage mapping is obtained by varying the *dq* and fault currents to obtain the flux linkage lookup tables. To test the fault detection technique, only the faulted phase-set out of the 3 phase-sets is simulated. In order to perform turn fault detection, detection structure given by Fig. 5-54 is chosen. It is based on the residual current approach applied to a 3-phase system. However, there are a few key differences:

1. The motor model is based on 4th order Runge-Kutta method
2. Multi-notch filter is utilised for filtering as shown in Fig. 5-55 because of ease of implementation and tuning.

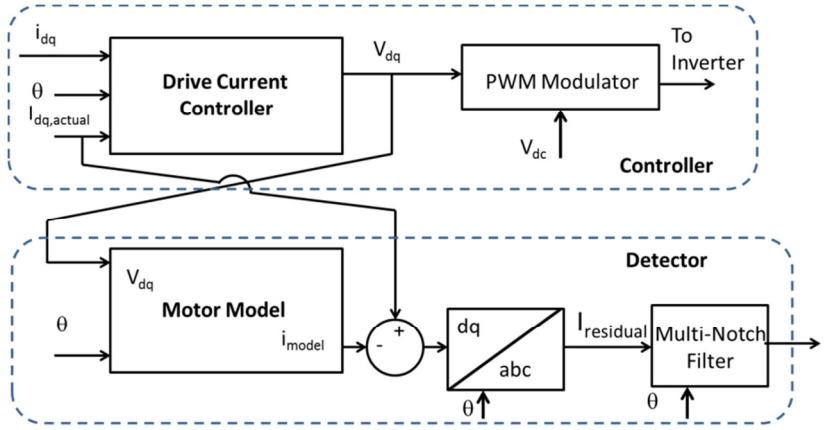

Fig. 5-54: Block diagram of the overall detection structure

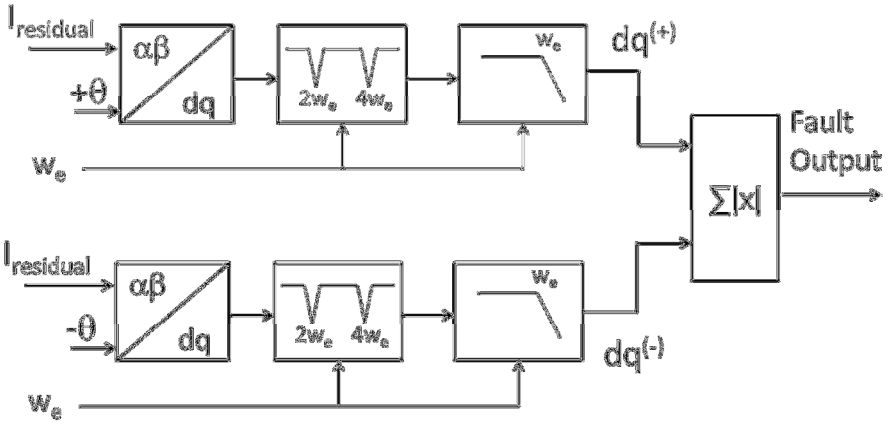

Fig. 5-55: Detector structure utilising multi-notch filter approach

To assess the performance of the turn fault detection, simulation test is first performed at motor speed of 1500 r/min. At 0.02s a step change of i_q (0-50A) is applied. Turn fault is initiated at 0.06s and removed at 0.11 sec. Fig. 5-56 shows the *dq* currents and the fault currents. It can be observed that there is a ripple in the *dq* axis current during fault. This is expected since the fault causes unbalance in the system and therefore suppression of the unbalance (2nd harmonic in *dq* frame) depends on the controller bandwidth.

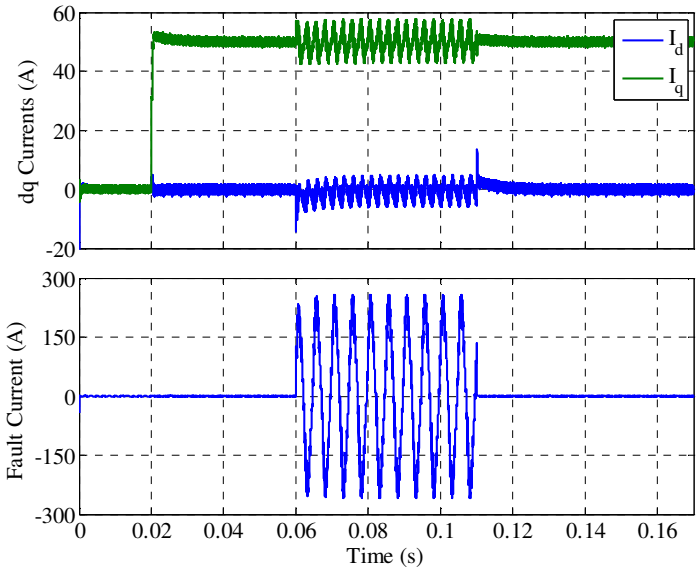

Fig. 5-56: *dq* and fault current (1500 r/min, i_q = 50A, turn fault (0.06s -> 0.11s))

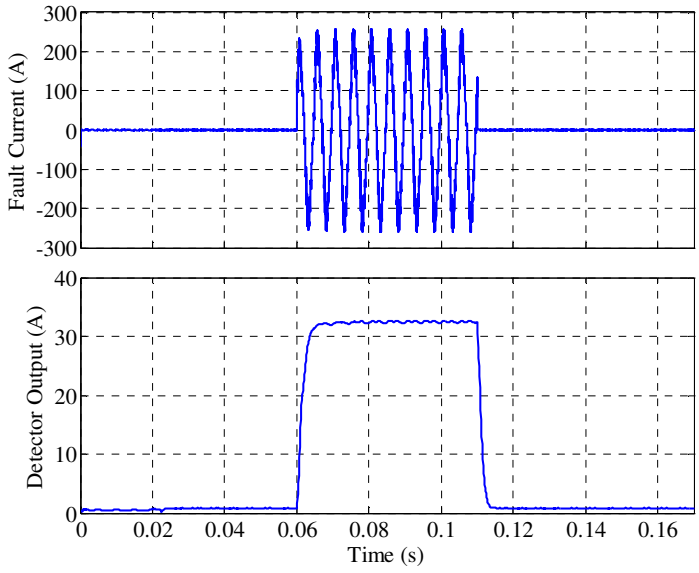

Fig. 5-57: Fundamental based Detector 1500 r/min, i_q = 50A, turn fault (0.06s -> 0.11s)

Fig. 5-57 shows the fundamental detector output and the fault current for the same conditions. It can be observed that the detector rejects the load current disturbance at 0.02s and picks up only during fault between 0.06 and 0.11s.

Fig. 5-58 shows the residual currents in *abc* frame at the time of fault initiation. It is to be noted that the faulted phase residual (phase-A) is in opposite phase to the other phases and is about 2 times the current in the healthy phases. This is expected result as given by (5.30). This particular property of the residual current enables the identification of the faulted phase (Ph-1).

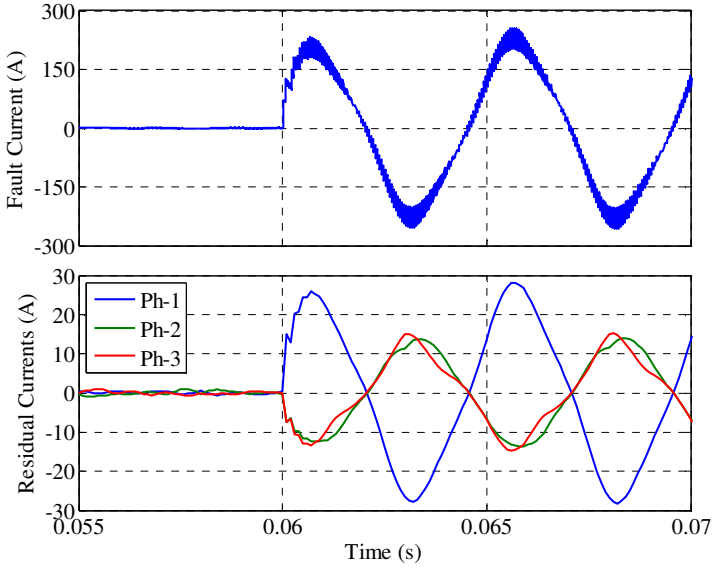

Fig. 5-58: Residual current based detector 1500 r/min, i_q = 50A, turn fault (0.06s -> 0.11s)

To further test the detector, turn fault is initiated at a different rotor speed of 3000 r/min. At 0.02s a step change of i_q (0-50A) is applied. Fault is initiated at 0.06s and removed at 0.11 sec. Fig. 5-59 shows the motor *dq* currents and the fault current. Fig. 5-60 shows the detector output and the fault current for the same conditions. It can be observed that the detector reject the load current disturbance at 0.02s and picks up only during fault between 0.06 and 0.11s.

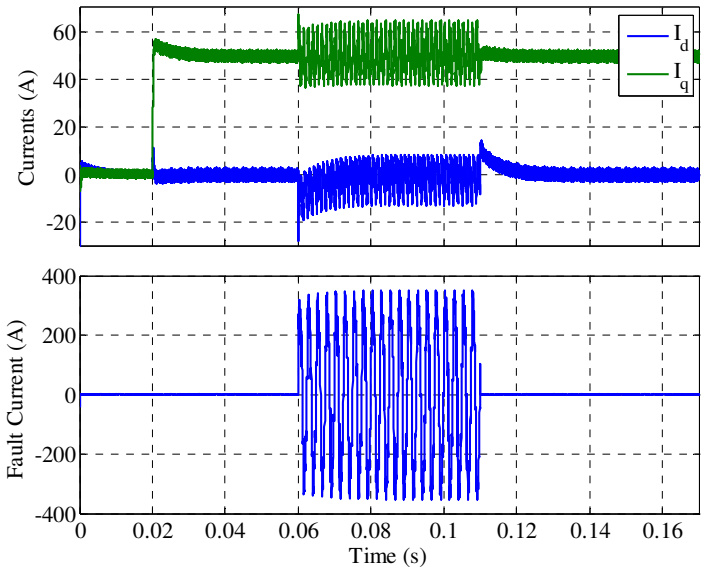

Fig. 5-59: Machine *dq* and fault currents (3000 r/min, i_q = 50A, turn fault (0.06s -> 0.11s))

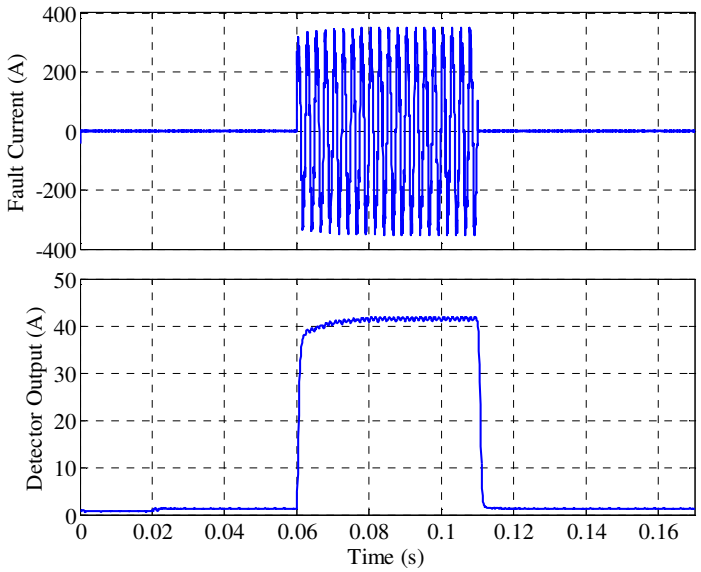

Fig. 5-60: Fault current and Detector output (3000 r/min, i_q = 50A, turn fault (0.06s -> 0.11s))

Fig. 5-61 shows the residual currents at the time of fault initiation. It is to be noted that the faulted phase residual (phase-1) is in phase opposition to the other phases and is about 2 times the current in the healthy phases. This is as expected from the residual current analysis.

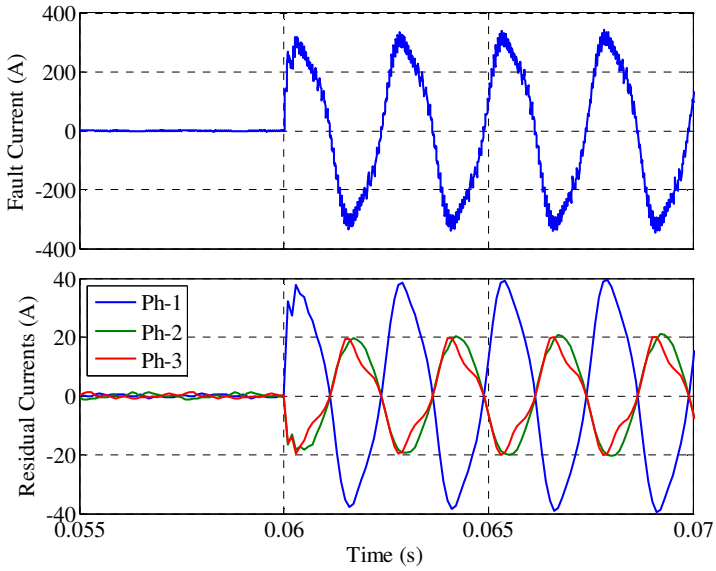

Fig. 5-61: Residual and fault currents (3000 r/min, i_q = 50A, turn fault(0.06s -> 0.11s))

It can be concluded from the simulation results that residual current method is also applicable to 3 phase IPM machines and can detect and localise the turn fault. It is to be noted that since the detector is model based, and since parameters of the 3-phase machine may be different from the FE simulation, an auto calibration was proposed along with the turn fault detector to acquire machine parameters in test.

The auto calibration algorithm is based on a simple concept that if a constant test current of known quantities is injected into the machine while the machine is held at a constant speed by the dynamometer machine parameters can be determined. It is known that in steady state, ignoring losses in the machine, the machine voltages can be expressed as (5.82). The machine parameters can be obtained by (5.83). It is to be noted that the voltages and currents should be averaged to remove any noise. The voltages referred to here are inverter command voltages.

$$\begin{aligned} V_d &= Ri_d - \omega_e L_q i_q \\ V_q &= Ri_q + \omega_e L_d i_d + \omega_e \psi_m \end{aligned} \tag{5.82}$$

$$\psi_m = \left.\frac{V_q}{\omega_e}\right|_{\substack{id=0\\iq=0}}$$

$$L_q = \left.\frac{-V_d}{\omega_e i_q}\right|_{\substack{id=0\\iq=40}} \tag{5.83}$$

$$R = \left.\frac{V_d}{i_d}\right|_{\substack{id=-40\\iq=0}}; \quad L_d = \left.\frac{V_q - \omega_e \psi_m}{\omega_e i_d}\right|_{\substack{id=-40\\iq=0}}$$

Fig. 5-62 shows the operation of the auto calibration and the fault detector. Auto calibration is performed until t = 0.45s. It is to be noted that when the model is not calibrated (t<0.45s) the detector output is high as shown in Fig. 5-62(b). This is expected since the machine parameters are different from the model parameters of the detector. Auto calibration algorithm generates 3 different current commands, (i_d= 0A, i_q= 0A), (i_d= 0A, i_q=20A) and (i_d= -20A, i_q= 0A) during the calibration sequence to determine the machine parameter. After 0.45s, the detector output is nearly zero and becomes high only when fault is applied (t=0.6-0.7s). It can be observed that a load step applied at 0.5s (i_q=0-40A) is completely rejected by the fault detector, implying correct parameter identification. Auto-calibration therefore can be utilised in a hardware setup wherein the actual machine parameters can deviate from that obtain from FE simulation, and can reduce the residual current under healthy operation in order to achieve adequate sensitivity in fault detection. For IPM machines which exhibit high magnetic saturation, a more sophisticated calibration, or online learning technique may be required to minimise the modelling error.

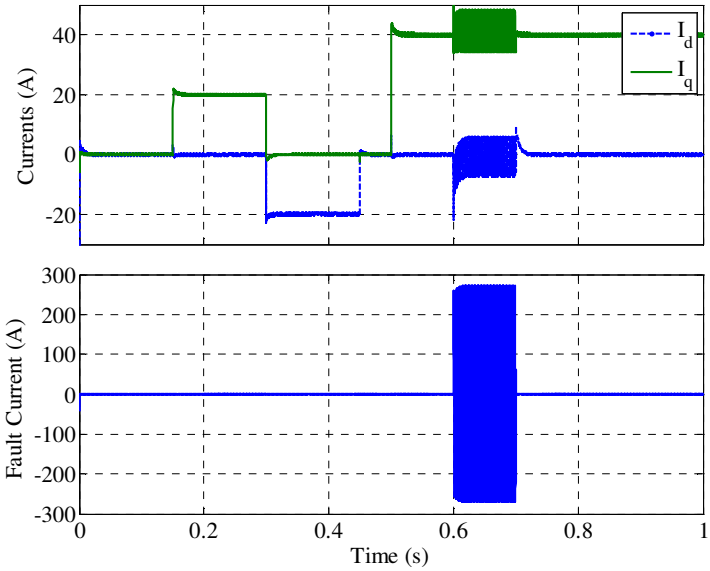

(a)

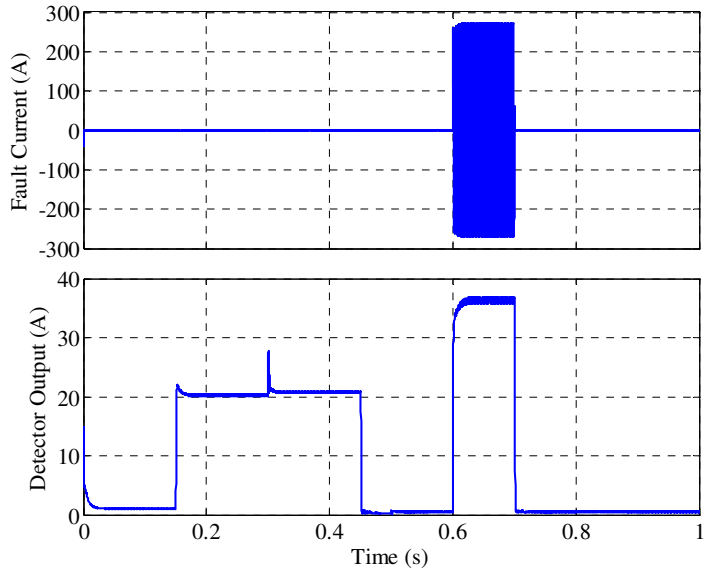

(b)

Fig. 5-62: Combined auto-calibration and fault detection. (a) Currents commands and fault current, (b) Fault current and detector response. Auto-calibration ends at 0.45s.

5.13 Conclusions

The chapter presents a combined fault detection scheme for inter-turn fault and high resistance connection. A thorough theoretical basis of the detection method is presented supported by real-time implementation of the fault detector. Extensive experimental data supports the analysis and proves that sensitive fault detection for

multi-phase SPM machines is possible. In addition the detection technique has been shown to be able to determine the faulted phase. This capability is crucial in multi-phase machines wherein identification of faulted phase and classification of the nature of fault can enable specific fault tolerant controls and mitigation strategies to be applied to keep the machine in operation rather than requiring a complete shutdown. This chapter also provides simulation studies performed to extend the approach to 3-phase IPM machines, which are subject to magnetic saturation in different operating conditions.

Chapter 6

Online Stator Turn Fault Detection Using PWM Ripple Current Measurement

The main contribution of this chapter is an online fault detection technique for inter-turn fault detection based on measurement of pulse width modulation (PWM) ripple current. The method uses the ripple current generated by the switching inverter as a means to detect inter-turn fault. High frequency impedance behaviour of healthy and faulted windings are analysed and modelled, and ripple current signature due to inter-turn faults is quantified. A simple analogue circuit is designed to extract the PWM ripple current using a band-pass filter and a root-mean-square (RMS) detector for fault detection. In addition, this method can also identify the faulted phase, which can be used for fault mitigation strategies. The method is tested experimentally on a five phase permanent magnet machine drive.

Major contents of this chapter were published by the author in [104].

6.1 Motivation

As explained in the previous chapter, inter-turn faults are one of the leading mechanisms to a complete winding failure, which in turn accounts for 21-37% of faults in electrical machines [7]–[11]. One of the observations in the test results presented in the previous chapter was the increase in ripple current most clearly observed in the fault current waveform. This implies that under fault the high frequency impedance of the machine changes. This chapter investigates utilising the change of switching ripple in the motor current for fault detection.

6.2 Literature Review

Stator inter-turn fault detection has been subject to intense investigation and numerous literatures exist on the topic. Detection schemes [94] can be broadly divided into fundamental quantity based [32], [33], [120]–[122] detection, high frequency based [21], [22], [123] detection and motor current signature analysis (MCSA) [19], [60]. Most of the methods under MCSA are computationally intensive since they rely on performing fast Fourier transformation (FFT) on stator currents to determine harmonic components and extract the fault signature. High frequency signal injection methods on the other hand, inject high frequency (HF) signal in the inverter voltage command and perform synchronous demodulation of the resultant currents in software to determine stator turn fault. In [21] a high frequency signal was injected in the *dq* control voltages and the negative sequence component of the high frequency currents so obtained is extracted in the *dq* frame to generate the fault indicator. In [22] the method of [21] is improved further by using lookup table based calibration of the *dq* high frequency signal in order to reduce the effect of magnetic saliency and saturation induced by load variation from affecting the detection. However, signal injection method introduces additional noise in the current and increases acoustic emissions of the motor-drive system [124], [125]. In addition, most of the methods in literature fail to identify the faulted phase which is of importance in a multi-phase machine in order to initiate fault mitigation and fault tolerant operation.

Most PM machines are fed through a pulse-width modulated (PWM) drive. The drive is a natural source of high frequency signal injection into the motor due to its switching. It is this inherent source of HF signal injection that is explored in this chapter for detection of turn fault. The proposed method uses the PWM ripple current generated by the drive to determine the presence of turn fault without the need to modify or inject additional HF signal [104]. The method is also able to identify the faulted phase which is essential to implement fault mitigation strategies.This chapter contributes to the body of knowledge in the following aspects:

1. Turn fault detection using PWM ripple current measurement.
2. Identification of faulted phase using the ripple current measurement.

6.3 Transient Machine Modelling under Stator Turn Fault

The machine under consideration is a 10-slot 12-pole, 5-phase surface permanent magnet (SPM) machine. Fig. 6-1 shows the geometry of the machine. Fig. 6-2 shows the schematic of a single winding of the machine under the turn fault condition with N_f faulted turns out of a total N number of turns. The parameters of the machine are given in Table 5-1. The switching and sampling frequency of the inverter is 10kHz.

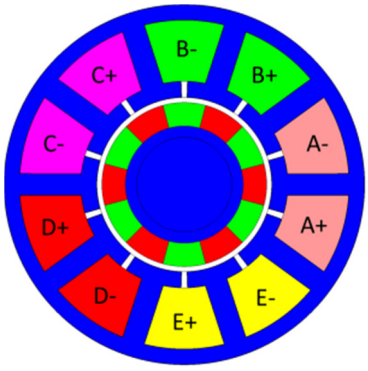

Fig. 6-1: Geometry of 10-slot, 12-pole SPM machine

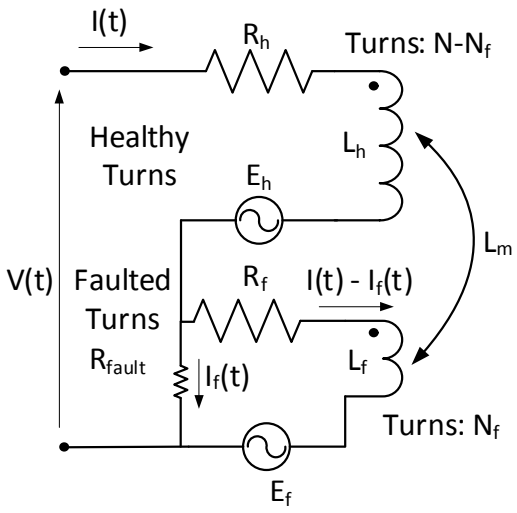

Fig. 6-2: Schematic of winding under turn fault

In order to evaluate the ripple current characteristics under PWM operation, it is necessary to determine the high frequency admittance of the winding under healthy and fault conditions. For the machine under study, the high frequency admittance can be obtained using (6.1) by setting the electromotive force (EMF) voltage components to zero in Fig. 6-2, where R_h, R_{f1}, L_h and L_f are the resistance and inductance of the healthy and fault turns, respectively and L_m is the mutual inductance between the two winding parts. R_{fault} *or* R_f is the external fault resistance and is assumed zero in this analysis for the sake of simplicity.

$$Y(j\omega) = \frac{I(j\omega)}{V(j\omega)} = \frac{1}{\left(R_h + j\omega L_h + \dfrac{\omega^2 L_m{}^2}{R_{f1} + j\omega L_f} \right)} \tag{6.1}$$

The parameters of the machine under healthy and fault conditions are given in Table 5-1 and Table 6-1. The parameters are derived using a similar procedure outlined in chapter 2 as explained in chapter 5. Since the machine under study employs a SPM topology in which saturation level is quite low, these parameters are constant. For machines with high level of saturation, the derivation is still valid given that the ripple current is small, and the parameters can be piece-wise linearized.

Table 6-1: Machine Data under Fault

Parameter	**Fault Condition**	
N_f	2 turn fault	20 turn fault
R_h	0.65Ω	0.46Ω
R_{fl}	0.021Ω	0.21Ω
L_h	2.6mH	1.3mH
L_f	2.8μH	0.28mH
L_m	83μH	0.6mH

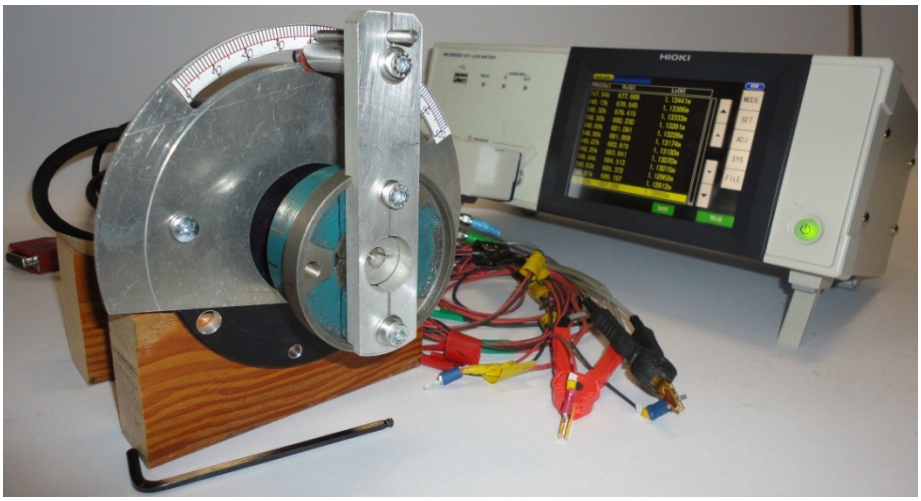

Fig. 6-3: Experimental setup for measurement of HF impedance

In deriving (6.1) the iron loss in the laminations, the eddy loss of the magnet and the skin effect in the winding coils was ignored. However, in a real machine these effects will affect the machine parameters especially at PWM ripple frequencies. Modelling these effects analytically can be quite cumbersome and inaccurate, and therefore an experimental measurement of the parameters is required. Fig. 6-3 shows the experimental setup wherein the machine rotor is locked and the winding resistance and inductance is measured using an impedance analyzer (Hioki IM3533-01).

Fig. 6-4 shows the variation of equivalent series resistance and inductance of a healthy winding measured by the impedance analyser under locked rotor condition. The variation occurs due to the interaction of various loss resistances in series and parallel combination with the nominal resistance and inductance of the winding when excitation frequency is varied.

In order to ascertain the dependence of high frequency admittance to rotor position, the rotor was locked at different electrical angles and a frequency sweep performed on the stator coil of phase-4 using the LCR meter. Fig. 6-5 shows the admittance plot of the coil for various rotor positions. It can be observed that rotor position has minimal effect on the measured admittance and is consequently neglected in the rest of the chapter.

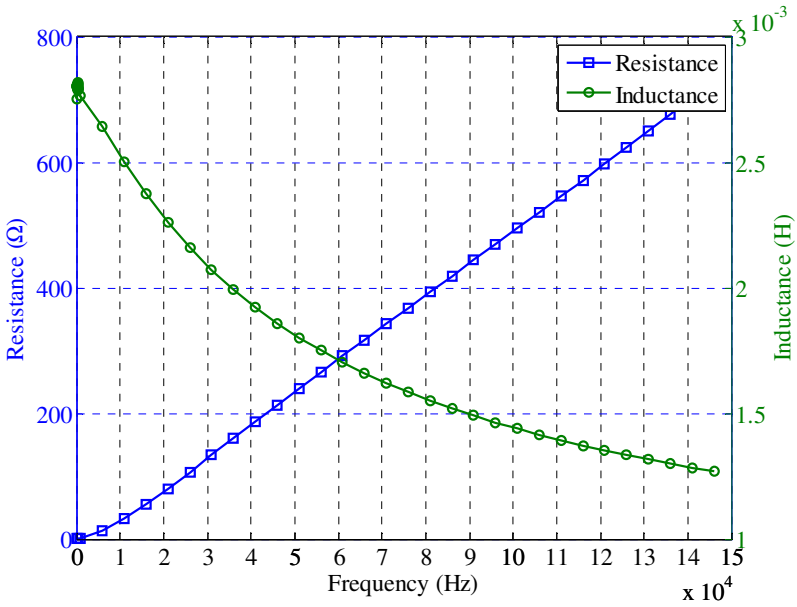

Fig. 6-4: Equivalent terminal resistance and inductance of healthy winding under locked rotor condition

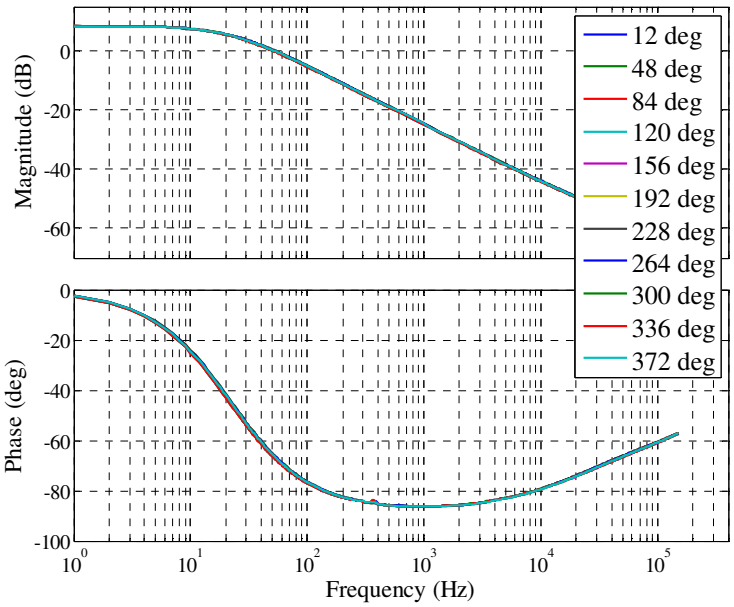

Fig. 6-5: Measured healthy winding admittance (Y) plot for varying rotor position (electrical)

Fig. 6-6 shows the comparison of the theoretical and experimentally measured locked rotor admittance of the winding under healthy and fault condition. The theoretical plot is obtained by using (6.1) and the parameters from Table 5-1 and Table 6-1. It can be observed that under the fault conditions the admittance increases

particularly in the frequency range of 10-20 kHz compared to healthy condition. It is also to be noted that the admittance predicted by theory is different from that obtained from experiments and is especially evident in case of 2-turn fault. The difference between the theoretical and measured admittance is expected and attributed to extra impedance introduced by the external leads to create the fault, and iron losses (eddy, hysteresis loss) as well as high frequency losses due to skin and proximity effects in the measured data which is not accounted for in the simple theoretical model. Also, as the number of faulted turn increases from 0 (healthy) to 2 turns and finally to 20 turn the admittance progressively increases above 10 kHz. Higher admittance translates to lower impedance and hence higher currents for the same voltage. It is to be observed that although there is difference between experimental and simplified theoretical predictions both the measurement and prediction points towards an increase of high frequency admittance and this is due to the shorted turns which reduce the overall impedance of the winding.

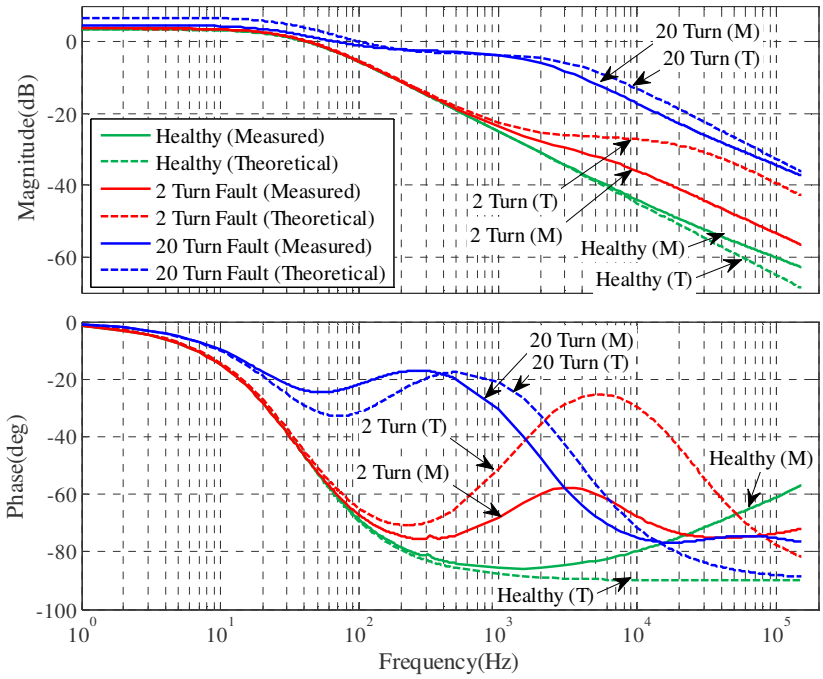

Fig. 6-6: Admittance (Y) magnitude and phase of winding under healthy, 2 turn and 20 turn fault. Theoretical (T) – dashed, Measured (M) – solid

Therefore, if the motor can be excited with a voltage in the frequency range of 10 kHz-20 kHz, the measured current will show an increase under fault condition which can be used as a measure to detect turn fault. A PM motor is usually fed from a PWM

drive which generates not only the fundamental voltage for the motor, but also switching voltage ripple at the terminals. The resultant PWM ripple current can be used as detector for inter-turn faults. For the purpose of simulation a sine-PWM drive, with a switching frequency of 10 kHz is assumed.

In order to model the winding behaviour to be close to the actual physical measurements, a hybrid modelling approach is employed. This entails using the impedance/admittance data obtained from experimental measurement and combining it with the analytical model to obtain a more accurate representation of the actual circuit condition. In order to use the experimental data in simulation, the experimental measurement is fitted with a 5th order transfer function as given by (6.2) using least squares fitting to obtain $Y_{f,expt}(s)$ and $Y_{h,expt}(s)$ for faulted and healthy winding respectively.

$$Y(s)=\frac{b_5s^5+b_4s^4+b_3s^3+b_2s^2+b_1s^1+b_0}{a_5s^5+a_4s^4+a_3s^3+a_2s^2+a_1s^1+a_0} \tag{6.2}$$

Fig. 6-7 and Fig. 6-8 show the transfer function fitting for healthy condition and for 2-turn and 20-turn short circuit conditions, respectively. The circuit equations of a generic faulted winding as shown in Fig. 6-2 can be expressed in *s* domain and are given by (6.3)-(6.4). I(s)-I_f(s) can be eliminated from the voltage equation (6.3) to obtain (6.5)-(6.6).

$$R_{fault}I_f(s)=\left(R_{f1}+sL_f\right)\left(I(s)-I_f(s)\right)+sL_mI(s)+E_f(s) \tag{6.3}$$

$$V(s)=\left(R_h+sL_h\right)I(s)+sL_m\left(I(s)-I_f(s)\right)+E_h(s)+R_{fault}I_f(s) \tag{6.4}$$

$$\begin{aligned}V(s)=&\frac{R_{fault}-sL_m}{sL_f+R_{f1}+R_{fault}}E_f(s)+E_h(s)\\&+I(s)\left(R_h+s\left(L_h+L_m\right)+\frac{\left(R_{fault}-sL_m\right)\left(s\left(L_f+L_m\right)+R_{f1}\right)}{sL_f+R_{f1}+R_{fault}}\right)\end{aligned} \tag{6.5}$$

$$\Rightarrow V(s)=\frac{1}{Y_f(s)}I(s)+\frac{R_{fault}-sL_m}{sL_f+R_{f1}+R_{fault}}E_f(s)+E_h(s) \tag{6.6}$$

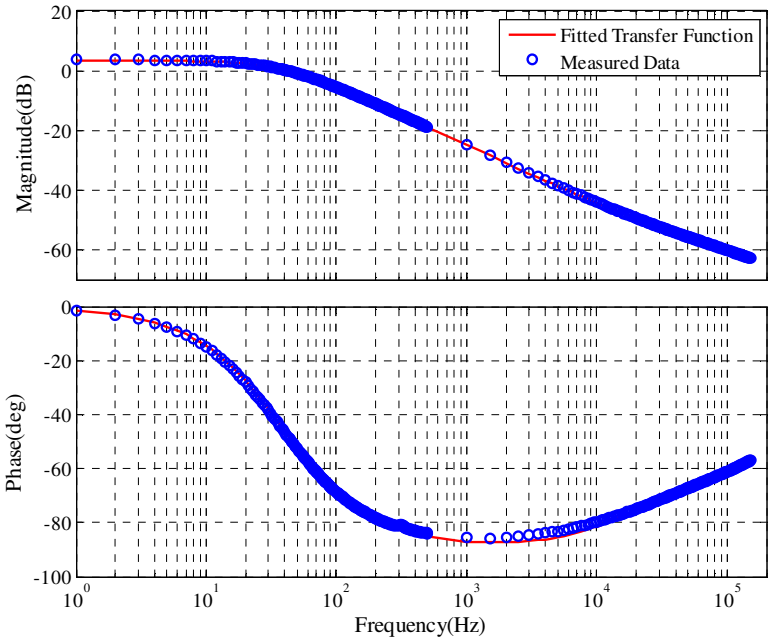

Fig. 6-7: Fitted Admittance Function ($Y_{h,expt}(s)$) for Healthy Condition

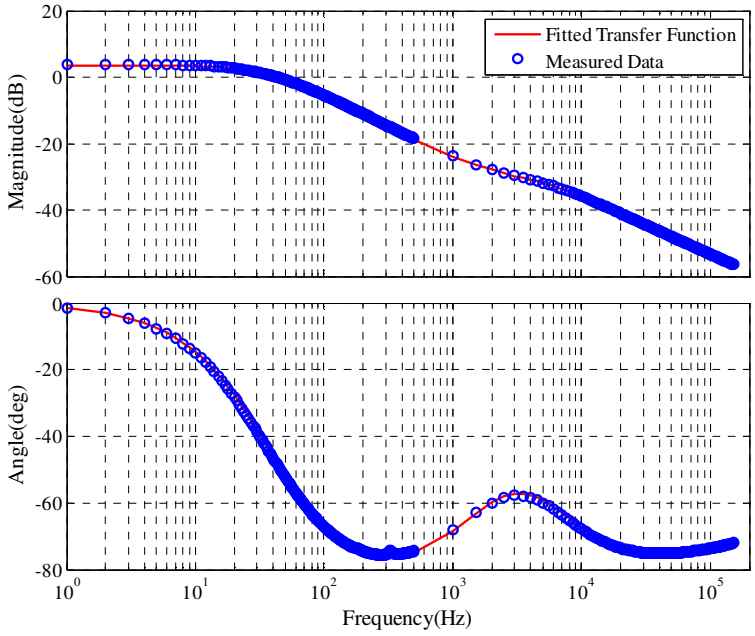

(a)

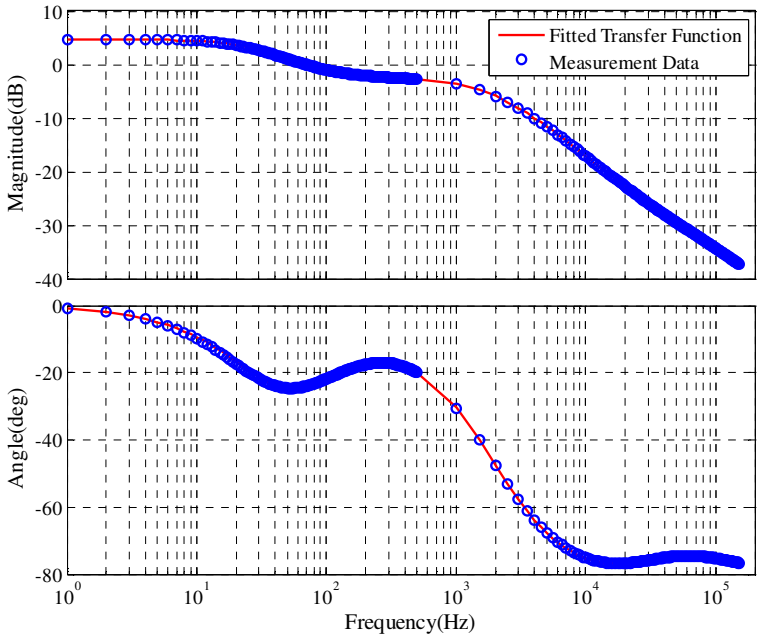

(b)

Fig. 6-8: Fitted Admittance function ($Y_{f,expt}(s)$) for (a) 2 turn and (b) 20 turn fault condition

Since the measured winding admittance is a high order transfer function, the model equation needs to be modified to account for the high frequency losses. A close look at (6.6) reveals that the first term corresponds both to the high frequency and low frequency admittance ($Y_f(s)$), whereas the other two terms are only related to the back-EMF components. Hence, it is possible to substitute the experimentally derived admittance instead of the theoretically derived one, resulting in the hybrid model equation for the faulted phase in (6.7). Therefore, (6.7) contains a part of parameters obtained through experiment and the rest is calculated from theoretical model, and is therefore referred to as a hybrid model.

$$V(s) = \frac{1}{Y_{f,\text{expt}}(s)} I(s) + \frac{R_{fault} - sL_m}{sL_f + R_{f1} + R_{fault}} E_f(s) + E_h(s) \tag{6.7}$$

In the 5-phase experimental motor, the winding fault is assumed to occur in phase 4 as shown in Fig. 6-9. Thus, (6.7) can be re-written as (6.8) noting that $E_h = E_i - E_f$ where E_i is the healthy back-EMF of the i^{th} phase. Zero sequence voltage (V_{nN}) is added into (6.8)-(6.9) to account for the fact that the voltages generated by the inverter are referred with respect to the negative DC supply N while the phase voltages are referred to the floating neutral 'n' of the motor. The model for other healthy windings

can be written as (6.9). In order to simulate the system the zero sequence voltage V_{nN} needs to be eliminated from the model equations. V_{nN} can be calculated by summing (6.8)-(6.9) over all phases, and noting that the sum of the phase currents is zero, to obtain (6.10). Substituting (6.10) back into (6.8)-(6.9), the final model equations (6.11)-(6.12) can be obtained.

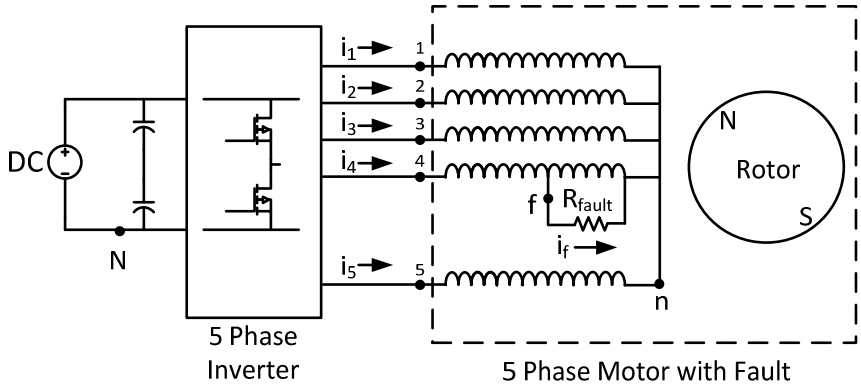

Fig. 6-9: Schematic representation of 5-phase SPM machine with turn fault on a single phase

$$V_{iN}(s)=\frac{1}{Y_{f,\text{expt}}(s)}I_i(s)+\frac{R_{fault}-sL_m}{sL_f+R_{f1}+R_{fault}}E_f(s)+E_i(s)-E_f(s)+V_{nN} \tag{6.8}$$

$$V_{iN}(s)=\frac{1}{Y_{h,\text{expt}}(s)}I_i(s)+E_i(s)+V_{nN}\ ;\ \forall i\neq 4 \tag{6.9}$$

$$\begin{aligned}5V_{nN}=&-\left(\frac{1}{Y_{f,\text{expt}}(s)}-\frac{1}{Y_{h,\text{expt}}(s)}\right)I_4(s)-\frac{R_{fault}-sL_m}{sL_f+R_{f1}+R_{fault}}E_f(s)\\&+E_f(s)+\sum_{i=1}^{5}V_{iN}(s)\end{aligned} \tag{6.10}$$

$$\begin{aligned}V_{iN}(s)=&\left(\frac{4}{5}\frac{1}{Y_{f,\text{expt}}(s)}+\frac{1}{5}\frac{1}{Y_{h,\text{expt}}(s)}\right)I_i(s)-\frac{4}{5}\frac{sL_m-R_{fault}}{sL_f+R_{f1}+R_{fault}}E_f(s)\\&+E_i(s)-\frac{4}{5}E_f(s)+\frac{1}{5}\sum_{i=1}^{5}V_{iN}(s);\ i=4\end{aligned} \tag{6.11}$$

$$\begin{aligned}V_{iN}(s)=&\frac{1}{Y_{h,\text{expt}}(s)}I_i(s)+\frac{1}{5}\left(\frac{sL_m-R_{fault}}{sL_f+R_{f1}+R_{fault}}+1\right)E_f(s)+E_i(s)\\&-\frac{1}{5}\left(\frac{1}{Y_{f,\text{expt}}(s)}-\frac{1}{Y_{h,\text{expt}}(s)}\right)I_4(s)+\frac{1}{5}\sum_{i=1}^{5}V_{iN}(s)\ ;\forall i\neq 4\end{aligned} \tag{6.12}$$

6.4 PWM Ripple Current Based Detector Design

In order to extract the high frequency current, first, an appropriate frequency band needs to be selected. In order to aid the design process, the harmonic currents can be analytically calculated under different operating conditions in steady state assuming ideal sine PWM. The PWM harmonic voltages for sine triangle modulation can be calculated using (6.13) [126], where ω_f and ω_c is the angular frequency of the fundamental and carrier respectively, J_n corresponds to the nth order Bessel function of the first kind n and m are the harmonic orders of ω_f and ω_c respectively and V_{dc} is set as 140V for the calculation, which corresponds to the highest possible DC link voltage of the test inverter. Fig. 6-10 shows a typical frequency spectrum plot of only the harmonic voltages obtained using (6.13) at modulation index of 0.9 and a fundamental and carrier frequency of 300 Hz and 10kHz respectively. Harmonic line currents can then be calculated using the line voltage equation as given in (6.14).

$$\begin{aligned} V_{i,h}(t) &= \frac{2V_{dc}}{\pi}\sum_{m=1}^{\infty}\frac{1}{m}J_0\left(m\frac{\pi}{2}M_i\right)\cos(m\omega_c t)\sin\left(m\frac{\pi}{2}\right) \\ &+2\frac{V_{dc}}{\pi}\sum_{m=1}^{\infty}\sum_{n=1}^{\infty}\left[\begin{array}{l}\frac{1}{m}J_n\left(m\frac{\pi}{2}M_i\right)\cos\left(m\omega_c t+n\left(\omega_f t+\theta_i\right)\right)\\ .\sin\left((m+n)\frac{\pi}{2}\right)\end{array}\right] \end{aligned} \tag{6.13}$$

$$\begin{bmatrix} V_{1,h}-V_{2,h} \\ V_{2,h}-V_{3,h} \\ V_{3,h}-V_{4,h} \\ V_{4,h}-V_{5,h} \end{bmatrix} = \begin{bmatrix} Z_1 & -Z_2 & 0 & 0 \\ 0 & Z_2 & -Z_3 & 0 \\ 0 & 0 & Z_3 & -Z_4 \\ Z_5 & Z_5 & Z_5 & Z_4+Z_5 \end{bmatrix} \begin{bmatrix} I_{1,h} \\ I_{2,h} \\ I_{3,h} \\ I_{4,h} \end{bmatrix} \tag{6.14}$$

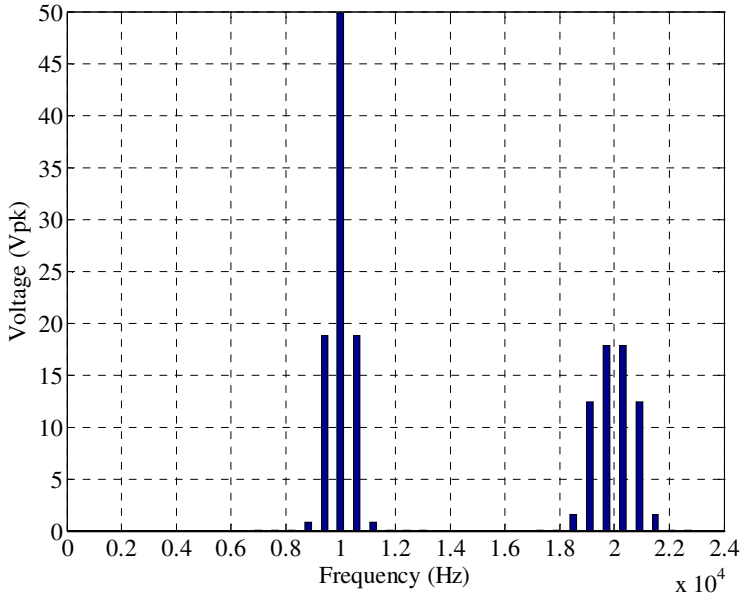

Fig. 6-10: Harmonic voltage spectrum of a sine-PWM inverter leg w.r.t negative DC supply rail at modulation index = 0.9, V_{dc}=140V, fundamental frequency (ω_f) = 2π.300 rad.s^{-1}

Fig. 6-11(a) shows the RMS harmonic current plots for each phase when phase 4 has a 2-turn fault at the maximum current of 6A when only 10 kHz carrier frequency sidebands are considered and Fig. 6-11(b) shows the RMS harmonic current plots when both 10 kHz and 20 kHz carrier frequency sidebands are considered.

It is evident from the plots that by considering both the 10 kHz and 20 kHz current ripple a greater magnitude and separation between the faulted phase and healthy phases can be obtained specially in low speed range. This will also improve signal to noise ratio. Thus, a pass-band of 10-20 kHz is selected for optimal detection of fault. The separation in RMS current ripple between faulted and healthy phases allow for easy identification of fault. It should be noted that the harmonic voltages and hence the harmonic currents are a function of modulation index and therefore as speed or load change the harmonic currents also vary.

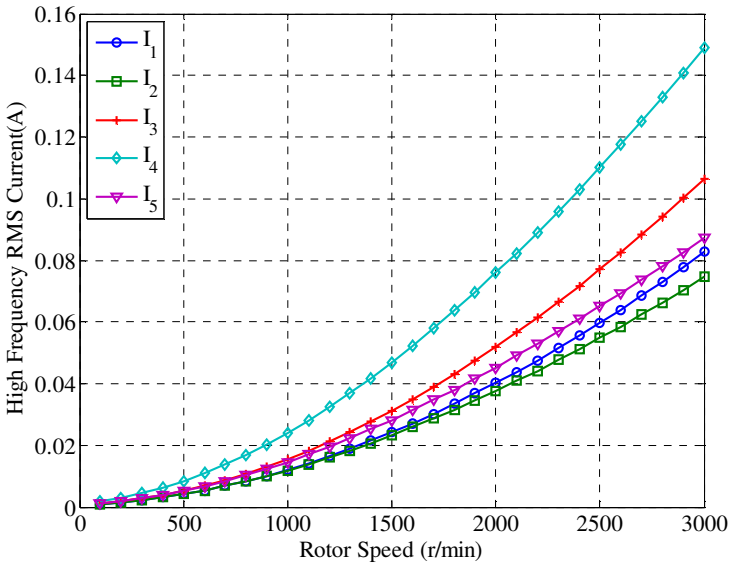

(a)

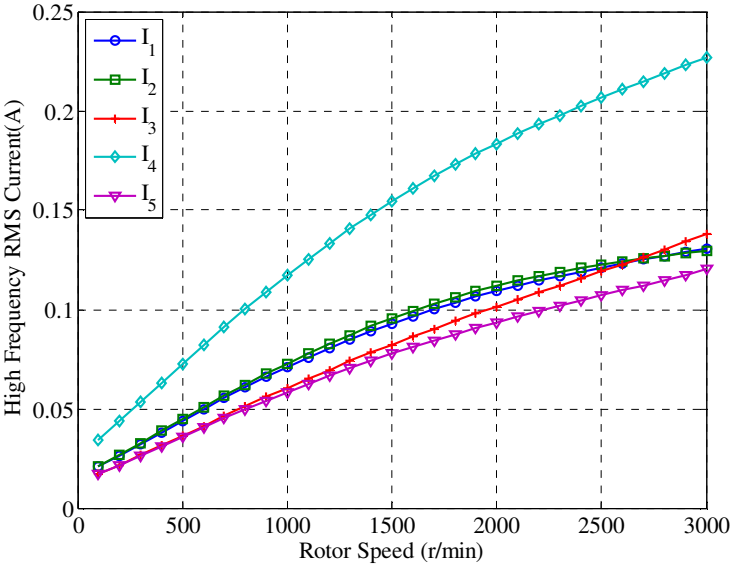

(b)

Fig. 6-11: RMS harmonic current with 2 turn fault with V_{dc} = 140V considering (a) only 10kHz carrier and sidebands, (b) 10kHz and 20kHz carrier frequency harmonics and sidebands.

Extraction of harmonic currents can be done in many different ways. One direct approach is the use of high speed sampling of the stator current waveform and application of signal processing to extract the harmonics. However, the ripple current is very small compared to the fundamental current and therefore the ADC employed would have to have a high resolution (>16 bits) to be able to measure the PWM ripple current accurately. Moreover, the sampling frequency of the ADC has to be at least 5-10

times the highest ripple current frequency and the corner frequency of the anti-alias filter has to be increased accordingly. Therefore, although this approach has the benefit of flexibility of application of advanced signal processing to extract harmonic currents it requires high speed, high resolution ADC's and advanced DSP processor to perform the signal acquisition and processing.

Due to processing limitations of the control hardware, an alternate approach is employed, wherein the RMS value of the PWM ripple current is obtained by using an analog circuit. RMS ripple current so extracted is of low frequency and can be easily sampled by the DSP using the same ADC sample rate (10 kHz) as that employed for current controller. The analog signal processing chain is shown in Fig. 6-12, consisting of a second order band-pass filter, RMS detector and output buffer. The band-pass (BP) filter must provide sufficient attenuation at fundamental frequency to prevent changes in fundamental current from affecting the result of the RMS detector. For the particular motor, a stop-band attenuation of -38dB (at 300Hz) is found to be adequate to remove the fundamental current influence. The pass-band gain of 20 dB is found to be sufficient for the detection. The bode gain plot of the BP filter is given in Fig. 6-13. The output buffer provides a further gain of +26dB.

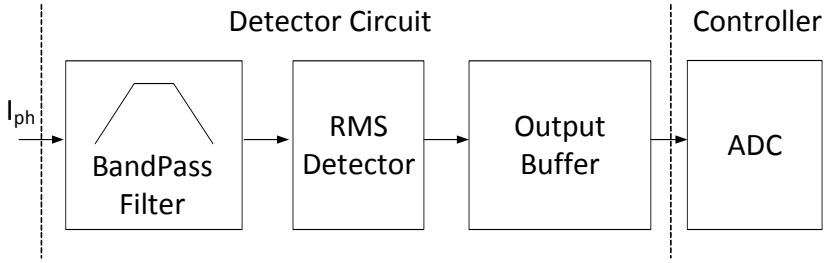

Fig. 6-12: HF detection signal processing chain. ADC sampling rate is 10 kHz.

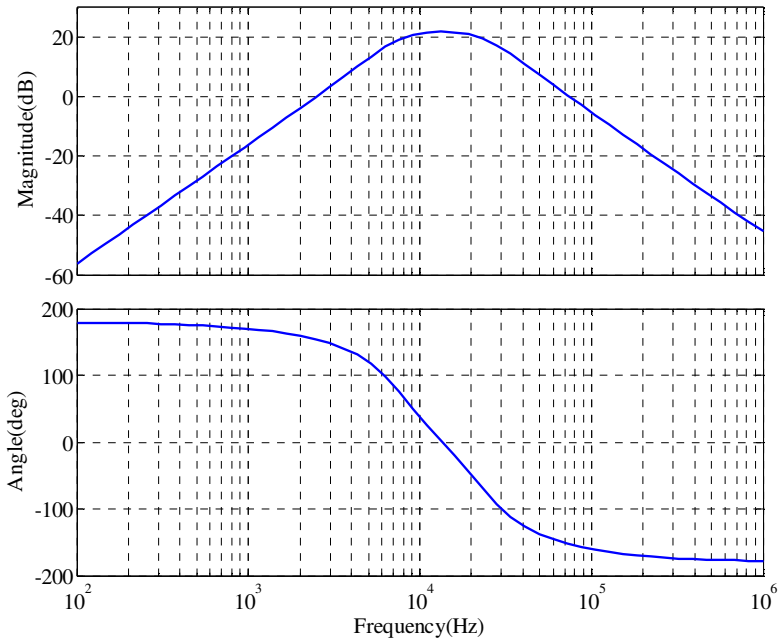

Fig. 6-13: Band-pass Filter Bode Plot

6.5 Circuit Implementation of the Detector

Fig. 6-14 shows the schematic of the analog signal processing circuit. The current signal from the transducer is first fed to the high pass filter (HPF) U1 and then through the low pass filter (LPF) U2 into the RMS detector U3 and finally into the ADC buffer U4. The LEM current sensor selected for the inverter is LTS-25P which gives a unipolar output and therefore the entire HF signal chain is designed to operate on unipolar supply. To realize the LPF and HPF transfer functions multiple-feedback topology is used. OPA364 is selected as the operational amplifier (opamp) for the circuit due to its excellent BW and low offset voltage and is suitable for unipolar circuit realization. The RMS detector is LTC1968 which is a precision wide bandwidth, RMS-to-DC converter from Linear Technology [127]. LTC1968 has a differential input range of 1Vpk and to avoid saturating the RMS detector under worse case fault, a gain of 20dB is selected for the band-pass divided equally over the HPF and LPF. Finally the ADC buffer provides additional gain of +26dB on the detected RMS value. A point to be noted for the signal chain is that the sequence of the block in the chain is critical to obtaining the desired performance. For example, swapping the position of HPF and LPF in the signal chain would saturate the opamps in the circuit although the transfer function of the circuit would have remained unaltered. This is because the LPF will pass

the fundamental current signal with a gain of +10dB and will saturate the opamps in the circuit.

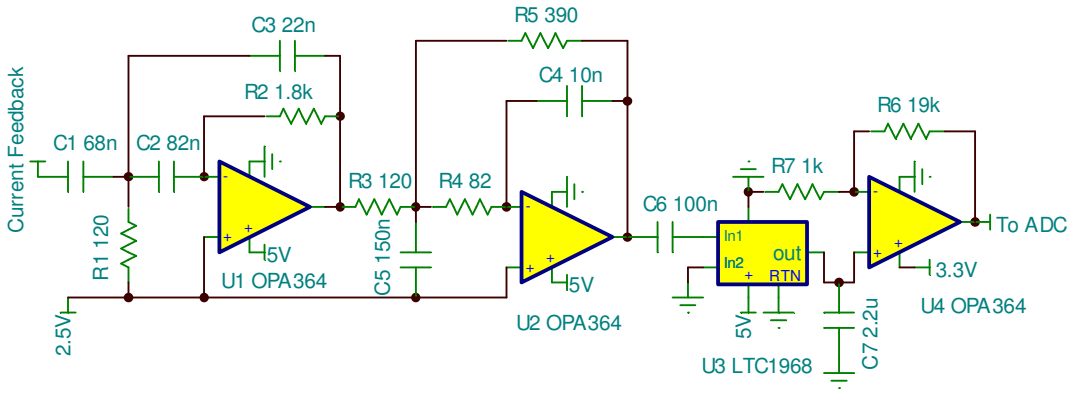

Fig. 6-14: Detector Circuit Implementation

6.6 Simulation Results

Fig. 6-15 shows the simulation results obtained from the model derived in the foregoing section connected to a current controlled voltage source inverter at rotor speed of 500 r/min with i_q = 6A under a 2 turn fault condition with V_{dc} = 60V. Standard *dq* based current control as employed in [118] is utilized to control the fundamental current. The difference in high frequency ripple can be observed in the actual phase current plots, and is clearly identifiable in the detector output shown in Fig. 6-16, where phase -4 shows a higher output than the rest of the phases and hence is identified as the phase with fault. The ripple in the detector output is caused by the currents in sidebands of the carrier frequency which give rise to a beat frequency at twice the fundamental frequency.

Fig. 6-17 shows simulation results obtained at rotor speed of 1000 r/min with i_q = 6A under 20 turn fault condition with V_{dc} = 60V. The phase currents are slightly unbalanced and this is expected since 20 turn fault introduces unbalance which cannot be completely compensated using conventional positive sequence *dq* controller. The difference in the ripple current is quite apparent and is expected at higher speeds and higher fault ratios. Fig. 6-18 shows the detector output and phase 4 can be clearly identified.

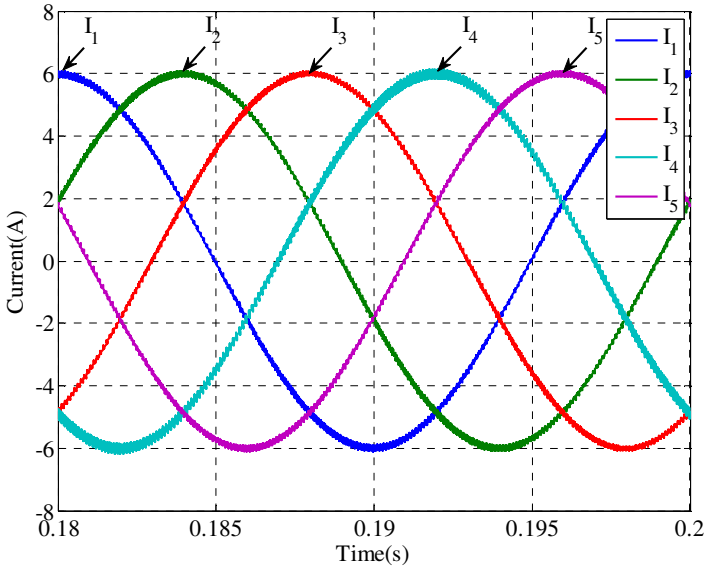

Fig. 6-15: Simulated phase currents with a 2 turn fault in phase-4 at rotor speed of 500 r/min.

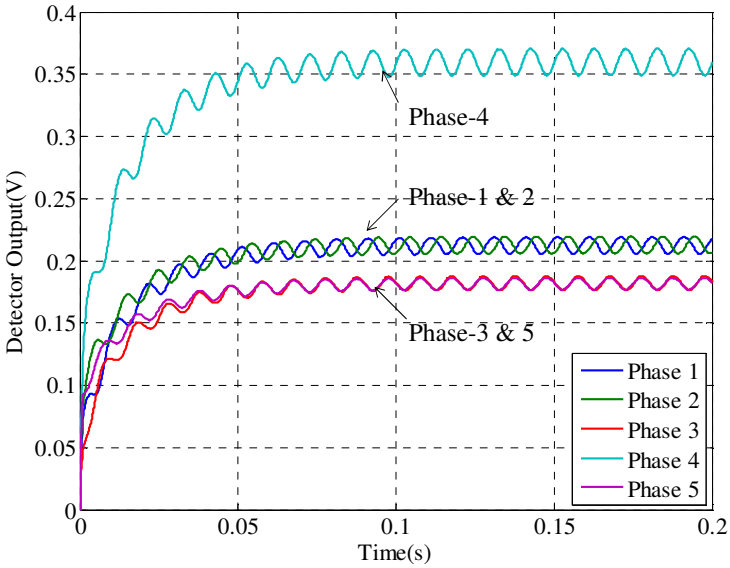

Fig. 6-16: Simulated detector output with a 2 turn fault in phase-4 at rotor speed of 500 r/min.

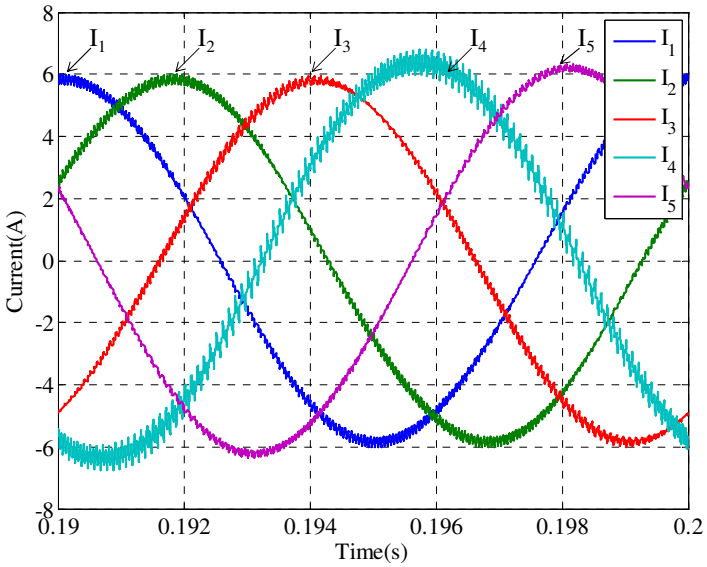

Fig. 6-17: Simulated phase currents with a 20 turn fault in phase-4 at rotor speed of 1000 r/min.

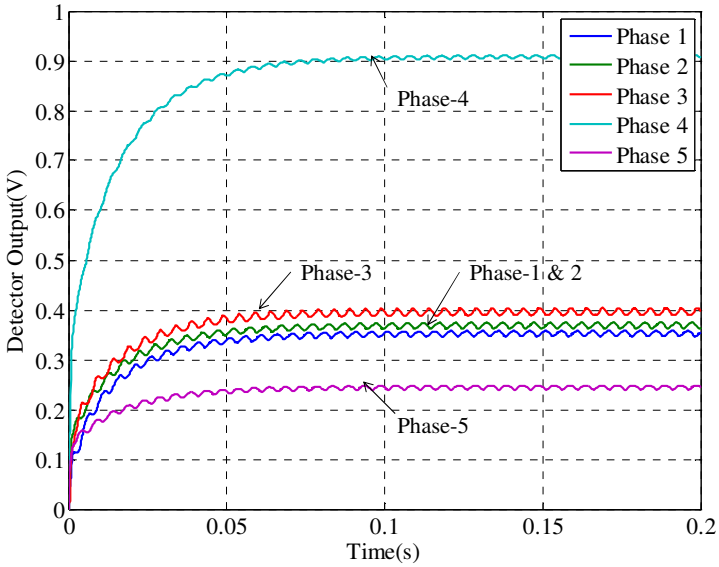

Fig. 6-18: Simulated detector output with a 20 turn fault in phase-4 at rotor speed of 1000 r/min.

6.7 Experimental Testing

To test the fault detection technique the same test-rig as explained in Chapter 5 and Appendix has been utilised. Fig. 6-19 shows the PWM ripple detector board mated to the 5-phase inverter board.

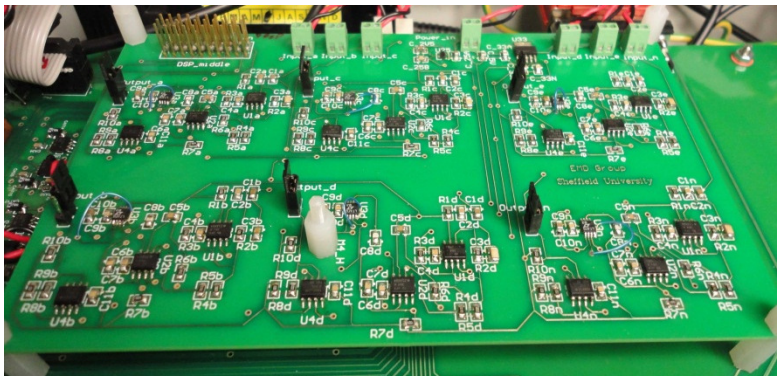

Fig. 6-19: PWM ripple detector board

Fig. 6-20(a) and (b) show the detector output at i_q = 6A at 2 turn fault and rotor speed of 500 r/min and 1000 r/min, respectively, captured using yokogawa oscilloscope, where Ch4 is the detector output of the faulted phase. It can be observed that each detector channel has a different output before fault is initiated. This is to be expected since each phase has slightly different impedances due to fabrication process, and there is variation in each detector channel. This variation can be easily compensated by implementing a software based calibration explained in the next section. During fault, phase -4 detector output shows clear change of output from the pre-fault level.

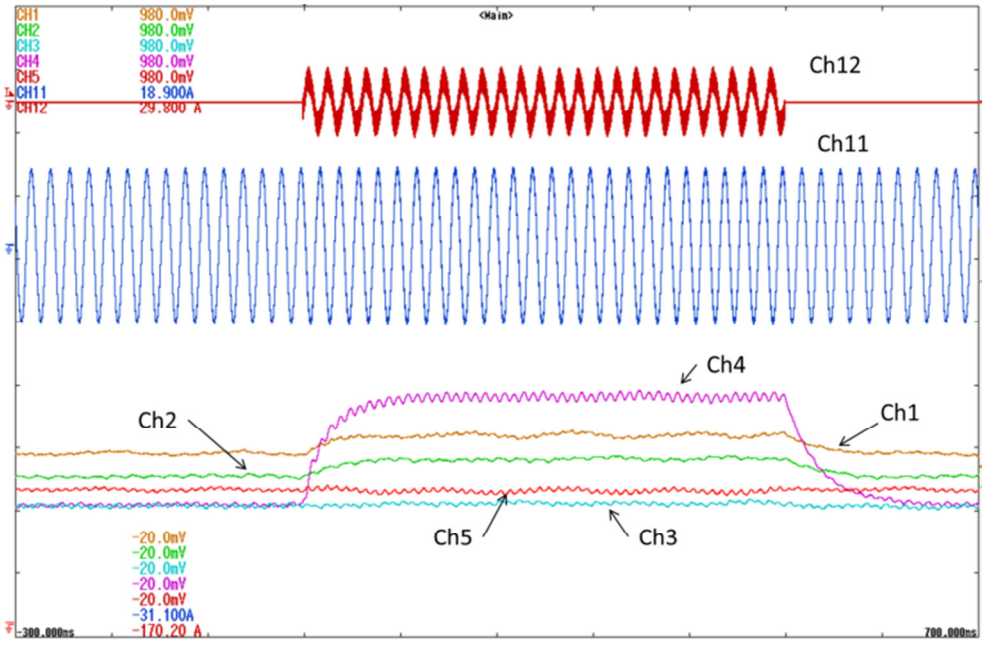

(a)

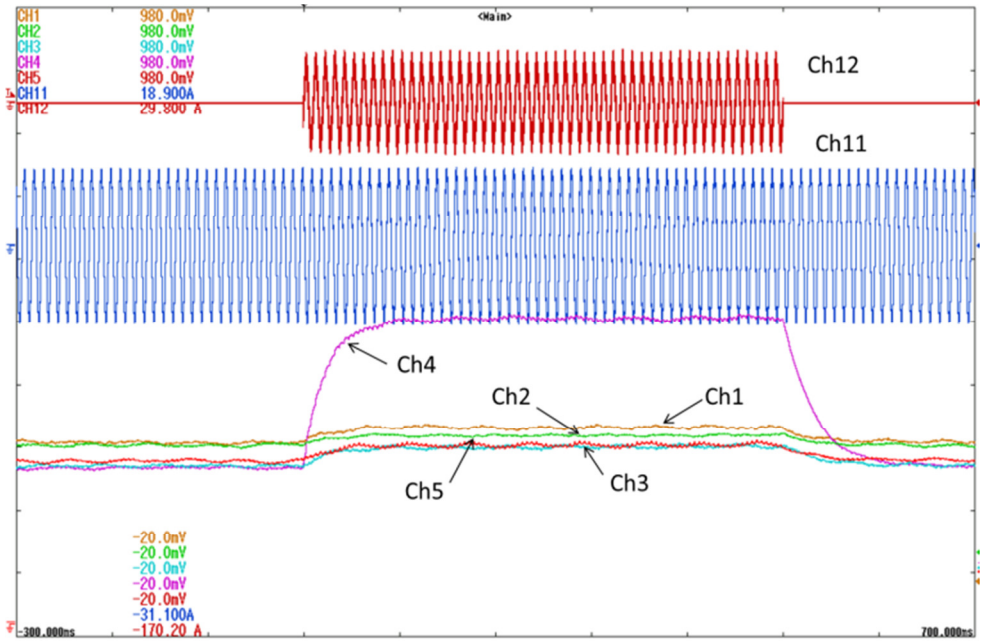

(b)

Fig. 6-20: Detector output with 2 turn fault in phase-4 with i_q =6A at (a) 500 r/min, (b) 1000 r/min. Ch1- Ch5 - detector outputs for phase 1 through phase 5 respectively (100mV/div), Ch11 - phase 4 current (5A/div), Ch12 is fault current (20A/div). Time scale – 100ms/div.

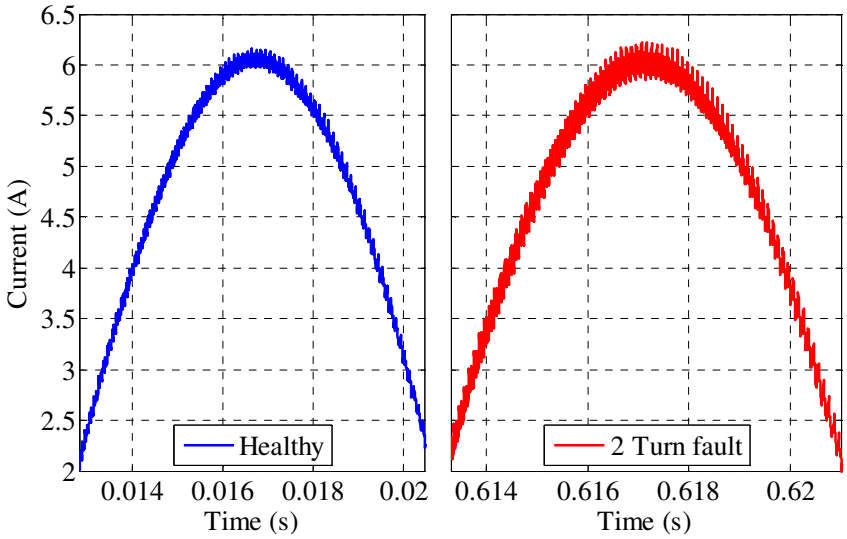

Fig. 6-21: Zoomed portion of measured Ph-4 (faulty phase) line current with i_q=6A at 500 r/min under healthy and 2 turn fault.

The change of the PWM ripple current can be appreciated in Fig. 6-21, where zoomed portion of the ph-4 (faulty phase) is shown under healthy and 2 turn fault at 500 r/min.

Fig. 6-22 (a) and (b) show the detector output at i_q = 6A with 20 turn fault and rotor speed of 500 r/min and 1000 r/min, respectively. Similar response to 2 turn fault case with different output levels can be clearly observed.

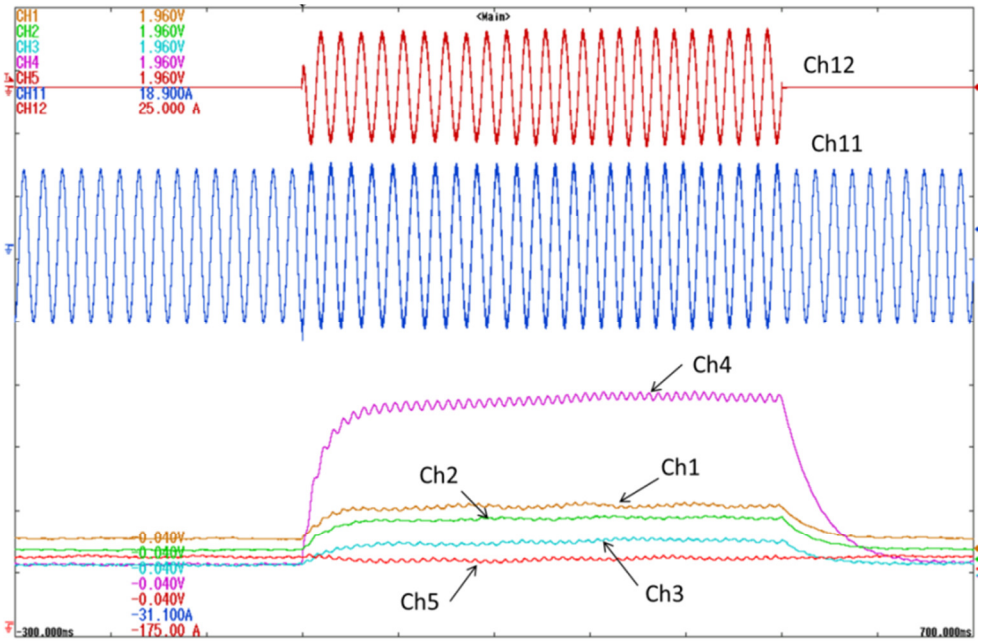

(a)

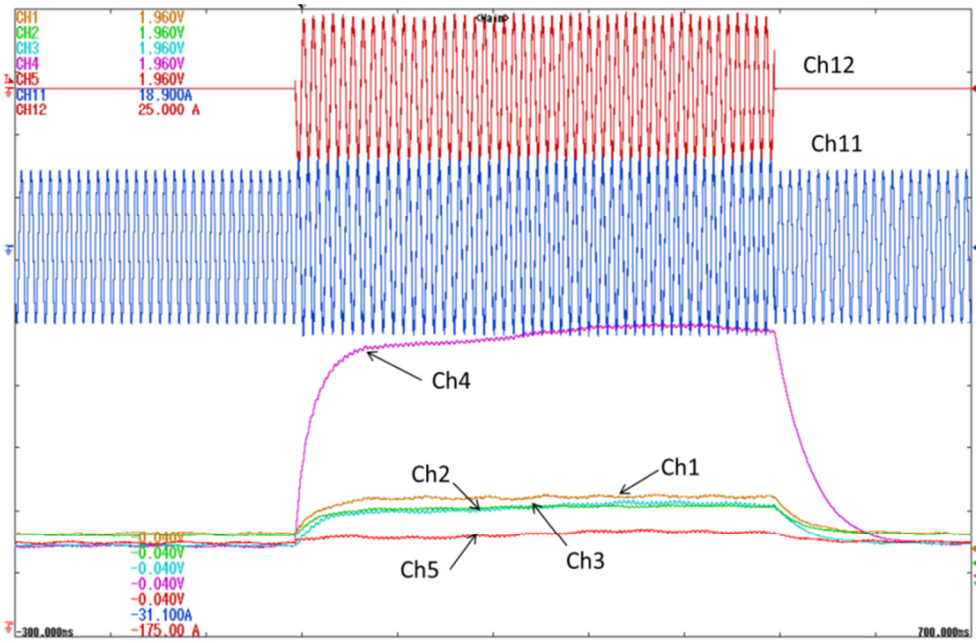

(b)

Fig. 6-22: Detector output with 20 turn fault in phase-4 with i_q=6A at (a) 500 r/min, (b) 1000 r/min. Ch1-Ch5 - detector outputs for phase 1 through phase 5 respectively (200mV/div), Ch11 - phase 4 current (5A/div), Ch12 is fault current (20A/div). Time scale – 100ms/div

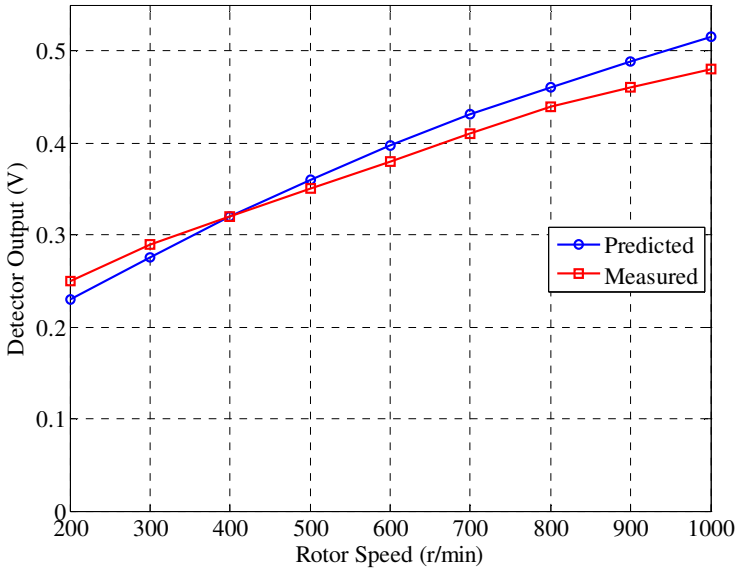

(a)

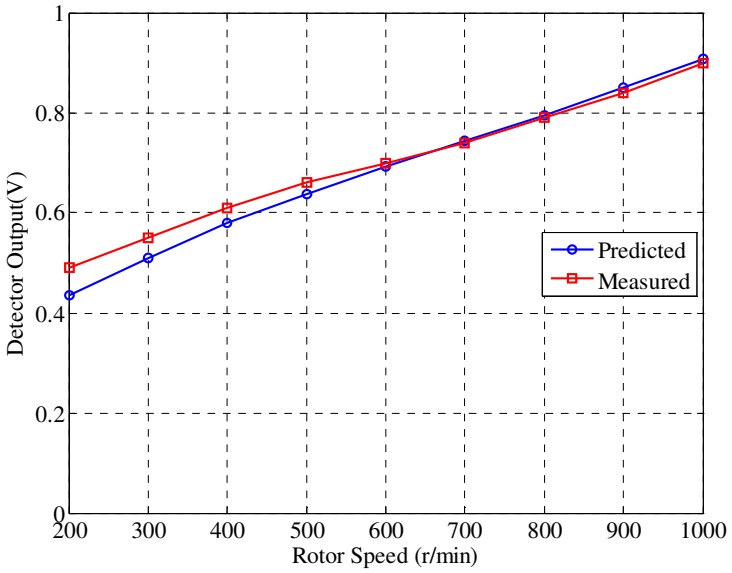

(b)

Fig. 6-23: Comparison of measured and predicted detector output at i_q =6A, with varying speeds at (a) 2 turn fault and (b) 20 turn fault

Fig. 6-23(a) compares predicted and measured detector output variations with speed for 2 turn fault at load current of 6A. A similar comparison is given in Fig. 6-23 (b) for 20 turn fault. It is to be noted that the high frequency admittance was measured using LCR meter with a very low current excitation (20mA). As load current changes it is expected that the inductance of the machine will change due to saturation which will affect the PWM ripple currents. Further, there is also a 4% variation of individual phase

impedances at 10 kHz as measured using the impedance analyzer. Another effect that can cause difference is the contactor impedance used to create the turn fault. However, as previously pointed out the variation are to be expected and can be cancelled out as explained in the next section.

6.8 Fault Detection

In order to detect turn fault, it is required that the variation of PWM ripple current under healthy operation with varying speed and loading be accounted for and removed. This is particularly true in the case of faults with low number of short-circuited turns, where the increase in the PWM ripple current due to the fault is low. By way of example, the variation of measured phase-4 detector output (phase with turn fault) with speed and current under healthy and 2-turn fault operation is shown in Fig. 6-24(a). It can be observed that at higher speed (>600 r/min) there exists a clear difference between the healthy and fault operation in the detector output, however at lower speeds there exists some overlap between the healthy and fault cases. As the speed and load are varied the overall inverter command voltage increases and this causes an increase in the healthy PWM ripple current, which makes fault detection using a simple threshold comparison difficult.

Harmonic current under healthy condition is a function of the modulation index magnitude as given by (6.13)-(6.14) irrespective of the current (i_d or i_q) or speed. In order to eliminate the ripple current contribution due to healthy operation of the machine, a simple algorithm based on linear curve fit is proposed. It can be observed from Fig. 6-24(b) that the detector output varies almost linearly with the fundamental modulation index. Detector data from 2 test points corresponding to two different modulation indexes at two different speeds (300 and 1000 r/min) and current loading (0A and 6A) under healthy operation as shown in Fig. 6-24 are extracted and a linear fit is performed using (6.15).

$$\text{detector}_h = a_4 M_4 + b_4 \tag{6.15}$$

The 2 fitted parameters are a_4 = 0.208V and b_4 = 0.103V. Using the obtained parameters, calibrated detector output for phase-4 is generated by using (6.16).

$$\text{calibrated detector} = \text{detector} - \text{detector}_h \tag{6.16}$$

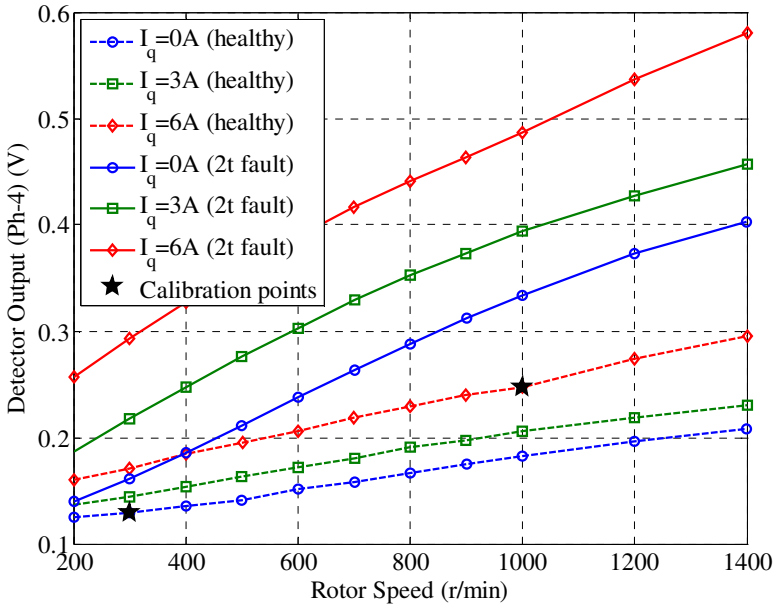

(a)

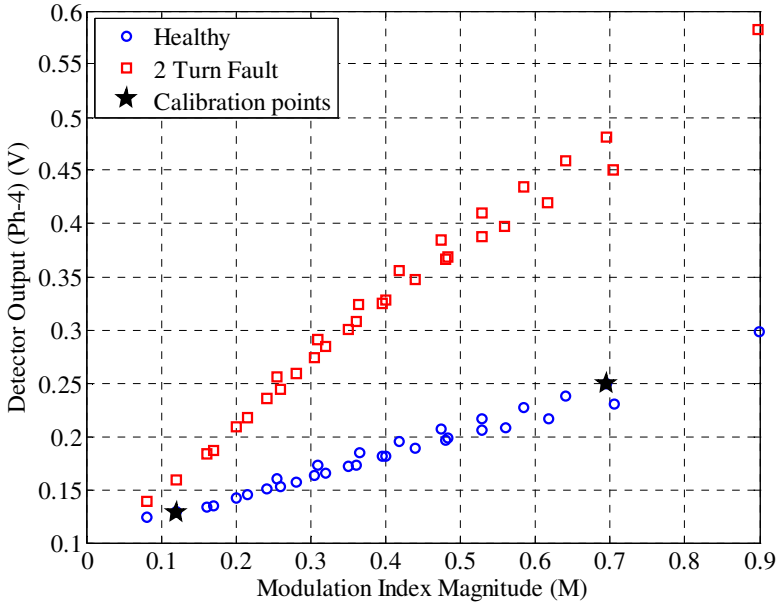

(b)

Fig. 6-24: Variation of measured detector output (ph-4) with load current (0%, 50%, 100%) and speed plotted with respect to (a) speed, (b) modulation index. Dashed curves refer to healthy operation and solid lines refer to 2-turn fault condition. Stared points are the selected test points for detector calibration.

The output of the calibrated detector is shown in Fig. 6-25 for the same current and speed variation under healthy and 2-turn fault. It can be observed in Fig. 6-25 that the variation of the detector under healthy operation due to load and speed has been

effectively cancelled. Slight error does exists however, as can be observed in the healthy case with i_q=0, 3A at higher speed due to use of the simple calibration technique. More advanced calibration algorithms using neural networks or lookup tables can also be used, which can result in improved sensitivity and robustness of the detection.

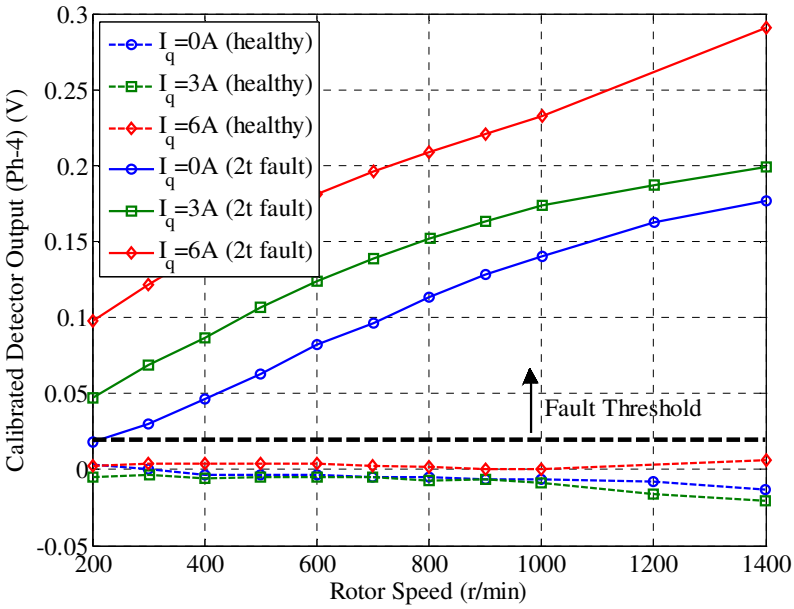

Fig. 6-25: Variation of calibrated detector output (ph-4) at various loading (0%,50%,100%) with varying speed. Dashed curves refer to healthy motor operation and solid lines refer to 2-turn fault condition.

Using a threshold value of 0.02, the calibrated detector output can be employed to classify healthy or faulted operation as shown in Fig. 6-25. A higher value of detector threshold will be more robust to detector noise at the expense of low sensitivity at lower speed and fault currents.

Under ideal conditions, one set of the fitted parameters can be used to calibrate all the phases. However, due to differences in individual detector channels and machine asymmetry, the proposed calibration procedure is performed for the other phases as well, resulting in a total of 10 constants required to perform calibration for all phases. It is to be noted that only 2 operating point data are needed to completely determine all the 10 constants. Fig. 6-26 shows the comparison of the calibrated detector output (ph-4) verses calibrated detector output of all phases under healthy condition. It can be seen that after calibration the detector output under healthy condition with different loading

and speed is much lower than that of faulted phase (ph-4) detector output under fault condition.

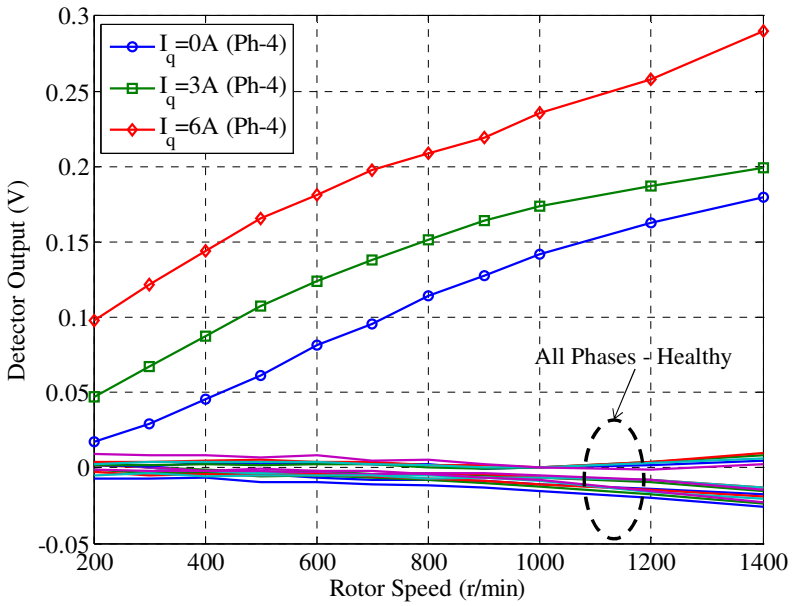

Fig. 6-26: Comparison of calibrated detector output of faulted phase (Ph-4) under 2 turn fault verses calibrated detector output of all phases under healthy condition.

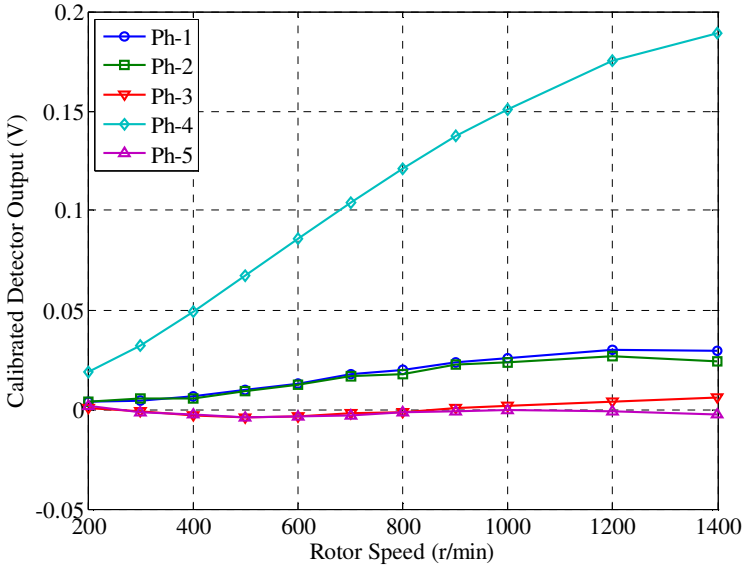

Fig. 6-27: Variation of all calibrated detector outputs at i_q=0A with varying speed under 2 turn fault. Ph-4 is the faulted phase.

Fig. 6-27 shows the calibrated detector output of all the phases for 2 turn fault for i_q=0A which is the worst case scenario for fault detection due to the low fault

signature. It can be observed in Fig. 6-27 that by quantifying the maximum of the detector outputs of all the phases, the faulted phase (ph-4) can be readily identified.

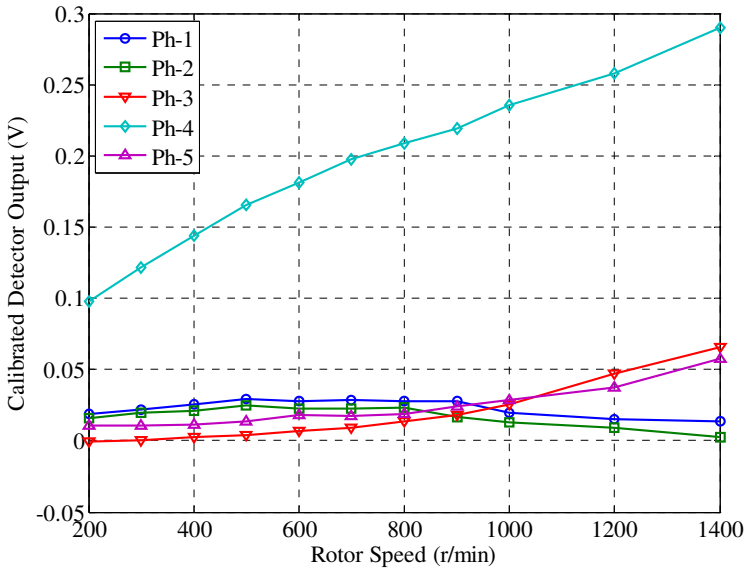

Fig. 6-28: Variation of all calibrated detector outputs at i_q=6A with varying speed under 2 turn fault. Ph-4 is the faulted phase.

Fig. 6-28 shows the calibrated detector output of all the phases for 2 turn fault under for i_q=6A. It also shows similar trend to Fig. 6-27 and the faulted phase can be clearly identified.

Similar results were also obtained for the 20 turn fault condition. Fig. 6-29 shows the un-calibrated data obtained under 20 turn fault with (0%, 50%, 100%) current loading and varying speed. Fig. 6-30 shows the calibrated detector output under 20 turn fault condition using the same calibration data utilized for the 2 turn case. It can be seen that calibration reduces the detector output variation under healthy condition and enables use of simple threshold to achieve detection. Fig. 6-31 shows the calibrated detector output for all phases under 20 turn fault with i_q=6A. It can be observed from the plot that the faulted phase can be easily identified by quantifying the maximum of the detector outputs of all the phases.

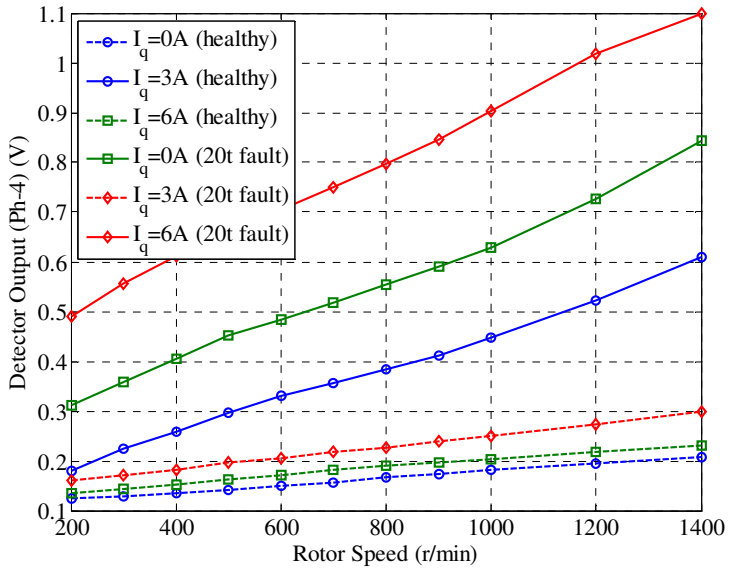

Fig. 6-29: Variation of measured detector output (ph-4) with load current (0%, 50%, 100%) and speed plotted with respect to speed. Dashed curves refer to healthy operation and solid lines refer to 20-turn fault condition.

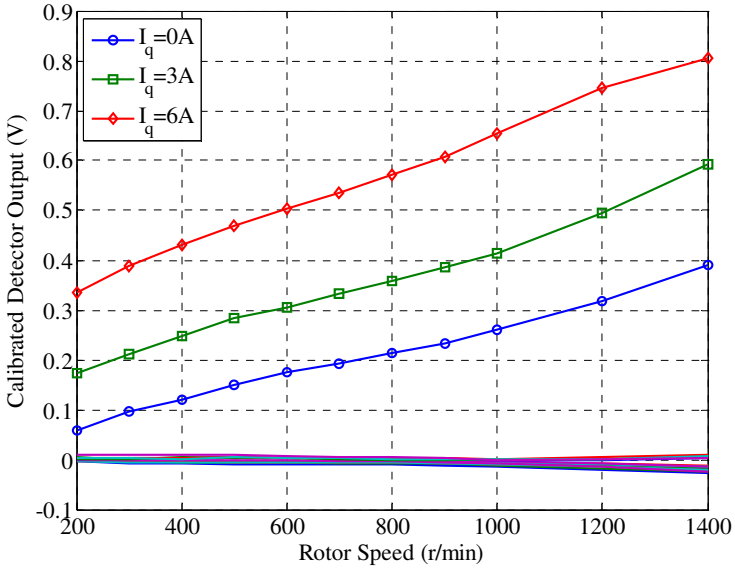

Fig. 6-30: Comparison of calibrated detector output of faulted phase (Ph-4) under 20 turn fault verses calibrated detector output of all phases under healthy condition.

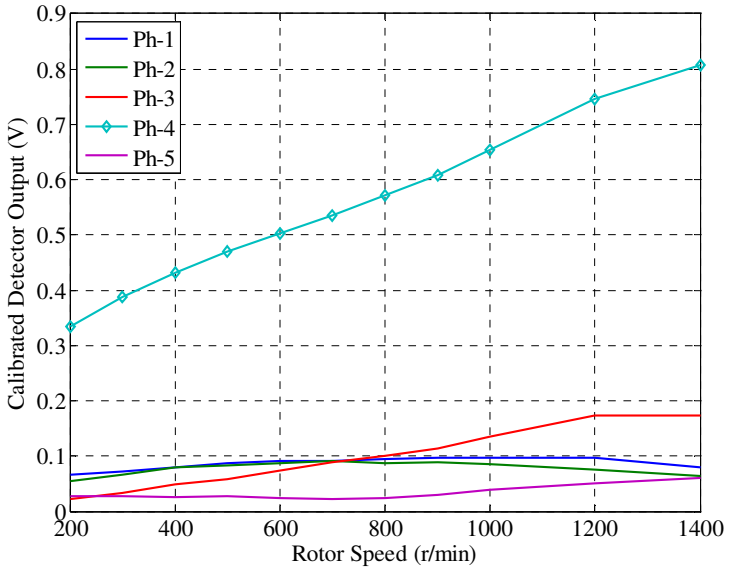

Fig. 6-31: Variation of all calibrated detector outputs at i_q=6A with varying speed under 20 turn fault. Ph-4 is the faulted phase.

6.9 PWM Ripple Current under High resistance Connection

The PWM ripple current measurement is not expected to show significant changes under high resistance connection (HRC). This is due to the fact that the impedance at PWM frequencies is high and therefore not affected by small changes in the resistance of the stator. Fig. 6-32 shows the effect of HRC fault on the detector output. The change due to the fault is very small and in case of i_q =2A less than the healthy detector output at i_q=6A. It can therefore be concluded that HRC fault has minimal effect of PWM based ripple detection and the detection is sensitive only to turn faults.

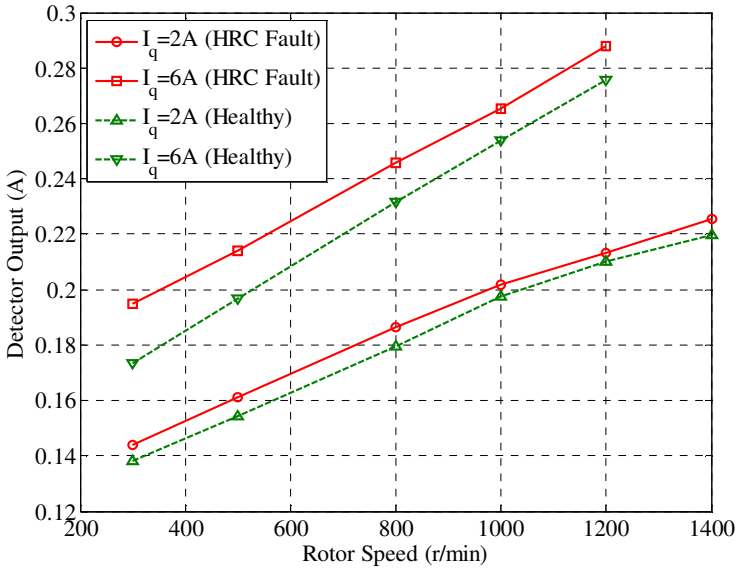

Fig. 6-32: Variation of detector output (Ph-4) to HRC fault (0.66Ω) at various loading (33% and 100%) with varying speed.

6.10 Conclusions

A new technique to detect turn fault using PWM ripple currents has been described in this chapter. A machine model based on measured high frequency winding parameters to capture the high frequency behaviour of the winding has been developed. Based on the analytical simulations, a detector circuit to extract the PWM ripple current has been designed. Experiments confirm that PWM ripple based method can be used to successfully detect turn faults in the machine. A simple and effective software calibration technique has been proposed to cancel the ripple current expected under healthy operation to obtain a calibrated detector output. Application of simple fault threshold on the calibrated detector has been shown to be sufficient to determine fault. By quantifying the maximum of the detector outputs of all the phases, the faulted phase can be identified.

Compared with the residual current based fault detection proposed in the previous chapter, the high frequency detection requires additional hardware but has lower compute demand for detection whereas as although the residual current method requires no hardware modification it has significant compute requirement. Moreover, the residual current technique can detect HRC fault whereas HF detection is insensitive to it. However, the residual current technique requires careful calibration of the machine

parameters and its back-EMF, whereas the calibration for HF detection is fairly simple and straightforward. The HF detection method is expected to be more robust to temperature variation of the motor as can be inferred from its insensitivity to HRC fault (increase of phase resistance) whereas the residual current technique will require temperature based parameter compensation to maintain adequate sensitivity to turn fault.

PWM current ripple based fault detection can be easily incorporated into drives as an add-on card and connected to controller using analog input channels. Since most of the high frequency signal processing is done on the card, a low frequency sampling of the detector output by the controller is sufficient. Test show that the detection can be performed at low speeds and low currents which are of advantage compared to fundamental component based methods which have difficulty due to low signal to noise ratio.

Chapter 7

Stationary (abcde) Frame Fault Tolerant Current Control of Poly-phase PM Machines under Open-Circuit and Short-Circuit Faults

The main contribution of this chapter is to present a stationary frame control strategy to achieve optimal current control for star connected poly-phase permanent magnet machine under asymmetric phase faults, namely phase-open circuit (OC) and phase-short circuit (SC) condition. In the previous two chapters different turn fault detection methods were explored and the detection relied on picking up very small change between healthy and fault conditions. Due to the high fault current generated in the shorted turns which leads to high localised heating, fault detection needs to be fast and reliable. However, due to the small fault signature it is likely that some turn faults can go undetected and can cause a complete failure of the winding leading to either OC or SC faults. Such faults will immediately trip conventional drive controls due to loss of a degree of freedom. Fault tolerant control is the last line of defence in preventing a complete shutdown of the motor-drive system in case incipient winding faults cannot be predicted or detected leading to a complete winding failure in form of OC or SC fault. Current regulation under these faults is particularly challenging because optimal torque control strategy generates non-sinusoidal current references with unbalance in both fundamental and higher order working harmonics, to achieve minimal copper losses and torque ripple under fault condition. Under field weakening operation, voltage limit introduces additional control problems. This chapter describes a solution for the control issues by employing a novel controller in stationary frame. This control strategy allows minimal reconfiguration of the control structure from healthy to post-fault operation.

Extensive simulation and experimental results are presented as validation for the proposed strategy.

Major contents of this chapter were published by author in [128].

7.1 Motivation

Fault tolerant controls are increasingly becoming important in improving reliability and safety of electric drives specially in aerospace and automotive sectors [4], [129]. Several surveys on reliability of industrial motors conducted by Electric Power Research Institute (EPRI) [7] and IEEE [8]–[11] concluded that stator winding failures accounts for about 21-37% of faults in electrical machines. Operation under fault condition commonly known as "limp-home" mode [39] is essential for providing high degree of availability, and reliability demanded in safety critical application like electric vehicles. To further improve fault handling capability, multi-phase machines have been proposed in [4], [112] due to more degrees of freedom available for control compared to conventional 3-phase machines.

However, under fault condition the symmetry of the machine is lost. Most conventional controllers based on synchronous *dq* frame, are not suitable for control under fault conditions. Most of the work presented in literature so far, focus on modification of the conventional controller to achieve control under fault. However, most of the work reported so far are only focussed on operation below base speed and have been tested at only a few operating speeds. The effect of changing speed and operation close to voltage limit of the inverter or healthy to fault transitioning has received little attention in the literature so far.

7.2 Literature Review

The issues associated with fault tolerant operation in permanent magnet machines can be divided into two major tasks.

The first task is to generate appropriate current references which produce minimum torque ripple and minimum losses under fault conditions. In [130]–[133], zero torque ripple under open circuit fault was achieved by adjusting phase current angles to produce forward rotating stator magneto-motive force (MMF). However this method is

applicable when rotor flux is purely sinusoidal and does not lead to minimum copper loss. The performance deteriorates further in practical PM machines which have higher order harmonics in Back-EMF [118]. In [134]–[136] current references was optimized for maximum torque based on offline calculations accounting for third harmonic in back-EMF for a 5-phase machine with different winding configurations under open circuit (OC) fault. In [137]–[141] an online optimal current reference generation technique was presented for phase short circuit (SC) and OC faults which minimized the overall stator copper losses. However operation under field weakening mode was not addressed in both the online and offline methods. Optimal torque control (OTC) proposed in [113] obtained minimum stator copper loss with online computation of the current references under both OC and SC faults. Furthermore with application of a weighting factor on the flux linkage, the OTC could be used in field weakening regime. However this method was only applied to 5-phase machine with each phase driven individually by H-bridge converters. Modifying the current references such that OTC can be applied to star connected machines can extend the applicability of the technique to a larger class of machines.

The second task is the tracking control of the generated current references. Tracking the current references obtained through the OTC or other current reference generation techniques is quite challenging. This is because under fault conditions, the machine loses its symmetry and the standard synchronous frame based current control is no longer effective due to presence of time varying components. This is particularly problematic in the OTC since the current references generated by the OTC algorithm are typically unbalanced and have higher order harmonics [113]. Hysteresis current controller is typically employed for fault tolerant current controls [113], [130]–[133], [135]–[139]. However, this result in variable switching frequency which increase switching loss and electromagnetic interference (EMI) emission and therefore current control with fixed switching frequency PWM is preferred [142]. In [142], [143] a synchronous frame current control technique based on modified clarke transformation was proposed for pulse width modulated (PWM) drives under OC fault. However, higher order harmonics in back-EMF was ignored in torque computation and operation under phase short circuit (SC) fault, field weakening as well as transition of control from healthy to fault were not addressed. In [144] post fault control of 6-phase

induction machine was presented for low speed operation using additional negative sequence controllers under OC fault operation. In the various control methods proposed in literature, a general control technique for tracking current references which are unbalanced and contains higher order harmonics under inverter voltage limit has not been addressed.

One solution to tracking time varying signals is proportional resonant (PR) controllers [145]–[147] which have been employed for applications in active harmonic filtering in grid applications. However they are optimized to operate around a fixed fundamental frequency since the grid fundamental frequency varies only slightly. In variable speed drives, however, the fundamental frequency of motor currents is speed dependent. Analysis of transient response of resonant controller for variable speed drive application was performed in [148] only for a narrow range of frequency (30-50Hz). However fundamental frequencies vary over a wide range especially in multi-pole PM drives. In addition the standard PR controllers are not suitable for operation near the inverter modulation limit due to their inherently high open loop gain, which may cause stability problem under voltage saturation [149]. To improve performance under voltage saturation, an anti-windup scheme was proposed in [149] for the PR controller, albeit only operation under single excitation frequency was demonstrated. In [150] an alternative control strategy was proposed to solve the anti-windup problem for operation under fixed fundamental frequency.

This chapter is concerned with control of a fault tolerant PM machine under OC or SC fault with a unified control strategy which allows for smooth transition between healthy and fault modes of operation. It contributes to the body of knowledge in the following aspects:

1. Extension of the OTC reference generation for star connected PM machine.
2. A new stationary frame resonant current controller structure operating with fixed PWM switching frequency, which is capable of tracking time varying current references with multiple frequency components which vary with drive speed, and capable of stable operation near inverter voltage limit.
3. Voltage injection technique under fault condition to increase modulation range and DC link voltage utilization in conjunction with the proposed resonant control.

4. Field weakening algorithm based on a search algorithm for operation under healthy and fault operation in conjunction with the proposed resonant control.

7.3 Optimal Current Reference Generation

In order to obtain optimal currents under fault condition, the demand torque should be met and the ohmic losses should be minimized [151]. This is because windings are limited in their heat dissipation capacity and injecting more current to obtain pre-fault torque level will lead to overheating of the winding possibly leading to further failure. However, minimizing ohmic losses does not result in optimal currents under field weakening condition, since inverter output voltage is limited by the DC link voltage and the drive will not be able to realize the reference currents due to control saturation. Hence a cost function which minimizes both currents and voltage is needed. This can be achieved using the optimal torque control, wherein for a given torque demand T_d, the phase current references of an m-phase SPM machine can be obtained by minimizing a cost function given by (7.1),

$$f = \sum_{j=1}^{m} \left(L i_j + k_{fld} F_j \lambda_j \right)^2 \tag{7.1}$$

where, L is the phase inductance, k_{fld} is a dimensionless weighting factor representing the degree of field weakening and i_j and λ_j are the j^{th} phase current and flux linkage respectively. F_j is a binary parameter, which denotes whether the phase is healthy (=1) or faulty (=0) and is defined by (7.2), where l is the faulted phase.

$$F_j = \begin{cases} 1 \; ; j \neq l \\ 0 \; ; j = l \end{cases} \tag{7.2}$$

The flux linkage, λ_j, and the instantaneous torque, T_j of j^{th} phase can be expressed by (7.3),

$$\begin{aligned} \lambda_j &= \Psi_{m1} \cos\left(\theta - (j-1)2\pi/m\right) + \Psi_{m3} \cos\left(3\left(\theta - (j-1)2\pi/m\right)\right) \\ T_j &= a_j(\theta) i_j = p\left(\frac{d\lambda_j}{d\theta}\right) i_j \end{aligned} \tag{7.3}$$

where, Ψ_{m1} and Ψ_{m3} denotes the first and third harmonic magnitude of magnet flux-linkage respectively and p is the number of pole pairs. The currents references have to satisfy the torque demand constraint given by (7.4),

$$T_d = \sum_{j=1}^{m} F_j a_j(\theta) i_j \tag{7.4}$$

For the case of a short-circuit fault in phase l, the pulsating torque T_f, given by (7.5),

$$T_f = \begin{cases} 0, & Open\,circuit\,fault \\ a_l(\theta) i_l, & Short\,circuit\,fault \end{cases} \tag{7.5}$$

Since the phase windings of the fault tolerant machine considered are star connected, Kirchhoff current law for the healthy phases given by (7.6), needs to be considered in the overall minimization, i.e.,

$$0 = \sum_{j=1}^{m} i_j F_j \tag{7.6}$$

The objective function of the constrained optimization problem can be obtained by applying the method of Lagrange multipliers expressed by (7.7), where γ_1 and γ_2 are the Lagrange multipliers.

$$\Lambda = \sum_{j=1}^{m} \left(L i_j + k_{fld} F_j \lambda_j \right)^2 + \gamma_1 \left(T_d - T_r - \sum_{j=1}^{m} \left(F_j a_j(\theta) i_j \right) \right) + \gamma_2 \sum_{j=1}^{m} i_j F_j \tag{7.7}$$

The instantaneous current in phase j can then be derived by minimizing the objective function and is given by (7.8),

$$\frac{d\Lambda}{di_j} = 0 \Rightarrow 2\left(L i_j + k_{fld} F_j \lambda_j \right) L - \gamma_1 a_j + \gamma_2 F_j = 0 \tag{7.8}$$

(7.8) can be re-arranged to obtain the current reference value given in (7.9).

$$i_j = \frac{-\gamma_2 F_j + \gamma_1 F_j a_j - 2 k_{fld} F_j \lambda_j L}{2L^2} \tag{7.9}$$

As can be observed from (7.9) the current reference is dependent on the undetermined Lagrange multipliers. In order to obtain the expression for the Lagrange multipliers, (7.9) is substituted back into constraint equations (7.4) and (7.6) to obtain (7.10)-(7.11).

$$0 = \sum_{j=1}^{m} i_j F_j \Rightarrow -\gamma_2 \sum_{j=1}^{m} F_j + \gamma_1 \sum_{j=1}^{m} F_j a_j - 2 k_{fld} L \sum_{j=1}^{m} F_j \lambda_j = 0 \tag{7.10}$$

$$\begin{aligned} T_d &= \sum_{j=1}^{m} F_j a_j(\theta) i_j \\ \Rightarrow -\gamma_2 \sum_{j=1}^{m} a_j F_j &+ \gamma_1 \sum_{j=1}^{m} F_j a_j{}^2 - 2k_{fld} L \sum_{j=1}^{m} F_j a_j \lambda_j - 2L^2 T_d = 0 \end{aligned} \tag{7.11}$$

It is to be noted that F_j being a binary value, the square of F_j is equal to the original value. (7.10) and (7.11) are linear equations in terms of γ_1 and γ_2 and can be solved to obtain the expression for the Lagrange multipliers as given by (7.12) and (7.13).

$$\gamma_2 = \frac{\left(\gamma_1 \sum_{j=1}^{m} F_j a_j - 2k_{fld} L \sum_{j=1}^{m} F_j \lambda_j \right)}{\sum_{j=1}^{m} F_j} \tag{7.12}$$

$$\gamma_1 = \frac{\left[2L^2 (T_d - T_r) \sum_{j=1}^{m} F_j + 2k_{fld} L \left\{ \begin{array}{l} +\sum_{j=1}^{m} F_j \left(\sum_{j=1}^{m} F_j a_j \lambda_j \right) \\ -\sum_{j=1}^{m} F_j \lambda_j \left(\sum_{j=1}^{m} F_j a_j \right) \end{array} \right\} \right]}{\left\{ \sum_{j=1}^{m} F_j \left(\sum_{j=1}^{m} F_j a_j{}^2 \right) - \left(\sum_{j=1}^{m} F_j a_j \right)^2 \right\}} \tag{7.13}$$

For the purpose of simulation and experimental validation a 5-phase fault tolerant PM machine shown in Fig. 3-1 is considered and its specification and parameters are given in Table 7-1. It is to be noted that this machine topology has negligible mutual inductance between phases [15].

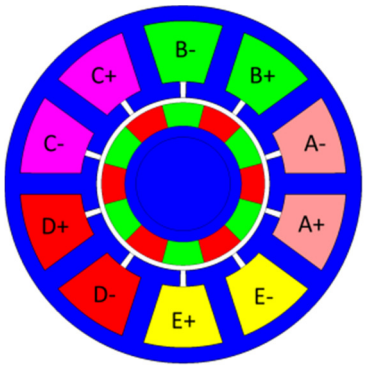

Fig. 7-1: Five phase fault tolerant SPM machine

Table 7-1: Specification of the Prototype Five-Phase Fault-Tolerant PM Machine

Parameter	**Value**	**Parameter**	**Value**
Maximum speed	3000 r/min	Phase Resistance	380mΩ
Rated Torque	1.86Nm	Phase inductance	2.8mH
Rated RMS	6.5/√2A	Cable Resistance/phase	380mΩ
Number of phases	5	DC link voltage	50V
Number of pole-pairs	6	Fundamental flux linkage magnitude (Ψ_{m1})	19.1mVs
Switching/Sampling frequency	10kHz	Third harmonic flux linkage magnitude (Ψ_{m3})	416uVs

Using (7.9) along with (7.12)-(7.13) current references can be generated online. Fig. 7-2 shows the current references and their spectrums generated from the optimal current control technique with T_d = 0.7Nm, and k_{fld} =0.7 when phase 1 (i.e. phase A) is open-circuited.

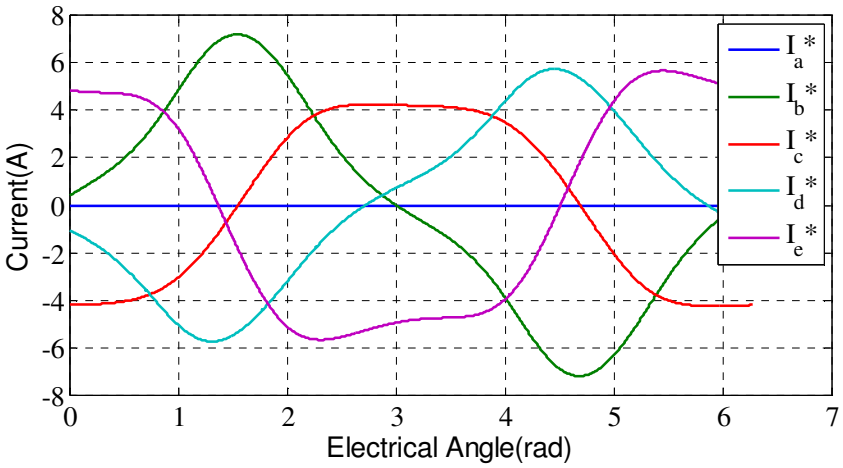

(a)

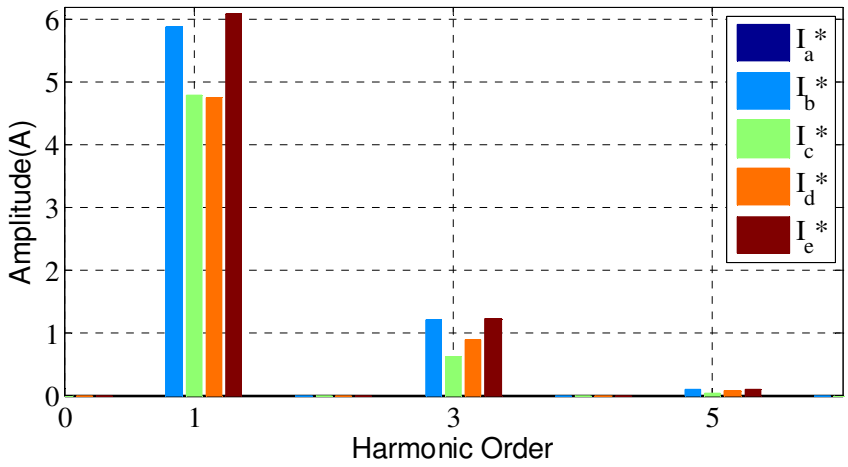

(b)

Fig. 7-2: Optimal torque control with open circuit fault in Phase-A with T_d = 0.7Nm and k_{fld} =0.7, (a) instantaneous currents, (b) FFT

It can be clearly seen that the currents have 1st, 3rd and 5th harmonic although the 5th harmonic is quite small. This is expected since back-EMF of the machine contains only 1st and 3rd harmonic components, the interaction of the same frequency components contribute to average torque. By minimizing the ohmic losses, even order harmonics will not be present since it does not contribute to average torque. It can also be seen from the FFT plots that the fundamental and third harmonic components in each phase are different. Current references for a phase SC fault exhibit the similar features to those of the OC fault. The next section elaborates the controller design.

7.4 Discrete-Time Plant Model

Fig. 7-3 shows one phase representation of a PM machine fed by a PWM modulator. The continuous time model of the plant (PM machine) can be represented by (7.14). Since the PWM modulator holds the modulation command value constant for 1 sample time, it is represented by a sampler followed by a zero-order hold. The DSP controller introduces a 1 sample delay due to computation time required for calculations. The discrete time model of the plant (G_{pz}) with the ZOH and delay can be obtained as shown in (7.15) [150].

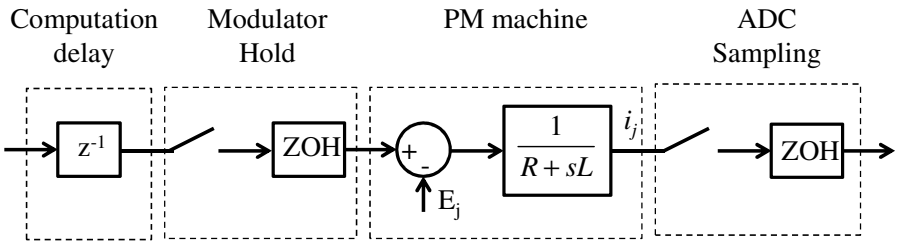

Fig. 7-3: Discrete domain plant modelling

$$G_p(s) = \frac{1}{R + sL} \tag{7.14}$$

$$\begin{aligned} G_{pz}(z) &= \frac{1}{z}\left(1 - z^{-1}\right) \not{Z} \left\{ \frac{G_p(s)}{s} \right\} \\ &= \frac{1}{z}\frac{1}{R}\frac{1 - e^{-T_s/T_p}}{z - e^{-T_s/T_p}}; \quad T_p = \frac{L}{R} \end{aligned} \tag{7.15}$$

7.5 Current Control

Traditionally current control in PM drives is performed in synchronous reference frame [152], in order to convert sinusoidal current references which are time varying into direct current (DC) references. This control structure is effective only if a machine operates in symmetrical or balanced conditions. However, the balanced condition is no longer true when a fault occurs. Although many authors have proposed modified control structure in synchronous reference in order to maintain operation under fault condition [142]–[144], [153], most of the methods are focused on the open circuit fault, assuming current and back-EMF to be single frequency and operating in the constant torque region.

To track the reference currents generated by the OTC, current control in the natural stationary frame (*abcde*) is proposed. The benefit of the tracking control in the natural stationary frame is that the controller structure remains the same in healthy and fault conditions, except for turning off the controls for a faulted phase. In doing so, the controllers in the other healthy phases are not affected. Secondly, under field weakening operation, voltage saturation can be dealt with individually for each phase rather than combined in the form of space vectors. However, the drawback of this method is that the control references are no longer constant quantities but is time varying with higher order harmonics which make the controller design more challenging.

One of the effective methods for tracking periodic time-varying currents in stationary reference frame is proportional resonant control and its variants [145]–[147], [154]. For tracking multiple frequencies references a number of resonant controllers are usually employed in parallel. Since the resonant poles are located at frequencies of interest, steady state tracking is guaranteed. However, one of the limitations of the proportional-resonant control is that the location of its open-loop zeroes is not placed directly. This can be appreciated using an example of single proportional resonant controller in (7.16).

$$\begin{aligned} H(s) &= K_p + K_{I1}\frac{s}{s^2+\omega_1^2} \\ &= K_p\frac{s^2+2\left(K_{I1}/\left(2\omega_1 K_p\right)\right)\omega_1 s+\omega_1^2}{s^2+\omega_1^2} \end{aligned} \tag{7.16}$$

It can be seen that the order of the numerator is the same as that of the denominator. However there is only one degree of freedom (damping coefficient) which can be specified by gain selection for K_p and K_{I1} whereas the natural resonant frequency in the numerator has to equal the frequency ω_1 of the tracking reference. Moreover the location of the zeros can change as more resonant controllers are added in parallel to track references with more than one frequency components. It is well known that open-loop zeroes affect the transient performance [155], therefore although the above structure will enable zero steady state tracking error, the control system performance may be limited by the inability to place the zeroes optimally [150].

The restriction on open loop zeros can be solved by employing an alternate control law given in (7.17).

$$H(s) = K_\infty \prod_{n=1,3,\ldots,\mathrm{n}} \frac{s^2+2\xi_n\omega_{zn}s+\omega_{zn}^2}{s^2+\omega_{pn}^2} \tag{7.17}$$

where, ω_{zn}, ξ_{zn} is the resonant frequency and damping factor of the nth complex zero respectively and ω_{pn} is the resonant frequency of the nth complex pole, corresponding to the desired frequency component to be tracked by the controller. This controller enables independent selection of locations of its resonant poles and zeroes.

Resonant controllers are prone to discretization issues when transforming from *s* domain to *z*-domain for purposes of real-time implementation [156]. It is therefore

preferable to design the controller in z-domain, to avoid performance deterioration introduced by discretization [150]. The control law given by (7.17) can be discretized using matched-z transformation to maintain the location of poles and zeros. The resonant controllers may also have stability problem when the delay introduced by digital sampling is significant with respect to the fundamental frequency [156], [157]. In order ensure control stability at high fundamental frequencies, a predictive compensation technique is used [150], resulting in the final controller structure given by (7.18)-(7.19) and shown in Fig. 7-4.

$$H(z) = K_{\infty} \frac{z}{z + p_1} \prod_{n=1,3,\ldots,n} \frac{z^2 - a_{1n} z + a_{2n}}{z^2 - 2z\cos\omega_{pn} T_s + 1} \tag{7.18}$$

$$\begin{aligned} a_{1n} &= 2e^{\sigma}\cos(\upsilon_{zn} T_s) \\ a_{2n} &= e^{2\sigma} \\ \sigma &= -\xi_n \omega_{zn} T_s \\ \upsilon &= \omega_{zn}\sqrt{1-\xi_n^{\,2}} \end{aligned} \tag{7.19}$$

where, a_{1n} and a_{2n} are the controller coefficients corresponding to the n^{th} complex zero and T_s is the sampling time, assumed to be 100us in this study. Further, n is limited to 3, in this study, implying only 1st and 3rd harmonic of the current reference is actively controlled.

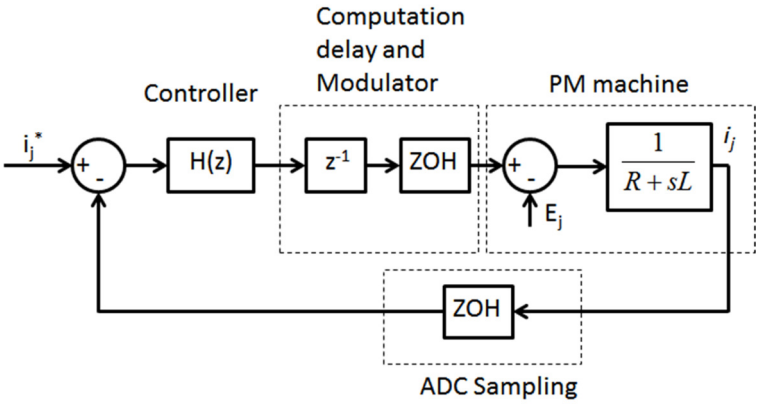

Fig. 7-4: Controller Structure

Due to speed, hence frequency variations, it is necessary to tune the controller over a wide speed operating range. This is particularly challenging since it implies that,

as the resonant poles move with operating speed of the machine, the closed-loop poles and zeroes, and the open-loop resonant poles of the system will move with the system frequencies. Therefore, the open-loop zeroes have to be modified as a function of system frequencies in order to achieve acceptable control performance. From the previous section it is known that for 5-phase machine to take an example, at least two current harmonics needs to be controlled, namely the fundamental and the third harmonic.

In order to keep the complexity of the controls to minimum, the poles and zeroes of the system are scaled as a linear function with respect to the system fundamental electrical frequency, *f*, expressed by (7.20).

$$\begin{aligned}
&\omega_{p1} = 2\pi f ; \omega_{p3} = 3\times 2\pi f \\
&\omega_{z1} = \omega_{z1c} + k_{z1\omega} f \\
&\xi_1 = \xi_{1c} + k_{1\xi} f \\
&\omega_{z3} = \omega_{z3c} + k_{z3\omega} f \\
&\xi_3 = \xi_{3c} + k_{3\xi} f \\
&p_1 = p_{1c} + k_{p1} f
\end{aligned} \tag{7.20}$$

where, (ω_{z1c}, $k_{z1\omega}$), and (ω_{z3c}, $k_{z3\omega}$), are constant intercepts and frequency scaling coefficients of the resonant frequencies of the complex zeroes (ω_{z1}, ω_{z3}), respectively. (ξ_{1c}, $k_{1\xi}$) and (ξ_{3c}, $k_{3\xi}$) are the constants and frequency scaling coefficients for the damping factor of the 1st and 3rd complex zero, respectively. (p_{1c}, k_{p1}) are the constant and frequency scaling coefficients for the real pole p_1. The 11 tunable parameters of the system are selected through an optimization process to minimize the integral-square-error (ISE) as given in (7.21) [158].

$$C = \sum_f \int \left(y(t) - u(t) \right)^2 dt \tag{7.21}$$

where *y(t)* and *u(t)* denoted the output and input (reference) of the closed-loop system at system frequency *f*. The objective function, C is the sum of the ISE errors over the target system frequency range [30Hz-300Hz], corresponding to speed range of [300 r/min – 3000 r/min]. Operation below 30 Hz can simply be achieved using only proportional gain since the gain bandwidth product will be sufficient to obtain desirable current tracking. The optimization is performed using *patternsearch* function in the global optimization toolbox in Matlab [79].

Some constraints need to be imposed during optimization in order to reduce computation time and avoid searching unfeasible controller parameters. Since the controller is not actively tracking 5th harmonic while the OTC algorithm does generate a small 5th harmonic in the reference, the closed-loop transfer function should have a gain of 0dB or less at 5th harmonic frequency to ensure that the 5th harmonic will not be amplified under healthy conditions, and it can be expressed as (7.22).

$$20\log\left(\left|CLTF\right|_{\omega=5\omega_e}\right)\le 0 \tag{7.22}$$

The closed loop transfer function should have a low peak gain such that in events of speed change, the delay in speed measurement will not lead to excessive overshoots. This condition can be expressed in (7.23).

$$\max\left(20\log\left(\left|CLTF\right|\right)\right)\le 1.8 \tag{7.23}$$

The maximum value of controller proportional gain is a tradeoff between transient response and noise sensitivity, and is limited to 16 in order to limit the open loop bandwidth to about $f_s/10$. To constrain the optimization search, the maximum frequency of zeroes is restricted to 6 times the system angular frequency. The search constraints for parameters are given in (7.24) and the results of the optimal design are summarized in Table 7-2.

$$\begin{aligned}
&1\le K_\infty \le 16\\
&-1\le p_1 \le 1\\
&0.01\omega_e \le \omega_{z1} \le 6\omega_e\\
&0\le \xi_1 \le 4\\
&0.01\omega_e \le \omega_{z3} \le 6\omega_e\\
&0\le \xi_3 \le 4
\end{aligned} \tag{7.24}$$

Table 7-2: Optimised Controller Parameters

Parameter	Value	Parameter	Value
K_∞	16.00	ω_{z3c}	-14.84
ω_{z1c}	21.311	$k_{z3\omega}$	14.42
$k_{z1\omega}$	2.835	ξ_{3c}	0
ξ_{1c}	0.9633	$k_{3\xi}$	0
$k_{1\xi}$	-3.2e-3	p_{1c}	0.72
		k_{p1}	6.02e-4

It can be observed from the optimized controller parameters that both $k_{3\xi}$ and ξ_{3c} is zero and therefore damping ratio ξ_3 need not be computed online but simply set to 0. Fig. 7-5 show the bode plot of the open-loop transfer function (OLTF) for two rotor speeds. It can be observed that for the plot associated with each speed there are two resonant poles corresponding to 1st and 3rd harmonic. In the lower speed regime only one zero with low damping corresponding to ω_{z3c} can be observed, whereas in the high speed operation both zeroes exhibit low damping as expected from the damping factor frequency scaling coefficients (ξ_{1c}, $k_{1\xi}$). It is worth mentioning that the developed current controller will also work with other methods of current reference generation.

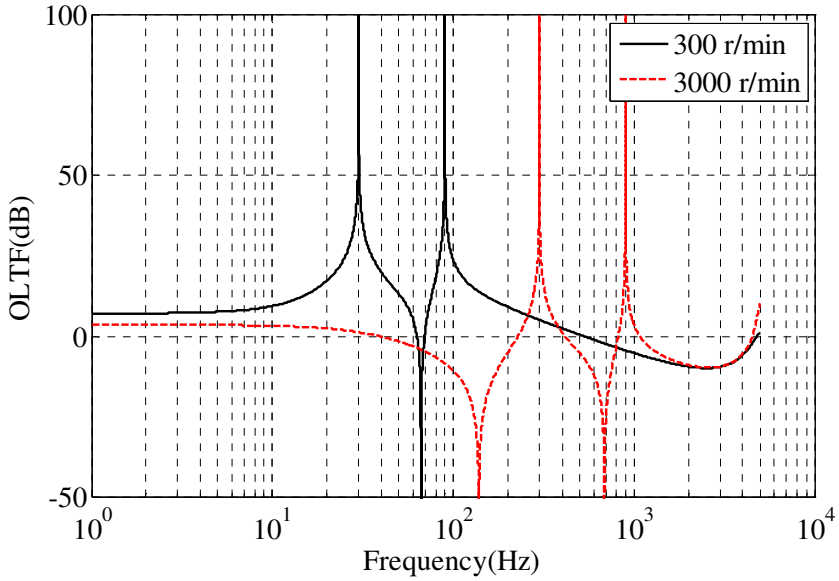

Fig. 7-5: Open loop transfer function magnitude plots at 300 r/min and 3000 r/min.

Fig. 7-6 shows the controller tracking response at 300 r/min and 3000 r/min. It can be observed that the controller is able to track the references within 1.2 electrical cycle. In order to quantify this further, theoretical settling time of the controller at various operating speed of the machine is shown in Fig. 7-7. The average settling time of the controller is less than 1.2 electrical cycles. It should be pointed out that it is possible to tune resonant controller(s) for a fast settling time of less than a quarter cycle of a reference with fixed frequency as reported in [150]. However, this is not the case if the frequency of a reference varies unless the proportional gain is increased to a high value which would compromise noise rejection property.

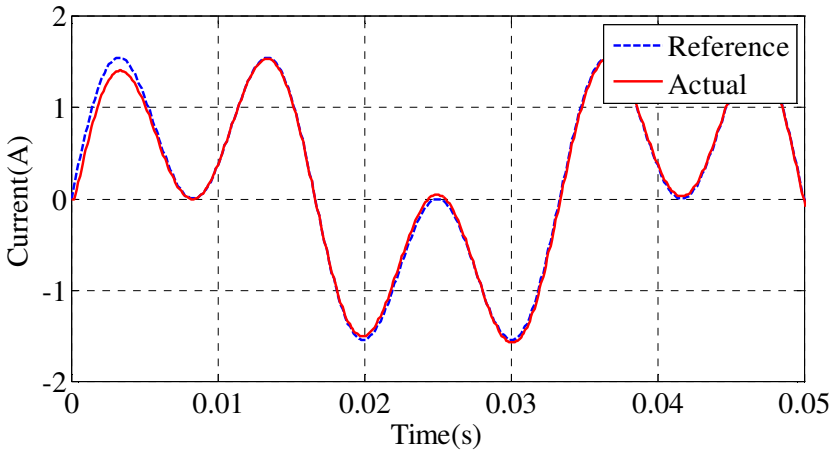

(a)

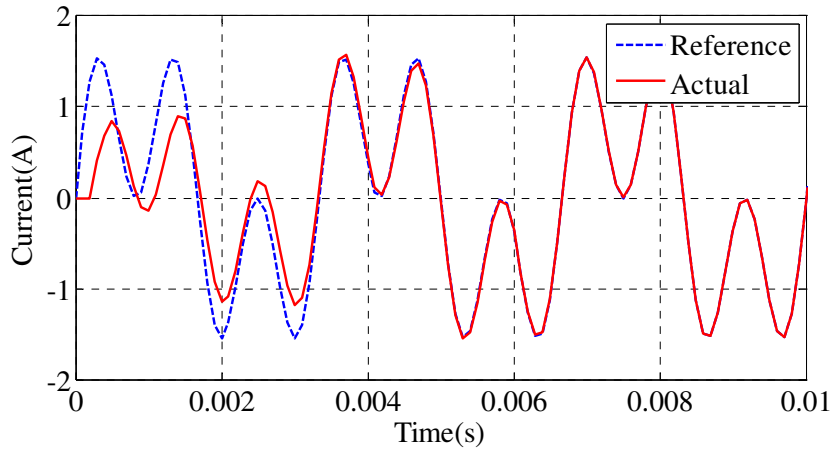

(b)

Fig. 7-6: Controller closed loop response at (a) 300 r/min and (b) 3000 r/min

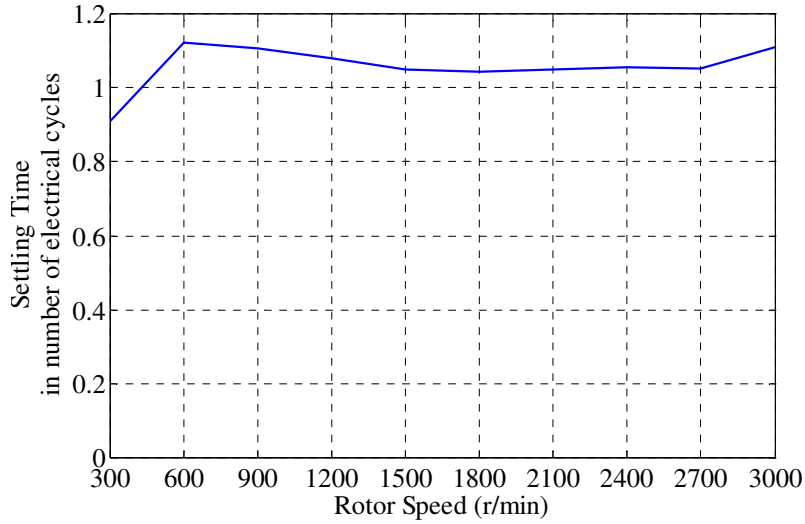

Fig. 7-7: Settling time variation in number of electrical cycles (+/- 4% criterion) with motor speed

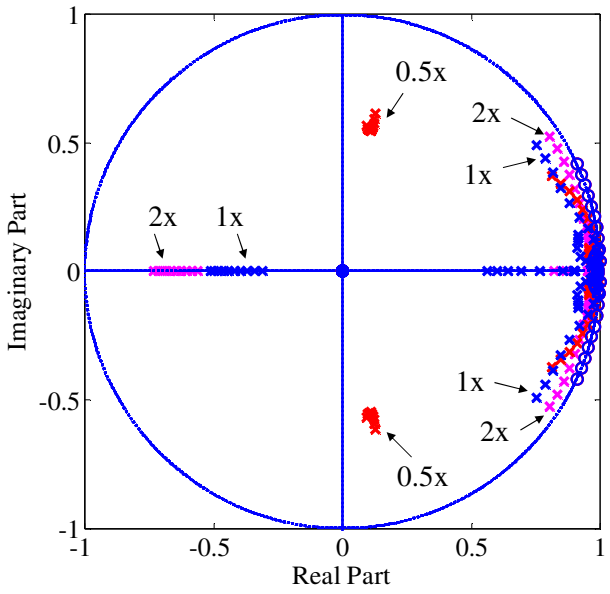

Fig. 7-8: Variation of closed loop poles and zeros with changing plant parameters. Blue – 1x , Red – 0.5x, magenta – 2x times nominal resistance and inductance.

Fig. 7-8 shows the variations of closed loop poles when the motor parameters are varied from 0.5 to 2 times their nominal values. It can be seen that although the poles/zeroes are shifted from those designed with the motor nominal parameters, they are within the unit circle and hence the system is robust even with 4 times variations in parameters.

Resonant controllers due to its inherently high gain at the resonant frequency, can quickly windup when operating close to voltage limit. In [149] anti windup techniques for resonant controllers was investigated. One of the techniques proposed was to increase damping coefficient in the resonant controller to reduce the gain, however the authors noted this can have an adverse effect on the tracking performance of the control An anti-winding up protection similar to that reported in [150], [155] shown in Fig. 7-9. It can be shown that under linear condition (no saturation) the closed loop transfer function of the inner controller feedback loop is equal to *H(z)* as given by (7.23). Since the term in the forward path of the controller is only a proportional gain and all the states of the controller (present in the feedback path) are driven only by the actual (saturated) values, windup does not occur [155].

$$\frac{V(z)}{U(z)} = \frac{K_\infty}{1+\left(H(z)^{-1} - K_\infty{}^{-1}\right)K_\infty} = H(z) \tag{7.25}$$

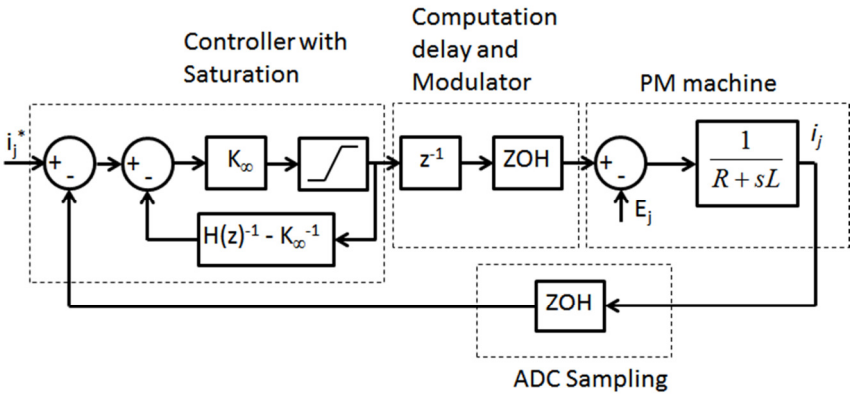

Fig. 7-9: Controller structure with anti-windup

7.6 Zero Sequence Voltage Injection

By employing the proposed resonant controller, the current in each phase is controlled separately. The PWM signals for each inverter leg are also generated separately from the controller output voltage for each phase. To boost inverter output voltages, zero sequence voltage is injected into the modulator inputs [159], as shown in Fig. 7-10.

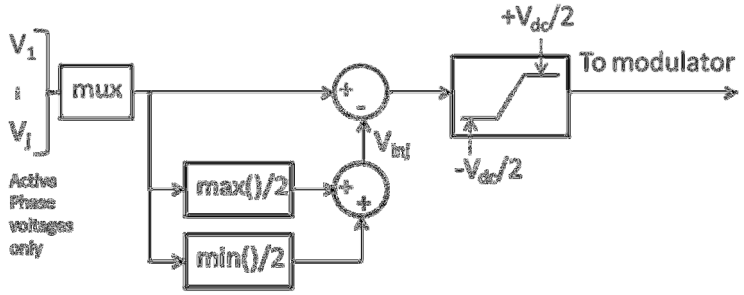

Fig. 7-10: Zero sequence voltage injection block

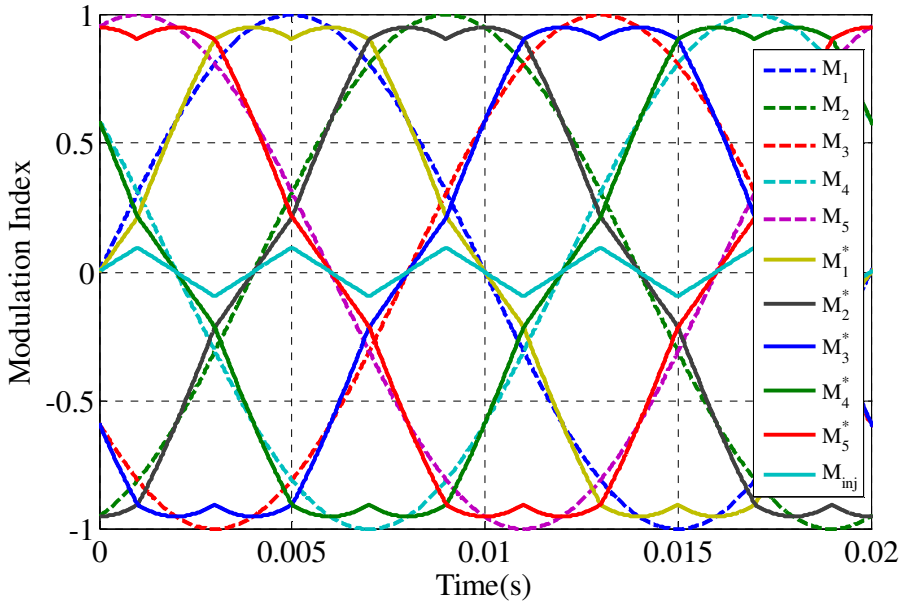

Fig. 7-11: Modulation index with and without voltage injection

The injection of the zero sequence voltage reduces the peak voltage command to the modulator without affecting the line-to-line voltage. By way of example, Fig. 7-11 compares sinusoidal modulation index command (M_i) in healthy conditions with the output of the voltage injection block. It can be seen that the output (M_i*) is lower in magnitude than (M_i) and this can improve the torque speed characteristic especially in the field weakening region.

7.7 Torque Speed Characteristics

Fig. 7-12 compares the torque speed characteristics of the 5-phase PM machine under healthy and fault conditions with and without the zero sequence voltage injection. They are obtained by application of the OTC algorithm to generate phase current references under the voltage and current limits (7.26) and using (7.27) for voltage calculation, assuming that tracking of these references are perfect. The weight factor for field weakening at a given speed is obtained by a search algorithm to maximize the torque under the voltage and current constraints. It can be observed that with the zero sequence voltage injection, torque capability of the drive can be improved by around 9.18% in healthy case, around 22% in OC fault case, and around 30.8% in SC fault case at a speed of 1800 r/min.

$$\max\left(V_j(t)\right) \le \frac{V_{dc}}{2}$$
$$\max\left(RMS\left(I_j\right)\right) \le I_{rms,\max} \tag{7.26}$$

$$V_j(t) = Ri_j(t) + L\frac{di_j(t)}{dt} + E_j(t) - V_{inj}(t)$$
$$V_{inj}(t) = 0.5\left(\max\left(...,V_j,...\right) + \min\left(...,V_j,...\right)\right) \quad \forall j \neq l \tag{7.27}$$

Fig. 7-13 shows the final controller structure including voltage injection block, where $V_{j,unsat}$ is the output of the j^{th} phase proportional gain controller K_∞.

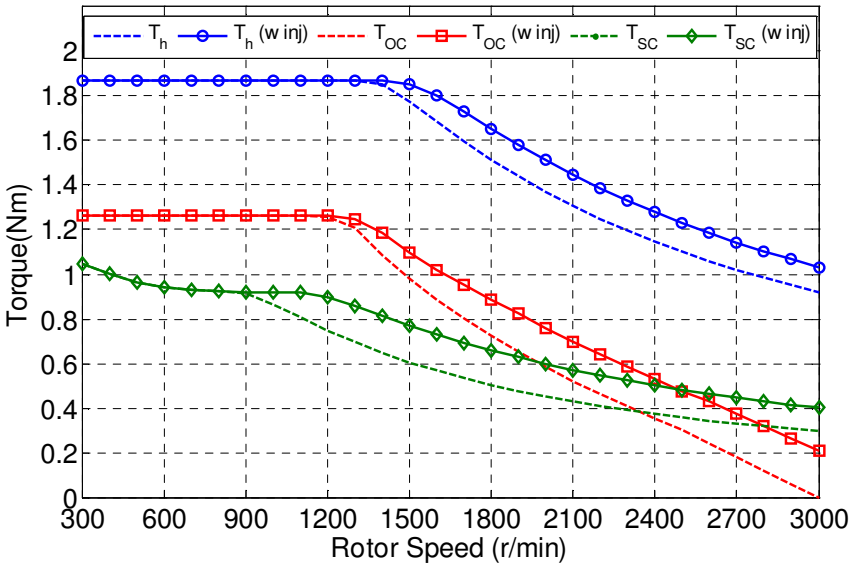

Fig. 7-12: Torque speed characteristic under healthy (h), single phase open circuit (OC) and single phase short circuit (SC) with (w inj) and without voltage injection.

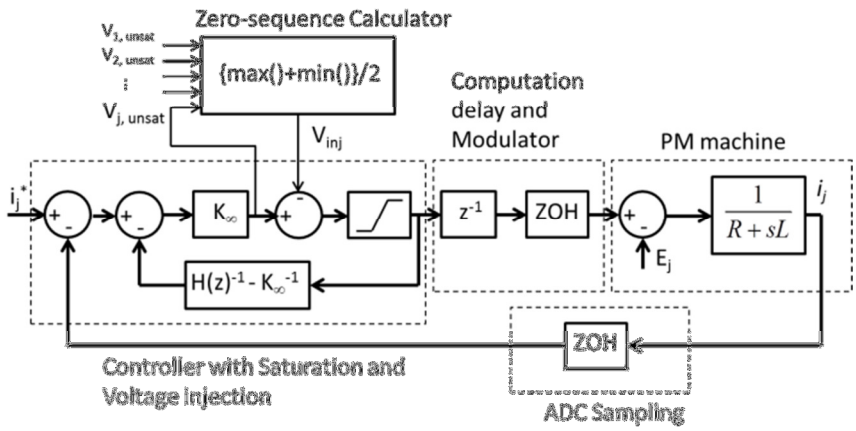

Fig. 7-13: Final controller structure including voltage injection

7.8 Field Weakening

Field weakening can be performed in the optimal torque control scheme by changing the field weakening constant k_{fld}. The effect of changing k_{fld} in (7.1), leads to an increase in the current at the same torque set point so that the overall flux in the machine is reduced.

In [113] it was proposed that torque error be utilized for determining amount of field weakening. This was performed since the control in [113] utilized hysteresis current controller and it is not possible to determine command voltages generated by the modulator. However traditional field weakening control for PM machines utilizes voltage command to determine field weakening [160]. Fig. 7-14 shows the simulation result of varying k_{fld} on peak current and voltages, at a fixed load torque T_d=0.71Nm, and speed of 2000 r/min. It can be observed that as k_{fld} is varied peak current increases monotonically, however peak voltage first decreases and then increases. Therefore, a key requirement for the k_{fld} -update algorithm is to reduce the peak voltage and this is achieved using perturb and observe (P&O) algorithm. This is quite different from the traditional field weakening algorithm in healthy machines due to the unbalanced currents demanded by the OTC in fault condition. In this method the sign of the last perturbation, i.e., change of k_{fld}, and the sign of the last peak voltage change, is used to determine the direction of next change in value of k_{fld}. If the peak voltage demand is less than $V_{dc}/2$, k_{fld} is reduced in order to reduce current demand and thereby reducing the copper losses. Due to the non-sinusoidal currents generated by the OTC under fault condition, voltage waveforms are also non-sinusoidal. Hence, peak voltage (V_{pk}) cannot be determined apriori, therefore is measured every electrical cycle by the controller. The field weakening algorithm is detailed in a flowchart shown in Fig. 7-15, where V_{th} is a threshold voltage used to reduce the effect of voltage noise on the algorithm. V_{th} is set at 1V in experiments. The algorithm is evaluated every 4 electrical cycles denoted by q in order to allow the controller to settle after change in k_{fld}. Although this field weakening controller will have a slower response compared to conventional field weakening control in healthy machines, it should be appreciated that under fault condition the conventional field weakening controller cannot be used due to presence of unbalance and harmonic voltages.

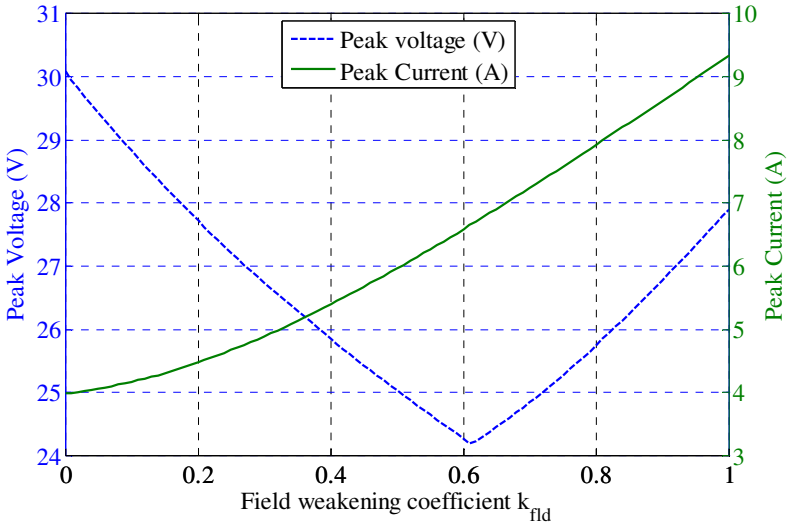

Fig. 7-14: Effect of varying field weakening coefficient on voltage (T_d = 0.71Nm at 2000 r/min)

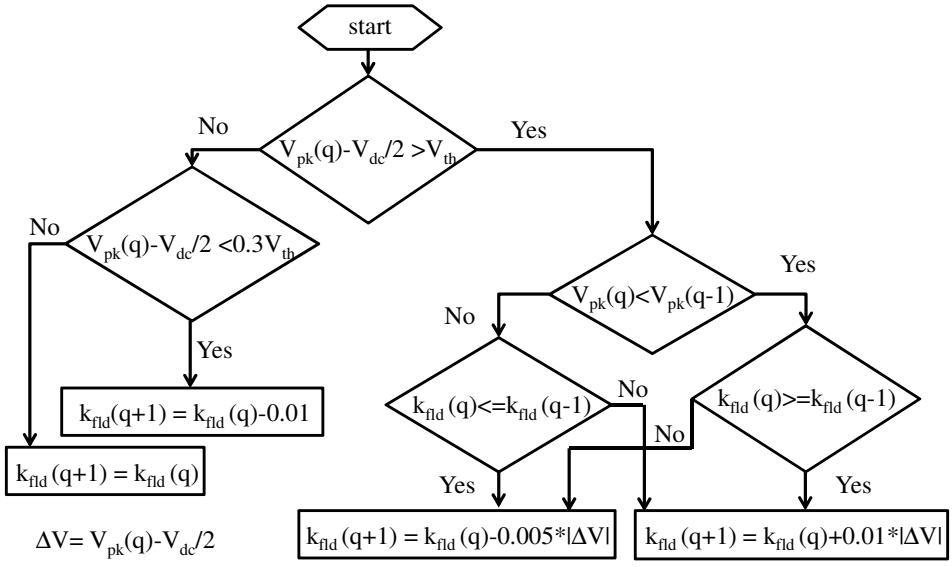

Fig. 7-15: k_{fld} -update algorithm

7.9 Experimental Validations

To validate the developed fault tolerant control strategy, a 5 phase PM machine fed by 5 phase custom inverter described in chapter 5 is utilised. It is to be noted though, that the controller described in Appendix is not used here, the proposed controller described in this chapter is used instead. Fig. 7-16 shows the simplified schematic of the fault setup.

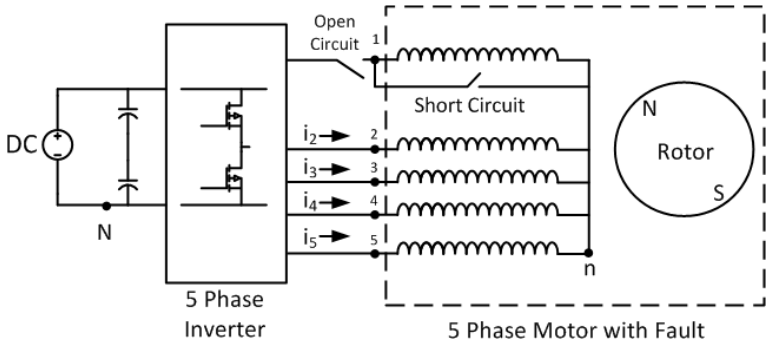

Fig. 7-16: Simplified schematic of the test setup

To validate the design, first steady state torque-speed characteristics are obtained, by sweeping the T_d and k_{fld} command until maximum torque is obtained without violating the voltage or current limit. Fig. 7-17 shows the predicted and measured torque-speed characteristics and variation of k_{fld} with speed. The reduction in the measured torque is expected and is attributed to voltage drop in the devices, controller tracking error, and to variation in back-EMFs over a mechanical cycle due to tolerance on magnet properties and dimensions. Fig. 7-18 and Fig. 7-19 show similar comparisons for the OC and SC fault in phase 1, respectively.

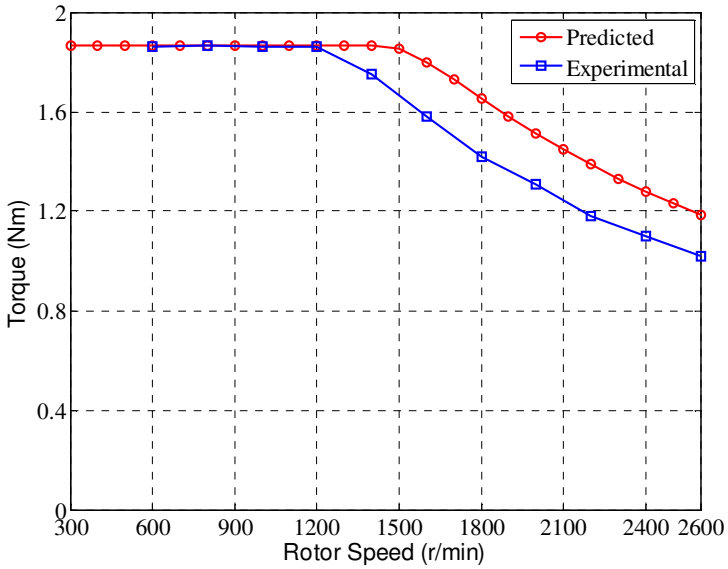

(a)

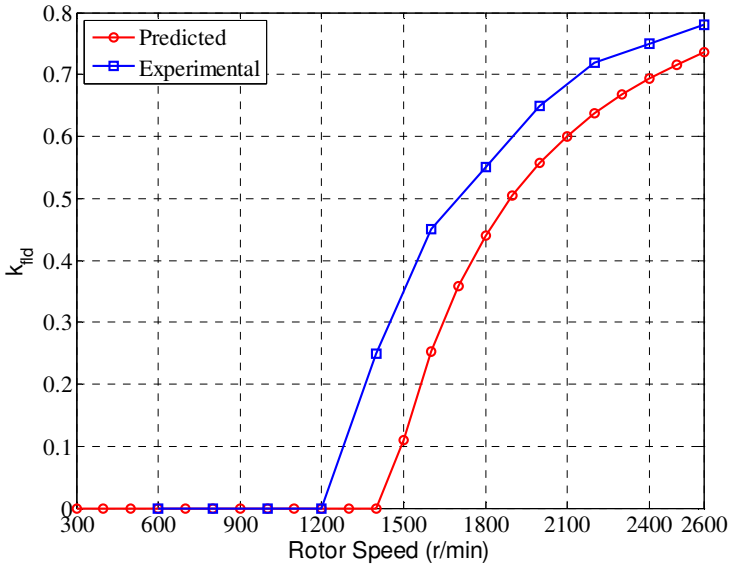

(b)

Fig. 7-17: (a) Torque-speed and (b) k_{fld}-speed plots for healthy operation

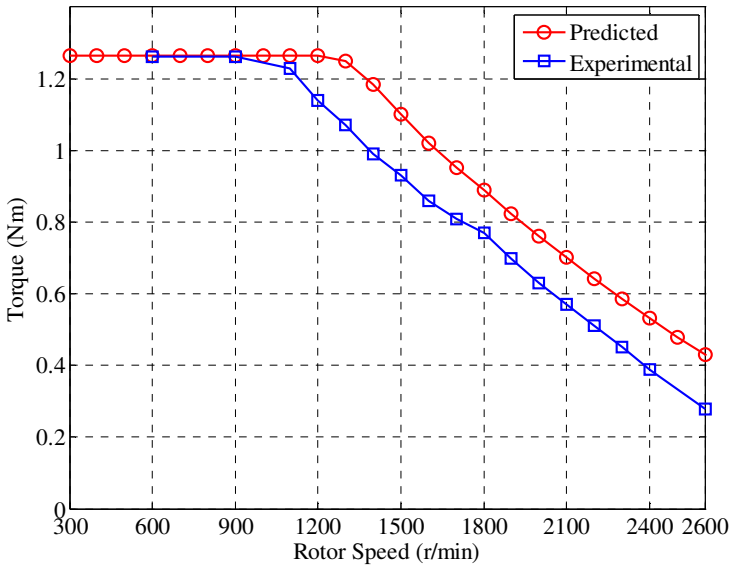

(a)

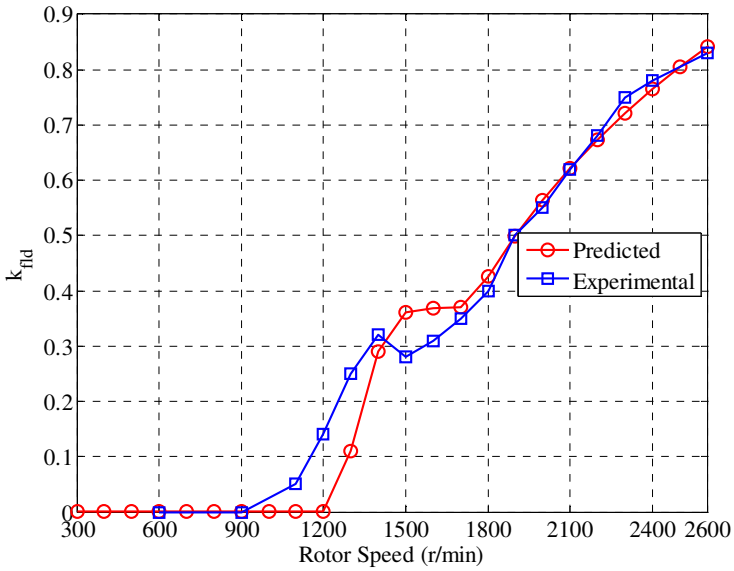

(b)

Fig. 7-18: (a) Torque-speed and (b) k_{fld} -speed plots for single phase open circuit operation

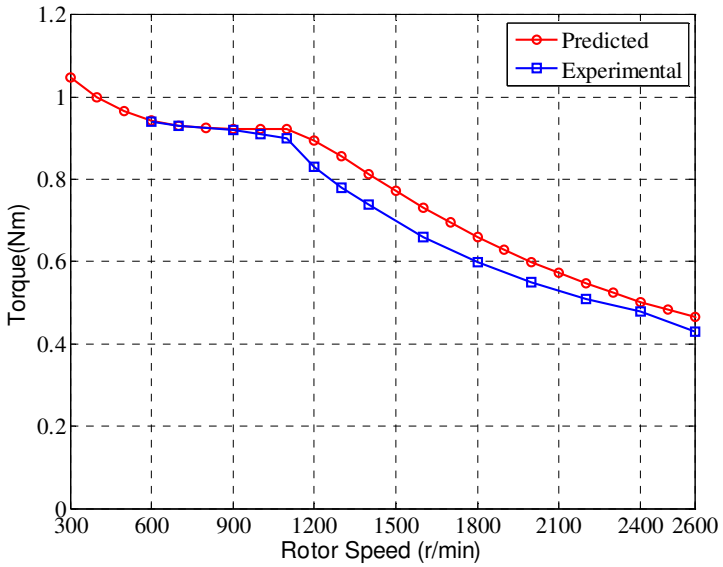

(a)

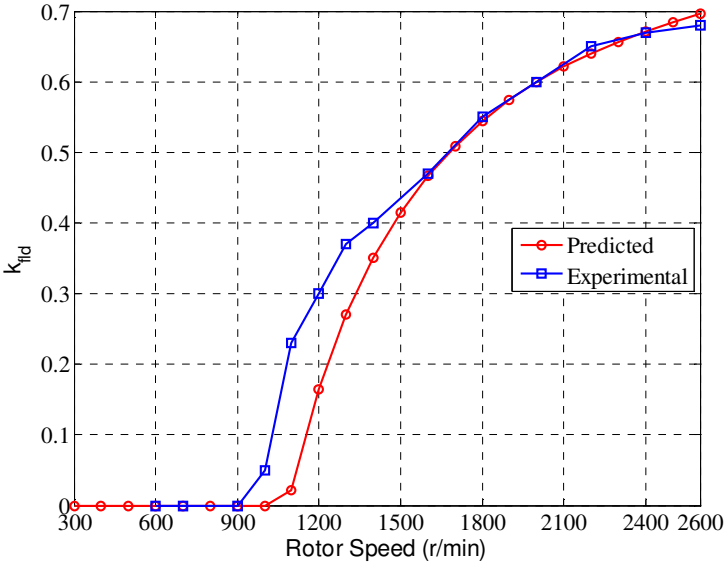

(b)

Fig. 7-19: (a) Torque-speed and (b) k_{fld} -speed plots for single phase short operation

To test the transient response of the current controller, step loading of 1Nm (53% nominal load) is performed at 600 r/min and 2000 r/min under healthy condition as shown in Fig. 7-20. The controller settles within 1.5 electrical cycles. Due to limitations of number of oscilloscope channels only 4 currents waveforms are shown.

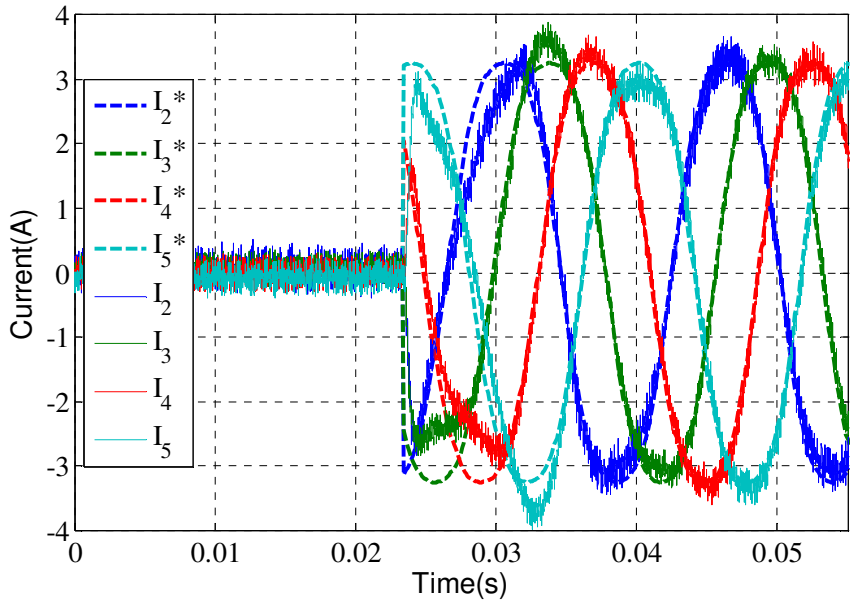

(a)

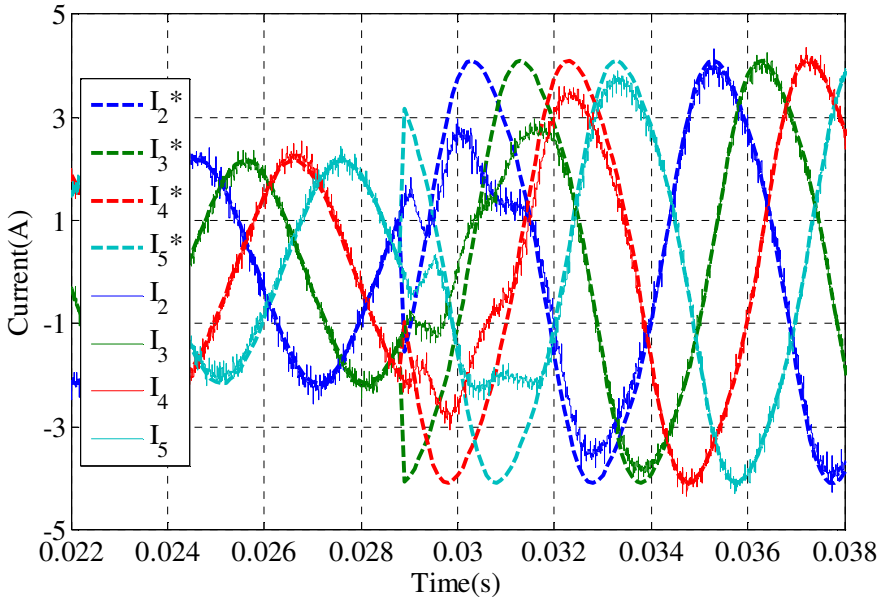

(b)

Fig. 7-20: Current responses to step change in torque demand of 1 Nm under healthy operation (a) at 0.023s with k_{fld} =0 at 600 r/min (60Hz) and (b) at 0.0287s with k_{fld} = 0.3 at 2000 r/min (200Hz).

To test the performance of the controller during transition from healthy to fault operating mode, an OC phase fault is initiated in phase-1 by opening phase-1 contactor at 0.03s at 600 r/min and 0.024s at 1200 r/min. The resultant current waveforms are

shown in Fig. 7-21. It can be observed that the controller tracks new references within 1.5 electrical cycles.

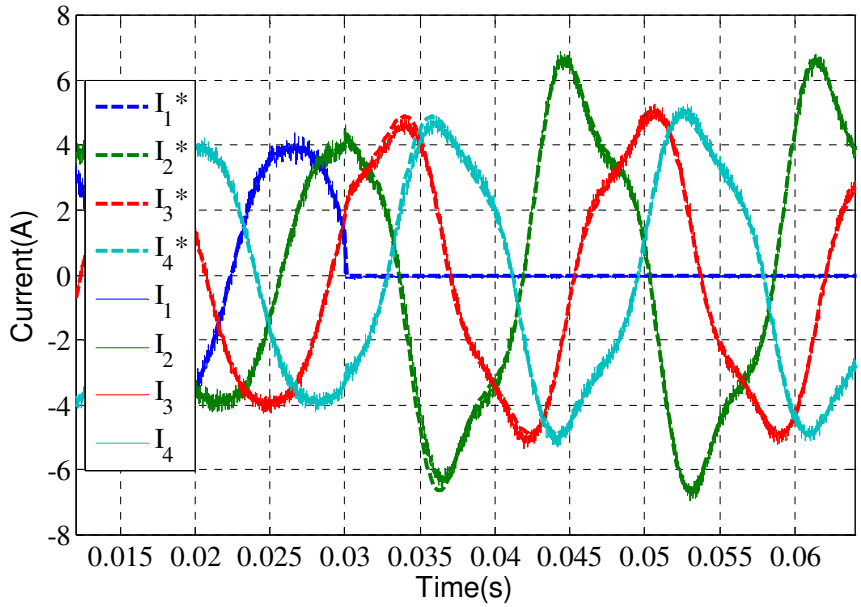

(a)

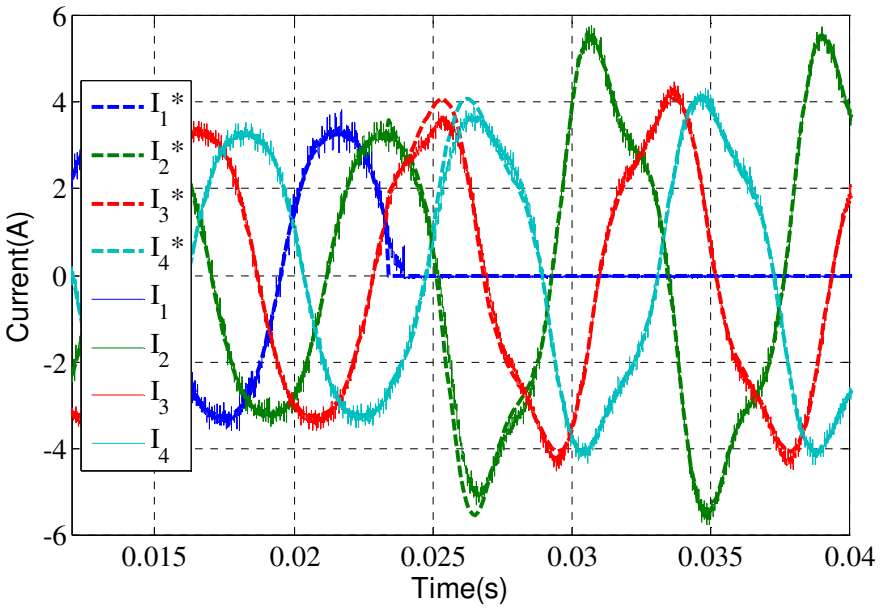

(b)

Fig. 7-21: Current responses to transition from Healthy to phase-1 OC (a) at 0.03s with T_d=1.2Nm at 600 r/min (60Hz) (b) at 0.024s with T_d=1Nm at 1200 r/min (120Hz).

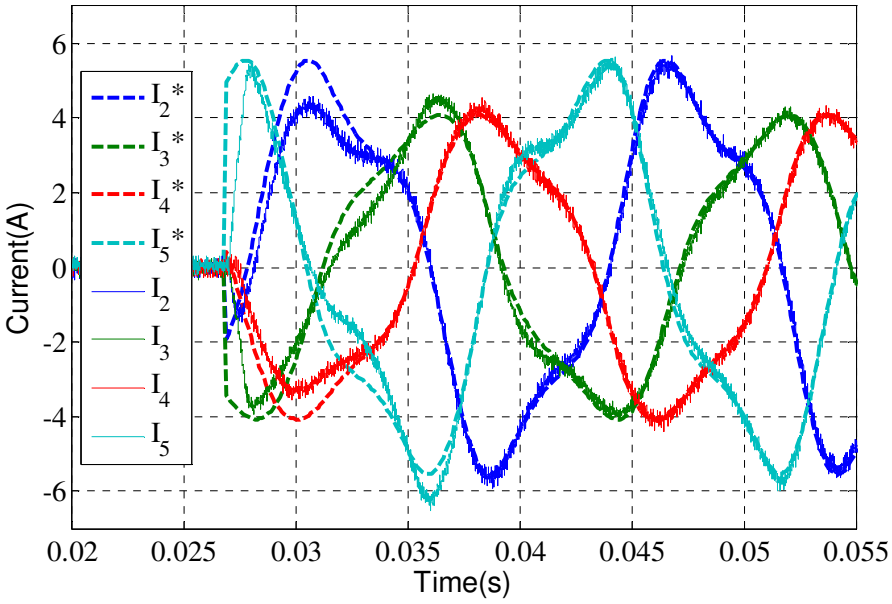

(a)

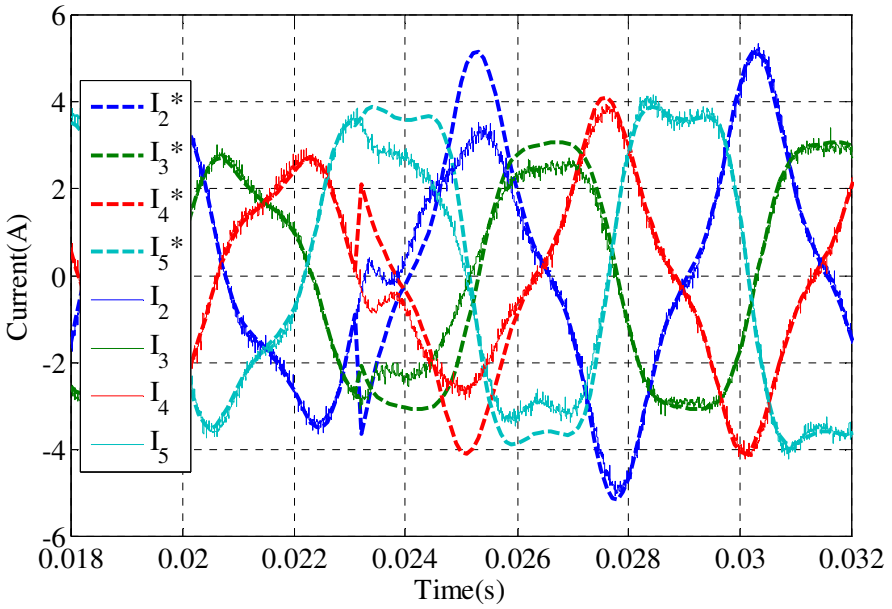

(b)

Fig. 7-22: Current responses to torque step change under phase-1 OC at (a) T_d *=0 to 1Nm at 0.027s* with k_{fld}=0 at 600 r/min (b) T_d*=0 to 0.6Nm at 0.023s with* k_{fld} =0.45 at 2000 r/min

Torque step responses under the OC are tested at 600 r/min and 2000 r/min and the results are shown in Fig. 7-22. It can be observed that the current settles in less than 1.5 electrical cycles. Similar tests are performed under the SC fault in phase-1 at 600 r/min and 2000 r/min and the current waveforms are shown in Fig. 7-23. It is to be noted that under the SC condition current references are not 0 even with k_{fld} =0 (no field

weakening). This is expected since the OTC generates current references to cancel out the pulsating torque due to phase-1 SC. It is also worth mentioning that the speed regulation of the dynamometer used in the test-setup is not ideal and a step load change also causes a speed deviation of approximately 80 r/min which causes slightly sluggish response compared to simulation.

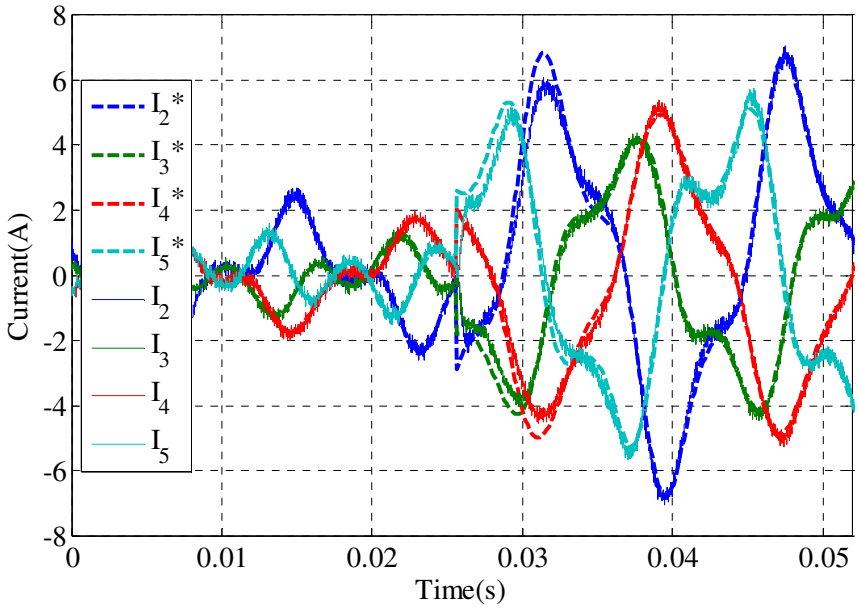

(a)

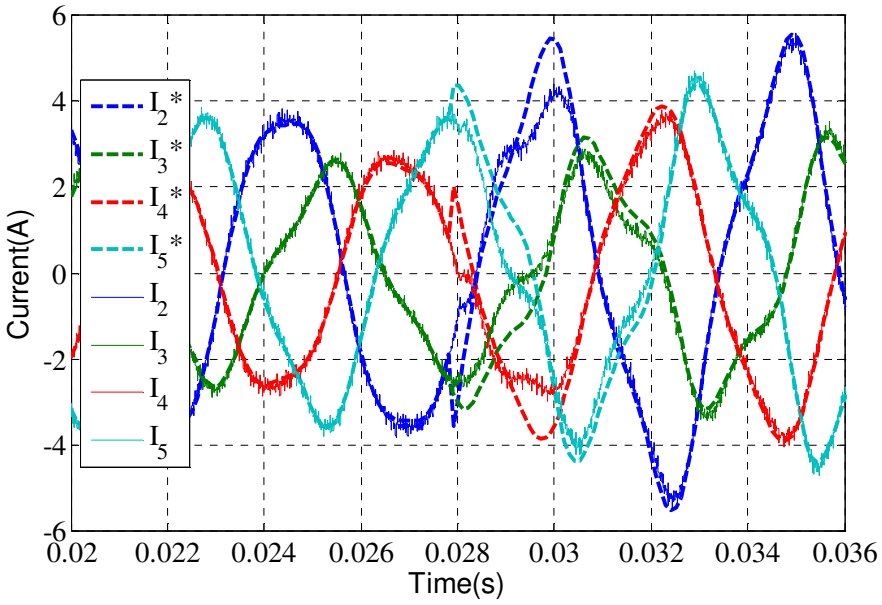

(b)

Fig. 7-23: Current responses to torque step change under phase-1 SC (a) T_d=*0 to 0.8Nm at 0.025s with* k_{fld} =0 at 600 r/min (b) T_d=0 to 0.45Nm at 0.0278s with k_{fld} =0.45 at 2000 r/min. I_1 is the short circuit current flowing in phase-1.

Fig. 7-24 shows the response of field weakening controller at 2200 r/min with a torque step from 0.2Nm to 0.5Nm. The peak voltage error is the difference between the maximum peak voltage demand and the maximum inverter phase voltage Vdc/2. It can be seen from the plot that the current tracking error is minimal after 0.2 sec. It is to be noted that the torque step causes the speed of the machine to change and this results is the variation of k_{fld} to continue after 0.2 sec.

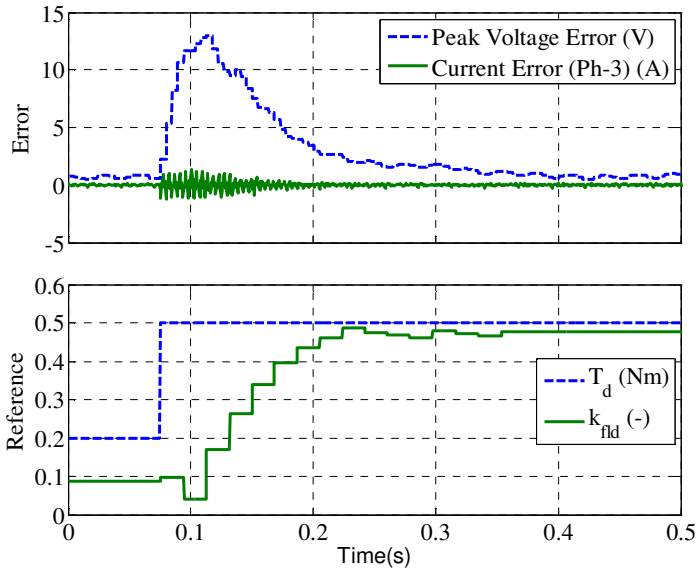

Fig. 7-24: Responses of voltage error, current tracking error and the field weakening factor to torque step change from 0.2Nm to 0.5Nm under phase-1 OC at 2200 r/min.

The effect of the OTC on torque ripple reduction can be appreciated in measured torque in SC condition at T_d =0 as shown in Fig. 7-25. It proves the efficacy of the OTC in achieving ripple torque reduction.

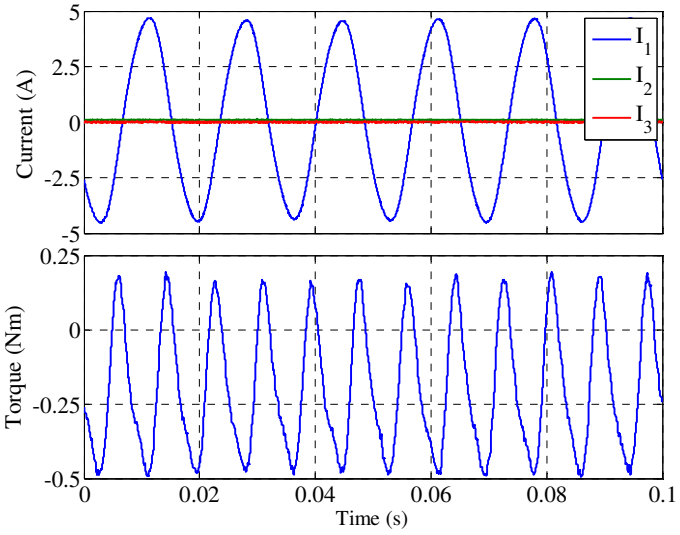

(a)

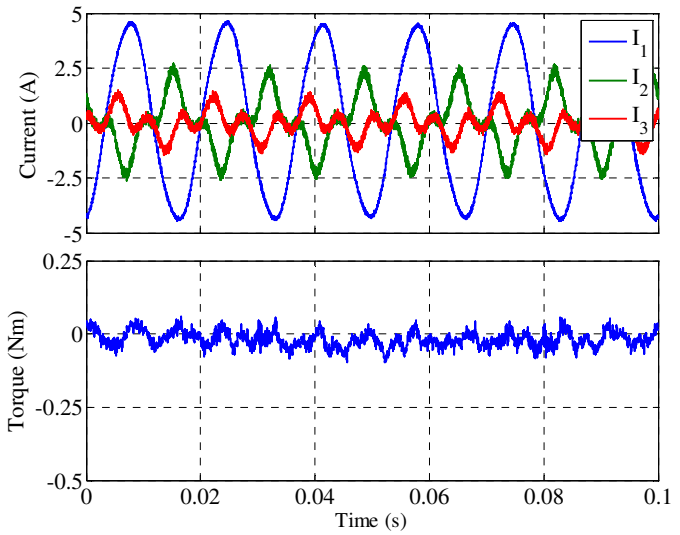

(b)

Fig. 7-25: Current and torque waveforms under SC (phase -1) at 600 r/min (a) without OTC control (b) with OTC (T_d=0). Scale: I_1: 5A/div, I_2: 5A/div, I_3: 5A/div, Torque: 1Nm/div. I_1 is the short circuit current flowing in phase-1

7.10 Conclusions

This chapter has described and validated a novel current controller in natural stationary frame for fault tolerant operation of poly-phase machines. The unique contribution of the work described in this chapter is a resonant control structure which allows pole-zero placements adapted to variable speed operations. It also incorporates zero sequence voltage injection and a suitable field weakening control to increase torque

and speed operating range of a fault tolerant permanent magnet machine drive. It has been shown that the proposed control is capable of tracking unbalanced and non-sinusoidal current references over a wide speed range, including field weakening. The proposed control operates under both healthy and fault conditions with minimum reconfiguration. The methods presented in this chapter provide new insights into the design of stationary frame resonant controls for variable speed drives.

Chapter 8

Conclusions and Future Work

8.1 Conclusions

The increasing application of permanent magnet machines in safety critical applications like electric vehicles and aircraft fuel pump systems necessitates research into reliable fault modelling, diagnostics and fault tolerant controls. This thesis has investigated and contributed to the existing body of knowledge in the areas of stator winding fault modelling, detection and fault mitigation techniques. The main contributions of the research are summarised as follows:

1. **Analytical Modelling of Stator Turn Fault in Surface Permanent Magnet Machines**

Stator inter-turn faults create a large circulating current in the faulted turns and can cause complete failure of the windings. An analytical method of calculating the parameters of a surface mounted permanent magnet (SPM) machine under stator turn fault has been presented. The model predicts the fault inductances and fault current to within a maximum error of 8% compared to FE simulations. The developed modelling technique is general and can be applied to any winding configuration SPM machine. The model can be utilised in analysing fault behaviour and development of fault detection techniques.

2. **Transient Modelling of Interior Permanent Magnet Machine with Stator Turn Fault**

Modelling stator turn fault in interior permanent magnet (IPM) machines is a difficult problem since the machine has a non-linear magnetic behaviour even under

healthy conditions. Under fault condition accurately capturing the non-linear behaviour is quite challenging. One approach proposed in this thesis is the use of extensive FE simulations with turn fault to obtain a current to flux linkage map. Once this non-linearity map of the machine has been determined it is combined with the voltage equation of a faulted machine to obtain the transient model of the machine under fault. In order to reduce the number of FE computations for skewed rotors an analytical approach is proposed and investigated which enable the use of only one rotor slice FE simulations to calculate the current-flux linkage mapping for the entire rotor. Thus it leads to the reduction of number of FE cases for an *n*-stepped rotor by a factor of *n*. It is shown through simulation and experiments that the model established with the proposed method is accurate and computationally efficient, and is able to capture the harmonics in the fault current and the *dq* current in sufficient detail. The proposed modelling technique can also be used for modelling stator turn faults in other electrical machines including surface PM machines, switched reluctance machines, switched flux machines and wound field synchronous machines. The proposed model provides an effective tool for assessing inter-turn short-circuit fault behaviour and for evaluation of associated fault detection techniques and mitigation strategies.

3. Semi-Analytical Model of IPM Machine with Stator Turn Fault

Stator turn fault modelling using direct FE based extraction of current-flux mapping although more accurate, require a lot of computation time to evaluate all the FE cases. Therefore there exists a need for a quick method of simulating an IPM machine with turn fault without extensive FE simulation. A semi-analytical modelling approach is presented in this thesis to obtain a representative model of the machine under fault using only the average current-to-flux linkage map. Therefore, the model enable drive engineers to develop a representative fault model with only limited healthy machine data already available to them for control of the machine. Experimental validations show that the model is accurate and the prediction error of fault current is around 12%.

4. Online Stator Fault Detection Using Residual Currents

Stator turn fault detection requires quick and robust detection to enable the application of fault mitigation techniques. The easiest technique is to use the controller data like command voltages and feedback currents to determine the presence of a fault. In this thesis, a combined fault detection scheme based on model based approach for inter-turn fault and high resistance connection is investigated. A thorough theoretical basis of the detection method is presented supported by real-time implementation of the fault detector. The method is shown to be able to reject disturbances due to load and speed changes and can distinguish the faulted winding from other healthy windings of the machine. In addition it is able to classify the fault as an inter-turn fault or a high resistance connection. Extensive experimental testing has been performed of a 5-phase machine to prove the efficacy of this method.

5. Online Stator Turn Fault Detection Using PWM Ripple Current Measurement

A new technique to detect turn fault using the ripple current generated by the PWM inverter has been presented in this thesis. It has been shown that under turn fault condition, the high frequency impedance of the winding decreases and thus causes an increase in the ripple current. A simulation modelling technique has been developed to model the fault using measured winding impedance under healthy and fault condition. Based on the simulations, a detector circuit to extract the PWM ripple current has been designed. Experiments confirm that PWM ripple based method can be used to successfully detect turn faults in the machine. A simple and effective software calibration technique has been proposed to cancel the ripple current expected under healthy operation to obtain a calibrated detector output. Application of simple fault threshold on the calibrated detector has been shown to be sufficient to determine fault. By quantifying the maximum of the detector outputs of all the phases, the faulted phase can be identified.

6. **Optimal Current Control of Poly-phase PM Machines under Open-Circuit and Short-Circuit Faults**

Open circuit and short circuit failure are two types of common winding failures in an electrical machine. In multi-phase machines due to higher degrees of control freedom, it is possible to control the machine under these faults, albeit with a reduced torque-speed envelope. In this thesis a method of generating optimal currents which minimize copper losses under healthy and fault condition for star connected 5-phase machine has been investigated. It has been shown that optimal torque control (OTC) algorithm generates current commands which are unbalanced both in fundamental and third harmonic frequencies. A novel stationary frame resonant current controller is proposed to track the current commands generated by the OTC. The benefit of the proposed stationary frame control is that the controller structure remains same in healthy and fault conditions, except for turning off the individual controller of the faulted phase. In doing so, the controllers in the other healthy phases are not affected. Secondly, under field weakening condition, voltage saturation can be dealt with individually for each phase rather than combined in the form of space vectors, thus simplifying the control structure. It has been shown that the proposed control structure can track the current references over wide frequency ranges and is stable under voltage saturation. Zero sequence voltage injection and a field weakening control is proposed to increase the operating torque and speed range of a fault tolerant permanent magnet machine drive. The proposed control structure is validated experimentally under both healthy and fault conditions. The method presented in this thesis is expected to provide new insights into the design of stationary frame resonant controls for variable speed drives.

8.2 Future Work

Although several novel techniques were presented in this thesis, further research is required to improve their performance and robustness as summarised below.

1. **Analytical Modelling of Stator Turn Fault in Surface Permanent Magnet Machines**

Although this thesis presents a generalised analytical modelling of turn fault for SPM machine, it was shown that the simplified calculation of leakage inductance is not very accurate for non-overlapped windings. This is the main reason for the 8% error in the prediction by the developed model verses FE simulations. This error stems from the assumption of parallel leakage flux lines to the slot bottom in the slot area. One approach to improve the fidelity of the prediction can be by using the technique in [54] and extending it to the fault case. Therefore further research is required to remove the mathematical difficulties in extending the approach of [54] to the fault case.

2. **Transient Modelling of Interior Permanent Magnet Machine with Stator Turn Fault**

FE based model proposed in the thesis attempts to capture the effect of turn fault and magnetic non-linearity in a set of current-flux linkage maps. However, the effect of iron losses and temperature is not accounted for in the model. One approach could be to utilise technique as given in [67], [161] and applying it to the fault model. However, it is to be noted that the method in [67], [161] needs to be modified substantially since the fault divided the winding into two separate parts and losses and thermal model of the machine is very different from that of a healthy machine. The model also does not account for any demagnetisation that can occur in the machine due to the fault, which could be necessary to certain fault detection algorithms. Further research is needed to solve these issues.

3. **Semi-Analytical Model of IPM Machine with Stator Turn Fault**

The semi analytical model is a quick approximate model using only healthy data of the machine to build a fault model. It assumes that the MMF wave consists primarily of the fundamental frequency with little or no other contribution from other higher order harmonics. It has been shown to work well in case of a distributed winding machine. It requires further investigation on its applicability to fractional slot machines. Also

incorporation of iron losses and thermal effects into the fault model requires further research.

4. Online Stator Fault Detection Using Residual Currents

Fundamental model and non-model based approach was investigated and tested experimentally on a 5-phase SPM machine. Simulation for IPM machine was performed, and the results showed that it is possible to utilise the same method for fault detection in IPM machines. However, experimental validation needs to be performed to evaluate the robustness of this technique to magnetic saturation. Another important point is the effect of temperature. It is known that temperature changes the parameters of the machine such as back-EMF. In this thesis, temperature was assumed constant. Therefore, accounting temperature variation in the internal motor model and means of compensation of fault thresholds needs further investigation.

5. Online Stator Turn Fault Detection Using PWM Ripple Current Measurement

PWM current ripple based stator turn fault detection was tested with a 5-phase SPM machine. The method can be extended to IPM machines, and further simulation and hardware testing is required to test its validity for IPM machines in presence of magnetic saturation.

6. Optimal Current Control of Poly-phase PM Machines under Open-Circuit and Short-Circuit Faults

A novel fault tolerant controller was proposed and experimentally validated in this thesis. However it was noted that the field weakening algorithm was slow because of use of perturb and observe algorithm to perform field weakening. Therefore, field weakening control requires further investigation in order to reduce the settling times. The OTC reference generation proposed in the thesis only applies to SPM machines with constant machine parameters. Further investigation is required to extend this technique for IPM machine with load dependent saturation.

Bibliography

[1] Z. Q. Zhu and D. Howe, "Electrical Machines and Drives for Electric, Hybrid, and Fuel Cell Vehicles," *Proceedings of the IEEE*, vol. 95, no. 4, pp. 746 –765, Apr. 2007.

[2] N. Bianchi, M. D. Pré, and S. Bolognani, "Design of a fault-tolerant IPM motor for electric power steering," *IEEE Transactions on Vehicular Technology*, vol. 55, no. 4, pp. 1102–1111, Jul. 2006.

[3] K. T. Chau, C. C. Chan, and C. Liu, "Overview of Permanent-Magnet Brushless Drives for Electric and Hybrid Electric Vehicles," *IEEE Transactions on Industrial Electronics*, vol. 55, no. 6, pp. 2246–2257, Jun. 2008.

[4] J. W. Bennett, G. J. Atkinson, B. C. Mecrow, and D. J. Atkinson, "Fault-Tolerant Design Considerations and Control Strategies for Aerospace Drives," *Industrial Electronics, IEEE Transactions on*, vol. 59, no. 5, pp. 2049 –2058, May 2012.

[5] J. A. Haylock, B. C. Mecrow, A. G. Jack, and D. J. Atkinson, "Operation of fault tolerant machines with winding failures," *IEEE Transactions on Energy Conversion*, vol. 14, no. 4, pp. 1490–1495, 1999.

[6] J. Haylock, B. Mecrow, A. Jack, and D. Atkinson, "Operation of a fault tolerant PM drive for an aerospace fuel pump application," in *Electric Power Applications, IEE Proceedings-*, 1998, vol. 145, pp. 441–448.

[7] "Improved Motors for Utility Applications, Volume 1: Industry Assessment Study: Update and Analysis," EPRI, Technical Report EL-4286-V1, Oct. 1982.

[8] "Report of Large Motor Reliability Survey of Industrial and Commercial Installations, Part I," *IEEE Transactions on Industry Applications*, vol. IA-21, no. 4, pp. 853–864, 1985.

[9] "Report of Large Motor Reliability Survey of Industrial and Commercial Installations, Part II," *IEEE Transactions on Industry Applications*, vol. IA-21, no. 4, pp. 865–872, 1985.

[10] O. V. Thorsen and M. Dalva, "A survey of faults on induction motors in offshore oil industry, petrochemical industry, gas terminals, and oil refineries," *IEEE Transactions on Industry Applications*, vol. 31, no. 5, pp. 1186–1196, 1995.

[11] A. H. Bonnett and C. Yung, "Increased Efficiency Versus Increased Reliability," *IEEE Industry Applications Magazine*, vol. 14, no. 1, pp. 29–36, 2008.

[12] S. Grubic, J. M. Aller, B. Lu, and T. G. Habetler, "A Survey on Testing and Monitoring Methods for Stator Insulation Systems of Low-Voltage Induction Machines Focusing on

Turn Insulation Problems," *IEEE Transactions on Industrial Electronics*, vol. 55, no. 12, pp. 4127–4136, 2008.

[13] I. Culbert, B. Lloyd, and G. Stone, "Stator insulation problems caused by variable speed drives," in *PCIC Europe, 2009. PCIC EUROPE '09. Conference Record*, 2009, pp. 187–192.

[14] A. H. Bonnett and G. C. Soukup, "Cause and analysis of stator and rotor failures in three-phase squirrel-cage induction motors," *IEEE Transactions on Industry Applications*, vol. 28, no. 4, pp. 921–937, 1992.

[15] Z. Sun, J. Wang, D. Howe, and G. Jewell, "Analytical Prediction of the Short-Circuit Current in Fault-Tolerant Permanent-Magnet Machines," *IEEE Transactions on Industrial Electronics*, vol. 55, no. 12, pp. 4210 –4217, Dec. 2008.

[16] P. Arumugam, T. Hamiti, C. Brunson, and C. Gerada, "Analysis of Vertical Strip Wound Fault-Tolerant Permanent Magnet Synchronous Machines," *IEEE Transactions on Industrial Electronics*, vol. 61, no. 3, pp. 1158–1168, Mar. 2014.

[17] Y.-S. Lee, K.-T. Kim, and J. Hur, "Finite-Element Analysis of the Demagnetization of IPM-Type BLDC Motor With Stator Turn Fault," *IEEE Transactions on Magnetics*, vol. 50, no. 2, pp. 889–892, Feb. 2014.

[18] G. M. Joksimovic and J. Penman, "The detection of inter-turn short circuits in the stator windings of operating motors," *IEEE Transactions on Industrial Electronics*, vol. 47, no. 5, pp. 1078–1084, Oct. 2000.

[19] B.-M. Ebrahimi and J. Faiz, "Feature Extraction for Short-Circuit Fault Detection in Permanent-Magnet Synchronous Motors Using Stator-Current Monitoring," *IEEE Transactions on Power Electronics*, vol. 25, no. 10, pp. 2673–2682, 2010.

[20] A. G. Espinosa, J. A. Rosero, J. Cusido, L. Romeral, and J. A. Ortega, "Fault Detection by Means of Hilbert -Huang Transform of the Stator Current in a PMSM With Demagnetization," *IEEE Transactions on Energy Conversion*, vol. 25, no. 2, pp. 312–318, Jun. 2010.

[21] F. Briz, M. W. Degner, A. Zamarron, and J. M. Guerrero, "Online stator winding fault diagnosis in inverter-fed AC machines using high-frequency signal injection," *IEEE Transactions on Industry Applications*, vol. 39, no. 4, pp. 1109–1117, 2003.

[22] J. Arellano-Padilla, M. Sumner, and C. Gerada, "Winding condition monitoring schemefor a permanent magnet machine using high-frequency injection," *IET Electric Power Applications*, vol. 5, no. 1, pp. 89–99, 2011.

[23] J. Penman, H. G. Sedding, B. A. Lloyd, and W. T. Fink, “Detection and location of interturn short circuits in the stator windings of operating motors,” *IEEE Transactions on Energy Conversion*, vol. 9, no. 4, pp. 652–658, Dec. 1994.

[24] T. Assaf, H. Henao, and G.-A. Capolino, “Simplified axial flux spectrum method to detect incipient stator inter-turn short-circuits in induction machine,” in *2004 IEEE International Symposium on Industrial Electronics*, 2004, vol. 2, pp. 815–819 vol. 2.

[25] K. Toni, M. Slobodan, and B. Aleksandar, “Detection of Turn to Turn Faults in Stator Winding with Axial Magnetic Flux in Induction Motors,” in *Electric Machines Drives Conference, 2007. IEMDC ’07. IEEE International*, 2007, vol. 1, pp. 826–829.

[26] Z. Sun, J. Wang, D. Howe, and G. W. Jewell, “An online winding fault detection technique for fault-tolerant PM machines,” *International Journal of Systems Science*, vol. 40, no. 3, pp. 289–296, Mar. 2009.

[27] Y. Da, X. Shi, and M. Krishnamurthy, “A New Approach to Fault Diagnostics for Permanent Magnet Synchronous Machines Using Electromagnetic Signature Analysis,” *IEEE Transactions on Power Electronics*, vol. 28, no. 8, pp. 4104–4112, Aug. 2013.

[28] P. Neti and S. Nandi, “Stator Interturn Fault Detection of Synchronous Machines Using Field Current and Rotor Search-Coil Voltage Signature Analysis,” *IEEE Transactions on Industry Applications*, vol. 45, no. 3, pp. 911–920, 2009.

[29] J. Yun, K. Lee, K.-W. Lee, S. B. Lee, and J.-Y. Yoo, “Detection and Classification of Stator Turn Faults and High-Resistance Electrical Connections for Induction Machines,” *IEEE Transactions on Industry Applications*, vol. 45, no. 2, pp. 666–675, Mar. 2009.

[30] J. Hang, J. Zhang, M. Cheng, and J. Huang, “Online Inter-turn Fault Diagnosis of Permanent Magnet Synchronous Machine Using Zero Sequence Components,” *IEEE Transactions on Power Electronics*, vol. PP, no. 99, pp. 1–1, 2015.

[31] M. van der Geest, H. Polinder, J. A. Ferreira, A. Veltman, J. J. Wolmarans, and N. Tsiara, “Analysis and Neutral Voltage-Based Detection of Interturn Faults in High-Speed Permanent-Magnet Machines With Parallel Strands,” *IEEE Transactions on Industrial Electronics*, vol. 62, no. 6, pp. 3862–3873, Jun. 2015.

[32] T. Boileau, N. Leboeuf, B. Nahid-Mobarakeh, and F. Meibody-Tabar, “Synchronous Demodulation of Control Voltages for Stator Interturn Fault Detection in PMSM,” *IEEE Transactions on Power Electronics*, vol. 28, no. 12, pp. 5647–5654, Dec. 2013.

[33] J. Quiroga, L. Liu, and D. A. Cartes, “Fuzzy logic based fault detection of PMSM stator winding short under load fluctuation using negative sequence analysis,” in *American Control Conference, 2008*, 2008, pp. 4262 –4267.

[34] S. Cheng, P. Zhang, and T. G. Habetler, “An Impedance Identification Approach to Sensitive Detection and Location of Stator Turn-to-Turn Faults in a Closed-Loop Multiple-Motor Drive,” *IEEE Transactions on Industrial Electronics*, vol. 58, no. 5, pp. 1545–1554, 2011.

[35] B. Aubert, J. Régnier, S. Caux, and D. Alejo, “Kalman-Filter-Based Indicator for Online Interturn Short Circuits Detection in Permanent-Magnet Synchronous Generators,” *IEEE Transactions on Industrial Electronics*, vol. 62, no. 3, pp. 1921–1930, Mar. 2015.

[36] A. Sarikhani and O. A. Mohammed, “Inter-Turn Fault Detection in PM Synchronous Machines by Physics-Based Back Electromotive Force Estimation,” *IEEE Transactions on Industrial Electronics*, vol. 60, no. 8, pp. 3472–3484, Aug. 2013.

[37] B. Sen and J. Wang, “Analytical modelling of stator turn fault in surface mounted permanent magnet machines,” in *2013 IEEE Energy Conversion Congress and Exposition (ECCE)*, 2013, pp. 4445–4452.

[38] A. H. Bonnett and G. C. Soukup, “Cause and analysis of stator and rotor failures in three-phase squirrel-cage induction motors,” *IEEE Transactions on Industry Applications*, vol. 28, no. 4, pp. 921–937, 1992.

[39] T. G. Habetler and Y. Lee, “Current-based condition monitoring and fault tolerant operation for electric machines in automotive applications,” in *International Conference on Electrical Machines and Systems, 2007. ICEMS*, 2007, pp. 2011 –2016.

[40] M. Dai, A. Keyhani, and T. Sebastian, “Fault analysis of a PM brushless DC Motor using finite element method,” *IEEE Transactions on Energy Conversion*, vol. 20, no. 1, pp. 1 – 6, Mar. 2005.

[41] O. A. Mohammed, S. Liu, and Z. Liu, “FE-based physical phase variable model of PM synchronous machines under stator winding short circuit faults,” *IET Science, Measurement & Technology*, vol. 1, no. 1, p. 12, 2007.

[42] B. Vaseghi, N. Takorabet, and F. Meibody-Tabar, “Fault Analysis and Parameter Identification of Permanent-Magnet Motors by the Finite-Element Method,” *IEEE Transactions on Magnetics*, vol. 45, no. 9, pp. 3290 –3295, Sep. 2009.

[43] B. Vaseghi, B. Nahid-mobarakh, N. Takorabet, and F. Meibody-Tabar, “Inductance Identification and Study of PM Motor With Winding Turn Short Circuit Fault,” *IEEE Transactions on Magnetics*, vol. 47, no. 5, pp. 978 –981, May 2011.

[44] R. M. Tallam, T. G. Habetler, and R. G. Harley, “Transient model for induction machines with stator winding turn faults,” *IEEE Transactions on Industry Applications*, vol. 38, no. 3, pp. 632–637, 2002.

[45] J. A. Farooq, T. Raminosoa, A. Djerdir, and A. Miraoui, "Modelling and simulation of stator winding inter-turn faults in permanent magnet synchronous motors," *COMPEL: The International Journal for Computation and Mathematics in Electrical and Electronic Engineering*, vol. 27, no. 4, pp. 887–896, Jul. 2008.

[46] L. Romeral, J. C. Urresty, J.-R. Riba Ruiz, and A. Garcia Espinosa, "Modeling of Surface-Mounted Permanent Magnet Synchronous Motors With Stator Winding Interturn Faults," *IEEE Transactions on Industrial Electronics*, vol. 58, no. 5, pp. 1576 – 1585, May 2011.

[47] K.-T. Kim, J.-K. Park, J. Hur, and B.-W. Kim, "Comparison of the Fault Characteristics of IPM-Type and SPM-Type BLDC Motors Under Inter-Turn Fault Conditions Using Winding Function Theory," *IEEE Transactions on Industry Applications*, vol. 50, no. 2, pp. 986–994, Mar. 2014.

[48] Z. Q. Zhu, D. Howe, E. Bolte, and B. Ackermann, "Instantaneous magnetic field distribution in brushless permanent magnet DC motors. I. Open-circuit field," *IEEE Transactions on Magnetics*, vol. 29, no. 1, pp. 124 –135, Jan. 1993.

[49] Z. Q. Zhu and D. Howe, "Instantaneous magnetic field distribution in brushless permanent magnet DC motors. II. Armature-reaction field," *IEEE Transactions on Magnetics*, vol. 29, no. 1, pp. 136–142, 1993.

[50] Z. Q. Zhu and D. Howe, "Instantaneous magnetic field distribution in brushless permanent magnet DC motors. III. Effect of stator slotting," *IEEE Transactions on Magnetics*, vol. 29, no. 1, pp. 143–151, 1993.

[51] Z. Q. Zhu and D. Howe, "Instantaneous magnetic field distribution in permanent magnet brushless DC motors. IV. Magnetic field on load," *IEEE Transactions on Magnetics*, vol. 29, no. 1, pp. 152 –158, Jan. 1993.

[52] Z. Q. Zhu, D. Howe, and C. C. Chan, "Improved analytical model for predicting the magnetic field distribution in brushless permanent-magnet machines," *IEEE Transactions on Magnetics*, vol. 38, no. 1, pp. 229–238, Jan. 2002.

[53] J. Wang, Z. P. Xia, and D. Howe, "Three-phase modular permanent magnet brushless Machine for torque boosting on a downsized ICE vehicle," *IEEE Transactions on Vehicular Technology*, vol. 54, no. 3, pp. 809 – 816, May 2005.

[54] Z. Q. Zhu, D. Howe, and J. K. Mitchell, "Magnetic field analysis and inductances of brushless DC machines with surface-mounted magnets and non-overlapping stator windings," *IEEE Transactions on Magnetics*, vol. 31, no. 3, pp. 2115–2118, May 1995.

[55] Y. Lee and T. G. Habetler, "A Phase Variable Simulation Model for Interior PM Synchronous Motor Drives with Stator Turn Faults," presented at the Power Electronics and Motion Control Conference, EPE-PEMC 2006, 2006, pp. 1074 –1079.

[56] I. Boldea, L. N. Tutelea, L. Parsa, and D. Dorrell, "Automotive Electric Propulsion Systems With Reduced or No Permanent Magnets: An Overview," *IEEE Transactions on Industrial Electronics*, vol. 61, no. 10, pp. 5696–5711, Oct. 2014.

[57] D. Dorrell, L. Parsa, and I. Boldea, "Automotive Electric Motors, Generators, and Actuator Drive Systems With Reduced or No Permanent Magnets and Innovative Design Concepts," *IEEE Transactions on Industrial Electronics*, vol. 61, no. 10, pp. 5693–5695, Oct. 2014.

[58] K. Kamiev, J. Montonen, M. P. Ragavendra, J. Pyrhonen, J. A. Tapia, and M. Niemela, "Design Principles of Permanent Magnet Synchronous Machines for Parallel Hybrid or Traction Applications," *IEEE Transactions on Industrial Electronics*, vol. 60, no. 11, pp. 4881–4890, Nov. 2013.

[59] P. Lazari, J. Wang, and L. Chen, "A Computationally Efficient Design Technique for Electric Vehicle Traction Machines," *IEEE Transactions on Industry Applications*, vol. 50, no. 5, pp. 3203–3213, Oct. 2014.

[60] J. A. Rosero, L. Romeral, J. A. Ortega, and E. Rosero, "Short-Circuit Detection by Means of Empirical Mode Decomposition and Wigner-Ville Distribution for PMSM Running Under Dynamic Condition," *IEEE Transactions on Industrial Electronics*, vol. 56, no. 11, pp. 4534–4547, Nov. 2009.

[61] O. A. Mohammed, Z. Liu, S. Liu, and N. Y. Abed, "Internal Short Circuit Fault Diagnosis for PM Machines Using FE-Based Phase Variable Model and Wavelets Analysis," *IEEE Transactions on Magnetics*, vol. 43, no. 4, pp. 1729–1732, Apr. 2007.

[62] Y. Lee, "A Stator Turn Fault Detection Method and a Fault-Tolerant Operating Strategy for Interior PM Synchronous Motor Drives in Safety-Critical Applications," PhD Thesis, Georgia Institute of Technology, 2007.

[63] K.-T. Kim, J. Hur, B. Kim, and G.-H. Kang, "Circulating current calculation using fault modeling of IPM type BLDC motor of inter-turn fault," in *2011 International Conference on Electrical Machines and Systems (ICEMS)*, 2011, pp. 1 –5.

[64] K.-T. Kim, J. Park, B. Kim, and J. Hur, "Comparison of the fault characteristics of IPM-type and SPM-type BLDC motors under Inter-Turn Faults conditions using Winding Function Theory," in *2012 IEEE Energy Conversion Congress and Exposition (ECCE)*, 2012, pp. 1262 –1269.

[65] N. Leboeuf, T. Boileau, B. Nahid-Mobarakeh, N. Takorabet, F. Meibody-Tabar, and G. Clerc, "Inductance Calculations in Permanent-Magnet Motors Under Fault Conditions," *IEEE Transactions on Magnetics*, vol. 48, no. 10, pp. 2605–2616, Oct. 2012.

[66] T. J. E. Miller, M. Popescu, C. Cossar, and M. McGilp, "Performance estimation of interior permanent-magnet brushless motors using the voltage-driven flux-MMF diagram," *IEEE Transactions on Magnetics*, vol. 42, no. 7, pp. 1867–1872, Jul. 2006.

[67] X. Chen, J. Wang, B. Sen, P. Lazari, and T. Sun, "A High-Fidelity, Computationally Efficient Model for Interior Permanent Magnet Machines Considering the Magnetic Saturation, Spatial Harmonics and Iron Loss Effect," *IEEE Transactions on Industrial Electronics*, vol. 62, no. 7, pp. 4044–4055, Jul. 2015.

[68] M. Boesing, M. Niessen, T. Lange, and R. De Doncker, "Modeling spatial harmonics and switching frequencies in PM synchronous machines and their electromagnetic forces," in *2012 XXth International Conference on Electrical Machines (ICEM)*, 2012, pp. 3001–3007.

[69] L. Chedot and G. Friedrich, "A cross saturation model for interior permanent magnet synchronous machine. Application to a starter-generator," in *Conference Record of the 2004 IEEE Industry Applications Conference, 2004. 39th IAS Annual Meeting*, 2004, vol. 1, p. 4 vol.(lvi+2822).

[70] N. Bianchi and S. Bolognani, "Magnetic models of saturated interior permanent magnet motors based on finite element analysis," in *The 1998 IEEE Industry Applications Conference, 1998. Thirty-Third IAS Annual Meeting*, 1998, vol. 1, pp. 27–34 vol.1.

[71] X. Chen, J. Wang, V. I. Patel, P. Lazari, L. Chen, and P. Lombard, "Reluctance Torque Evaluation for Interior Permanent Magnet Machines Using Frozen Permeability," in *7th IET International Conference on Power Electronics, Machines and Drives (PEMD 2014)*, Manchester, 2014, pp. 1–6.

[72] A. Sarikhani and O. A. Mohammed, "Inter-turn fault modeling of a variable speed pm wind generator using physics-based approach," in *Electric Machines Drives Conference (IEMDC), 2011 IEEE International*, 2011, pp. 636–641.

[73] S. Nadarajan, S. K. Panda, B. Bhangu, and A. K. Gupta, "Hybrid Model for Wound-Rotor Synchronous Generator to Detect and Diagnose Turn-to-Turn Short-Circuit Fault in Stator Windings," *IEEE Transactions on Industrial Electronics*, vol. 62, no. 3, pp. 1888–1900, Mar. 2015.

[74] Y. Kano, K. Watanabe, T. Kosaka, and N. Matsui, "A Novel Approach for Circuit-Field-Coupled Time-Stepping Electromagnetic Analysis of Saturated Interior PM Motors," *IEEE Transactions on Industry Applications*, vol. 45, no. 4, pp. 1325–1333, Jul. 2009.

[75] P. Lazari, B. Sen, J. Wang, and X. Chen, "Accurate d-q axis modelling of Synchronous Machines with Skew accounting for Saturation," presented at the IEEE International Magnetics Conference (INTERMAG - 2014), Dresden, 2014.

[76] E. Levi, "Saturation modelling in d-q axis models of salient pole synchronous machines," *IEEE Transactions on Energy Conversion*, vol. 14, no. 1, pp. 44 –50, Mar. 1999.

[77] Paul C. Krause, Oleg Wasynczuk, Scott D. Sudhoff, Steven Pekarek, *Analysis of Electric Machinery and Drive Systems*, 3rd Edition. Wiley-IEEE Press.

[78] *Saber version 2011.09*. Synopsys, Mountain View, CA 94043: Synopsys, Inc., 2011.

[79] *MATLAB version 7.10.0*. Natick, Massachusetts: The MathWorks Inc., 2010.

[80] R. Siebert, J. Schneider, and E. Beyer, "Laser Cutting and Mechanical Cutting of Electrical Steels and its Effect on the Magnetic Properties," *IEEE Transactions on Magnetics*, vol. 50, no. 4, pp. 1–4, Apr. 2014.

[81] A. Clerc and A. Muetze, "Measurement of Stator Core Magnetic Degradation During the Manufacturing Process," *IEEE Transactions on Industry Applications*, vol. 48, no. 4, pp. 1344–1352, Jul. 2012.

[82] P. Lazari, K. Atallah, and J. Wang, "Effect of laser cut on the performance of Permanent Magnet Assisted Synchronous Reluctance Machines," *IEEE Transactions on Magnetics*, vol. PP, no. 99, pp. 1–1, 2015.

[83] R. Islam, I. Husain, A. Fardoun, and K. McLaughlin, "Permanent-Magnet Synchronous Motor Magnet Designs With Skewing for Torque Ripple and Cogging Torque Reduction," *IEEE Transactions on Industry Applications*, vol. 45, no. 1, pp. 152–160, 2009.

[84] F. Piriou and A. Razek, "A model for coupled magnetic-electric circuits in electric machines with skewed slots," *IEEE Transactions on Magnetics*, vol. 26, no. 2, pp. 1096–1100, Mar. 1990.

[85] S. Williamson, T. J. Flack, and A. F. Volschenk, "Representation of skew in time-stepped two-dimensional finite-element models of electrical machines," *IEEE Transactions on Industry Applications*, vol. 31, no. 5, pp. 1009–1015, 1995.

[86] J. J. C. Gyselinck, L. Vandevelde, and J. A. A. Melkebeek, "Multi-slice FE modeling of electrical machines with skewed slots-the skew discretization error," *IEEE Transactions on Magnetics*, vol. 37, no. 5, pp. 3233–3237, 2001.

[87] Y. S. Chen, Z. Q. Zhu, and D. Howe, "Calculation of d- and q-axis inductances of PM brushless ac machines accounting for skew," *IEEE Transactions on Magnetics*, vol. 41, no. 10, pp. 3940 – 3942, Oct. 2005.

[88] G. Qi, J. T. Chen, Z. Q. Zhu, D. Howe, L. B. Zhou, and C. L. Gu, "Influence of Skew and Cross-Coupling on Flux-Weakening Performance of Permanent-Magnet Brushless AC Machines," *IEEE Transactions on Magnetics*, vol. 45, no. 5, pp. 2110 –2117, May 2009.

[89] B. Sen, J. Wang, and P. Lazari, "A detailed transient model of Interior Permanent Magnet motor accounting for saturation under stator turn fault," in *2013 IEEE Energy Conversion Congress and Exposition (ECCE)*, 2013, pp. 3548–3555.

[90] M. Meyer and J. Bocker, "Optimum Control for Interior Permanent Magnet Synchronous Motors (IPMSM) in Constant Torque and Flux Weakening Range," in *Power Electronics and Motion Control Conference, 2006. EPE-PEMC 2006. 12th International*, 2006, pp. 282 –286.

[91] P. Lazari, J. Wang, L. Chen, and X. Chen, "Design optimisation and performance evaluation of a rare-earth-free Permanent Magnet Assisted Synchronous Reluctance Machine for electric vehicle traction," in *7th IET International Conference on Power Electronics, Machines and Drives (PEMD 2014)*, 2014, pp. 1–6.

[92] J. Faiz and I. Tabatabaei, "Extension of winding function theory for nonuniform air gap in electric machinery," *IEEE Transactions on Magnetics*, vol. 38, no. 6, pp. 3654 – 3657, Nov. 2002.

[93] B. Sen and J. Wang, "A fast detection technique for stator inter-turn fault in multi-phase permanent magnet machines using model based approach," in *7th IET International Conference on Power Electronics, Machines and Drives (PEMD 2014)*, 2014, pp. 1–6.

[94] A. Gandhi, T. Corrigan, and L. Parsa, "Recent Advances in Modeling and Online Detection of Stator Interturn Faults in Electrical Motors," *IEEE Transactions on Industrial Electronics*, vol. 58, no. 5, pp. 1564–1575, 2011.

[95] IEEE Machinery Committee and Institute of Electrical and Electronics Engineers, *IEEE guide for testing turn-to-turn insulation on form-wound stator coils for alternating-current rotating electric machines*. New York, N.Y.: Institute of Electrical and Electronics Engineers, 1992.

[96] "IEEE Guide to the Measurement of Partial Discharges in Rotating Machinery," *IEEE Std 1434-2000*, pp. 1–64, Aug. 2000.

[97] C. Gerada, K. J. Bradley, M. Sumner, P. Wheeler, S. Pickering, J. Clare, C. Whitley, and G. Towers, "The results do mesh," *IEEE Industry Applications Magazine*, vol. 13, no. 2, pp. 62–72, Mar. 2007.

[98] C. Wang, X. Liu, and Z. Chen, "Incipient Stator Insulation Fault Detection of Permanent Magnet Synchronous Wind Generators Based on Hilbert #x2013;Huang Transformation," *IEEE Transactions on Magnetics*, vol. 50, no. 11, pp. 1–4, Nov. 2014.

[99] J.-R. Riba Ruiz, J. A. Rosero, A. G. Espinosa, and L. Romeral, "Detection of Demagnetization Faults in Permanent-Magnet Synchronous Motors Under Nonstationary Conditions," *IEEE Transactions on Magnetics*, vol. 45, no. 7, pp. 2961–2969, Jul. 2009.

[100] R. M. Tallam, S. B. Lee, G. C. Stone, G. B. Kliman, J. Yoo, T. G. Habetler, and R. G. Harley, "A Survey of Methods for Detection of Stator-Related Faults in Induction Machines," *IEEE Transactions on Industry Applications*, vol. 43, no. 4, pp. 920 –933, Aug. 2007.

[101] S. Djurovic, D. Vilchis-Rodriguez, and A. C. Smith, "Vibration monitoring for wound rotor induction machine winding fault detection," in *2012 XXth International Conference on Electrical Machines (ICEM)*, 2012, pp. 1906–1912.

[102] M. Iorgulescu, R. Beloiu, and M. O. Popescu, "Vibration monitoring for diagnosis of electrical equipment's faults," in *2010 12th International Conference on Optimization of Electrical and Electronic Equipment (OPTIM)*, 2010, pp. 493–499.

[103] M. Tsypkin, "Induction motor condition monitoring: Vibration analysis technique - A practical implementation," in *Electric Machines Drives Conference (IEMDC), 2011 IEEE International*, 2011, pp. 406–411.

[104] B. Sen and J. Wang, "Stator inter-turn fault detection in SPM machines using PWM ripple current measurement," in *7th IET International Conference on Power Electronics, Machines and Drives (PEMD 2014)*, 2014, pp. 1–6.

[105] F. Immovilli, C. Bianchini, E. Lorenzani, A. Bellini, and E. Fornasiero, "Evaluation of Combined Reference Frame Transformation for Interturn Fault Detection in Permanent-Magnet Multiphase Machines," *IEEE Transactions on Industrial Electronics*, vol. 62, no. 3, pp. 1912–1920, Mar. 2015.

[106] N. Leboeuf, T. Boileau, B. Nahid-Mobarakeh, G. Clerc, and F. Meibody-Tabar, "Real-Time Detection of Interturn Faults in PM Drives Using Back-EMF Estimation and Residual Analysis," *IEEE Transactions on Industry Applications*, vol. 47, no. 6, pp. 2402–2412, 2011.

[107] N. Leboeuf, T. Boileau, B. Nahid-Mobarakeh, N. Takorabet, F. Meibody-Tabar, and G. Clerc, "Effects of Imperfect Manufacturing Process on Electromagnetic Performance and Online Interturn Fault Detection in PMSMs," *IEEE Transactions on Industrial Electronics*, vol. 62, no. 6, pp. 3388–3398, Jun. 2015.

[108] L. Zarri, M. Mengoni, Y. Gritli, A. Tani, F. Filippetti, G. Serra, and D. Casadei, "Detection and Localization of Stator Resistance Dissymmetry Based on Multiple Reference Frame Controllers in Multiphase Induction Motor Drives," *IEEE Transactions on Industrial Electronics*, vol. 60, no. 8, pp. 3506–3518, 2013.

[109] P. M. de la Barrera, G. R. Bossio, and R. Leidhold, "Online Voltage Sensorless High-Resistance Connection Diagnosis in Induction Motor Drives," *IEEE Transactions on Industrial Electronics*, vol. 62, no. 7, pp. 4374–4384, Jul. 2015.

[110] P. M. de la Barrera, G. R. Bossio, and J. A. Solsona, "High-Resistance Connection Detection in Induction Motor Drives Using Signal Injection," *IEEE Transactions on Industrial Electronics*, vol. 61, no. 7, pp. 3563–3573, Jul. 2014.

[111] M. Mengoni, L. Zarri, Y. Gritli, A. Tani, F. Filippetti, and S. B. Lee, "Online Detection of High-Resistance Connections With Negative-Sequence Regulators in Three-Phase Induction Motor Drives," *IEEE Transactions on Industry Applications*, vol. 51, no. 2, pp. 1579–1586, Mar. 2015.

[112] E. Levi, "Multiphase Electric Machines for Variable-Speed Applications," *Industrial Electronics, IEEE Transactions on*, vol. 55, no. 5, pp. 1893 –1909, May 2008.

[113] Z. Sun, J. Wang, G. W. Jewell, and D. Howe, "Enhanced Optimal Torque Control of Fault-Tolerant PM Machine Under Flux-Weakening Operation," *IEEE Transactions on Industrial Electronics*, vol. 57, no. 1, pp. 344 –353, Jan. 2010.

[114] D. Ishak, Z. Q. Zhu, and D. Howe, "Comparison of PM brushless motors, having either all teeth or alternate teeth wound," *IEEE Transactions on Energy Conversion*, vol. 21, no. 1, pp. 95 – 103, Mar. 2006.

[115] C. L. Fortescue, "Method of Symmetrical Co-Ordinates Applied to the Solution of Polyphase Networks," *American Institute of Electrical Engineers, Transactions of the*, vol. XXXVII, no. 2, pp. 1027 –1140, Jul. 1918.

[116] "Drives for Industry," *Emerson Industrial*. [Online]. Available: http://www.emersonindustrial.com.

[117] P. Rodriguez, J. Pou, J. Bergas, J. I. Candela, R. P. Burgos, and D. Boroyevich, "Decoupled Double Synchronous Reference Frame PLL for Power Converters Control," *IEEE Transactions on Power Electronics*, vol. 22, no. 2, pp. 584 –592, Mar. 2007.

[118] L. Parsa and H. A. Toliyat, "Five-Phase Permanent-Magnet Motor Drives," *IEEE Transactions on Industry Applications*, vol. 41, no. 1, pp. 30–37, Jan. 2005.

[119] B.-H. Bae and S.-K. Sul, "A compensation method for time delay of full-digital synchronous frame current regulator of PWM AC drives," *Industry Applications, IEEE Transactions on*, vol. 39, no. 3, pp. 802 – 810, Jun. 2003.

[120] Y. Lee and T. G. Habetler, "An On-Line Stator Turn Fault Detection Method for Interior PM Synchronous Motor Drives," presented at the APEC 2007 - Twenty Second Annual IEEE Applied Power Electronics Conference, 2007, pp. 825–831.

[121] C. Bianchini, E. Fornasiero, T. N. Matzen, N. Bianchi, and A. Bellini, "Fault detection of a five-phase Permanent-Magnet machine," in *34th Annual Conference of IEEE Industrial Electronics, 2008. IECON 2008*, 2008, pp. 1200–1205.

[122] I. Jeong, B. J. Hyon, and K. Nam, "Dynamic Modeling and Control for SPMSMs With Internal Turn Short Fault," *IEEE Transactions on Power Electronics*, vol. 28, no. 7, pp. 3495–3508, 2013.

[123] F. Briz, M. W. Degner, P. Garcia, and A. B. Diez, "High-Frequency Carrier-Signal Voltage Selection for Stator Winding Fault Diagnosis in Inverter-Fed AC Machines," *IEEE Transactions on Industrial Electronics*, vol. 55, no. 12, pp. 4181–4190, 2008.

[124] S. Kim, J.-I. Ha, and S.-K. Sul, "PWM Switching Frequency Signal Injection Sensorless Method in IPMSM," *IEEE Transactions on Industry Applications*, vol. 48, no. 5, pp. 1576–1587, Sep. 2012.

[125] A. A. Khan and O. Mohammed, "Neural network based modeling of audible noise for high frequency injection based position estimation for PM synchronous motors at low and zero speed," in *IEEE Electric Ship Technologies Symposium, 2009. ESTS 2009*, 2009, pp. 119–122.

[126] D. G. Holmes and T. A. Lipo, *Pulse Width Modulation for Power Converters: Principles and Practice*. Wiley-IEEE Press, 2003.

[127] "LTC1968 - Precision Wide Bandwidth, RMS-to-DC Converter - Linear Technology." [Online]. Available: http://www.linear.com/product/LTC1968. [Accessed: 09-Jan-2014].

[128] B. Sen and J. Wang, "Stationary Frame Fault Tolerant Current Control of Poly-phase Permanent Magnet Machines under Open-Circuit and Short-Circuit Faults," *IEEE Transactions on Power Electronics*, vol. PP, no. 99, pp. 1–1, 2015.

[129] M. E. H. Benbouzid, D. Diallo, and M. Zeraoulia, "Advanced Fault-Tolerant Control of Induction-Motor Drives for EV/HEV Traction Applications: From Conventional to Modern and Intelligent Control Techniques," *IEEE Transactions on Vehicular Technology*, vol. 56, no. 2, pp. 519–528, Mar. 2007.

[130] T.-H. Liu, J.-R. Fu, and T. A. Lipo, "A strategy for improving reliability of field-oriented controlled induction motor drives," *IEEE Transactions on Industry Applications*, vol. 29, no. 5, pp. 910–918, Sep. 1993.

[131] J.-R. Fu and T. . Lipo, "Disturbance-free operation of a multiphase current-regulated motor drive with an opened phase," *IEEE Transactions on Industry Applications*, vol. 30, no. 5, pp. 1267–1274, Sep. 1994.

[132] H. A. Toliyat, "Analysis and simulation of five-phase variable-speed induction motor drives under asymmetrical connections," *IEEE Transactions on Power Electronics*, vol. 13, no. 4, pp. 748 –756, Jul. 1998.

[133] H. Xu, H. A. Toliyat, and L. J. Petersen, "Resilient current control of five-phase induction motor under asymmetrical fault conditions," in *Seventeenth Annual IEEE Applied Power Electronics Conference and Exposition, 2002. APEC 2002*, 2002, vol. 1, pp. 64–71 vol.1.

[134] N. Bianchi, S. Bolognani, and M. D. Pre, "Strategies for the Fault-Tolerant Current Control of a Five-Phase Permanent-Magnet Motor," *Industry Applications, IEEE Transactions on*, vol. 43, no. 4, pp. 960 –970, Aug. 2007.

[135] S. Dwari and L. Parsa, "Fault-Tolerant Control of Five-Phase Permanent-Magnet Motors With Trapezoidal Back EMF," *Industrial Electronics, IEEE Transactions on*, vol. 58, no. 2, pp. 476 –485, Feb. 2011.

[136] A. Mohammadpour and L. Parsa, "A Unified Fault-Tolerant Current Control Approach for Five-Phase PM Motors With Trapezoidal Back EMF Under Different Stator Winding Connections," *IEEE Transactions on Power Electronics*, vol. 28, no. 7, pp. 3517 –3527, Jul. 2013.

[137] S. Dwari and L. Parsa, "Disturbance Free Operation of Permanent Magnet Motor Drives Under Short Circuit Faults Using Center-Split Winding," in *Conference Record of the 2007 IEEE Industry Applications Conference, 2007. 42nd IAS Annual Meeting*, 2007, pp. 1329–1334.

[138] S. Dwari and L. Parsa, "Optimum Fault-Tolerant Control of Multi-phase Permanent Magnet Machines for Open-Circuit and Short-Circuit Faults," in *Applied Power Electronics Conference, APEC 2007 - Twenty Second Annual IEEE*, 2007, pp. 1417 – 1422.

[139] S. Dwari, L. Parsa, and T. A. Lipo, "Optimum Control of a Five-phase Integrated Modular Permanent Magnet Motor Under Normal and Open-Circuit Fault Conditions," in *Power Electronics Specialists Conference, 2007. PESC 2007. IEEE*, 2007, pp. 1639 – 1644.

[140] A. Mohammadpour and L. Parsa, "Post-fault control technique for multi-phase PM motor drives under short-circuit faults," in *2013 Twenty-Eighth Annual IEEE Applied Power Electronics Conference and Exposition (APEC)*, 2013, pp. 817–822.

[141] A. Mohammadpour, S. Mishra, and L. Parsa, "Fault-Tolerant Operation of Multiphase Permanent-Magnet Machines Using Iterative Learning Control," *IEEE Journal of Emerging and Selected Topics in Power Electronics*, vol. 2, no. 2, pp. 201–211, Jun. 2014.

[142] H.-M. Ryu, J.-W. Kim, and S.-K. Sul, "Synchronous-frame current control of multiphase synchronous motor under asymmetric fault condition due to open phases," *Industry Applications, IEEE Transactions on*, vol. 42, no. 4, pp. 1062 –1070, Aug. 2006.

[143] F. Baudart, B. Dehez, E. Matagne, D. Telteu-Nedelcu, P. Alexandre, and F. Labrique, "Torque Control Strategy of Polyphase Permanent-Magnet Synchronous Machines With Minimal Controller Reconfiguration Under Open-Circuit Fault of One Phase," *Industrial Electronics, IEEE Transactions on*, vol. 59, no. 6, pp. 2632 –2644, Jun. 2012.

[144] H. S. Che, M. J. Duran, E. Levi, M. Jones, W.-P. Hew, and N. Abd Rahim, "Postfault Operation of an Asymmetrical Six-Phase Induction Machine With Single and Two Isolated Neutral Points," *IEEE Transactions on Power Electronics*, vol. 29, no. 10, pp. 5406–5416, Oct. 2014.

[145] X. Yuan, W. Merk, H. Stemmler, and J. Allmeling, "Stationary-frame generalized integrators for current control of active power filters with zero steady-state error for current harmonics of concern under unbalanced and distorted operating conditions," *IEEE Transactions on Industry Applications*, vol. 38, no. 2, pp. 523 –532, Apr. 2002.

[146] D. N. Zmood and D. G. Holmes, "Stationary frame current regulation of PWM inverters with zero steady-state error," *IEEE Transactions on Power Electronics*, vol. 18, no. 3, pp. 814 – 822, May 2003.

[147] C. Lascu, L. Asiminoaei, I. Boldea, and F. Blaabjerg, "High Performance Current Controller for Selective Harmonic Compensation in Active Power Filters," *IEEE Transactions on Power Electronics*, vol. 22, no. 5, pp. 1826 –1835, Sep. 2007.

[148] A. Yepes, A. Vidal, F. D. Freijedo, J. Malvar, O. Lopez, and J. Doval-Gandoy, "Transient response evaluation of resonant controllers for AC drives," in *2012 IEEE Energy Conversion Congress and Exposition (ECCE)*, 2012, pp. 471–478.

[149] S. . Richter and R. W. De Doncker, "Digital proportional-resonant (PR) control with anti-windup applied to a voltage-source inverter," in *Proceedings of the 2011-14th European Conference on Power Electronics and Applications (EPE 2011)*, 2011, pp. 1–10.

[150] B. P. McGrath, S. G. Parker, and D. G. Holmes, "High-Performance Current Regulation for Low-Pulse-Ratio Inverters," *IEEE Transactions on Industry Applications*, vol. 49, no. 1, pp. 149 –158, Feb. 2013.

[151] K. Atallah, J. Wang, and D. Howe, "Torque-ripple minimization in modular permanent-magnet brushless machines," *IEEE Transactions on Industry Applications*, vol. 39, no. 6, pp. 1689 – 1695, Dec. 2003.

[152] H.-M. Ryu, J.-H. Kim, and Seung-Ki Sul, "Analysis of multiphase space vector pulse-width modulation based on multiple d-q spaces concept," *IEEE Transactions on Power Electronics*, vol. 20, no. 6, pp. 1364 – 1371, Nov. 2005.

[153] A. Tani, M. Mengoni, L. Zarri, G. Serra, and D. Casadei, "Control of Multiphase Induction Motors With an Odd Number of Phases Under Open-Circuit Phase Faults," *IEEE Transactions on Power Electronics*, vol. 27, no. 2, pp. 565 –577, Feb. 2012.

[154] R. I. Bojoi, G. Griva, V. Bostan, M. Guerriero, F. Farina, and F. Profumo, "Current control strategy for power conditioners using sinusoidal signal integrators in synchronous reference frame," *IEEE Transactions on Power Electronics*, vol. 20, no. 6, pp. 1402–1412, 2005.

[155] G. C. Goodwin, S. F. Graebe, and M. E. Salgado, *Control system design*. Upper Saddle River, N.J.: Prentice Hall, 2001.

[156] A. G. Yepes, F. D. Freijedo, J. Doval-Gandoy, O. López, J. Malvar, and P. Fernandez-Comesaña, "Effects of Discretization Methods on the Performance of Resonant Controllers," *IEEE Transactions on Power Electronics*, vol. 25, no. 7, pp. 1692 –1712, Jul. 2010.

[157] A. G. Yepes, F. D. Freijedo, O. Lopez, and J. Doval-Gandoy, "Analysis and Design of Resonant Current Controllers for Voltage-Source Converters by Means of Nyquist Diagrams and Sensitivity Function," *IEEE Transactions on Industrial Electronics*, vol. 58, no. 11, pp. 5231 –5250, Nov. 2011.

[158] K. J. Astrom and T. Hagglund, *PID Controllers: Theory, Design and Tuning*, 2nd Revised edition edition. Research Triangle Park, N.C: ISA, 1995.

[159] A. Iqbal and S. Moinuddin, "Comprehensive Relationship Between Carrier-Based PWM and Space Vector PWM in a Five-Phase VSI," *IEEE Transactions on Power Electronics*, vol. 24, no. 10, pp. 2379 –2390, Oct. 2009.

[160] T.-S. Kwon and S.-K. Sul, "Novel Antiwindup of a Current Regulator of a Surface-Mounted Permanent-Magnet Motor for Flux-Weakening Control," *Industry Applications, IEEE Transactions on*, vol. 42, no. 5, pp. 1293 –1300, Oct. 2006.

[161] F. Fernandez-Bernal, A. Garcia-Cerrada, and R. Faure, "Determination of parameters in interior permanent-magnet synchronous motors with iron losses without torque measurement," *IEEE Transactions on Industry Applications*, vol. 37, no. 5, pp. 1265–1272, 2001.

List of Figures

Fig. 1-1: Distribution of faults 5
Fig. 2-1: Geometry of 12 slot, 14 pole SPM Machine 15
Fig. 2-2: FE model with turn fault (circled) in phase A for model validation 16
Fig. 2-3: Schematic representation of SPM machine with turn fault on a single phase.....17
Fig. 2-4: Slot numbering convention 20
Fig. 2-5: Slot dimension nomenclature. Fault turns are denoted by N_s.....21
Fig. 2-6: Rotor topology of the machine.....22
Fig. 2-7: Current density distribution of a coil.....26
Fig. 2-8: Elemental Coil Diagram.....29
Fig. 2-9: Flowchart for air-gap inductance calculations 30
Fig. 2-10: Slot leakage flux paths 31
Fig. 2-11: Slot geometry and coordinate system for slot wedge flux calculation.....32
Fig. 2-12: Slot geometry and coordinate system for flux calculation in the winding area 34
Fig. 2-13: Leakage inductance computation algorithm.....36
Fig. 2-14: Comparison of flux iso-lines for (a) half slot coil side and (b) full slot coil side.....41
Fig. 2-15: Comparison for peak fault current prediction by proposed and classical model with direct-FE model under 1 turn fault for loaded condition for varying position of fault coil inside the slot (I_q=84A).....43
Fig. 3-1: Schematic representation of IPM machine with turn fault in 'C' phase. 49
Fig. 3-2: Schematic of ODE solver based fault model.....52
Fig. 3-3: FE model of 36 slot, 6 pole IPM Machine with 2 turn fault in C phase (a) full FE model, (b) zoomed portion of model containing turn fault showing excitation currents. (+, - signs depicts coil current direction. + represents current direction into the plane of the paper).....53
Fig. 3-4: Flux linkage map of machine at a sample case i_d=-30A and θ_m=0. (a) *d*-axis flux linkage. (b) *q*-axis flux linkage (c) *cs2*(*f*) flux linkage 55
Fig. 3-5: Rotor skew slices at mechanical angle of (a) 0 (rad) skew, (b) β_{sk} (rad) skew 57
Fig. 3-6: Flux linkage and current vectors for rotor skewed by β_{sk} (mech) angle.....58
Fig. 3-7: Comparison between multi-slice FE and proposed method (calc) at (i_d= -40A, i_q= -40A, i_f= -200A) (a) *d*- axis flux linkage, (b) *q*- axis flux linkage, (c) faulted turn flux linkages (d) Torque.....61

Fig. 3-8: Current prediction errors due to table inversion at i_d=-50A and θ_m=0 (a) d- axis current error, (b) q- axis current error and (c) fault current error. 64
Fig. 3-9: Fault current comparison of FE verses model (ODE) solved by ODE solver at load of 2.2Ω at 3500 r/min 65
Fig. 3-10: Phase current comparison of FE verses model (ODE) solved by ODE solver at load of 2.2Ω at 3500 r/min 65
Fig. 3-11: Fault current comparison of FE verses model (DAE) solved by DAE solver at load of 2.2Ω at 3500 r/min 66
Fig. 3-12: Phase and fault current comparison of FE verses model (ODE) under transient condition at 3500 r/min. Step resistive load (2.2Ω) applied at θ_{elect}=0.5236 rad and 2 turn fault (R_f=5.5mΩ) at θ_{elect} =10.472 rad. 67
Fig. 3-13: Phase and fault current comparison of FE verses model (ODE) under transient condition at 3500 r/min with 10x nominal fault resistance (R_f =55mΩ). Step resistive load applied at θ_{elect}=0.5236 rad and 2 turn fault at θ_{elect}=10.472 rad. 68
Fig. 3-14: (a) Stator winding with 2 turn fault in phase C (b) 3 step rotor and shaft 69
Fig. 3-15: Experimental Setup (a) Motor Dynamometer setup (b) Resistive load 69
Fig. 3-16: Comparison of measured (meas) and FE model predicted (pred) phase back-EMF at 2100 r/min. 70
Fig. 3-17: Comparison of measured and predicted fault current variations with speed and load (a) No-load, (b) 2.2Ω load, (c) 1Ω load and (d) 0.69Ω load. 71
Fig. 3-18: Comparison of measured (meas) and predicted (pred) fault current at (a) 1500 r/min at no load, (b) 5500 r/min at no-load, (c) 1500 r/min at 0.69 Ω load and (d) 5500 r/min at 0.69 Ω load. 72
Fig. 3-19: Comparison of measured (meas) and predicted (pred) fault current (I_f) at 3500 r/min and 2.2Ω load. Turn fault initiated at θ_e = 95 rad. 73
Fig. 3-20: Comparison of measured (meas) and predicted (pred) *dq* current ripple at (a) @5500 r/min and 2.2Ω load, (b) @5500 r/min and 0.69Ω load and @3500 r/min and 2.2Ω load. .. 74
Fig. 4-1: Geometry of 36 slot, 6 pole IPM Machine (1/3rd symmetry model) 80
Fig. 4-2: Flux linkage map of healthy machine. (a) *d*-axis flux linkage. (b) *q*-axis flux linkage 80
Fig. 4-3: Inductance map of healthy machine (a) d-axis inductance (b) q-axis inductance 81
Fig. 4-4: FE models for fault model validation (fault winding circled) 82
Fig. 4-5: Schematic representation of IPM machine with turn fault in 'A' phase. 83
Fig. 4-6: Comparison of fault current prediction by FEM simulation and classical model at R_f = 0.1mΩ, V_d = -65V, and V_q=13V 87

Fig. 4-7: Series connected coils of phase-A....88
Fig. 4-8: MMF Phasor diagram of two coils in Phase A in healthy condition....88
Fig. 4-9: Comparison of flux linkages predicted by proposed model and by FE 1/3 symmetric Model, No leakage. (i_d = -50A, i_q = 50A, i_f = 300A) under 1 turn fault. 90
Fig. 4-10: Comparison of flux linkages predicted by proposed model and by FE 1/3 symmetric Model, No leakage. (i_d = -50A, i_q = 50A, i_f = 150A) under 3 turn fault. 91
Fig. 4-11: Comparison of predicted flux linkages of faulted pole-pair (PP3) by proposed model and by FE, Full Model, No leakage. (i_d = -50A, i_q = 50A, i_f = 300A) under 1 turn fault. 91
Fig. 4-12: Comparison of predicted flux linkages of faulted pole-pair (PP3) by proposed model and by FE, Full Model, No leakage. (i_d = -50A, i_q = 50A, i_f = 150A) under 3 turn fault. 92
Fig. 4-13: Turn functions (n) of phase A, B, C coils (located in pole pair 1) and winding function (N_f) of fault winding (located in pole-pair 3) 94
Fig. 4-14: Flux linkage comparison under different pole pairs (FE) with i_d = -50A, i_q=50A and fault current (i_f =300A) in the fault winding (1 turn)....95
Fig. 4-15: Comparison of *dq* flux linkages of FE simulation verses model for healthy pole pair (PP1,PP2) flux linkages without slot leakage flux (i_d = -50A, i_q = 50A, i_f = 150A) under 3 turn fault....96
Fig. 4-16: Comparison of predicted *dq* flux linkages of classical and proposed model verses FE simulation of full model without slot leakage flux (i_d = -50A, i_q = 50A, i_f = 300A) under 1 turn fault....97
Fig. 4-17: Comparison of predicted *dq* flux linkages of proposed model verses FE simulation of full model without slot leakage flux (i_d = -50A, i_q = 50A, i_f = 150A) under 3 turn fault. ..98
Fig. 4-18: Comparison of *dq* flux linkage prediction of classical and proposed model verses FE simulation of full model with slot leakage flux (i_d = -50A, i_q = 50A, i_f = 300A) under 1 turn fault....99
Fig. 4-19: Comparison of *dq* flux linkage prediction of classical and proposed model verses FE simulation of full model with slot leakage flux (i_d = -50A, i_q = 50A, i_f = 150A) under 3 turn fault....99
Fig. 4-20: Comparison of faulted coil flux linkage prediction of classical and proposed model verses FE simulation of full model with slot leakage flux (i_d = -50A, i_q = 50A, i_f = 300A) under 1 turn fault....100
Fig. 4-21: Comparison of faulted coil flux linkage prediction of classical and proposed model verses FE simulation of full model with slot leakage flux (i_d = -50A, i_q = 50A, i_f = 150A) under 3 turn fault....101

Fig. 4-22: Comparison of current prediction of classical and proposed model verses FE simulation under 1 turn fault (V_d = -65V, V_q= 13V, R_f = 0.1mΩ) (operating point i_d ~= -50A, i_q ~= 50A) 103
Fig. 4-23: Comparison of current prediction of classical and proposed model verses FE simulation under 1 turn fault (V_d = -3.485V, V_q= 7.33V, R_f = 0.1mΩ) (operating point i_d ~= -50A, i_q ~=0A). 103
Fig. 4-24: Comparison of current prediction of classical and proposed model verses FE simulation under 3 turn fault (V_d = -65V, V_q= 13V, R_f = 10mΩ) (operating point i_d ~= -50A, i_q ~= 50A) 104
Fig. 4-25: Comparison of current prediction of classical and proposed model verses FE simulation under 3 turn fault (V_d = -57V, V_q= 30V, R_f = 10mΩ) (operating point i_d ~= 0A, i_q ~= 40A) 104
Fig. 4-26: Geometry of the test machine, including additional air-gaps and short pitched coils.106
Fig. 4-27: Comparison of measured and predicted fault current variations with speed and load (a) No-load, (b) 2.2Ω load, (c) 1.01Ω load and (d) 0.69Ω load. 106
Fig. 4-28: Comparison of measured (meas) and predicted (pred) fault current at (a) 1500 r/min at no load, (b) 5500 r/min at no-load, (c) 1500 r/min at 0.69 Ω load and (d) 5500 r/min at 0.69 Ω load 108
Fig. 4-29: Comparison of measured (meas) and predicted (pred) *dq* current ripple at (a) @5500 r/min and 2.2Ω load, (b) @5500 r/min and 0.69Ω load and (c) @3500 r/min and 2.2Ω load. 110
Fig. 5-1: Five phase fault tolerant SPM machine 118
Fig. 5-2: Schematic representation of 5 phase SPM machine with turn fault on phase-4 118
Fig. 5-3: Voltage Based Detector Structure 122
Fig. 5-4: Sequence components and the phase relationship. 123
Fig. 5-5: Simplified residual current detector structure 127
Fig. 5-6: Schematic of machine with high resistance connection in phase-4 130
Fig. 5-7: Relationship between *dqxy* and sequence components 139
Fig. 5-8: Cross coupled detector structure 141
Fig. 5-9: Negative sequence step response of the cross coupled filter to varying k_f. 142
Fig. 5-10: Positive sequence disturbance step rejection response of the cross-coupled filter to varying k_f. 143
Fig. 5-11: Multi-notch filter based detector 144
Fig. 5-12: Bode plot of multi-notch filter 145

Fig. 5-13: Negative sequence step response of the cross coupled filter to varying ξ.....146
Fig. 5-14: Positive sequence disturbance step rejection response of the cross-coupled filter to varying ξ. 146
Fig. 5-15: Comparison of cross-coupled filter and multi-notch filter.....147
Fig. 5-16: Direct form II implementation of notch filter 149
Fig. 5-17: Potential sites for delay insertion 150
Fig. 5-18: Residual Current block diagram.....151
Fig. 5-19: Euler solver (dashed) verses motor current.....153
Fig. 5-20: RK4 solver (dashed) verses motor current.....154
Fig. 5-21: Timing Diagram of sampling, computation and PWM output.....155
Fig. 5-22: Effect of delay compensation on residual currents 155
Fig. 5-23: Speed ramp and pulse load test. 20 turn Fault is initiated at 1s and removed at 1.1s.157
Fig. 5-24: Speed ramp and pulse loading test of fault detector. 20 turn Fault is initiated at 1s and removed at 1.1s. 157
Fig. 5-25: Speed ramp and pulse loading test response of residual magnitude extraction. 20 turn Fault is initiated at 1s and removed at 1.1s. 158
Fig. 5-26: Comparison of classifier output to a 20 turn fault and HRC connection (+60% R) at 500 r/min and i_q=6A. Fault initiated at 0.1s and removed at 0.2s.....158
Fig. 5-27: Motor stator winding with fault taps 159
Fig. 5-28: (a) Dynamometer setup with test machine with fault relays and (b) 5 phase inverter board 160
Fig. 5-29: Back-EMF of the machine at 800 r/min in (a) stationary frame and (b) in *dq1dq3* frame 161
Fig. 5-30: Effect of back-EMF lookup method on 2 turn fault detection at 800 r/min, i_{q1}=6A. Fault is initiated at 0.07s and removed at 0.21s. 163
Fig. 5-31: Parameter fitting result. 164
Fig. 5-32: Measured model response to step changes to i_q current (0 to 4A step) at 800 r/min. i_d=0A. 164
Fig. 5-33: Measured model response to step changes to i_d current (0 to -3A step). i_q=0A. 165
Fig. 5-34: Measured variation of steady state fault current due to 2 turn fault to loading and speed. 166
Fig. 5-35: (a) Controller command voltage and feedback current plots and (b) detector output, at 600 r/min and i_{q1}=3A under a 2 turn fault. Fault initiated at 0.07s and removed at 0.21s 167

Fig. 5-36: Detector response to 2 turn fault at 1000 r/min. C1, C2 current in phase-4 and 5 respectively (5A/div), C3 is fault current (20A/div) and C4 is detector output, 0.5V/div. Ph-4 is the faulted phase. 168
Fig. 5-37: Detector response to 20 turn fault at 1000 r/min. C1, C2 current in phase-4 and 5 respectively (5A/div), C3 is fault current (20A/div) and C4 is detector output, 2V/div. Ph-4 is the faulted phase. 168
Fig. 5-38: Detector response to turn faults at 1000 r/min under various steady load currents to 2 turn fault. Step i_q (0-4A) response of detector under healthy condition is added for comparison. Fault and load step transient initiated at 0.07s and removed at 0.21s. 169
Fig. 5-39: Detector response to turn faults at 1000 r/min under various steady load currents to 20 turn fault. Step i_q (0-4A) response of detector under healthy condition is added for reference. Fault and load step transient initiated at 0.07s and removed at 0.21s 170
Fig. 5-40: Residual Current magnitude extraction for fault localisation at i_q =6A at 1000 r/min for 2 turn fault. Ph-4 has the turn fault. 170
Fig. 5-41: Residual Current magnitude extraction for fault localisation at i_q =6A at 1000 r/min for 20 turn fault. Ph-4 has the turn fault. 171
Fig. 5-42: Detector response under various load currents at 800 r/min with HRC fault initiated in phase-4 at 0.07s and removed at 0.21s with 0.22 Ω HRC. 172
Fig. 5-43: Detector response under various load currents at 800 r/min with HRC fault initiated in phase-4 at 0.07s and removed at 0.21s with 0.66 Ω HRC. 172
Fig. 5-44: Residual Current magnitude extraction for fault localisation at i_q =6A at 800 r/min with HRC fault initiated in phase-4 at 0.07s and removed at 0.21s with 0.22 Ω HRC. Ph-4 is the phase with HRC. 173
Fig. 5-45: Residual Current magnitude extraction for fault localisation at i_q =6A at 800 r/min with HRC fault initiated in phase-4 at 0.07s and removed at 0.21s with 0.66Ω HRC. Ph-4 is the phase with HRC. 173
Fig. 5-46: Residual Current fault classification at i_q =6A at 800 r/min (a) 2 turn fault (b) High resistance fault (0.22Ω). 175
Fig. 5-47: Variation of fault detector output (measured) to varying loads and speeds (a) 2 turn fault, (b) 20 turn fault 176
Fig. 5-48: Variation of residual current magnitude at i_q=0A and varying speed (a) 2 turn fault, (b) 20 turn fault. Ph-4 is the faulted phase. 177
Fig. 5-49: Variation of fault detector output (measured) to varying loads and speeds (a) 0.22Ω HRC, (b) 0.66Ω HRC. 178

Fig. 5-50: Variation of residual current magnitude at i_q=6A and varying speed (a) 0.22Ω HRC, (b) 0.66Ω HRC. Ph-4 is the faulted phase 179
Fig. 5-51: Comparison of classifier output at different loading and speed with 2 turn fault and 0.22Ω HRC fault. 180
Fig. 5-52: 18-slot 16-pole spoke type IPM machine 181
Fig. 5-53: Schematic of the 18-slot 16-pole IPM machine showing winding configuration for the faulted set. 181
Fig. 5-54: Block diagram of the overall detection structure 182
Fig. 5-55: Detector structure utilising multi-notch filter approach 182
Fig. 5-56: *dq* and fault current (1500 r/min, i_q = 50A, turn fault (0.06s -> 0.11s)) 183
Fig. 5-57: Fundamental based Detector 1500 r/min, i_q = 50A, turn fault (0.06s -> 0.11s) 183
Fig. 5-58: Residual current based detector 1500 r/min, i_q = 50A, turn fault (0.06s -> 0.11s) 184
Fig. 5-59: Machine *dq* and fault currents (3000 r/min, i_q = 50A, turn fault (0.06s -> 0.11s)) ...185
Fig. 5-60: Fault current and Detector output (3000 r/min, i_q = 50A, turn fault (0.06s -> 0.11s))185
Fig. 5-61: Residual and fault currents (3000 r/min, i_q = 50A, turn fault(0.06s -> 0.11s)) 186
Fig. 5-62: Combined auto-calibration and fault detection. (a) Currents commands and fault current, (b) Fault current and detector response. Auto-calibration ends at 0.45s. 188
Fig. 6-1: Geometry of 10-slot, 12-pole SPM machine 193
Fig. 6-2: Schematic of winding under turn fault 193
Fig. 6-3: Experimental setup for measurement of HF impedance 195
Fig. 6-4: Equivalent terminal resistance and inductance of healthy winding under locked rotor condition 196
Fig. 6-5: Measured healthy winding admittance (Y) plot for varying rotor position (electrical)196
Fig. 6-6: Admittance (*Y*) magnitude and phase of winding under healthy, 2 turn and 20 turn fault. Theoretical (T) – dashed, Measured (M) – solid 197
Fig. 6-7: Fitted Admittance Function ($Y_{h,expt}(s)$) for Healthy Condition 199
Fig. 6-8: Fitted Admittance function ($Y_{f,expt}(s)$) for (a) 2 turn and (b) 20 turn fault condition ...200
Fig. 6-9: Schematic representation of 5-phase SPM machine with turn fault on a single phase201
Fig. 6-10: Harmonic voltage spectrum of a sine-PWM inverter leg w.r.t negative DC supply rail at modulation index = 0.9, V_{dc}=140V, fundamental frequency (ω_f) = 2π.300 rad.s^{-1}.....203
Fig. 6-11: RMS harmonic current with 2 turn fault with V_{dc} = 140V considering (a) only 10kHz carrier and sidebands, (b) 10kHz and 20kHz carrier frequency harmonics and sidebands.....204
Fig. 6-12: HF detection signal processing chain. ADC sampling rate is 10 kHz.....205
Fig. 6-13: Band-pass Filter Bode Plot.....206

Fig. 6-14: Detector Circuit Implementation 207
Fig. 6-15: Simulated phase currents with a 2 turn fault in phase-4 at rotor speed of 500 r/min.208
Fig. 6-16: Simulated detector output with a 2 turn fault in phase-4 at rotor speed of 500 r/min.208
Fig. 6-17: Simulated phase currents with a 20 turn fault in phase-4 at rotor speed of 1000 r/min. 209
Fig. 6-18: Simulated detector output with a 20 turn fault in phase-4 at rotor speed of 1000 r/min. 209
Fig. 6-19: PWM ripple detector board..... 210
Fig. 6-20: Detector output with 2 turn fault in phase-4 with i_q =6A at (a) 500 r/min, (b) 1000 r/min. Ch1- Ch5 - detector outputs for phase 1 through phase 5 respectively (100mV/div), Ch11 - phase 4 current (5A/div), Ch12 is fault current (20A/div). Time scale – 100ms/div.211
Fig. 6-21: Zoomed portion of measured Ph-4 (faulty phase) line current with i_q=6A at 500 r/min under healthy and 2 turn fault. 211
Fig. 6-22: Detector output with 20 turn fault in phase-4 with i_q=6A at (a) 500 r/min, (b) 1000 r/min. Ch1-Ch5 - detector outputs for phase 1 through phase 5 respectively (200mV/div), Ch11 - phase 4 current (5A/div), Ch12 is fault current (20A/div). Time scale – 100ms/div212
Fig. 6-23: Comparison of measured and predicted detector output at i_q =6A, with varying speeds at (a) 2 turn fault and (b) 20 turn fault 213
Fig. 6-24: Variation of measured detector output (ph-4) with load current (0%, 50%, 100%) and speed plotted with respect to (a) speed, (b) modulation index. Dashed curves refer to healthy operation and solid lines refer to 2-turn fault condition. Stared points are the selected test points for detector calibration. 215
Fig. 6-25: Variation of calibrated detector output (ph-4) at various loading (0%,50%,100%) with varying speed. Dashed curves refer to healthy motor operation and solid lines refer to 2-turn fault condition. 216
Fig. 6-26: Comparison of calibrated detector output of faulted phase (Ph-4) under 2 turn fault verses calibrated detector output of all phases under healthy condition. 217
Fig. 6-27: Variation of all calibrated detector outputs at i_q=0A with varying speed under 2 turn fault. Ph-4 is the faulted phase. 217
Fig. 6-28: Variation of all calibrated detector outputs at i_q=6A with varying speed under 2 turn fault. Ph-4 is the faulted phase. 218
Fig. 6-29: Variation of measured detector output (ph-4) with load current (0%, 50%, 100%) and speed plotted with respect to speed. Dashed curves refer to healthy operation and solid lines refer to 20-turn fault condition..... 219

Fig. 6-30: Comparison of calibrated detector output of faulted phase (Ph-4) under 20 turn fault verses calibrated detector output of all phases under healthy condition. 219
Fig. 6-31: Variation of all calibrated detector outputs at i_q=6A with varying speed under 20 turn fault. Ph-4 is the faulted phase. 220
Fig. 6-32: Variation of detector output (Ph-4) to HRC fault (0.66Ω) at various loading (33% and 100%) with varying speed 221
Fig. 7-1: Five phase fault tolerant SPM machine 229
Fig. 7-2: Optimal torque control with open circuit fault in Phase-A with T_d = 0.7Nm and k_{fld} =0.7, (a) instantaneous currents, (b) FFT 231
Fig. 7-3: Discrete domain plant modelling 232
Fig. 7-4: Controller Structure 234
Fig. 7-5: Open loop transfer function magnitude plots at 300 r/min and 3000 r/min. 237
Fig. 7-6: Controller closed loop response at (a) 300 r/min and (b) 3000 r/min 238
Fig. 7-7: Settling time variation in number of electrical cycles (+/- 4% criterion) with motor speed 238
Fig. 7-8: Variation of closed loop poles and zeros with changing plant parameters. Blue – 1x , Red – 0.5x, magenta – 2x times nominal resistance and inductance. 239
Fig. 7-9: Controller structure with anti-windup 240
Fig. 7-10: Zero sequence voltage injection block 240
Fig. 7-11: Modulation index with and without voltage injection 241
Fig. 7-12: Torque speed characteristic under healthy (h), single phase open circuit (OC) and single phase short circuit (SC) with (w inj) and without voltage injection. 242
Fig. 7-13: Final controller structure including voltage injection 242
Fig. 7-14: Effect of varying field weakening coefficient on voltage (T_d = 0.71Nm at 2000 r/min) 244
Fig. 7-15: k_{fld} -update algorithm 244
Fig. 7-16: Simplified schematic of the test setup 245
Fig. 7-17: (a) Torque-speed and (b) k_{fld}-speed plots for healthy operation 246
Fig. 7-18: (a) Torque-speed and (b) k_{fld} -speed plots for single phase open circuit operation 247
Fig. 7-19: (a) Torque-speed and (b) k_{fld} -speed plots for single phase short operation 248
Fig. 7-20: Current responses to step change in torque demand of 1 Nm under healthy operation (a) at 0.023s with k_{fld} =0 at 600 r/min (60Hz) and (b) at 0.0287s with k_{fld} = 0.3 at 2000 r/min (200Hz). 249
Fig. 7-21: Current responses to transition from Healthy to phase-1 OC (a) at 0.03s with T_d=1.2Nm at 600 r/min (60Hz) (b) at 0.024s with T_d=1Nm at 1200 r/min (120Hz). 250

Fig. 7-22: Current responses to torque step change under phase-1 OC at (a) T_d *=0 to 1Nm at 0.027s* with k_{fld}=0 at 600 r/min (b) T_d*=0 to 0.6Nm at 0.023s with* k_{fld} =0.45 at 2000 r/min . 251

Fig. 7-23: Current responses to torque step change under phase-1 SC (a) T_d*=0 to 0.8Nm at 0.025s with* k_{fld} =0 at 600 r/min (b) T_d=0 to 0.45Nm at 0.0278s with k_{fld} =0.45 at 2000 r/min. I_1 is the short circuit current flowing in phase-1. 252

Fig. 7-24: Responses of voltage error, current tracking error and the field weakening factor to torque step change from 0.2Nm to 0.5Nm under phase-1 OC at 2200 r/min. 253

Fig. 7-25: Current and torque waveforms under SC (phase -1) at 600 r/min (a) without OTC control (b) with OTC (T_d=0). Scale: I_1: 5A/div, I_2: 5A/div, I_3: 5A/div, Torque: 1Nm/div. I_1 is the short circuit current flowing in phase-1 254

List of Tables

Table 1-1: Popular Electric Vehicles Motor Specifications....4
Table 2-1: Machine Specifications....16
Table 2-2: Coil Definitions....19
Table 2-3: Fault Coil Definition....20
Table 2-4: Augmented Coil Definition....21
Table 2-5: Slot Specifications....31
Table 2-6: Back-EMF Comparison....37
Table 2-7: Air-Gap Inductance Comparison....37
Table 2-8: Slot Leakage Inductance Comparison....38
Table 2-9: Healthy Machine Inductance Comparison....38
Table 2-10: Inductance Comparison with 1 Turn Fault Located at Bottom of Slot (N_{ha}=0)....39
Table 2-11: Inductance Comparison with 1 Turn Fault Located in Middle of Slot (N_{ha}=3)....39
Table 2-12: Inductance comparison with 1 Turn Fault Located At Top of Slot (N_{ha}=7)....40
Table 2-13: Inductance Comparison with 3 Turn Fault Located in the Middle of the Slot (N_{ha}=3)....40
Table 2-14: Comparison of Inductance Predicted by Classical Approach for 1 Turn Fault (N_{ha}=7)....42
Table 3-1: IPM Machine Parameters....54
Table 3-2: Comparison of simulation times for generator mode operation with resistive load of 2.2Ω at 3500 r/min....67
Table 4-1: Comparison of Simulation Setup Time....111
Table 5-1: Specification of the Prototype Five-Phase Fault-Tolerant PM Machine....118
Table 5-2: Machine Parameters under Turn fault....120
Table 5-3: Machine Geometry Data....120
Table 5-4: Comparison of Computational Requirements for Cross-coupled and Multiple Notch Filter....148
Table 5-5: 18-slot, 16-pole IPM Machine Nominal Parameters....181
Table 6-1: Machine Data under Fault....194
Table 7-1: Specification of the Prototype Five-Phase Fault-Tolerant PM Machine....230
Table 7-2: Optimised Controller Parameters....236

Appendix

A 5-phase custom built MOSFET inverter is used to control the test motor. The inverter is controlled through a floating point eZdsp™ F28335 board from Spectrum Digital. Commands to the DSP board is issued using either CAN interface using LabView or through the JTAG connection via the TI Code Composer studio. DC link voltage is set at 60V for the experiments. Table A-1 shows the maximum rating of the inverter. Table A-2 gives the part numbers of the major components used in the board. Fig. A- 6 show the close up view and the major parts of the inverter board.

Table A-1: Inverter board specification

Parameter	**Value**
Maximum DC link Voltage	150V
Maximum Current	10A
Switching frequency	10kHz
Maximum no. of phases	6

Table A-2: Major components of the inverter board

Component	**Part. No.**
MOSFET	IRFP4332
Current Sensor	LTSR-25p
DC Voltage Sensor	HCPL-7800
Gate Driver	IR2110S
Opto-isolator	HCPL-063L
RS-485 transceiver	SN65HVD30
SPI DAC	TLV5638
DSP board	eZdsp F28335 board

Current Controller

The current controller used in the experiments (except in Chapter 7) is shown in Fig. A-1. It is based on control structure proposed in [118] for a 5-phase machine.

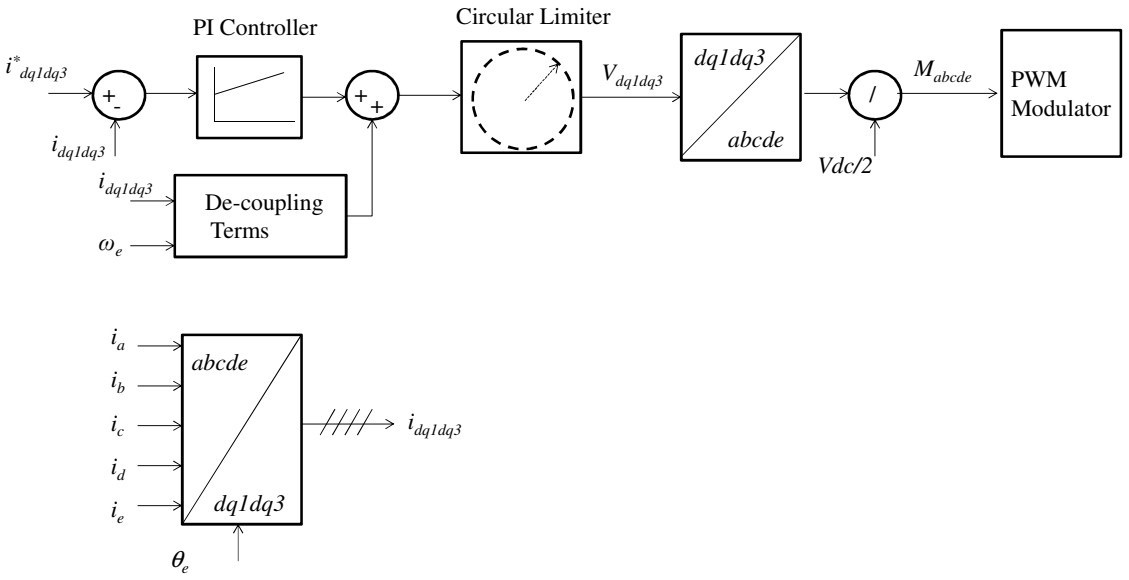

Fig. A-1: Current controller structure

The *abcde* to *dq1dq3* transformation is given in (A-1).

$$T_{dq1dq3,0} =$$

$$\frac{2}{5}\begin{bmatrix} \mathrm{s}(\theta) & \mathrm{s}(\theta-2\pi/5) & \mathrm{s}(\theta-4\pi/5) & \mathrm{s}(\theta-6\pi/5) & \mathrm{s}(\theta-8\pi/5) \\ \mathrm{c}(\theta) & \mathrm{c}(\theta-2\pi/5) & \mathrm{c}(\theta-4\pi/5) & \mathrm{c}(\theta-6\pi/5) & \mathrm{c}(\theta-8\pi/5) \\ \mathrm{s}(3\theta) & \mathrm{s}(3\theta-6\pi/5) & \mathrm{s}(3\theta-2\pi/5) & \mathrm{s}(3\theta-8\pi/5) & \mathrm{s}(3\theta-4\pi/5) \\ \mathrm{c}(3\theta) & \mathrm{c}(3\theta-6\pi/5) & \mathrm{c}(3\theta-2\pi/5) & \mathrm{c}(3\theta-8\pi/5) & \mathrm{c}(3\theta-4\pi/5) \\ 1/2 & 1/2 & 1/2 & 1/2 & 1/2 \end{bmatrix} \quad \text{(A-1)}$$

Using the nominal RL parameters (R=0.5Ω, L=2.8mH) of the machine, a current controller with -3dB bandwidth of 400Hz was designed (K_p=5, K_i=1000).

Experimental Validations

In order to validate the controller design, steady state and step loading is performed. Fig. A-2 shows the measured line voltage of the inverter operating at V_{dc} = 60V. Fig. A-3 shows the measured current and cos (θ) using a digital to analog converter. It can be observed that the two plots are in phase, as expected when i_q current is present. Fig. A-4 shows the step response of the current controller to a step change of i_q from 0 to 4A. Fig. A-5 shows the step response of the controller in *dq* domain as

measured by the DSP. It can be observed that the tracking response of the controller is good.

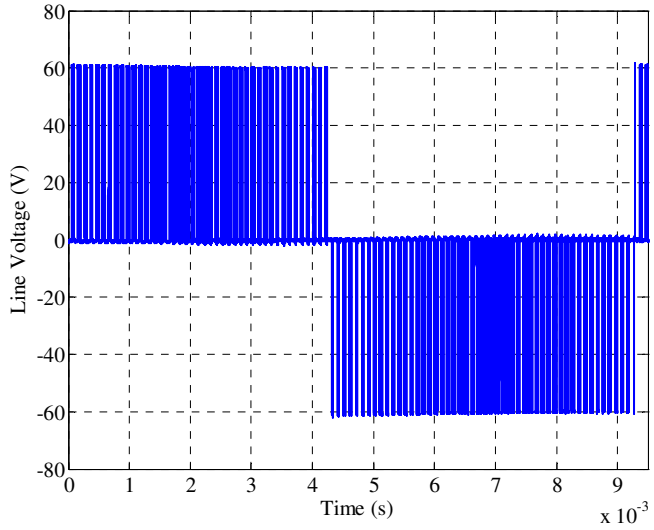

Fig. A-2: Measured Line voltage (V_{ab}) at 1000 r/min with i_q=6A

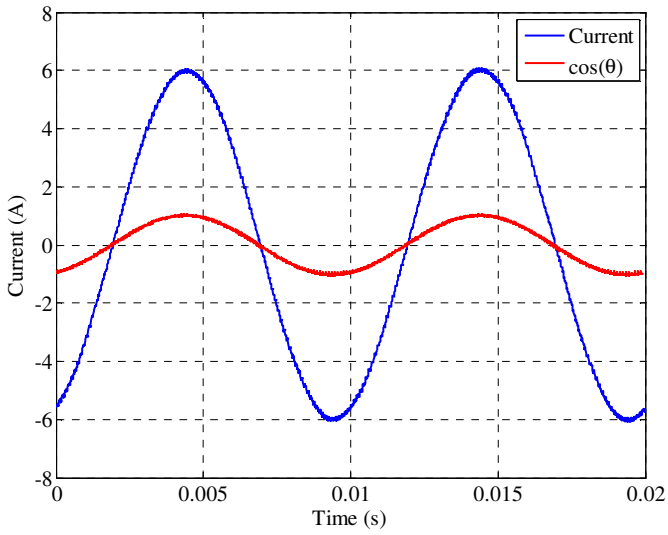

Fig. A-3: Current control tracking (i_q=6A). i_q is in phase with cos(θ) at 1000 r/min. Bandwidth limited to 100kHz.

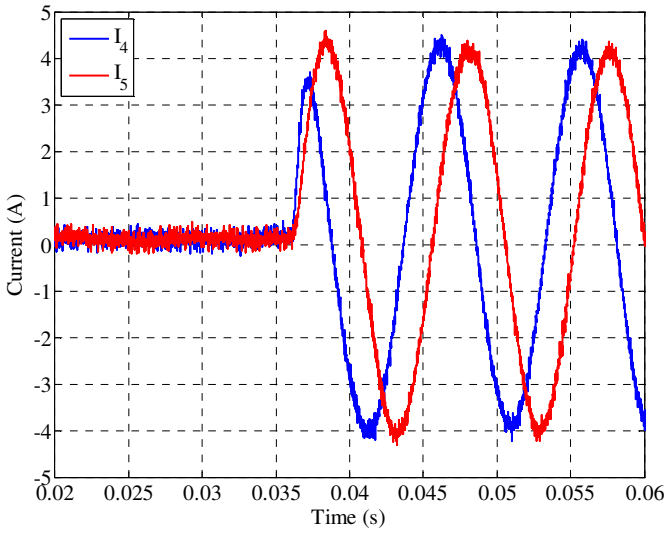

Fig. A-4: Current controller step response (i_q=4A step) at rotor speed of 1000 r/min. C1 – Phase-4 current, C2- Phase-5 current.

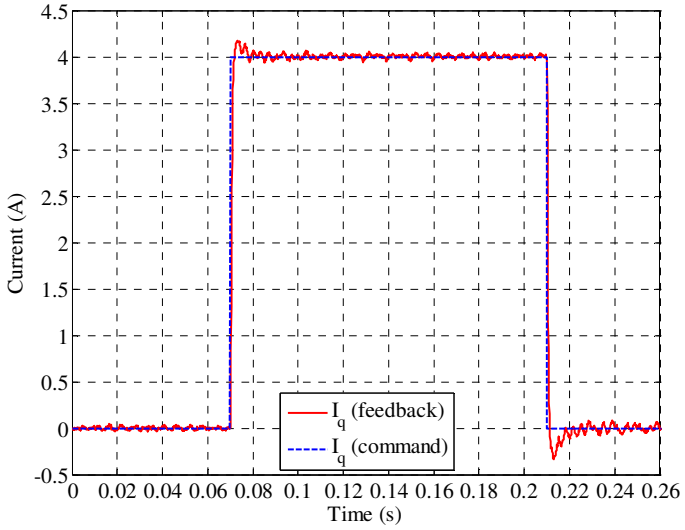

Fig. A-5: Current controller response to step loads (i_q=4A step) at 1000 r/min

Schematics

The schematics of the 5-phase inverter are attached in the following pages.

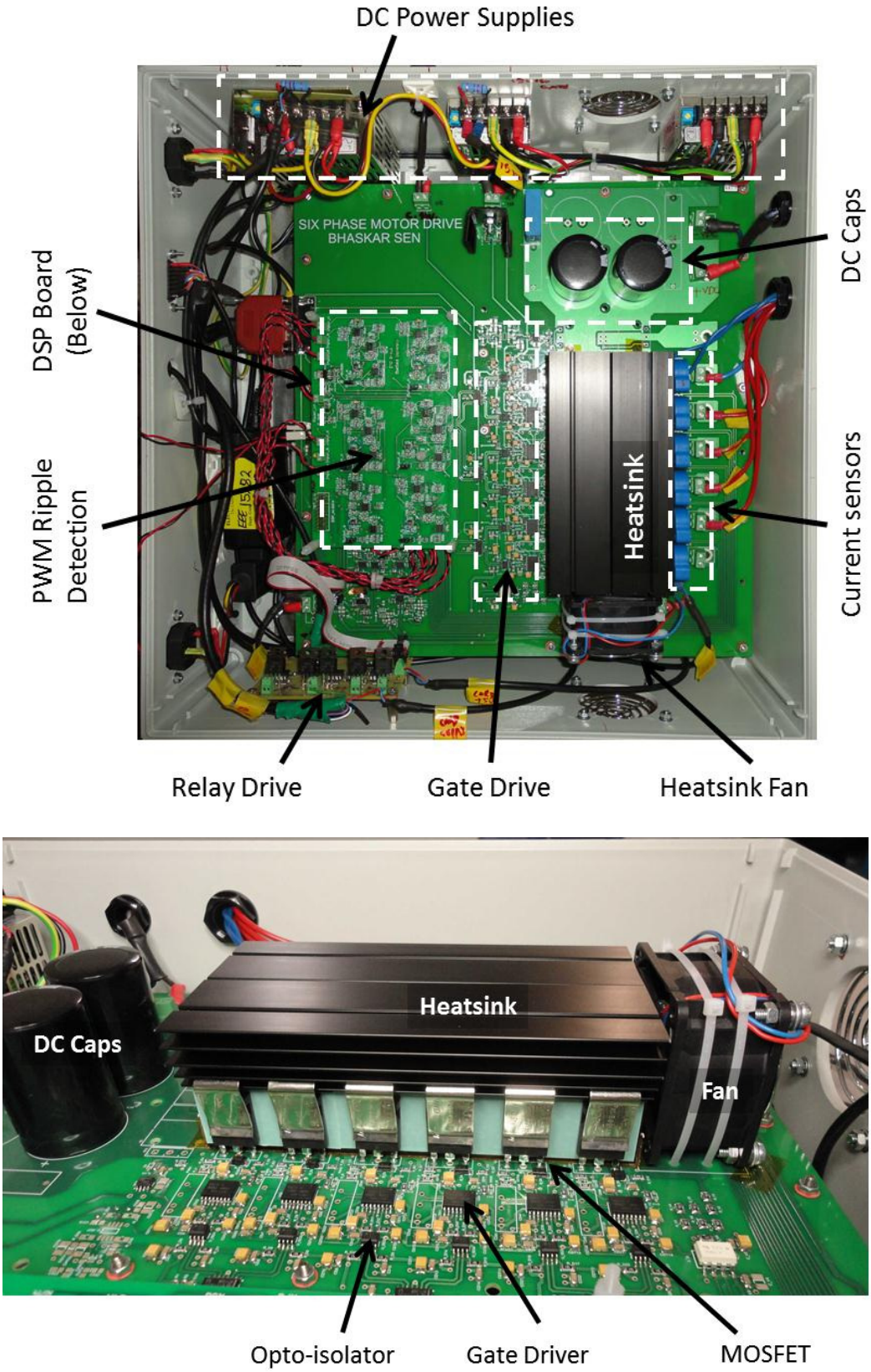

Fig. A- 6: Inverter Board

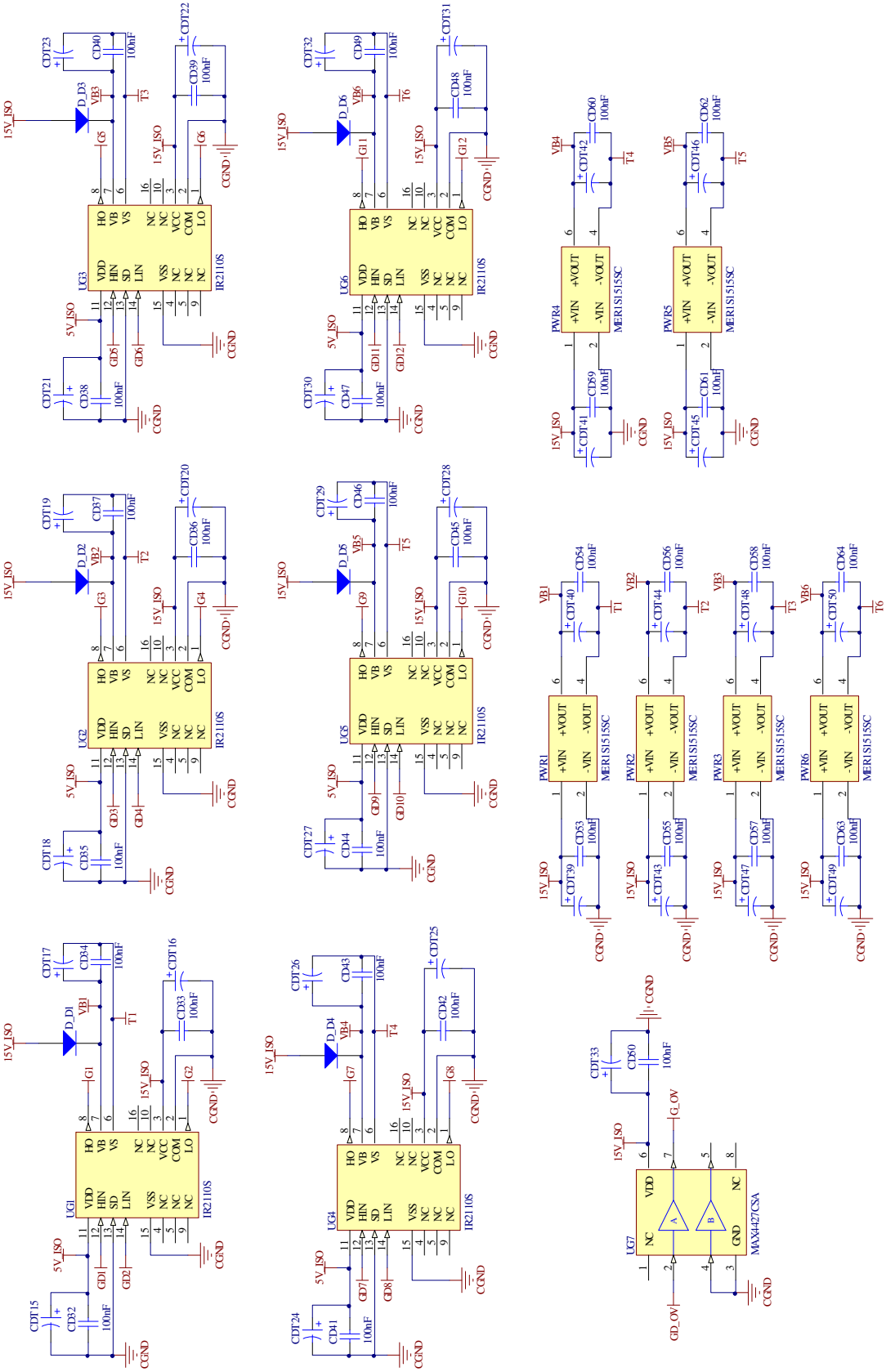

Gate driver Schematic

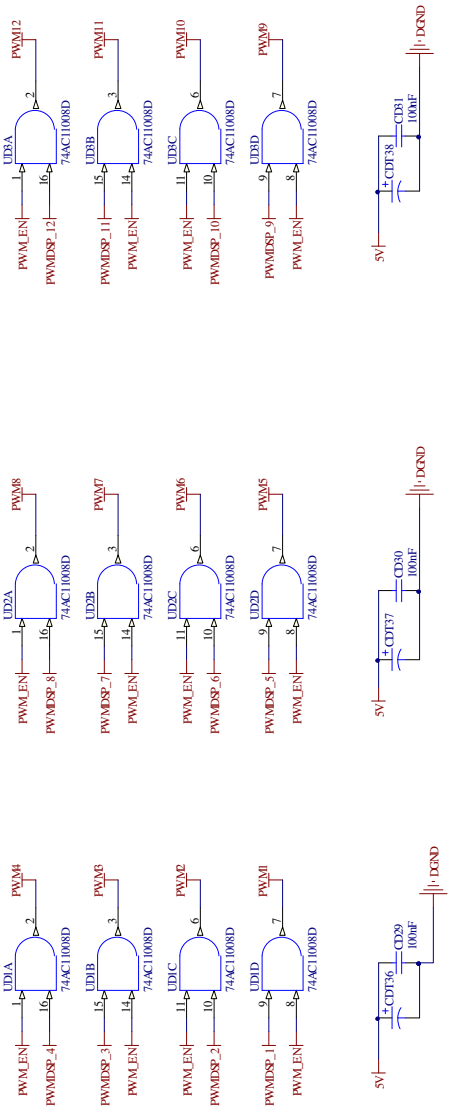

Gate Drive Interlock Schematic

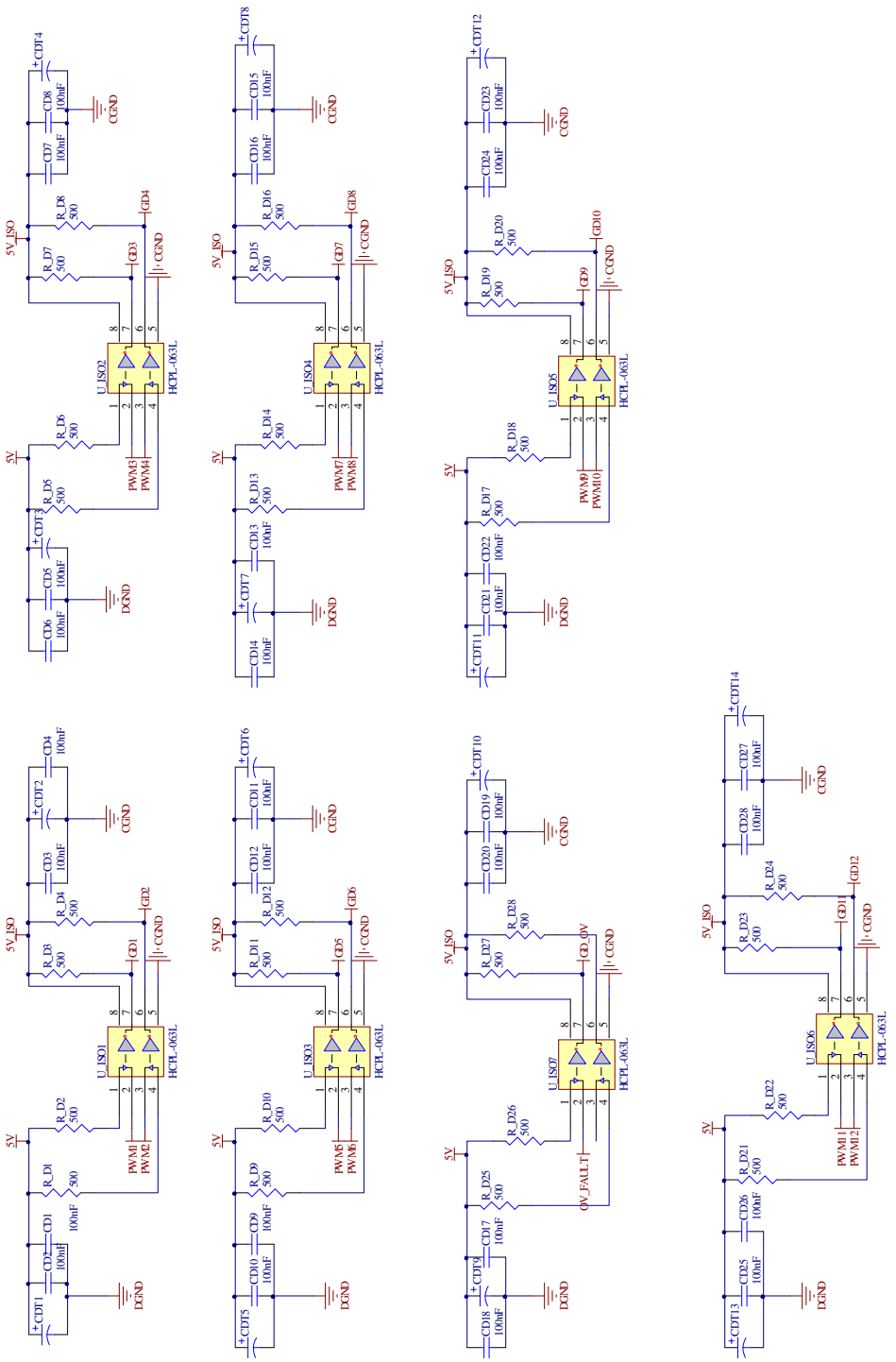

Gate Isolation Schematic

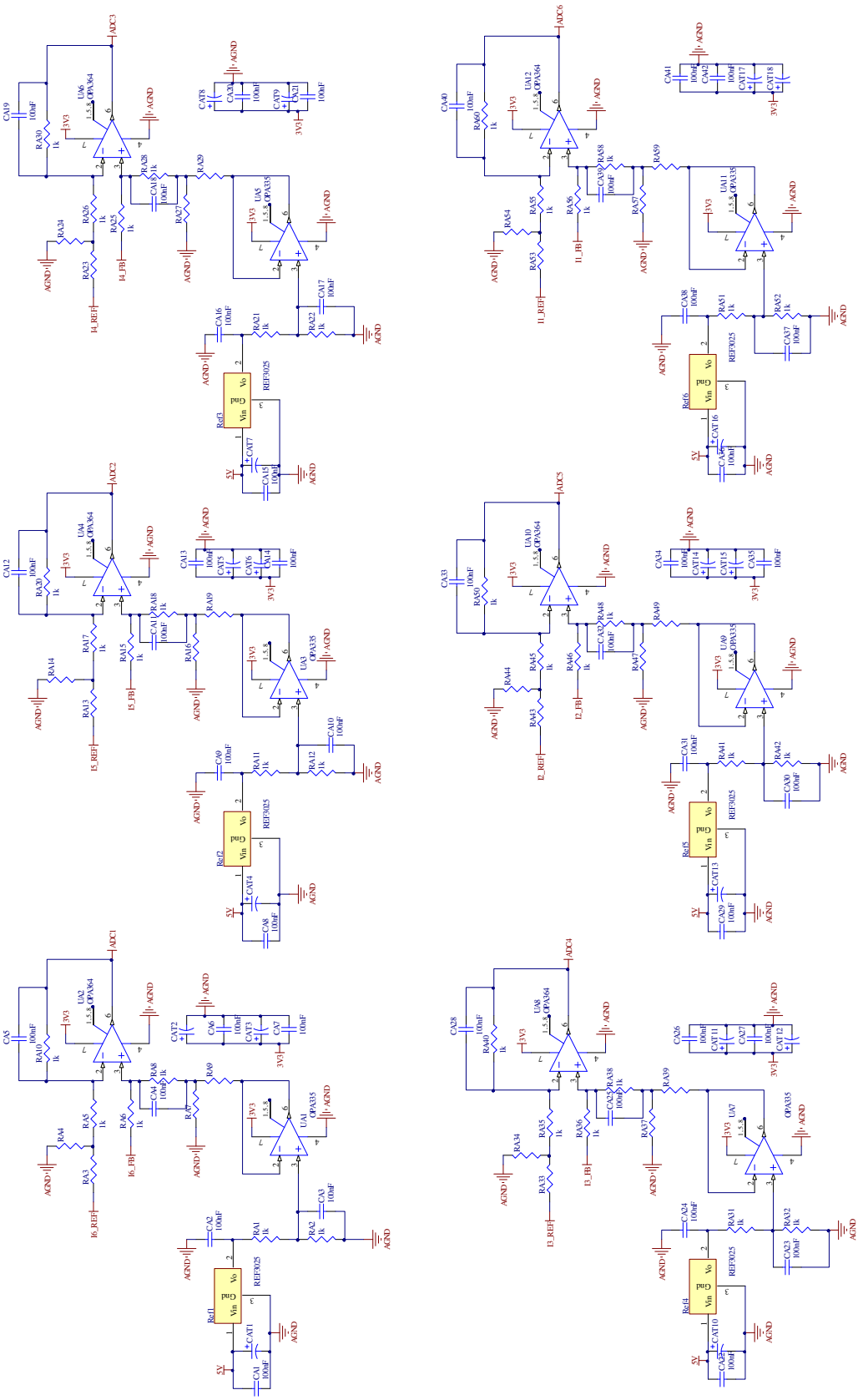

Analog Sensing (1/2)

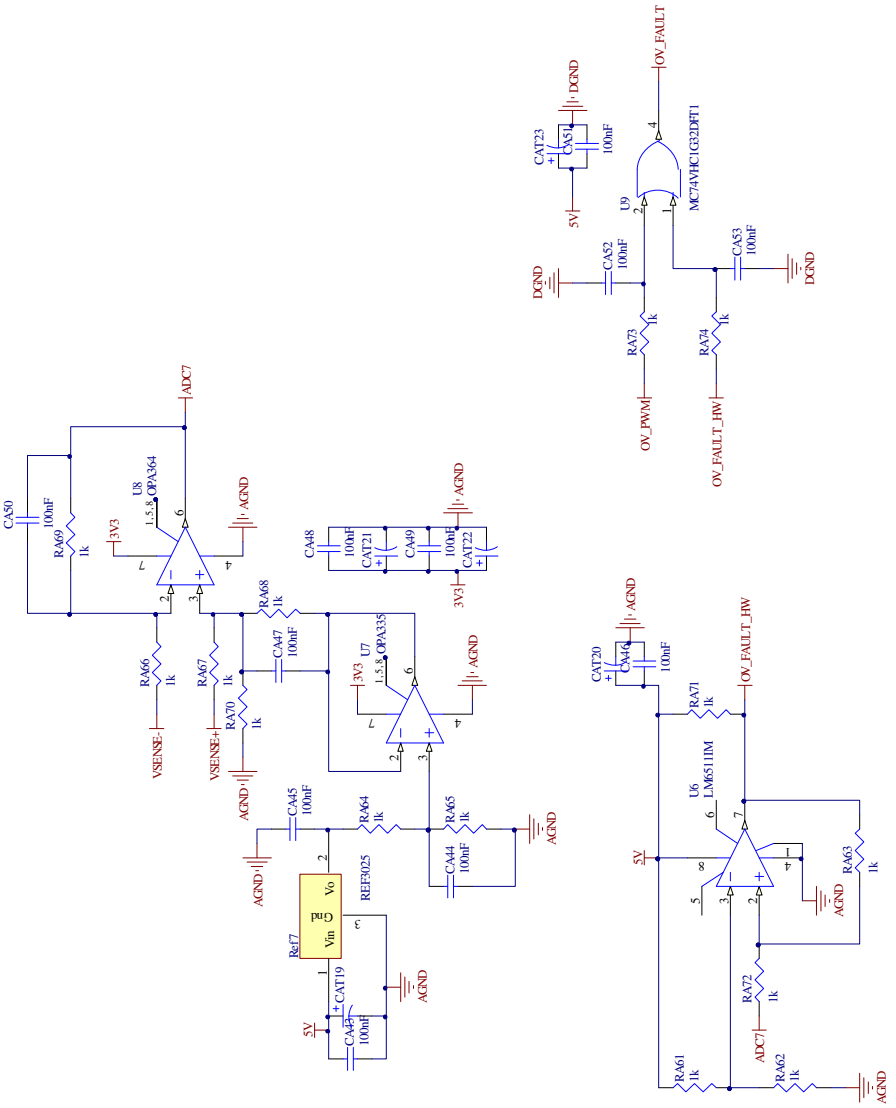

Analog Sensing (2/2)

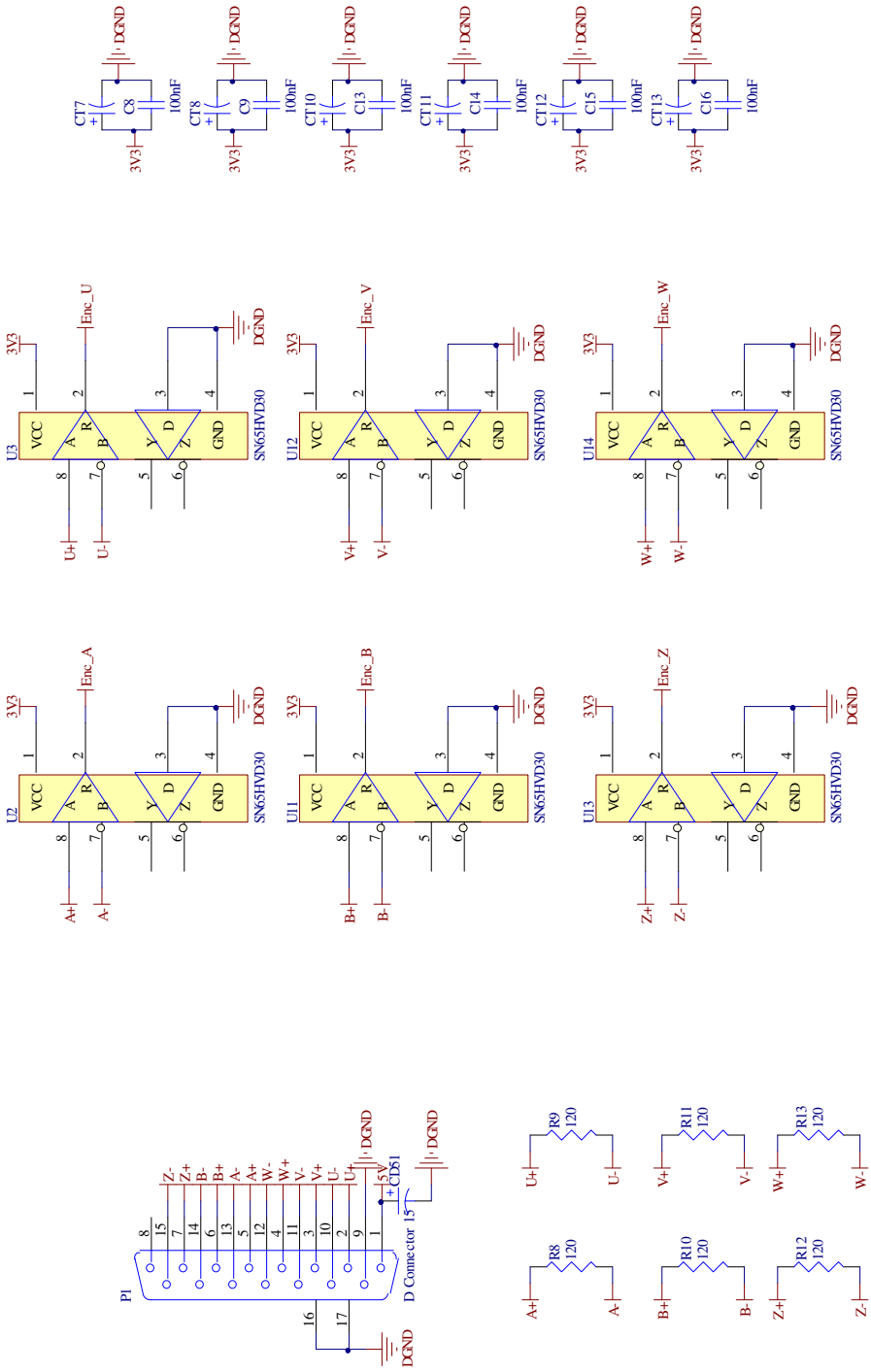

Encoder Interface Schematic

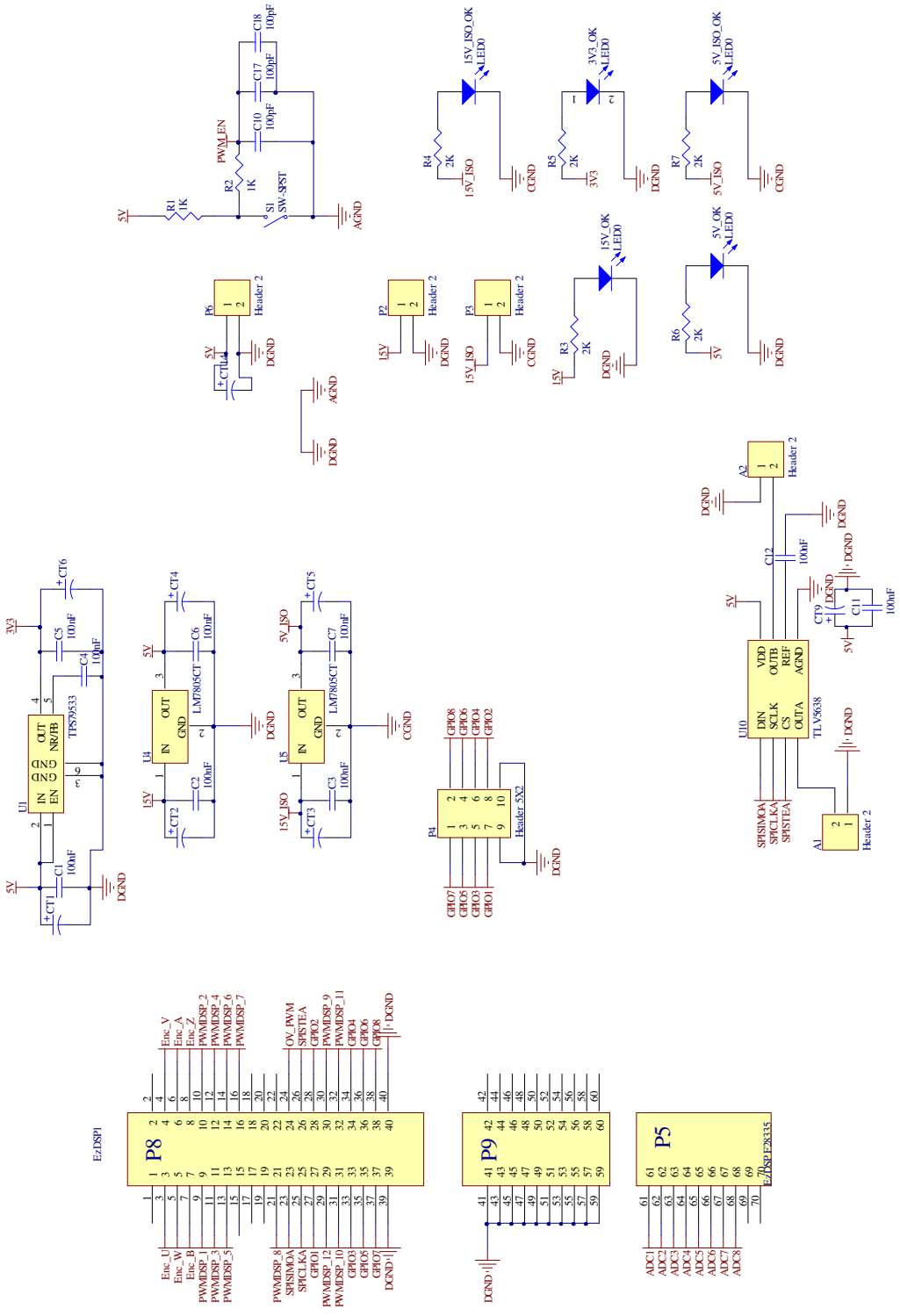

DSP Interface Schematic

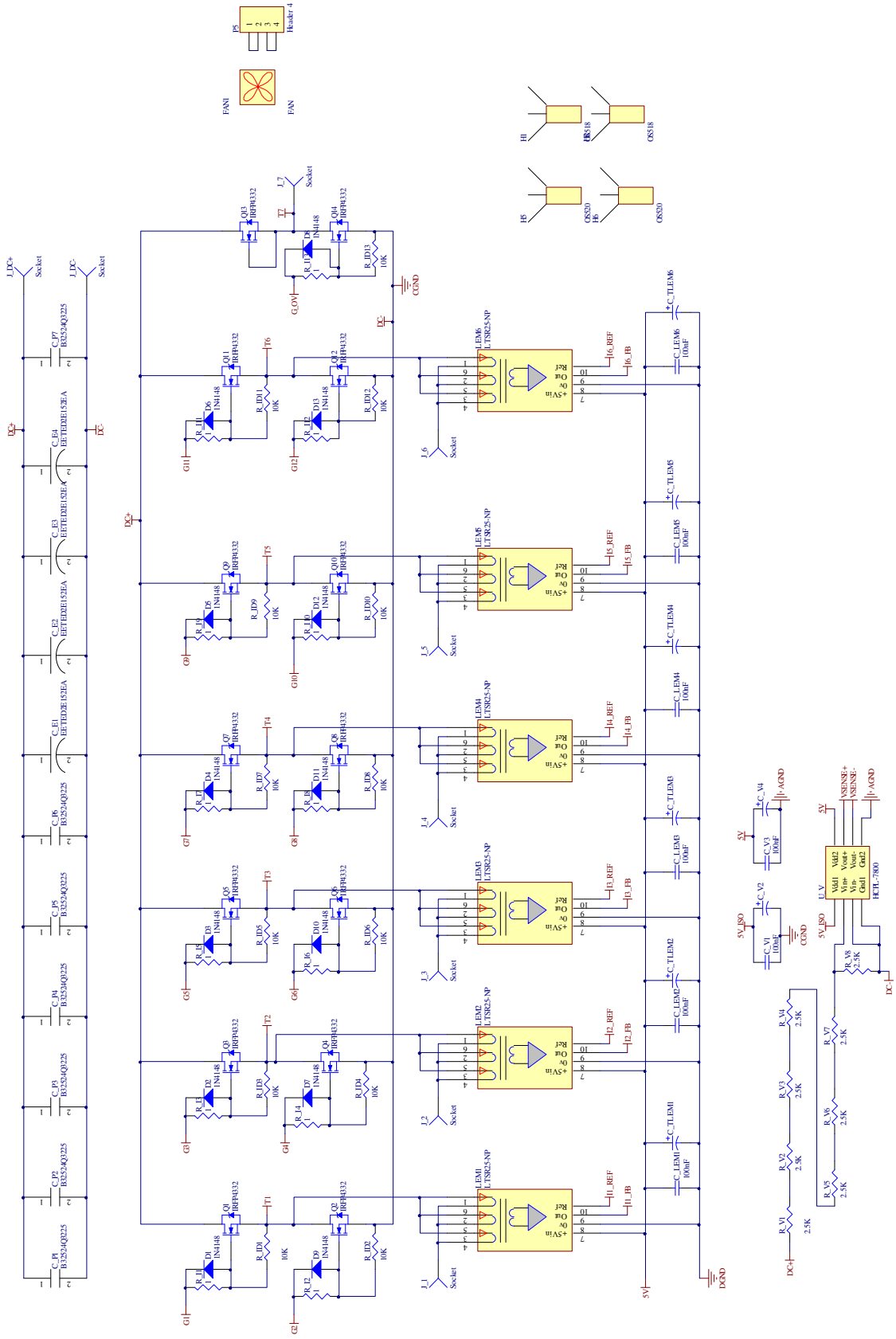

Inverter Schematic